Spiral wave dynamics and ventricular arrhythmias

Dit proefschrift kan ook worden bekeken op internet:
http://www-binf.bio.uu.nl/khwjtuss/PhDThesis
Op dit webadres staat niet alleen de tekst van het proefschrift, maar ook de filmpjes die van de simulaties uit de hoofdstukken 1, 3, 4, 5 en 6 zijn gemaakt.

This thesis can also be viewed on the internet:
http://www-binf.bio.uu.nl/khwjtuss/PhDThesis
At this webadress one can find both the text of this thesis and the movies that were made of the simulations from chapters 1, 3, 4, 5 and 6.

OMSLAG Kirsten ten Tusscher
DRUK Febodruk BV, Enschede
ISBN 90-393-3828-0

Spiral wave dynamics and ventricular arrhythmias

Spiraal golf dynamica en ventriculaire aritmieën

(met een samenvatting in het Nederlands)

Proefschrift

ter verkrijging van de graad van doctor aan de Universiteit Utrecht
op gezag van de Rector Magnificus, Prof. Dr. W. H. Gispen,
ingevolge het besluit van het College voor Promoties
in het openbaar te verdedigen op
maandag 29 november 2004 des middags te 14.30 uur

door

Kirsten Hendrika Wilhelmina Johanna ten Tusscher

geboren op 23 februari 1976
te Enschede.

Promotor:
Prof. Dr. P. Hogeweg
Faculteit Biologie
Universiteit Utrecht.

Co-Promotor:
Dr. A. V. Panfilov
Faculteit Biologie
Universiteit Utrecht.

The studies described in this thesis were performed at the department of Theoretical Biology and Bioinformatics at Utrecht University. The investigations were financially supported by the Priority Program Nonlinear Systems of the Netherlands Organization for Scientific Research (NWO).

Voor mijn ouders

Contents

1

General Introduction

Information transmission in the form of propagating waves of electrical excitation is the fastest form of long-range internal communication available to animals. It is used in both the nervous system and the heart. In the nervous system the electrical waves encode such diverse information as movements, perceptions and emotions, whereas in the heart the electrical waves initiate contracton of the cardiac muscle. Abnormal propagation of the electrical excitation wave has serious medical consequences, in the brain it is believed to be associated with epilepsy, whereas in the heart it leads to cardiac arrhythmias.

Among the most dangerous cardiac arrhythmias are the so-called reentrant ventricular arrhythmias: ventricular tachycardia and fibrillation, during which cardiac contraction rate is substantially increased, and, in the latter case, becomes completely disorganized. Ventricular fibrillation leads to sudden cardiac death and is the largest categorical cause of natural death in the industrialized world.

In this introduction we briefly discuss the important role of the specialized electrical conduction system of the heart in controlling normal heart rhythm, and the evolutionary and embryological development of the cardiac anatomy and conduction system of the mammalian heart. We than describe the two above mentioned reentrant arrhythmias that are the subject of this thesis, and discuss their possible mechanisms. Finally, we focus on the role of modeling studies in gaining a better understanding of cardiac arrhythmias and the model formalisms that are used. We end with a short outline of the modeling studies described in this thesis.

1.1 The Electrical Conduction Pathway of the Mammalian Heart

The mammalian heart consists of four chambers, the left and right atrium and the left and right ventricle. The right atrium and ventricle function as a pump for the pulmonary circulation, whereas the left atrium and ventricle function as a pump for the systemic circulation. For an effective pumping of this four-chambered heart a number of processes are important. First, all cells in the left and right atria should contract synchronously to ensure a fast and powerful atrial contraction and an efficient pumping of blood from the atria to the ventricles. Timing of the contraction of cardiac muscle cells is regulated via an electrical signal called action potential or excitation that serves as a trigger for contraction. Cardiac muscle cells generate such an action potential and subsequently contract when stimulated with an electrical current of a certain strength. Since cardiac cells are electrically coupled via so-called gap junctions, an action potential generated in a particular cell serves as a current source for a neighboring cell. As a consequence this neighboring cell also generates an action potential and contracts. Because of the strength of the electrical coupling between cardiac cells, fast propagating waves of electrical activity, called excitation waves, lead to virtually synchronous contraction of the cardiac muscle cells. Under normal conditions the excitation wave of the heart originates in the sino-atrial (SA) node, located in the upper right atrium. The SA node consists of so-called pacemaker cells that are automatically electrically active: they spontaneously generate action potentials with a certain frequency. From the SA node the electrical wave travels outward and excites all atrial cells, leading to atrial contraction.

As a next step, there should be a delay in cardiac activation and contraction between the atria and ventricles. This delay is necessary, because the ventricles should contract after being filled with blood supplied by the atria and hence after atrial contraction. The delay is regulated by the atrio-ventricular (AV) node. The atria and ventricles are electrically isolated except for the atrio-ventricular node, where the electrical signal is passed on from the atria to the ventricles with very low velocity, resulting in the required delay. From the AV node the electrical signal is passed on to the His bundle, the left and right bundle branches and the Purkinje fibers, which end on the endocardial surface of the left and right ventricular wall and septum, causing an electrical wave to spread through the ventricles that initiates ventricular contraction (Eckert *et al.*, 1988; Berne & Levy, 1993). The strong electrical coupling between the cardiac muscle cells again ensures a fast propagation of the excitation wave. This leads to a synchronized, powerful ventricular contraction and an efficient pumping of blood into the bloodstream.

Finally, cardiac output should be adapted to the oxygen demands of the organism. To achieve this, the autonomous nervous system regulates heart rate and contraction force, with sympathetic innervation increasing heart rate and force, and parasympathetic innervation having the opposite effect. Heart rate is regulated by changing the firing frequency of the SA node and the rate of transmission of the AV node (Eckert *et al.*, 1988; Berne & Levy, 1993). Contraction force is regulated by adapting intracellular calcium handling and tissue restitution properties.

1.2 Evolutionary and Embryological Development of the Mammalian Heart

In very small animals transport occurs through passive diffusion. In larger animals, where distances are too long for passive diffusion, hearts and circulatory systems evolved in parallel with increasing body sizes to efficiently transport respiratory gases, nutrients, waste products, hormones and heat.

Within the animal kingdom there is a great variety in circulatory systems. In invertebrates, circulatory systems vary from a body fluid moved by muscle contractions (small crustaceans), to single (some crustaceans and mollusks) or multiple (annelids, insects) tube-like hearts, to a complex, closed circulatory system (squids and octopuses) (Hill & Wyse, 1989; Withers, 1992). The multi-chambered vertebrate heart evolved from the tubular heart of a primitive chordate ancestor. Fishes have the most primitive vertebrate heart, consisting of four serially arranged compartments called sinus venosus, atrium, ventricle and conus arteriosus. These compartments arose through a looping process from the primitive tubular heart. In amphibians an atrial septum evolved, dividing the primitive atrium in a left and right atrium. In reptiles, birds and mammals two partially (some reptiles) or completely (the rest) separated ventricles evolved (Hill & Wyse, 1989; Withers, 1992; Moorman & Christoffels, 2003). Amphibians still have a sinus venosus and conus arteriosus. In reptiles, birds and mammals the sinus venosus is strongly reduced or lost, whereas the conus arteriosus has transformed into the pulmonary and aortic trunks from which the pulmonary and aortic arteries arise. The differences between the taxa are thought to reflect an evolutionary adaptation to increasing oxygen demands and changes in mode of respiration.

In parallel with the changes in overall heart morphology, changes occurred in the contractile function, electrical excitation properties, and intercellular electrical coupling of the cardiac muscle cells. The tubular heart of primitive chordates consists of automatically electrically active, weakly contracting, weakly electrically coupled muscle cells. This results in slow excitation waves and slow peristaltic contractions. In vertebrate hearts, only particular pacemaker cells have remained automatically electrically active. In addition, the muscle cells have become strongly electrically coupled and more powerfully contracting. These changes are due to changes in ionic currents, changes in intercellular gap junctional coupling and intracellular changes in numbers and organization of myofibrils, sarcoplasmic reticulum and mitochondria. Together, these changes lead to fast, synchronous contraction of the vertebrate heart (Moorman & Christoffels, 2003). To allow effective pumping of the chambered vertebrate hearts, the atria and ventricles should contract sequentially. This sequential contraction is regulated by the sino-atrial and atrio-ventricular nodes, the slow conducting parts of the specialized conduction system. It is thought that these slow conducting parts of the conduction system evolved from primitive tissue rings. These rings are positioned at the borders between chambers. They have kept their primitive properties, as opposed to the regions in between them that bulged out from the primitive tube to form the chambers (Moorman & Christoffels, 2003). These primitive rings initially led to regions of slow conduction and prolonged contraction between the chambers, thus ensuring sequential contraction. In a later stage these primitive rings evolved into the sino-atrial and atrio-ventricular node.

The embryonic development of the mammalian heart more or less recapitulates this evolutionary process. First, a primitive, peristaltically contracting tubular heart is formed that starts beating at day 22 in human embryonic development. This tubular heart develops into a four chambered fast and synchronously contracting heart, present by week 6 of development (for overviews of human cardiac embryology see http://embryology.med.unsw.edu.au/embryo.htm and http://www.visembryo.com/baby/index.html). The heart muscle tissue differentiates from automatically electrically active and weakly electrically coupled into strongly coupled with only pacemaker cells spontaneously firing action potentials. The primitive tissue rings between the chambers initially cause slow and prolonged contraction and later on transform into the sino-atrial and atrioventricular nodes (Gourdie *et al.*, 2003). The last part of the specialized conduction system that develops is the Purkinje system (Moorman & Christoffels, 2003), which leads to the reversal of the immature base-to-apex to the mature apex-to-base pattern of ventricular activation (Gourdie *et al.*, 2003).

1.3 Cardiac Arrhythmias

1.3.1 Types of Reentrant Cardiac Arrhythmias

Cardiac arrhythmias or heart rhythm disorders are conditions in which a failure in the timing and / or coordination of cardiac contraction occurs. Arrhythmias are mainly caused by abnormal formation of the excitation wave (abnormal automaticity or triggered activity), abnormal propagation of the excitation wave, or both. There are many different types of cardiac arrhythmias. The so-called reentrant arrhythmias that are caused by abnormal reentrant propagation of excitation waves are a frequently occurring and dangerous category.

Reentrant arrhythmias in the atria include *atrial tachycardia*, *atrial flutter* and *atrial fibrillation*. Atrial tachycardia is characterized by high but regular atrial excitation and contraction rates and is usually not dangerous. Atrial flutter is characterized by an even higher but still regular atrial rhythm. Atrial fibrillation is characterized by still higher atrial excitation rates, and a loss of coherence of atrial contraction. This leads to an increase of ventricular rhythm that results in a decrease of cardiac output and that may destabilize into ventricular fibrillation. Frequently occurring reentrant arrhythmias in the ventricles include *monomorphic* and *polymorphic ventricular tachycardia* and *ventricular fibrillation*. Monomorphic ventricular tachycardia and polymorphic ventricular tachycardia (among which *Torsade de Pointes*) lead to increased ventricular excitation and contraction rates and a decrease of cardiac output. In addition, both may destabilize into ventricular fibrillation. Ventricular fibrillation leads to a further increase in excitation rate and a loss of coherence of ventricular contraction that results in almost zero cardiac output. This will cause death to occur within minutes unless normal sinus rhythm is restored. In the United States sudden cardiac death accounts for $\sim 300,000$ deaths per year, of which $75 - 80\%$ are due to ventricular fibrillation. This is more than the number of deaths attributable to lung or breast cancer or AIDS (Zevitz, 2004). Ventricular tachycardia and fibrillation thus belong to the most dangerous cardiac arrhythmias. It is these two arrhythmias that are the subject of interest in this thesis.

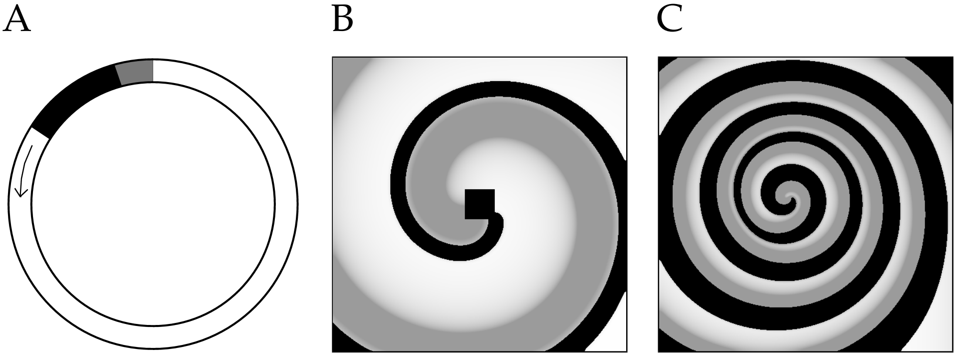

Figure 1.1: **A** Reentrant wave front in one-dimensional tissue: a single pulse traveling around a circular tissue cable. **B** Spiral wave rotating around an in-excitable square obstacle. **C** Free rotating spiral wave.

1.3.2 Mechanisms of Reentrant Cardiac Arrhythmias

The mechanism behind atrial flutter and a subset of cases of atrial tachycardia is thought to be so-called anatomical reentry. The term reentry was coined to describe a wave front that reenters and hence re-excites the same tissue again and again as opposed to the normal 'planar' wave front emitted by the sinus node that excites all tissue only once. If this re-excitation occurs at a rate higher than normal sinus rhythm, sinus rhythm gets suppressed and heart rhythm is controlled by the reentry, resulting in an increased heart rate. In one dimension, reentry is equivalent to a single pulse traveling around a circular cable of tissue (see Figure 1.1A) a phenomenon demonstrated both in experiments and models of excitable media (Mines, 1913; Wiener & Rosenblueth, 1946; Winfree, 1980). These dynamics are similar to what happens during tachycardia in the Wolff-Parkinson-White and Lown-Ganong-Levine syndromes in which an extra pathway connecting atria and ventricles is present. In two (or three) dimensions reentry can be caused by a spiral shaped wave front rotating around an inexcitable obstacle (see Fig. 1.1B). This was demonstrated using abstract models of excitable media (Wiener & Rosenblueth, 1946; Winfree, 1980; Zykov, 1987). This so-called anatomical reentry causes atrial flutter and some types of atrial tachycardia, by allowing fast rotation of the excitation wave around an anatomical obstacle such as a large vessel, tissue ridge or scar (Obel & Camm, 1997).

Ventricular tachycardia is also thought to be caused by a spiral shaped reentrant wave front. In modeling studies on excitable media it was shown that spiral waves do not necessarily rotate around an in-excitable obstacle, but can also rotate around a virtual, uninvadable object called spiral core that is formed by the refractory properties of the excitable medium (see Fig. 1.1C) (Selfridge, 1948). This type of reentry is called functional. Since the ventricles are more homogeneous, because they have much less tissue ridges and holes caused by large vessels relative to their tissue mass than the atria, ventricular reentry may be functional reentry. However, in particular cardiac diseases anatomical reentry

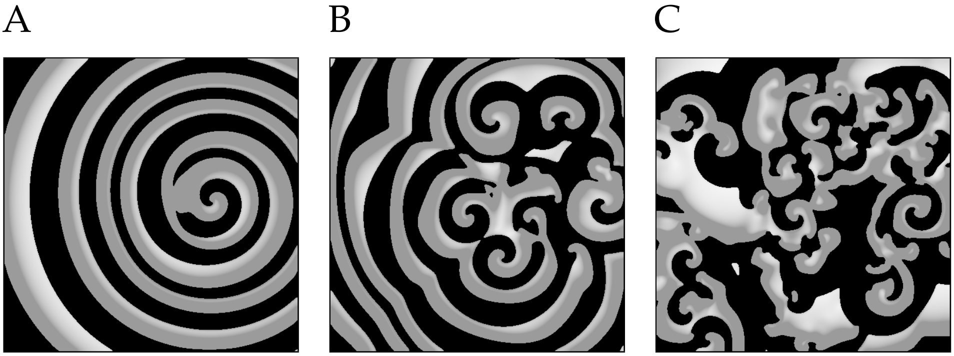

Figure 1.2: Formation of a turbulent state through spiral breakup. **A** Occurrence of the first wave break shortly after spiral wave formation. **B** Continued occurrence of wave breaks leads to the formation of multiple spirals. **C** After some time the turbulent state has spread across the entire medium. Spiral fragmentation occurs through the mechanism of so called steep restitution induced spiral breakup (for an explanation see section 1.3.3).

around the scar tissue formed in these diseases may also occur. Experimental proof of the possible presence of functionally reentrant spiral waves in cardiac tissue was first given by Allessie *et al.* (1973) in rabbit atrium, and later on by Davidenko *et al.* (1990, 1992) and Pertsov *et al.* (1993). It is nowadays a commonly accepted idea that most ventricular tachycardias are caused by a spiral shaped wave front.

Atrial and ventricular fibrillation are both thought to be caused by multiple chaotically wandering wavelets of excitation leading to chaotic uncoordinated contraction, an idea first formulated by Moe *et al.* (1964). However, opinions differ on how these wavelets arise. There are two main hypotheses (Rogers *et al.*, 1999; Panfilov & Pertsov, 2001; Weiss *et al.*, 2002; Choi *et al.*, 2002b). According to the spiral breakup hypothesis, the wavelets are the result of the fragmentation of an initial spiral wave (see Figure 1.2) (Panfilov & Pertsov, 2001; Weiss *et al.*, 2002). According to the fibrillatory conduction hypothesis the wavelets are the result of a single excitation source (see Figure 1.3) (Jalife *et al.*, 1998; Jalife, 2000; Zaitsev *et al.*, 2000). This source emits waves at such a high frequency that because of tissue heterogeneities they cannot be conducted at a 1 to 1 ratio in all parts of the tissue. This leads to local wave breaks and the formation of wavelets. The high frequency excitation source may either be a stable spiral wave or a so-called ectopic focus, a site other than the normal pacemaker sites that spontaneously fires action potentials. It has often been mentioned that there is a fundamental difference between the two hypothesized fibrillation mechanisms in self-sustenance of fibrillation. Spiral breakup fibrillation is necessarily self-sustained because of the instability of both initial spiral wave and subsequent wave fragments. In contrast, fibrillatory conduction is supposed to be non-sustained and supposed to end if the driving mother rotor or ectopic focus is abolished. However, this may perhaps only be true for small ventricles and atrial tissue (see next paragraph), where the wave fragments do not have enough space to form spiral waves, but

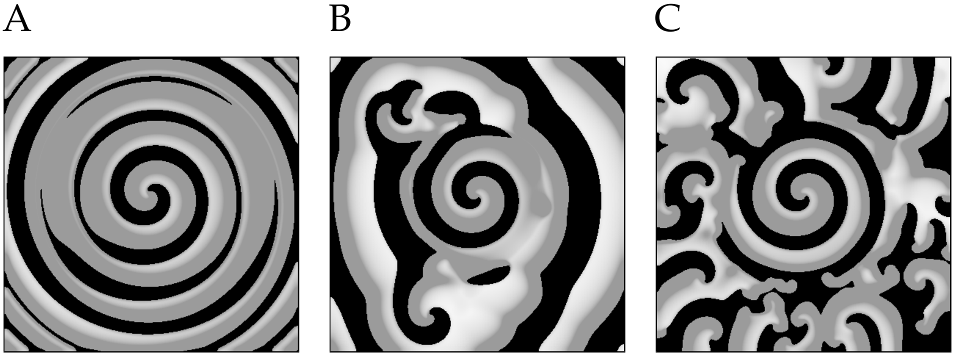

Figure 1.3: Occurrence of fibrillatory conduction in a medium that is heterogeneous in a parameter influencing spiral wave rotation period. In the middle of the medium is a circular area with the highest spiral wave rotation period. Outside this circle rotation period gradually declines equally in all directions. The initial spiral wave is formed with its tip inside the circle where spiral wave rotation is fastest. **A** Formation of the first wave breaks. **B** Subsequent occurrence of wave breaks leads to the formation of the first slower secondary spiral. **C** Continued occurrence of wave breaks leads to the formation of multiple slower secondary spirals. Note that the initial spiral wave remains present in the center of the medium, as opposed to the situation in Fig. 1.2.

not for larger ventricles were the wave fragments can give rise to multiple slower secondary spirals (see Fig. 1.3) (Ideker *et al.*, 2001).

Atrial fibrillation is thought to be caused most often by fibrillatory conduction (Jalife, 2003; Lemery, 2003; Waldo, 2003). This is consistent both with the highly heterogeneous character of the atria, and the fact that a lot of patients with atrial fibrillation can be cured through ablation of a site apparently serving as a source for the high frequency activity. However, currently it is not clear whether ectopic activity or (micro-) reentry serves as the source for fibrillatory conduction, and this may differ between different types of atrial fibrillation. For the very small guinea pig heart it has been shown that ventricular fibrillation can also be caused by fibrillatory conduction (Samie *et al.*, 2001; Warren *et al.*, 2003). However, in larger hearts fibrillatory conduction is considered unlikely and spiral breakup is considered to be the most likely mechanism underlying ventricular fibrillation (Choi *et al.*, 2002b; Rogers *et al.*, 2003; Valderrabano *et al.*, 2002).

1.3.3 Causes of Reentrant Ventricular Arrhythmias

Ventricular tachycardia In the case of ventricular tachycardia the question is what causes the normal ’planar’ wave front to change into a spiral shaped wave front. Spiral wave formation may occur in the presence of a large in-excitable obstacle. The obstacle can lead to a local block of a propagating wave front, and the breaking of the wave front into two separate wave fronts. Subsequent detachment of the two broken wave fronts from the obstacle leads to the formation of two spiral waves, a phenomenon called vortex shedding (see Figure 1.4) (Pan-

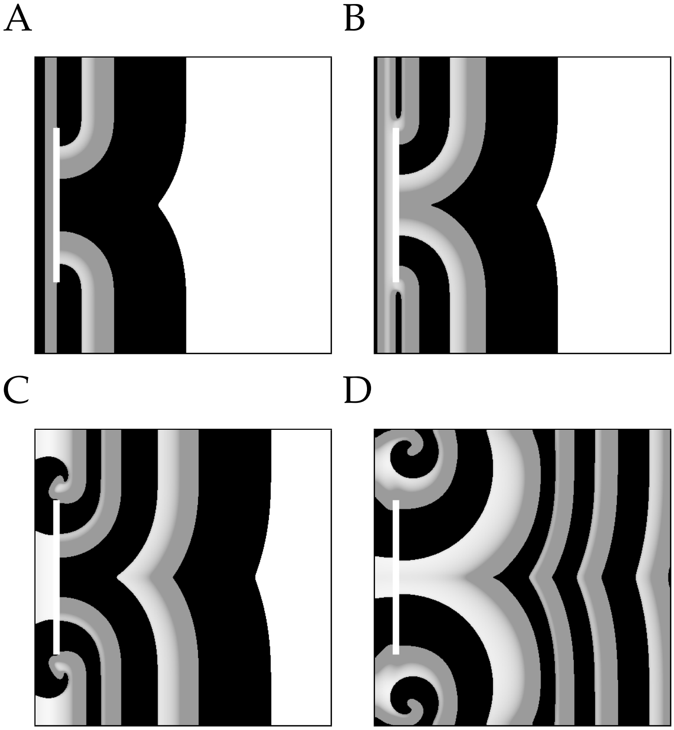

Figure 1.4: Formation of two spiral waves through vortex shedding: The white area represents an in-excitable obstacle present in the medium. The medium is stimulated at the left boundary, 3 stimuli are applied with a short coupling interval between the stimuli. **A** The waves initiated by the first two stimuli get temporally interrupted into two wave fronts by the obstacle but restore themselves by merging together into a single wave front again after they passed the obstacle. **B** The wave initiated by the third stimulus gets blocked and divides in to two wave fronts, but because of the low excitability caused by the partial refractoriness that remains after the two previous waves, instead of merging together, the two waves detach from the obstacle. **C** The ends of the two wave fronts curl around to form two spiral waves. **D** These two spiral waves subsequently remain stable.

filov & Keener, 1993a; Agladze *et al.*, 1994; Cabo *et al.*, 1996). A similar mechanism of spiral wave formation can occur in the presence of heterogeneity in the duration of the refractory period, when the regions with the longest refractory period serve as a functional rather than an anatomical block for wave propagation (Krinsky, 1966; Panfilov & Vasiev, 1991). A second mechanism for spiral wave formation occurs in the presence of a narrow isthmus (gap) between in-excitable obstacles. Waves propagating through a narrow isthmus experience a large so-called source-sink mismatch: the number of cells that are currently excited and serve as a current source is low for a wave propagating inside an isthmus, whereas the number of cells that need to be excited in order for the wave front to propagate and serve as a current sink is high just after the isthmus. This mismatch may lead to a local block of propagation just after the isthmus and a subsequent wave break and spiral wave formation (Cabo *et al.*, 1994; Fast & Kléber, 1997).

For an isthmus, or an anatomical or functional obstacle to actually result in conduction block, a new excitation wave should fall in the so-called vulnerable window of the tissue. This is the time frame after the previous excitation wave during which a new stimulation may lead to local conduction block and spiral wave formation. This vulnerable window is present under conditions of low excitability, high frequency of stimulation (see Figure 1.4), or a single short coupling interval between one stimulus and the next, and reflects the effects of tissue refractoriness. Below the lower limit of the vulnerable window, all tissue is still refractory and no wave propagation can occur. Beyond the upper limit of the vulnerable window no tissue is refractory any more and normal wave propagation occurs. It is between these two limits that local differences in tissue refractoriness allow local wave breaks to arise and persist. The width of the vulnerable window, and hence the vulnerability of the tissue to spiral wave formation, is enhanced under conditions of increased anatomical and functional tissue heterogeneity (Moe *et al.*, 1964; Krinsky, 1966; Kirchhof *et al.*, 1996; Behrens *et al.*, 1997; Ujhelyi *et al.*, 1999; Liu *et al.*, 2003; Antzelevitch *et al.*, 1999).

Clinically, ventricular tachycardia occurs in diseases in which the anatomical and/or functional heterogeneity of the heart is substantially enhanced, increasing both the chances for localized conduction block and the width of the vulnerable window for reentry formation. Ventricular tachycardia is associated with diseases such as coronary artery disease (myocardial infarction), cardiomyopathies, dysplasia and congenital heart diseases (Compton, 2002; Zevitz, 2004). In these diseases a remodeling of the cardiac tissue takes place, involving heterogeneous changes in ionic currents, calcium handling and gap junctional coupling of cardiac cells. In addition, an increase in in-excitable connective tissue (fibrosis) and an increased heterogeneity of nervous innervation occur. Ventricular tachycardia is also associated with inherited diseases such as the long QT and Brugada syndrome (Compton, 2002; Zevitz, 2004) in which ion channel mutations lead to a dramatic increase of the action potential duration dispersion present in the ventricular wall. Indeed, Wu *et al.* (1998) demonstrated a clear correlation between the site of conduction block and reentry and the local amount of fibrosis in explanted human hearts with dilated cardiomyopathy. In addition, Wu & Zipes (2001, 2002), and Akar *et al.* (2002) showed that transmural gradients in excitability and refractoriness induced under different conditions can lead to conduction block and reentry.

In addition to increasing the chances for conduction block and increasing the width of the vulnerable window, disease conditions can also enhance the occurrence of ectopic beats. Ectopic beats typically occur with a short coupling interval relative to one-another or the preceding sinus-induced beat. Therefore, these beats may fall in the vulnerable phase and serve as a triggering event for conduction block and spiral wave formation. Indeed, El-Sherif *et al.* (1997) demonstrated that reentrant arrhythmias in a dog model of the long QT syndrome were preceded by focal ectopic activity. In addition, Yan *et al.* (2001) showed that the focal activity triggering Torsade de Pointes in a rabbit long QT model was caused by early afterdepolarizations. The occurrence of early and delayed afterdepolarizations that lead to triggered, ectopic activity are linked to changes in intracellular calcium handling and action potential duration that typically occur in diseases such as the long QT syndrome, ischemia and heart failure (Volders *et al.*, 2000; Bers *et al.*, 2002). The subsequent formation and spread of a wave front initiated by an ectopic beat that can lead to the development of a reentrant arrhythmia is enhanced under conditions of reduced coupling, increased anisotropy and increased heterogeneity (see for example Wilders *et al.* (2000)) that also occur under these disease conditions.

Ventricular fibrillation In the case of ventricular fibrillation the question is how patterns of multiple chaotically meandering wavelets are formed. Clinically, ventricular tachycardia and fibrillation are linked to the same diseases. The occurrence of ventricular fibrillation is most often preceded by an initial phase of ventricular tachycardia. However, not much is known about the factors determining whether ventricular tachycardia remains stable or deteriorates into fibrillation. Ventricular tachycardia is organized by a rotating spiral wave and fragmentation of this spiral wave is considered to be the most likely mechanism leading to ventricular fibrillation. Therefore, the question which factors determine whether tachycardia deteriorates into fibrillation can be reformulated into the question under which conditions spiral breakup occurs. In theoretical and modeling research a number of hypotheses have been formulated regarding the mechanism through which spiral breakup occurs. Historically, heterogeneity in action potential duration and refractoriness was considered to play a major role in generating multiple wavelets (Moe *et al.*, 1964; Krinsky, 1966), whereas in the last decade dynamic heterogeneity induced by a steep action potential duration restitution (Nolasco & Dahlen, 1968; Guevara *et al.*, 1984), and three-dimensional heterogeneity caused by rotational anisotropy (Panfilov & Keener, 1995; Fenton & Karma, 1998) as well as transmural gradients of refractoriness (Pertsov & Jalife, 1995; Clayton & Holden, 2003) have received attention as mechanisms for spiral breakup.

The currently most actively pursued hypothesis for spiral breakup is the steep action potential duration restitution hypothesis. This steep restitution hypothesis relates the occurrence of alternans instability −the alternation of long and short action potentials− under high stimulation frequencies to the slope of the action potential duration (APD) restitution curve. The APD restitution curve relates the duration of an action potential to the duration of the preceding diastolic interval (DI), the interval between two consecutive action potentials in which ionic currents recover from refractoriness. APD alternans occurs if the slope of this curve exceeds one, because in this case small changes in diastolic interval lead to larger changes in action potential duration, which in turn lead to even larger changes in diastolic interval, etcetera (Guevara *et al.*, 1984; Nolasco & Dahlen, 1968; Courtemanche *et al.*, 1996). APD alternans can occur in one-dimensional tissue for the fast frequencies corresponding to spiral wave rotation and leads to oscillations in spiral arm wavelength that, when of large enough amplitude, lead to spiral wave breakup (Panfilov & Hogeweg, 1993; Karma, 1993, 1994; Qu *et al.*, 1999). Experimental support for the restitution hypothesis came from Koller *et al.* (1998), who showed that using a dynamic rather than the classical S1-S2 restitution protocol, slopes steeper than one could be obtained in myocardial tissue. Additional evidence came from studies showing that drugs that flatten APD restitution slope suppress fibrillation (Riccio *et al.*, 1999; Garfinkel *et al.*, 2000).

In recent years it has become evident from simulation studies using more realistic models for cardiac tissue that spiral wave stability not only depends on whether the APD restitution slope exceeds one but also on the range of diastolic intervals for which this is the case (Qu *et al.*, 1999; Garfinkel *et al.*, 2000). In addition, conduction velocity restitution and electrotonic interactions may both enhance or suppress steep restitution breakup (Cao *et al.*, 1999; Wu *et al.*, 2002; Wu & Patwardhan, 2004; Cherry & Fenton, 2004), and short term cardiac memory (Fenton *et al.*, 1999) may also suppress steep restitution breakup (Cherry & Fenton, 2004). Finally, the role of calcium dynamics in generating alternans and spiral breakup has recently received considerable attention (Shimizu & Antzelevitch, 1999; Chudin *et al.*, 1999; Omichi *et al.*, 2004; Pruvot *et al.*, 2004; Diaz *et al.*, 2004; Shiferaw *et al.*, 2003). In this context it is interesting to note that the drugs used to flatten APD restitution and suppress fibrillation work by blocking L-type calcium current (Riccio *et al.*, 1999; Garfinkel *et al.*, 2000). Given the fact that blocked calcium current leads to reduced calcium influx and accumulation, these experiments may just as well support the role of calcium alternans, rather than electrical restitution alternans, in spiral breakup and fibrillation.

Summarizing, ectopic activity and enhanced anatomical and functional heterogeneities are thought to play an important role in spiral wave formation. The interaction of these heterogeneities with dynamical tissue properties (restitution) and the instabilities (calcium overload) developing under the high frequencies of ventricular tachycardia are thought to play a role in the destabilization toward fibrillation. However, this knowledge is far from being complete or quantitative. What makes matters complex is that different factors may have different effects on initiation and maintenance of tachycardia, and destabilization toward and maintenance of fibrillation. As an example, we will show in chapter 3 how heterogeneity caused by small randomly distributed obstacles increases vulnerability to spiral wave formation, but at the same time suppresses spiral breakup.

As a final remark, it should be noted that ventricular tachycardia and fibrillation are not always caused by a reentrant wave pattern, but can also be caused by focal (triggered) activity, especially in the hearts of patients with cardiomyopathies (Chung *et al.*, 1997; Pogwizd *et al.*, 1998). These non-reentrant types of ventricular tachycardia and fibrillation are outside the scope of this thesis.

1.4 Modeling in cardiac electrophysiology

1.4.1 Why use models in cardiac electrophysiology

Modeling studies have a long-standing tradition and play an important role in cardiac electrophysiological research. One important reason to use models to study ventricular arrhythmias is that models are simpler than reality and therefore are a valuable tool for gaining more insight into complex processes. Many basic concepts involved in cardiac arrhythmias were first formulated based on simple, generalized models of excitable media. Examples are the multiple wavelet hypothesis for fibrillation (Moe *et al.*, 1964; Krinsky, 1966), spiral waves as the dynamics underlying tachycardia, spiral breakup and the subsequent spatiotemporal turbulence as the dynamics underlying fibrillation (Winfree, 1989; Panfilov & Holden, 1990), spiral wave generation induced by in-excitable obstacles (Agladze *et al.*, 1994), the vulnerable window of excitable media for spiral wave formation (Krinsky, 1966; Winfree, 1989), and the restitution hypothesis for spiral breakup and fibrillation (Nolasco & Dahlen, 1968; Guevara *et al.*, 1984; Panfilov & Hogeweg, 1993; Karma, 1993, 1994). In more recent years, models are used to help clarify the effect that ion channel mutations have on cellular action potential behavior (Wehrens *et al.*, 2000; Clancy & Rudy, 2002), and how aberrant cellular action potential behavior can lead to arrhythmogenesis in multicellular tissue (Viswanathan & Rudy, 2000; Akar *et al.*, 2002; Henry & Rappel, 2004).

Another reason for using models are the practical and ethical limitations to clinical and experimental research that do not apply to modeling research. Clinical research of human hearts is limited to noninvasive measurements such as ECGs and body surface mappings (Shimizu *et al.*, 2001; Saumarez & Grace, 2000; Stellbrink *et al.*, 1999), low risk invasive measurements such as catheter mapping and multi-electrode array mapping on hearts of people undergoing cardiac surgery (Shepard *et al.*, 1999; Moubarak *et al.*, 2000; Walcott *et al.*, 2002; Nash *et al.*, 2003; Nanthakumar *et al.*, 2004), and in vitro experiments on the few explanted human hearts available for research (Ikeda *et al.*, 1997; Wu *et al.*, 1998; Kawara *et al.*, 2001). In addition, more extensive research is performed on in vivo and in vitro hearts and tissues of guinea pigs (Samie *et al.*, 2001; Warren *et al.*, 2003; Gopalakrishnan & Malkin, 2003), rabbits (Mandapati *et al.*, 1973; Efimov *et al.*, 1999; Chen *et al.*, 2000; Wu *et al.*, 2002), dogs (Huang *et al.*, 2001, 2002) and pigs (Kim *et al.*, 1999a; Valderrabano *et al.*, 2001; Kim *et al.*, 1999b).

A further important problem with experimental research is that, due to the thickness of the ventricular wall, ventricular arrhythmias are a three-dimensional process. However, the experimental recording techniques, using electrodes and voltage sensitive dyes to map electrical activation, can only be applied with reasonable spatial resolution for surface recordings. The currently available extension of these techniques to the third dimension, using plunge needle electrodes (El-Sherif *et al.*, 1997), or voltage sensitive dyes in combination with tissue transillumination (Baxter *et al.*, 2001), or intramural optical fibers (Hooks *et al.*, 2001; Byars *et al.*, 2003) suffer respectively from poor spatial resolution, poor depth resolution and applicability only to tissue wedges, or are still under development. These problems are especially relevant given the rare observation of reentrant excitation patterns in surface recordings during ventricular tachycardia and fibrillation (Chen *et al.*, 1998; Kim *et al.*, 1998; Witkowski *et al.*, 1998; Rogers *et al.*, 1999; Zaitsev *et al.*, 2000; Nanthakumar *et al.*, 2004), and the possible intramural rather than transmural orientation of scroll waves (Aliev & Panfilov, 1996a; Valderrabano *et al.*, 2001) (see also chapter 6).

1.4.2 Model formalism

The excitable behavior of cardiac tissue has traditionally been described using either cellular automata (CA) models or partial differential equation (PDE) models. The first models used to study reentry by Wiener & Rosenblueth (1946) and fibrillation by Moe *et al.* (1964) were CA models. In these models, cells have a discrete state (resting, excited, refractory), and rules describe state transitions depending on the current state of the cell and its neighbors. Because of their computational simplicity, CA models have been used extensively in whole heart models to reproduce normal and abnormal excitation sequences (see Werner *et al.* (2000) for a recent example). However, in order to precisely model properties such as action potential duration and conduction velocity restitution and wave front curvature effects, large numbers of different states and a set of complex transition rules is needed. This will lead to the loss of computational simplicity of the CA model. Therefore, for studying the mechanisms behind onset and dynamics of reentrant arrhythmias, for which properties such as curvature and restitution are essential, usually PDE models are used.

The excitation process of a cardiac cell (or nerve cell) is governed by the flux of charged ions (predominantly Na^+, K^+, Ca^{2+} and Cl^-) through protein channels in the cell membrane. This ion flux leads to a change in transmembrane potential. This process can be mathematically described using the following differential equation (Keener & Sneyd, 1998):

$$C_m \frac{dV}{dt} = I_m + I \tag{1.1}$$

where C_m is the membrane capacitance, V is the transmembrane potential, I is the externally applied transmembrane current, and I_m is the sum of all transmembrane ionic currents. Integration of equation 1.1 gives us the time course of excitation of a single cardiac cell.

In cardiac tissue, the excitation wave spreads through the tissue because the cardiac cells are electrically coupled via gap junctions. To describe the propagation of the excitation wave from one cell to the next, equation 1.1 needs to be extended to incorporate the axial current flow between electrically coupled cardiac cells. This incorporation of axial currents is usually approximated as follows (Keener & Sneyd, 1998):

$$C_m \frac{\partial V}{\partial t} = I_m + I + \nabla D \nabla V \tag{1.2}$$

where D is a tensor describing the conductivity of the tissue and ∇ is the one, two or three-dimensional gradient operator. Integration of equation 1.2 gives us the time course of excitation and propagation of excitation in multicellular cardiac tissue.

1.4.3 FitzHugh-Nagumo and ionic models

To describe the excitable behavior of cardiac cells and tissues, we need, in addition to equation 1.1 or 1.2 from the previous section, one or more equations describing the dynamics of transmembrane ionic currents I_m.

There are two approaches for modeling the dynamics of I_m. One possible approach is to use phenomenological, two variable FitzHugh-Nagumo type models to describe the dynamics of I_m (FitzHugh, 1960, 1961; Nagumo *et al.*, 1962). By fitting the parameters of these models, they can reproduce important macroscopic characteristics of cardiac tissue such as activation threshold, duration of the refractory period, and action potential duration restitution (Kogan *et al.*, 1991; Aliev & Panfilov, 1996b; Fenton & Karma, 1998). The models have two main advantages. First of all, their simplicity makes them easy to understand, whereas parameter changes can easily be connected to particular conditions occurring in cardiac tissue. Second, their low dimensionality, combined with the fact that FitzHugh-Nagumo equations typically are less stiff than ionic equations, makes them computationally much less costly to solve in large spatial domains. As a consequence, FitzHugh-Nagumo type models have been used extensively to study the influence of macroscopic aspects such as three-dimensionality (Panfilov & Hogeweg, 1996), heterogeneity of action potential duration and refractoriness (Panfilov & Keener, 1993b; Clayton & Holden, 2003) and rotational anisotropy (Panfilov & Keener, 1995; Fenton & Karma, 1998; Qu *et al.*, 2000; Berenfeld & Pertsov, 1999) in three-dimensional tissue slabs, and of rotational anisotropy and anatomy in ventricular geometries (Panfilov, 1997; Aliev & Panfilov, 1996a; Panfilov, 1999; Clayton & Holden, 2004; Berenfeld & Jalife, 1998). However, the computationally efficient FitzHugh-Nagumo models have several important limitations. They lack the level of detail to investigate matters such as the effect of drugs acting on particular ionic currents, the effect of ion channel mutations, of different action potential shapes, and of intracellular calcium handling on spiral wave dynamics. To investigate these more detailed questions, ionic models are needed.

The second approach, applied in ionic models, is to use a set of equations that describe the dynamic behavior of individual ionic currents based on experimental voltage clamp data on the size, voltage and time dependence of these currents. Hodgkin & Huxley (1952) were the first who successfully applied this approach to describe the nerve action potential of the squid giant axon in 1952, and the approach was soon extended by Noble (1962) to describe cardiac action potential dynamics. Because of the development and improvement of experimental techniques, i.e., the change from multicellular to single cell voltage clamp, the development of the patch clamp technique, and of gene cloning and heterologous gene expression experiments, our knowledge of cardiac cells has expanded enormously over the last decades. It has become clear that cardiac action potentials are more complicated than nerve action potentials. In contrast to the short nerve action potentials, cardiac action potentials have a long lasting plateau phase that is necessary to ensure synchronous contraction across the myocardium. In addition, to couple excitation to contraction, cardiac cells have a complex intracellular calcium dynamics that feeds back on excitation. Finally, cardiac cells from the sinus node, atria, atrio-ventricular node, His bundles, Purkinje fibers and different parts of the ventricular wall differ in terms of upstroke velocities, durations, and responses to rate changes as a result of different types and sizes of ionic currents contributing to their action potentials.

The ongoing discovery of ionic currents and properties of intracellular calcium dynamics has driven the development of ever more complex cardiac cell models (Beeler & Reuter, 1977; DiFrancesco & Noble, 1985; Luo & Rudy, 1991, 1994; Noble *et al.*, 1998; Winslow *et al.*, 1999). The most frequently used ionic models are the Luo-Rudy phase 1 (simple) and phase 2 (more complex) models for guinea pig ventricular cells (Luo & Rudy, 1991, 1994), the Noble guinea pig ventricular cell model (Noble *et al.*, 1998), and the Winslow canine ventricular cell model (Winslow *et al.*, 1999). The most recent ionic cell models include a description of the intracellular ion dynamics and may consist of up to 60 ordinary differential equations. In addition, recently models have been developed that model whole-cell ionic currents as the summed stochastic behavior of a collection of individual ion channels, described using Markov state chain models. These models are used to explore the importance of locality and stochasticity of currents in determining action potential and calcium dynamics (Rice *et al.*, 1999; Greenstein & Winslow, 2002).

Because most experimental data are available for animal cardiac myocytes, most of the above mentioned models describe action potential dynamics for animals such as guinea pig and dog. In chapter 5 we develop an ionic model for human ventricular myocytes.

We use both ionic (chapters 2, 5 and 6) and FitzHugh-Nagumo type models (chapters 3 and 4) in this thesis.

1.5 This Thesis

In part I of this thesis (chapters 2, 3, and 4), our aim is to study general, basic properties of reentrant cardiac arrhythmias and how their dynamics are influenced by different forms of heterogeneity. We consider several types of heterogeneities that are known to be present in either healthy or diseased hearts: heterogeneity caused by a smooth gradient in current density (chapter 2), heterogeneity caused by fibrosis of cardiac tissue (chapter 3), and heterogeneity caused by the rotational anisotropy of the ventricular wall (chapter 4). The research described in part I is performed mainly using low dimensional (FitzHugh-Nagumo or simple ionic) models for cardiac cells and a simple, rectangular or cubic geometry for cardiac tissue.

In part II (chapters 5 and 6), our aim is to investigate specific features of ventricular tachycardia and fibrillation in the human heart. For that purpose we develop a new human ventricular cell model in chapter 5. All major ionic currents of the model are based on recent experimental data. In chapter 6 this model is used to study reentrant arrhythmias in an anatomically accurate human ventricular geometry.

Part I

In **chapter 2** we investigate the influence of linear gradients in ionic currents that affect action potential duration on the dynamics of spiral wave rotation. For this study we use the Luo-Rudy phase 1 ionic model (Luo & Rudy, 1991) to model tissue excitability.

In healthy hearts there are a number of gradients in ionic currents and action potential duration present. A well-known example is the epicardial-endocardial transmural gradient, caused by differences in density and dynamics of the transient outward current between epicardial and endocardial cells (Burton & Cobbe, 2001; Liu & Antzelevitch, 1995; Zygmunt *et al.*, 2000; Nabauer *et al.*, 1996; Wettwer *et al.*, 1994) and differences in density of slow delayed rectifier current and probably some other currents between non-M cells and M cells (Burton & Cobbe, 2001; Zygmunt *et al.*, 2000, 2001; Sakmann *et al.*, 2000). Other examples are the gradient between the left and right ventricle, caused by differences in density of the inward rectifier current (Samie *et al.*, 2001), transient outward current (Volders *et al.*, 1999; Di Diego *et al.*, 2002) and slow delayed rectifier current (Volders *et al.*, 1999); and the gradient between the base and apex of the heart, caused by differences in slow and rapid delayed rectifier currents (Burton & Cobbe, 2001). Apart from the gradients present in healthy hearts, new gradients may occur and already present gradients may be enhanced in particular diseases. As an example, local ischemia may lead to gradients in extracellular K^+ and H^+ concentrations (Burton & Cobbe, 2001), whereas in genetic disorders such as the Brugada and long QT syndrome, the ventricular transmural action potential duration gradient is enhanced (Antzelevitch & Fish, 2001; Clancy & Rudy, 2002; Wehrens *et al.*, 2002).

In **chapter 2** we investigate the influence of gradients in I_{K1} and I_K current density, both influencing action potential duration and spiral wave rotation period, on spiral wave dynamics. We show that both current density gradients lead to spiral wave drift. We quantify the effects of the gradients in terms of velocity and direction vector of the induced drift as a function of the magnitude of the gradient. By comparing and scaling the effects of the two different gradients we try to determine a general mechanism behind the gradient induced drift.

In **chapter 3** we investigate the influence of small randomly distributed inexcitable obstacles as a model for diffuse fibrosis on excitation wave propagation and the inducibility and stability of reentrant arrhythmias. This study was inspired by the clinical finding that people with large amounts of fibrotic, inexcitable tissue suffer substantially more often from ventricular arrhythmias, in particular tachycardia and fibrillation (De Bakker *et al.*, 1988; Wu *et al.*, 1998; Swynghedauw, 1999; Hsia & Marchlinski, 2002; Varnava *et al.*, 2001; Hayashi *et al.*, 2002; Jugdutt, 2003; Zevitz, 2004; Compton, 2002).

Fibrotic tissue is a type of connective tissue that is made by cells called fibroblasts that excrete materials (collagen and elastin primarily) that form the extracellular matrix that serves as a scaffold for the cardiomyocytes. Fibrotic tissue plays an important role in determining cardiac structure and passive mechanical properties (Bendall *et al.*, 2002; Jugdutt, 2003), but neither participates in electrical excitation nor in active contraction. Fibroblasts have been found to be electrically coupled to cardiomyocytes. However, the extracellular matrix materials of the fibrotic tissue electrically isolate cardiac muscle cells from each other and hence form obstacles for the electrical waves exciting the heart. In normal, healthy hearts fibrotic tissue makes up only 5-10% of the total cardiac tissue, but during the aging process, after an infarction, and in particular diseases such as cardiomyopathies, this may increase up to 35% (Ohtani *et al.*, 1995; Hein *et al.*, 2003).

Fibrotic tissue may occur in the form of localized, long fibrous strands, for example after an infarction, but it may also occur in the form of diffusely dispersed small pieces (Kawara *et al.*, 2001). Strand-like fibrosis can be modeled as an excitable medium in which a few large elongated obstacles are present. The influence of such obstacles on wave propagation has been studied extensively. It was shown that large obstacles blocking conduction can lead to vortex shedding and spiral wave formation (Panfilov & Keener, 1993a; Cabo *et al.*, 1996), and that narrow isthmuses present between the obstacles can also lead to local conduction block and spiral wave formation (Agladze *et al.*, 1994; Cabo *et al.*, 1994; Fast & Kléber, 1997). In addition, spiral waves may become anchored to an obstacle, leading to stabilization of spiral wave rotation. Diffuse fibrosis can be modeled as an excitable medium in which a large number of small in-excitable obstacles are randomly dispersed over the medium. The potential role of such obstacles in arrhythmogenesis has not yet been extensively investigated. Presumably, in this case it will be the collective influence of the obstacles on wave propagation, rather than the interaction of waves with individual obstacles, that will be of importance.

In **chapter 3** we use a FitzHugh-Nagumo type model to describe excitable media in which we randomly disperse large numbers of small, square in-excitable obstacles. To quantitatively study the influence of the obstacles we vary the percentage of grid points in the medium occupied by obstacles. We study the influence of the obstacles on various aspects of wave propagation: planar wave conduction velocity, curvature effects, the vulnerability of the medium to spiral wave formation, and the stability of spiral wave dynamics.

In **chapter 4** we develop and demonstrate a method for predicting the position and shape of filaments of stable scroll waves in three-dimensional excitable media with a complex diffusion tensor. The ability to predict the stable filament orientation of scroll waves present in complex excitable media such as the heart would allow us to investigate which are the most likely positions for scroll waves to reside in the ventricular wall. In a more general sense, by being able to predict filament orientation, we can investigate the dependence of filament position and shape on the tissue diffusivity tensor in an efficient manner without having to do time-consuming three-dimensional simulations of scroll wave behavior.

Cardiac tissue has a very complex structure that results in an asymmetric propagation of the excitation waves. The tissue consists of cardiac muscle cells that have an elongated shape and that are organized into muscle fibers in a head to tail orientation. This organization, together with the fact that intercellular resistance (across gap junctions) is much higher than intracellular resistance (myoplasm), causes wave propagation to be much faster parallel to the muscle fibers than in the direction perpendicular to the fibers. This asymmetry of propagation speeds is usually referred to as ‘tissue anisotropy’. Muscle fiber direction changes in a complex manner throughout the ventricular wall. Generally speaking it makes a smooth, counterclockwise rotation of about 120 degrees throughout the wall and than changes its direction abruptly at the border of the ventricular wall and the endocardial layer (Hort, 1957; Thomas, 1957; Streeter *et al.*, 1969; Streeter, 1979). This property of cardiac tissue is called 'rotational anisotropy'. Furthermore, the muscle fibers are organized into discrete muscle layers consisting of parallel oriented muscle fibers, separated from other layers by cleavage planes of interstitial connective tissue (LeGrice *et al.*, 1995; Hunter *et al.*, 1997; Hooks *et al.*, 2001). As a consequence, muscle fibers in the same plane are more strongly electrically coupled than muscle fibers in different planes. The orientation of these muscle planes changes through the ventricular wall. So, summarizing, in cardiac tissue three axes of different propagation speeds can be distinguished: parallel to the muscle fibers, parallel to the muscle fiber plane, and perpendicular to the muscle plane (Hunter *et al.*, 1997; Hooks *et al.*, 2001). This is called 'orthotropic anisotropy'.

From theoretical studies of scroll waves we know that in the case of positive filament tension non-closed filaments assume a stable conformation (Panfilov & Rudenko, 1987; Keener, 1988; Panfilov *et al.*, 1989; Biktashev *et al.*, 1994) which shape is determined by the anisotropy of the medium. Stable filaments have the shape of a straight line in isotropic and simple rotationally anisotropic media, but have a more complex shape in more complex anisotropic media (Berenfeld & Pertsov, 1999; Wellner *et al.*, 2000; Berenfeld *et al.*, 2001). Recently, Wellner *et al.* (2002) proposed a so-called minimal principle for rotor filaments that allows analytical prediction of filament shapes in anisotropic media. However, the practical application of their principle requires a priori knowledge of the medium's diffusivity tensor and of the position of the filament ends on the medium boundaries. In **chapter 4** we show that the minimal principle of Wellner *et al.* (2002) can be interpreted as a minimum travel time principle. As a consequence, the stable filament shape can be found as the path of shortest travel time for a wave propagating through the same medium as in which the scroll wave rotates. This implies that standard shortest path wave algorithms can be used to predict filament shape. Our method allows the prediction of filament shape and position without requiring a priori knowledge of the medium's diffusivity tensor or the position of filament ends on the medium's boundaries. As a consequence, provided that 3D arrival times can be determined in electrophysiological experiments, the method can be applied to real cardiac tissue. In **chapter 4** we perform numerical simulations of orthotropically anisotropic three-dimensional media. We simulate both scroll waves and normal wave propagation combined with shortest path wave algorithms and compare actual and predicted scroll wave filaments.

Part II

In **chapter 5** we develop a new, detailed electrophysiological model of the human ventricular myocyte.

The ultimate purpose of our research is to gain a better understanding of the mechanisms behind reentrant ventricular arrhythmias in the human heart. However, most experimental data and electrophysiological models are for guinea pig or dog myocytes. It is apparent that these animal's hearts differ substantially from human hearts in matters such as heart size, range of physiologically healthy heart rates, action potential duration, type, size and ratio of ionic currents, but also frequency and wave patterns of induced arrhythmias. These differences may all be relevant for if, how and which arrhythmias arise. Therefore, we would like to model human rather than animal ventricular cells and tissues. Currently, the only available model for human ventricular myocytes is that of Priebe & Beuckelmann (1998). This model was based on a limited set of data on human ventricular cells combined with formulations from the Luo-Rudy phase-2 guinea pig model (Luo & Rudy, 1994). In addition, the model results in unrealistically long action potential duration. Because of the current availability of voltage clamp data for all major human ventricular ionic currents, we decided to develop a new model for human ventricular myocytes. In **chapter 5** we describe the construction and characteristics of this new model.

We use detailed voltage clamp data on human ion channels to fit maximum conductance, and time constant and steady state voltage dependence of activation and inactivation gates of the Hodgkin-Huxley type formulations for the fast sodium, L-type calcium, transient outward, slow delayed rectifier, rapid delayed rectifier and inward rectifier currents. The new model has distinct formulations for human ventricular epicardial, endocardial and midmyocardial (M) cells based on experimentally found differences in ionic currents between these three cell types. We validate the model against experimental data on current-voltage curves, action potential shape, action potential duration restitution, and differences between the three different cell types. An important aspect of our model is its new sodium current formulation. Recently, a lot of detailed voltage clamp experiments have been performed on cloned human sodium channels (see for example (Nagatomo *et al.*, 1998; Wan *et al.*, 2001; Makita *et al.*, 2000)). Based on these data Markov state chain models have been formulated for the sodium current to compare the effects of wild type and mutant channels on action potential behavior (Clancy & Rudy, 2002; Wehrens *et al.*, 2000). However, these data have not yet been used to revise the Hodgkin-Huxley type sodium current formulation applied in large-scale spatial simulations. The formulation used in most spatial models is that of the Luo-Rudy phase-1 model (Luo & Rudy, 1991). This formulation is largely based on relatively old *multicellular* voltage clamp data from chicken *embryonic* heart cells (compare to section 1.2) (Ebihara *et al.*, 1980; Ebihara & Johnson, 1980), combined with data from a few other animal species (Gettes & Reuter, 1974; Beeler & Reuter, 1977). We decided to use the new cloned sodium channel data to construct a new Hodgkin-Huxley type sodium current formulation. This decision was based on the fact that sodium current dynamics determine conduction velocity restitution, which is considered to be an important determinant of spiral wave stability. We show that our new formulation results in conduction velocity restitution behavior that agrees much better with experimental data than the Luo-Rudy phase 1 sodium current formulation.

We want to keep our human ventricular cell model computationally efficient enough for the large-scale spatial simulations that are needed to study reentrant arrhythmias. Therefore, we incorporate a calcium dynamics of a complexity similar to that of other models used for spatial simulations, but much less complex than that of recently developed single cell models that are used to study details of calcium handling. The effectiveness of our calcium dynamics formulation is demonstrated by showing that our model is capable of reproducing the positive force-frequency staircase typical of human myocardium. We demonstrate the feasibility of performing spatial simulations using our model and investigate spiral wave dynamics in a large epicardial tissue sheet for the standard parameter settings of our model.

In **chapter 6** we use our new human ventricular myocyte model to study the dynamics of simulated reentrant arrhythmias in two-dimensional tissue sheets and in an anatomically accurate model of the human ventricles.

Most previous studies on reentrant ventricular arrhythmias in anatomically based geometries used canine ventricular anatomies combined with FitzHugh-Nagumo or Fenton-Karma type models for the excitable character of the muscle cells (Aliev & Panfilov, 1996a; Berenfeld & Jalife, 1998; Panfilov, 1999; Clayton & Holden, 2004). The canine ventricles are used because of the limited availability of human hearts, especially structurally normal ones. As a consequence, much less anatomical data are available for human hearts than for the extensively studied canine heart. The FitzHugh-Nagumo and Fenton-Karma models are used for simple reasons of computational tractability. Using this modeling approach, the role of a local inhomogeneity caused by an infarction and the role of the Purkinje network in arrhythmia initiation were investigated (Aliev & Panfilov, 1996a; Berenfeld & Jalife, 1998). In addition, the role of reentry in fibrillation was quantified by counting filaments, the organizing centers of scroll waves (Winfree & Strogatz, 1984; Panfilov, 1999; Clayton & Holden, 2004).

Recently, due to the increase in computational power, researchers have started to use ionic models in ventricular geometries to study reentrant arrhythmias. Xie *et al.* (2004) combined the Luo-Rudy phase 1 model with a canine ventricular geometry. They demonstrated that both the complex geometry and the anisotropy of the ventricles enlarged the region in parameter space where steep restitution mediated spiral breakup and fibrillation occur. Bernus *et al.* (2003) used a human ventricular geometry combined with a reduced version of the Priebe-Beuckelmann model (Bernus *et al.*, 2002; Priebe & Beuckelmann, 1998) to study reentrant arrhythmias. They showed that scroll wave stability depends on its position in the ventricular wall and demonstrated fibrillation-like dynamics after simulating the application of the potassium channel opener chromakalim.

The Xie *et al.* (2004) and Bernus *et al.* (2003) models are an improvement over the previous ones using FitzHugh-Nagumo and Fenton-Karma type models. They allow us to study the effect of changes in individual ion channel conductances, the effect of different action potential shapes, and the effect of APD and CV restitution on arrhythmia dynamics. However, both models do not incorporate intracellular ion dynamics. Given the accumulating evidence that intracellular calcium dynamics plays a critical role in arrhythmogenic phenomena such as afterdepolarizations and triggered activity (Volders *et al.*, 2000; Bers *et al.*, 2002; Choi *et al.*, 2002a) and alternans (Shimizu & Antzelevitch, 1999; Pruvot *et al.*, 2004; Diaz *et al.*, 2004), this is an important limitation of these models. Furthermore, although the work by Bernus *et al.* (2003) is the first study on reentrant arrhythmias in the human ventricles, it should be noted that the used Priebe-Beuckelmann model is still largely based on animal data, as discussed above.

In **chapter 6** we combine our recently developed human ventricular cell model that incorporates intracellular calcium dynamics with an anatomically detailed human ventricular geometry that incorporates fiber direction anisotropy. We perform a first, basic study of the dynamics of ventricular tachycardia and fibrillation. We compare the ECGs, activation frequencies, and surface wave patterns of our simulated arrhythmia episodes with clinical observations. Finally, we determine the number of scroll wave filaments present during fibrillation in the human ventricles. We demonstrate a good agreement between characteristics of simulated and clinically observed ventricular tachycardia and fibrillation. In addition, we show that fibrillation in the human ventricles may be organized by only a few reentrant sources.

Part I

The influence of heterogeneity on spiral wave dynamics

2

Reentry in heterogeneous cardiac tissue described by the Luo-Rudy ventricular action potential model

K. H. W. J. Ten Tusscher and A. V. Panfilov
Department of Theoretical Biology, Utrecht University
Padualaan 8, 3584 CH Utrecht, The Netherlands.

Am J Physiol Heart Circ Physiol **284**: H542–548 (2003)

Abstract

Heterogeneity of cardiac tissue is an important factor determining the initiation and dynamics of cardiac arrhythmias. In this paper we study the effects of gradients of electrophysiological heterogeneity on reentrant excitation patterns using computer simulations. We investigated the dynamics of spiral waves in a two-dimensional sheet of cardiac tissue described by the Luo-Rudy phase 1 (LR1) ventricular action potential model. A gradient of action potential duration (APD) was imposed by gradually varying the local current density of K^+ current or inward rectifying K^+ current along one axis of the tissue sheet.

We show that a gradient of APD resulted in spiral wave drift. This drift consisted of two components. The longitudinal (along the gradient) component was always directed toward regions of longer spiral wave period. The transverse (perpendicular to the gradient) component had a direction dependent on the direction of rotation of the spiral wave. We estimated the velocity of the drift as a function of the magnitude of the gradient and discuss its implications.

2.1 Introduction

Various experimental and theoretical investigations show that many dangerous cardiac arrhythmias are driven by reentrant sources of excitation (Allessie *et al.*, 1973; Gray *et al.*, 1995b; Winfree, 1989, 1994). In many of these cases, such reentrant sources are shown to be rotating spiral waves of excitation (Davidenko *et al.*, 1990, 1992; Lee *et al.*, 1996; Pertsov *et al.*, 1993; Starmer *et al.*, 1991). The dynamics of spiral waves is considered to be an important factor in determining the type of cardiac arrhythmia that will occur: stationary rotation of spiral waves is associated with monomorphic tachycardias, whereas non-stationary rotation or drift can cause polymorphic tachycardias and Torsade de Pointes (Garfinkel & Qu, 1999).

Spiral wave dynamics is in many ways affected by the ionic heterogeneity of cardiac tissue. Ionic heterogeneity is considered to be one of the main factors underlying the initiation of spiral waves in the heart (Krinsky, 1966; Moe *et al.*, 1964). In addition, ionic heterogeneity is thought to play an important role in the transition from a spiral wave excitation pattern to the spatiotemporally irregular pattern characteristic of fibrillation (Jalife, 2000; Moe *et al.*, 1964).

There are many types of ionic heterogeneity in the heart. Well-known examples are the base-apex (Burton & Cobbe, 2001) and the endocardial-epicardial (Burton & Cobbe, 2001; Liu & Antzelevitch, 1995; Zygmunt *et al.*, 2000) action potential duration (APD) gradients in the ventricles and differences in APD between left and right ventricles (Samie *et al.*, 2001). Other examples are the APD gradient running from the crista terminalis to the pectinate muscles in the right atrium (Schram *et al.*, 2002) and the difference in APD and effective refractory period between the left and right atria (Schram *et al.*, 2002).

Ionic heterogeneity in the heart increases under particular conditions, such as ischemia or chronic heart failure, or in genetic disorders such as those associated with the long QT and Brugada syndrome (Antzelevitch & Fish, 2001; Viswanathan & Rudy, 2000). In most of these cases, the increased ionic heterogeneity is associated with an increased occurrence of cardiac arrhythmias.

There have been several studies on the effects of stepwise ionic heterogeneities of cardiac tissue on spiral wave dynamics. Xie *et al.* (2001b) showed in a model study that stepwise heterogeneities could induce spiral breakup even if the action potential restitution slope is shallow. Experimental studies conducted by Fast & Pertsov (1990) showed that spiral waves drift along the border of a stepwise ionic heterogeneity induced by the local application of quinidine.

Another important type of organization of ionic heterogeneity is in the form of a smooth gradient. Such heterogeneities can occur either as a result of smooth variation of ionic properties of cardiac tissue or as a result of the smoothing effect of electrotonic interactions between cardiac cells, even if properties change abruptly from one cell to the next (Joyner, 1986; Viswanathan *et al.*, 1999). A well-known example of the latter type of heterogeneity is the endocardial-epicardial gradient across the ventricular wall, which is largely caused by the presence of the electrophysiologically distinct M cells (Liu & Antzelevitch, 1995).

So far, only research using simplified FitzHugh-Nagumo models of excitable tissue has been done on the effects of smooth ionic gradients on the dynamics of spiral waves (Rudenko & Panfilov, 1983). In these simplified models spiral waves had circular cores and action potential shapes were very different from those occurring in cardiac tissue. Therefore, the purpose of the present paper was to study the effect of gradients of electrophysiological properties on the dynamic behavior of spiral waves in computer simulations of a realistic ionic model of cardiac tissue. To model cardiac tissue, we chose the Luo-Rudy phase 1 (LR1) model for ventricular cardiomyocytes (Luo & Rudy, 1991), which was used previously by Xie *et al.* (2001b) to study the effects of stepwise ionic heterogeneities.

We show that, as in the case of FitzHugh-Nagumo models, drift can be decomposed into a longitudinal component, parallel to the gradient, and a transverse component, perpendicular to the gradient. Our main finding is that independent of the type of electrophysiological gradient, the longitudinal component of drift is always directed toward regions of longer spiral wave period. We find drift velocities on the order of $0.002mm/msec$ for period gradients of $0.2msec/mm$, amounting to a displacement of $2mm$ during $1s$ of spiral rotation.

These results may help in both predicting and understanding the behavior of reentrant wave patterns in the proximity of ischemic zones and other regions with a well-known effect on spiral period.

2.2 Material and Methods

Mathematical modeling

We used an ionic model to study the propagation of waves of excitation in cardiac tissue. Ignoring the discrete character of microscopic cardiac cell structure, cardiac tissue can be modeled as a continuous system using the following partial differential equation (PDE)

$$\frac{\partial V}{\partial t} = -\frac{I_{ion}}{C_m} + D(\frac{\partial^2 V}{\partial x^2} + \frac{\partial^2 V}{\partial y^2}) \tag{2.1}$$

Here V is membrane potential (in (mV)), t is time (in (ms)), $C_m = 1\mu F/cm^2$ is membrane capacitance, $D = 0.001cm^2/ms$ is the diffusion coefficient and I_{ion} is the sum of all transmembrane ionic currents (in (mA/cm^2)). For I_{ion}, we used the following equation: $I_{ion} = I_{Na} + I_{si} + I_K + I_{K1} + I_{Kp} + I_b$ as described in the LR1 model (Luo & Rudy, 1991), where I_{Na} is Na^+ current, I_{si} is slow inward current, I_{Kp} is K^+ plateau current, and I_b is background current. Here, $I_{Na} = G_{Na}m^3hj(V - E_{Na})$, $I_{si} = G_{si}df(V - E_{si})$, $I_K = G_K xx_1(V - E_K)$, $I_{K1} = G_{K1}K1_\infty(V - E_K)$, $I_{Kp} = G_{Kp}(V - E_K)$ and $I_b = G_b(V - E_b)$, where G is conductance, E is Nernst potential, and $K_{1\infty}$ models the inward rectification of I_{K1}. The gating variables m, h, j, d, f, and x are governed by a Hodgkin-Huxley-type differential equation.

The parameter settings were as in the original LR1 model except for the G_{si}, G_K and G_{K1} conductances. For G_{si}, values of 0, 0.030, 0.035 0.040 and 0.045 were used to vary the meander pattern (Xie *et al.*, 2001b). The upper value of 0.045

was chosen to avoid spiral breakup from occurring. Under homogeneous tissue conditions G_K was set to 0.705 to shorten APD (Xie *et al.*, 2001b) and G_{K1} was set to 0.6047 as in the original LR1 model.

We studied the effects of gradients of electrophysiological properties caused by local differences in I_K and I_{K1} densities. To simulate heterogeneity of I_{K1} density, a G_{K1} gradient was applied by varying G_{K1} linearly from a value of 0.42329 to a value of 0.6047. Similarly, to mimic heterogeneity of I_K density, G_K was varied linearly from a value of 0.600 to a value of 0.705. Gradients were applied such that the parameter value increased in the positive y-direction. To induce gradients with different slopes, tissue sizes were varied from 250×250 ($5cm \times 5cm$) to 700×700 ($14cm \times 14cm$) nodes.

Computer simulations

Two-dimensional tissue was simulated by integrating the PDE described in Eq. 2.1. To speed up computations, reaction and diffusion were separated using operator splitting. The diffusion PDE was solved using a time step $\Delta t = 0.1ms$. The reaction ordinary differential equation (ODE) was solved using a time-adaptive forward Euler scheme with two different time steps: $\Delta t_{large} = 0.1ms$ and $\Delta t_{small} = 0.02ms$. By default, the ODE was solved using Δt_{large}. However, if $\partial V/\partial t > 1$, the results were discarded and computations were repeated iterating five times over Δt_{small}. The equations for the gating variables were integrated using the Rush and Larsen scheme (Rush & Larsen, 1978). In all simulations, the space step was set to $\Delta x = 0.02cm$. We checked the accuracy of our variable time step integration method by comparing it with the conventional Euler integration scheme for a selected subset of the simulations and found similar results (data not shown).

Spiral wave reentry was initiated by applying a S1-S2 protocol with parallel electrode positioning. To establish meander patterns and drift, spiral tip trajectories were traced using the algorithm presented by Fenton & Karma (1998) along an isopotential line of $V = -35mV$.

All simulations were written in C^{++} and run on a Intel Pentium III personal computer with an 800-MHz central processing unit.

2.3 Results

2.3.1 Spiral dynamics in homogeneous tissue

Figure 2.1A shows the typical dynamics of a spiral wave in the LR1 model. The tip of the spiral wave followed a meandering trajectory with a distinctive hypo-cycloidal pattern made up of five outward petals.

Changing the excitability of cardiac tissue by changing G_{si} resulted in different spiral dynamics, as shown in Fig. 2.2. For $G_{si} = 0$ (low excitability) the spiral core was circular; for $G_{si} = 0.030$, the core had a hypo-cycloidal pattern similar to the one shown in Fig. 2.1. For ever higher excitability (from $G_{si} = 0.035$ to $G_{si} = 0.045$), this hypo-cycloidal pattern persisted; however, its size increased

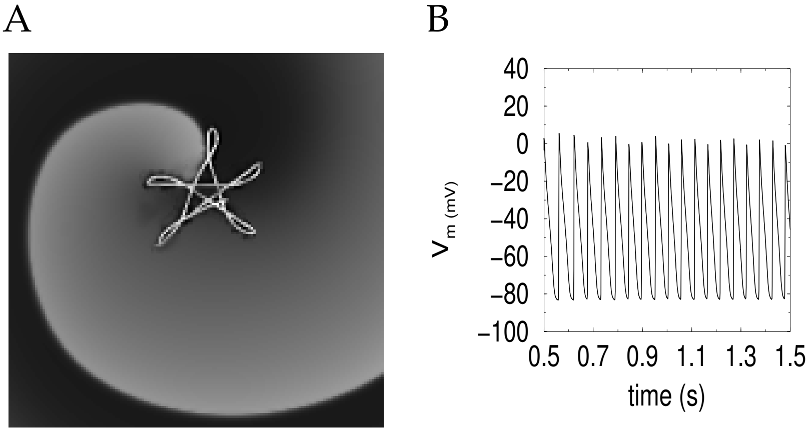

Figure 2.1: **A** Snapshot of a spiral wave and the spiral tip trajectory traced during a single period of rotation for maximal conductance of the slow inward current (G_{si}) $= 0.030$, maximal conductance of K^+ current (G_K) $= 0.600$, and maximal conductance of inwardly rectifying K^+ current (G_{K1}) $= 0.60470$. **B** Membrane potential (V_m) during spiral wave activity shown in A, recorded in point 5,100 during the 1s after initial stabilization of the spiral wave.

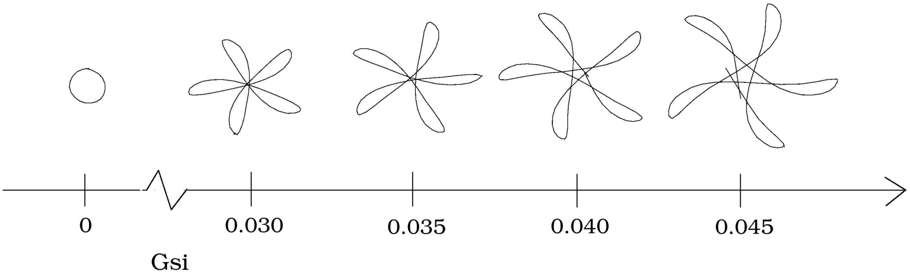

Figure 2.2: Change in spiral meander pattern as a function of increasing G_{si}. ($GK = 0.705$ and $G_{K1} = 0.60470$)

with increasing G_{si} values.

2.3.2 Spiral dynamics in tissue with a gradient of heterogeneity

We studied the dynamics of spiral waves in tissue with a gradient of heterogeneity. A gradient was created by gradually varying the local current density of either I_K or I_{K1} by varying G_K and G_{K1} values, respectively, similar to the approach taken by Xie *et al.* (2001b).

Figure 2.3 shows a series of snapshots of spiral wave dynamics in tissue with a G_K gradient ranging from $G_K = 0.600$ at the bottom of the medium to $G_K = 0.705$

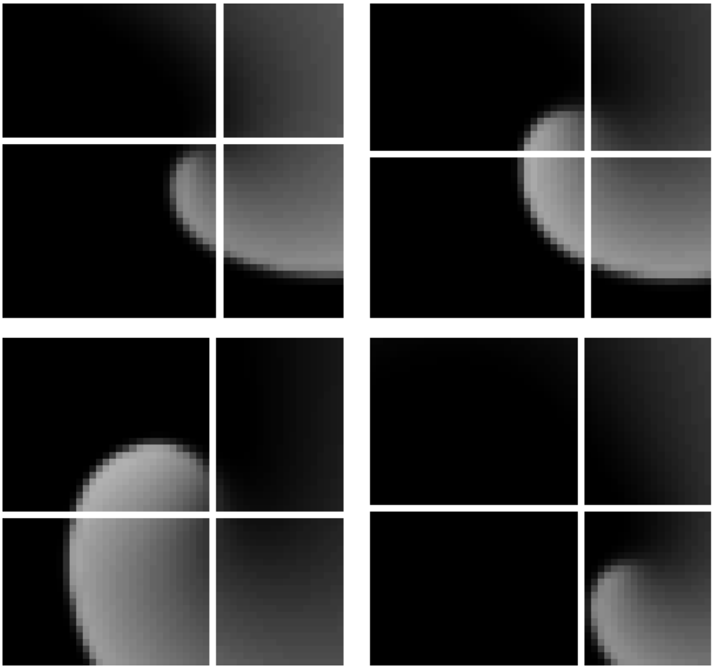

Figure 2.3: Series of snapshots of spiral wave dynamics under a G_K gradient ranging from $G_K = 0.600$ to $G_K = 0.705$ for $G_{si} = 0.030$ and $G_{K1} = 0.60470$. Only a central portion of $1cm^2$ of the medium is shown. Note that spiral wave drift is partly obscured by the spiral wave meander occurring simultaneously.

at the top of the medium. One can see that, over the course of time, the spiral wave gradually shifted from its initial position (indicated by the white quadrant) to a new position located down and to the right of that initial position.

Figure 2.4A shows the tip trajectory of the spiral from Fig. 2.3. Because of substantial meandering, the tip trajectory looks rather complicated; however, the net downward and to the right drift can be clearly seen. To separate the drift from the meandering, we averaged the trajectory from Fig. 2.4A over the characteristic time of the meandering pattern ($300ms$). We saw (Fig. 2.4B) that the spiral drift occurred at an approximately constant angle relative to the y-axis. Therefore, spiral drift can be regarded as a vector consisting of two components: one parallel to the gradient of heterogeneity (along the y-axis), and the other perpendicular to this gradient. We will call these the longitudinal and transverse components of drift, respectively.

In Figs. 2.3 and 2.4 the value of G_K increases with increasing y-coordinate, i.e., APD and hence the spiral wave period decreases along the positive y-direction. It thus follows that the longitudinal component of spiral drift was directed toward regions of longer period (Fig. 2.4C).

The direction of the transverse component of drift depends on the direction of rotation of the spiral wave (Rudenko & Panfilov, 1983). In figure 2.4D, we

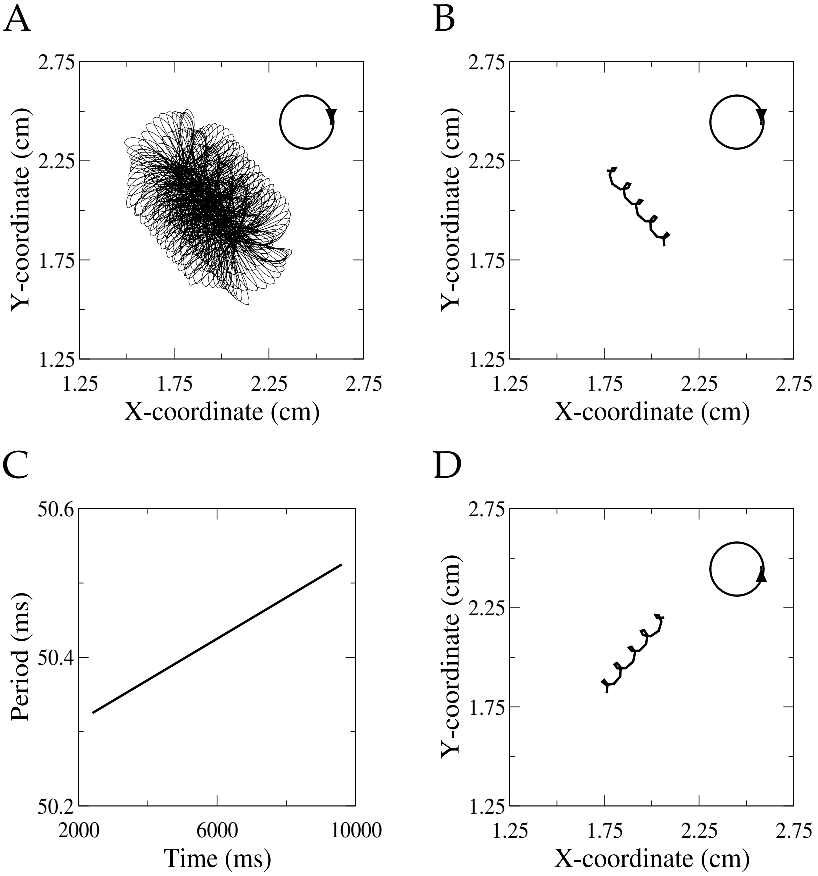

Figure 2.4: Spiral wave dynamics under a G_K gradient ranging from $G_K = 0.600$ to $G_K = 0.705$ for $G_{si} = 0.030$ and $G_{K1} = 0.60470$. **A** trajectory traced by the spiral tip showing both meander and drift. **B** time-averaged tip trajectory displaying drift without meander. **C** increase of spiral period in time during drift. **D** time-averaged tip trajectory for a spiral with an opposite direction of rotation.

show drift of a spiral with an opposite direction of rotation under the same parameter settings as in Fig. 2.4B. The longitudinal component of drift did not change, whereas the transverse component of drift had an opposite direction. From a mathematical point of view, this result is trivial as it follows from the symmetry of the system. The direction of transverse drift can be written as:

$$\vec{t} = \vec{l} \times \vec{\omega} \tag{2.2}$$

where $\vec{t}$ and $\vec{l}$ are unit vectors along the transverse and longitudinal drift components, respectively, and $\vec{\omega}$ is the unit vector of the angular velocity of the spiral wave (Rudenko & Panfilov, 1983). From Eq. 2.2, it follows that if the direction of rotation reverses ($\vec{\omega}$), the direction of transverse drift ($\vec{t}$) also reverses.

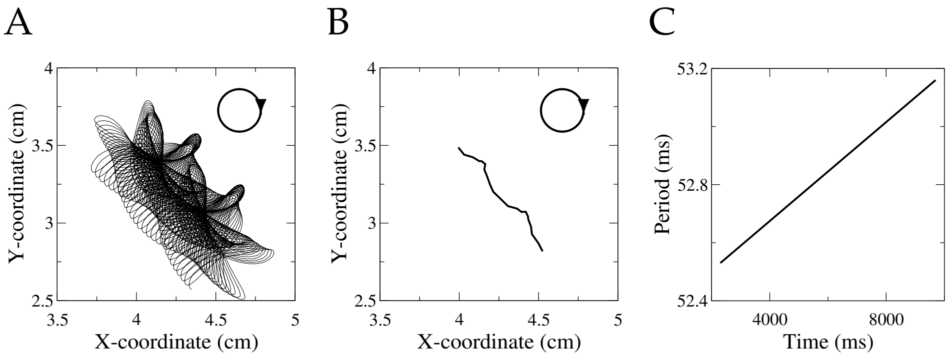

Figure 2.5: Spiral wave dynamics under a G_{K1} gradient ranging from $G_{K1} = 0.42329$ to $G_{K1} = 0.60470$ for $G_{si} = 0.030$ and $G_K = 0.705$. **A** trajectory traced by the spiral tip showing both meander and drift. **B** time-averaged tip trajectory displaying drift without meander. **C** increase of spiral period in time during drift.

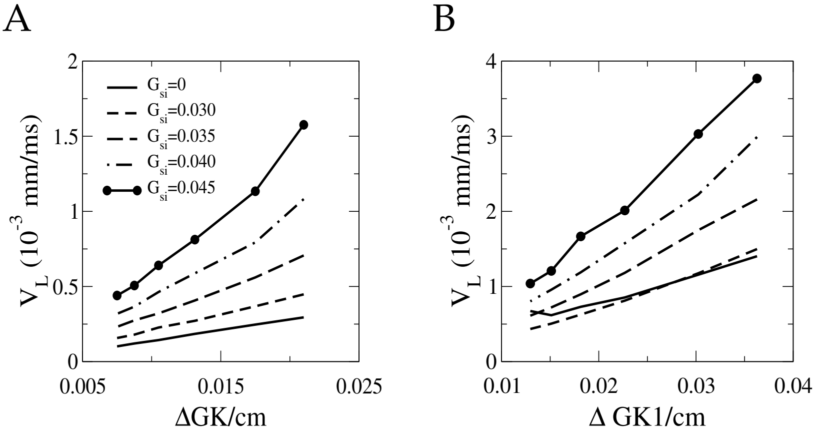

Figure 2.6: Longitudinal drift speed (V_L) as a function of the magnitude of G_K (**A**) and G_{K1} (**B**) gradients for different values of G_{si}. Note that longitudinal drift is toward the negative y-direction and that values used here are thus absolute values.

Similar computations were done with a gradient of I_{K1} density. All other parameters were kept the same as in Fig. 2.4. One can see (Fig. 2.5) that despite the different gradient, qualitative characteristics of drift remained the same: drift had two components, a longitudinal component, directed toward regions with longer spiral wave period; and a transverse component, with its direction given by Eq. 2.2.

In Figs. 2.4 and 2.5, the spiral wave had a meander pattern corresponding to a G_{si} value of 0.030. To investigate how the meander pattern affects spiral wave drift, we studied drift for all five meander patterns shown in Fig. 2.2. In addition, we investigated the influence of gradient magnitude on drift of the spiral wave.

Figure 2.6 shows the speed of the longitudinal drift of spiral waves for dif-

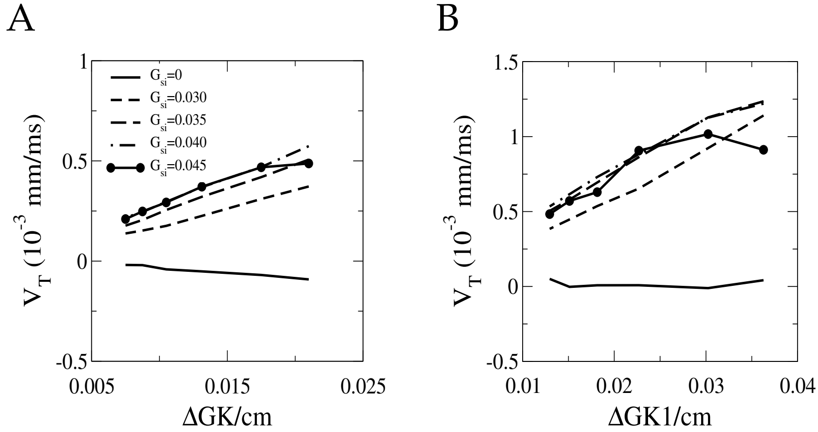

Figure 2.7: Transverse drift speed (V_T) as a function of G_K (**A**) and G_{K1} (**B**) gradient magnitudes for different values of G_{si}.

ferent meander patterns (values of G_{si}) as a function of G_K or G_{K1} gradient magnitudes. We saw that independent of the type (G_K or G_{K1}) and magnitude of the gradient and independent of the meander pattern of the spiral wave, the longitudinal drift was always directed toward regions of longer spiral wave period. It can also be seen that velocity increased approximately linearly with increasing magnitude of the gradient. In addition, we see in Figs. 2.6A and 2.6B that for higher values of G_{si}, longitudinal drift speed increases and the graphs have a steeper slope.

Figure 2.7 shows the dependence of transverse drift speed on the meander pattern and gradient magnitude. One can see that for most values of G_{si}, transverse drift velocity was positive, i.e., it coincided with the direction it had in Fig. 2.4B. However, for the lowest excitability ($G_{si} = 0$), transverse speed was virtually absent for the G_{K1} gradient, and was very small and even had an opposite direction for the G_K gradient.

For intermediate values of G_{si} (from 0.030 to 0.040) transverse drift speed showed the same linear dependence on gradient magnitude as longitudinal drift speed. However, for the lowest ($G_{si} = 0$) and highest excitability ($G_{si} = 0.045$), this dependency was substantially non-linear. Also, the influence of the G_{si} value on transverse drift speed was less strong than for longitudinal drift speed and displayed saturation from $G_{si} = 0.040$ onward.

From a comparison of Figs. 2.6 and 2.7 it follows that transverse drift speed was a factor two to three times smaller than longitudinal drift speed. In addition (looking only at intermediate values of G_{si}), it follows that the slope of the linear dependence of drift speed on magnitude of the gradient was less steep for transverse than for longitudinal drift. This implies that the angle of drift relative to the gradient decreased for increasing gradient magnitude.

In all cases studied above, the spiral waves drifted to regions of longer spiral wave period and did so faster for stronger gradients. This suggests that the gradi-

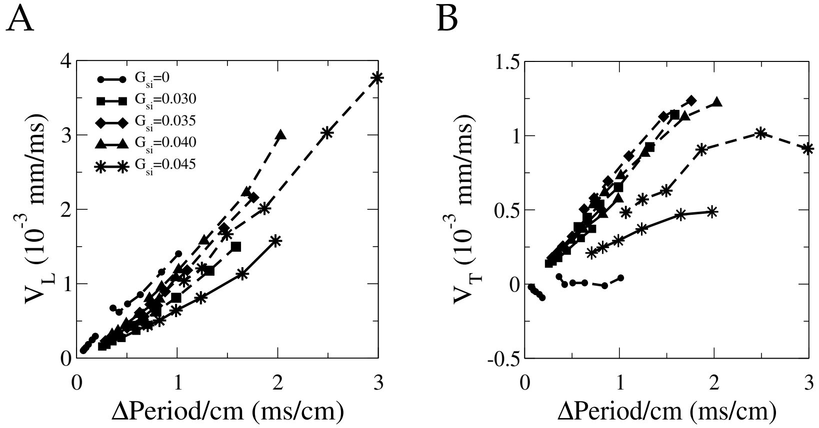

Figure 2.8: Dependence of V_L and V_T on the effective period gradient slope. Solid lines, G_K gradients; dashed lines, G_{K1} gradients.

ent in period (induced by a G_K or G_{K1} gradient) was the driving force behind the drift. In addition, we saw that the drift velocity also depended on the meandering pattern, which was varied by changing the parameter G_{si}. However, G_{si} not only influences meander pattern (Fig. 2.1) but also influences heterogeneity: for different values of G_{si} the same gradients in G_K or G_{K1} produce different gradients in spiral wave period. This raises the question of whether G_{si} affects the spiral drift by changing the gradient or by changing the dynamics of spiral wave meandering.

To answer the above question, we plotted the longitudinal drift speeds from Fig. 2.6 and the transverse drift speeds from Fig. 2.7 as a function of the magnitude of the effective period gradient induced by a particular combination of the G_K or G_{K1} gradient magnitude and G_{si} value. The resulting graphs are shown in Fig. 2.8. We can clearly see that the longitudinal drift velocities for the different values of G_{si} and the different gradient types have converged toward one another: the graphs have a similar slope and similar (extrapolated) intersection point with the y-axis. This suggests that longitudinal drift speed was linearly correlated to period gradient magnitude and that neither the meander pattern nor type of gradient played a role here.

For transverse drift, the situation is less obvious. For intermediate values of G_{si}, transverse drift speed graphs also converged, suggesting a linear dependence on period gradient magnitude. However, for the lowest excitability ($G_{si} = 0$) and highest excitability ($G_{si} = 0.45$), the graphs for both types of gradient lie below those for intermediate excitability levels (from $G_{si} = 0.030$ to $G_{si} = 0.040$). These results might indicate that transverse drift speed was not determined by period gradient magnitude alone. Meander pattern could have also played an important role here.

Note that all results were checked for dependence on initial conditions, and timing of S1-S2 stimulation. Found differences in longitudinal and transverse

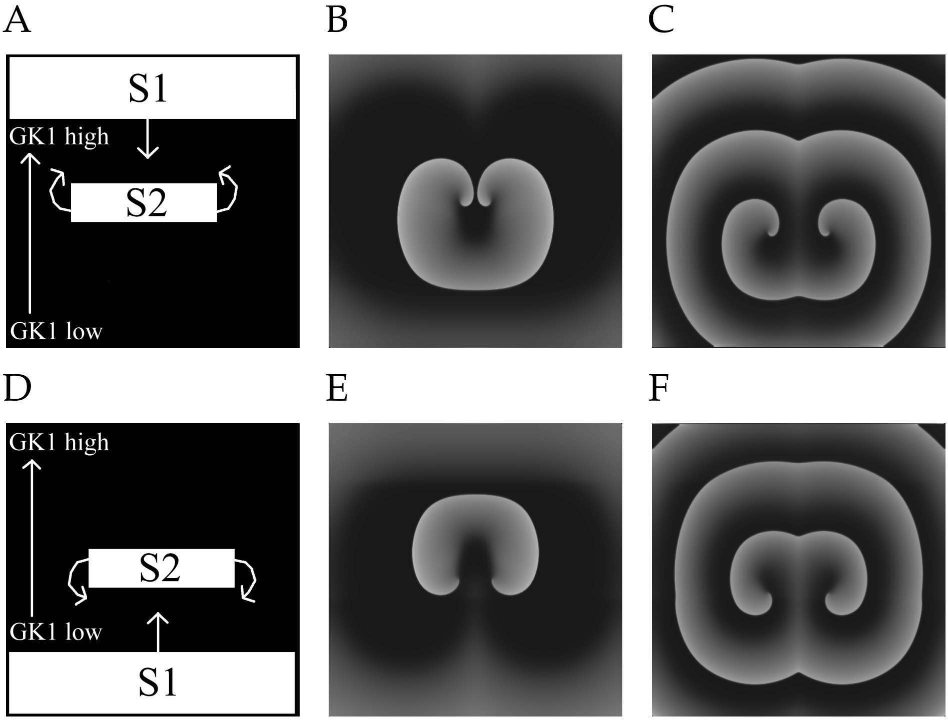

Figure 2.9: Drift of a figure-eight reentry. A-C: downward drift and divergence of the two spirals. D-F: downward drift and convergence of the two spirals. In both cases, $G_{si} = 0.030$, $G_K = 0.705$ and a G_{K1} gradient ranging from $G_{K1} = 0.42329$ to $G_{K1} = 0.60470$ was applied.

drift speeds stayed within 1%, indicating that drift behavior did not depend on the initial phase of rotation.

2.3.3 Figure-eight reentry in a gradient of heterogeneity

A frequently observed reentrant pattern is a so-called figure-eight reentry (Chen *et al.*, 1998), which is composed of two interconnected, counter-rotating spiral waves. Because the direction of transverse drift in a gradient of heterogeneity depends on the direction of spiral wave rotation relative to the gradient direction, two counter-rotating spirals should either diverge or converge (Panfilov & Vasiev, 1991; Ivanitsky *et al.*, 1989). Figure 2.9 shows drift patterns of figure-eight reentries in a medium with a G_{K1} gradient.

With the use of a S1-S2 protocol with different S1 electrode positions, we generated two differently oriented figure-eight reentries. As predicted by the results above, in Fig. 2.9, A-C, the two spirals diverged, whereas in Fig. 2.9, D-F, they converged. In both cases, the figure-eight reentry moved downward, i.e., toward longer spiral period. Note that convergence of spirals did not lead to mutual annihilation. Instead, we observed that after spirals had converged to some minimal distance, no further convergence occurred and only the longitudinal component of drift remained.

2.4 Discussion

We studied the effect of gradients of heterogeneity on the dynamics of spiral waves in the LR1 model. It was demonstrated that spiral waves drift in the presence of a gradient of heterogeneity and that this drift consists of two components: a longitudinal component (parallel to the gradient) and a transverse component (perpendicular to the gradient).

Longitudinal drift was always directed toward regions of longer spiral wave period. This result is similar to findings obtained using a two-equations FitzHugh-Nagumo model (Rudenko & Panfilov, 1983). The fact that this result generalizes across such very different models enables us to assume that it is a general phenomenon that should exist in other models of cardiac tissue as well as in experiments. In addition, we found that the velocity of longitudinal drift was linearly proportionate to the magnitude of the spiral period gradient and independent of spiral wave meander pattern.

The direction of the transverse component of drift was shown to be given by Eq. 2.2. This finding agrees with data from Fast & Pertsov (1990), who studied spiral wave dynamics under a stepwise heterogeneity in an experimental setup. For intermediate values of excitability, transverse speed was also linearly proportionate to the period gradient magnitude. For the lowest and highest excitability cases, the dependency was rather different, suggesting that meander pattern might play a role here.

One of the interesting implications of our findings is that we can predict how the dynamics of a spiral wave will be influenced by a particular gradient present in the heart. The ventricular base-apex gradient, for example, should cause a drift of transmurally oriented spirals toward the septum, where APD is longest (Schram *et al.*, 2002). The transmural endocardial-epicardial gradient should cause drift of intramurally oriented spirals toward the midmyocardial region, where APD is longest due to the presence of M cells (Liu & Antzelevitch, 1995). Note, however, that the influence of other factors, such as the three-dimensional nature of reentry in the ventricles and the presence of rotational anisotropy, should also be taken into account. Similar predictions can be made for spiral behavior in the proximity of an ischemic border zone, where a spiral wave should move away from the ischemic region, where APD is shortest. Note, however, that because multiple electrophysiological factors change during ischemia, spiral behavior under these conditions requires further study.

The drift velocity found in our computations is in the order of $0.002mm/msec$ in a period gradient of $0.2msec/mm$. During a single second of drift, a spiral wave thus can travel a distance of $\sim 2mm$, which can have a significant effect on cardiac arrhythmias and the appearance they make on an ECG.

In conclusion, the aim of the present study was to investigate the basic effects of gradients of ionic heterogeneity in cardiac tissue on spiral wave dynamics. We showed that these gradients lead to drift of spiral waves toward regions of longer period independent of the type of ionic heterogeneity. Our main conclusion is that differences in spiral wave period are the driving force behind drift of spiral waves.

Acknowledgments

This research was supported by the Netherlands Organization for Scientific Research (NWO) through grant number 620061351 of the Research Council for Physical Sciences (EW).

3

Influence of randomly distributed obstacles on wave propagation and spiral wave dynamics in excitable media

K. H. W. J. Ten Tusscher[1] and A. V. Panfilov[1,2]
[1]*Department of Theoretical Biology, Utrecht University*
Padualaan 8, 3584 CH Utrecht, The Netherlands.
[2]*Division of Mathematics, University of Dundee,*
23 Perth Road, Dundee DD1 4HN, United Kingdom.

Based on *Influence of nonexcitable cells on spiral breakup in two-dimensional and three-dimensional excitable media, Phys Rev E* **69**: 062902 (2003) and *Wave propagation in excitable media with randomly distributed obstacles, SIAM Multiscale Modeling and Simulation*, in press

Abstract

We study the effect of small, randomly distributed obstacles on wave propagation in two-dimensional (2D) and three-dimensional (3D) excitable media described by the Aliev-Panfilov model. We find that increasing the number of obstacles decreases the conduction velocity of plane waves and decreases the effective diffusion coefficient in the eikonal curvature equation. The presence of obstacles also increases the inducibility of wave breaks and spiral waves in 2D and 3D excitable media, but suppresses spiral breakup induced by a steep restitution curve mechanism. We discuss the mechanisms of the observed effects, the differences between 2D and 3D excitable media, as well as the relevance of our study to processes of wave propagation in cardiac tissue, including arrhythmogenesis in the presence of fibrosis in the myocardium.

3.1 Introduction

One of the most fundamental processes that occur in reaction-diffusion excitable systems is the propagation of nonlinear waves. Examples of such waves include chemical waves in the Belousov-Zhabotinsky reaction (Zaikin & Zhabotinsky, 1970), waves of CO oxidation on Pt catalytic surfaces (Imbihl & Ertl, 1995), electrical waves in retinal and cortical nerve tissue (Gorelova & Bures, 1983), where they may underlay neurological diseases such as epilepsy, and waves in heart muscle, where they may be involved in life-threatening cardiac arrhythmias (Allessie *et al.*, 1973; Davidenko *et al.*, 1992). In addition, nonlinear waves control the morphogenesis of *Dictyostelium discoideum* amoebae (Gerisch, 1965) and initiate the development of *Xenopus* oocytes after fertilization (Lechleiter *et al.*, 1991). Nonlinear waves in excitable media have been studied in numerous analytical and numerical studies (see (Grindrod, 1991; Zykov, 1987; Meron, 1992) for an overview). Most properties of nonlinear waves in excitable media, such as propagation with a constant speed that is independent from initial conditions, the annihilation of colliding waves, the dependence of propagation speed on wave front curvature, as well as the possibility of formation of rotating spiral waves (vortices) and the development of turbulent excitation patterns are general for all excitable systems listed above and follow from a general mathematical description of excitable systems (Krinsky, 1984).

The formation of spiral waves and especially the onset of spatiotemporal chaos (turbulence) have received a lot of interest in the context of cardiac arrhythmias. Electrical turbulence in the heart (ventricular fibrillation) is the main cause of sudden cardiac death in the world. There are several mechanisms for the onset of turbulence in excitable media. One of them is based on alternans instability (Nolasco & Dahlen, 1968; Guevara *et al.*, 1984), which occurs if the medium is excited and, instead of a periodic response (with the same period as the excitation), the durations of successive pulses of excitation (action potentials) alternate (e.g. short-long-short-long etc.). There is a simple criterion for alternans instability, based on the restitution curve of the tissue, which relates the action potential duration (APD) to the diastolic interval (DI, the time between the end of the previous action potential and the start of the next one). Alternans instability occurs if the slope of the restitution curve is more than one, leading to a flip bifurcation (Nolasco & Dahlen, 1968; Guevara *et al.*, 1984). This criterion was found from analytical studies of one-dimensional maps and was later extended to an integral-delay equation for pulse propagation on a one-dimensional ring of excitable tissue (Courtemanche *et al.*, 1993), where the instability occurred as an infinite dimensional Hopf bifurcation. However, recent studies show that a restitution slope steeper than one not necessarily leads to alternans instability and that memory effects and conduction velocity restitution may also play an important role (Tolkacheva *et al.*, 2003; Banville & Gray, 2002).

Numerical studies of alternans instability in two dimensions showed that instability due to a steep restitution curve can cause spiral breakup: fragmentation of a single spiral wave into a spatiotemporally chaotic pattern comprising many wavelets of various sizes (Panfilov & Holden, 1990; Courtemanche & Winfree, 1991; Ito & Glass, 1991; Karma, 1993). Spiral breakup due to a steep restitution curve is now one of the most actively pursued hypotheses for the occurrence of ventricular fibrillation (Panfilov & Holden, 1990; Courtemanche & Winfree, 1991; Ito & Glass, 1991; Karma, 1993; Garfinkel *et al.*, 2000). Recent experimental measurements have confirmed the role of steep restitution curves in ventricular fibrillation (Koller *et al.*, 1998; Garfinkel *et al.*, 2000). However, the measured values of the maximal slopes of the restitution curves were remarkably close to the boundary of the onset of instability (slope 1). This implies that small changes in the characteristics of cardiac tissue could be potentially crucial for promoting or preventing breakup in the heart.

One important characteristic affecting wave propagation is the conductance of gap junctions, the specialized membrane structures connecting adjacent cardiac cells (Jongsma & Wilders, 2000). The number of gap junctions changes substantially during cardiovascular disease (Jongsma & Wilders, 2000). In a previous article we showed that decreased gap junctional conductivity can suppress spiral breakup by increasing the diastolic interval of a spiral wave (Panfilov, 2002). Another important characteristic influencing wave propagation in the heart is the presence of so-called fibrotic, nonexcitable tissue. In recent years it has become clear that there is a strong correlation between the increased presence of fibrotic tissue in the heart and the occurrence of dangerous cardiac arrhythmias. Fibrotic tissue consists of specialized cells called fibroblasts and the materials these cells excrete (collagen, elastin). These materials make up the so-called extracellular matrix, which serves to hold the cells of the heart in place (Jugdutt, 2003). Fibrotic tissue thus plays an important role in determining the structure of cardiac tissue, but since fibroblasts and extracellular matrix are nonexcitable they form obstacles for waves propagating through the heart. In healthy hearts fibrotic tissue makes up only 5% of the total tissue, but during the process of aging, in particular cardiac diseases related to heart failure (cardiac myopathies), and after an infarction this may increase up to 35%. All these conditions that lead to an increase of fibrotic tissue are also linked to a much larger incidence of cardiac arrhythmias, thus suggesting a potential causal relationship (De Bakker *et al.*, 1988; Wu *et al.*, 1998; Swynghedauw, 1999; Hsia & Marchlinski, 2002; Varnava *et al.*, 2001; Hayashi *et al.*, 2002; Jugdutt, 2003). Whereas after infarction, fibrotic tissue increases locally and appears in the form of long fibrous strands, during aging or in certain diseases fibrotic tissue is present in a more diffuse form, forming small randomly dispersed patches.

From a mathematical point of view fibrotic tissue serves as multiple obstacles for wave propagation in cardiac tissue. Fibrotic strands can be modeled as long one-dimensional (1D) obstacles, whereas diffuse fibrosis can be represented as multiple small obstacles randomly distributed over the cardiac tissue. The influence of a single or few large obstacles on wave propagation in excitable media has been extensively studied over the years. It was shown that obstacles affect various aspects of wave propagation, including wave front shape, and that they can induce spiral waves through vortex shedding or by causing localized conduction block in narrow isthmuses formed between obstacles (Panfilov & Keener, 1993a; Agladze *et al.*, 1994; Cabo *et al.*, 1994, 1996; Fast & Kléber, 1997). In addition, obstacles can stabilize spiral wave rotation by anchoring the spiral wave (Davidenko *et al.*, 1992; Pertsov *et al.*, 1993). The question what happens to wave propagation in the presence of large numbers of small obstacles, when the collective effects of multiple obstacles, rather than the interaction of waves with solitary obstacles are relevant, has so far largely remained unanswered. The basic ideas for modeling the effects of multiple objects were developed in (Pertsov, 1997), which introduced a model of textured cardiac tissue as an excitable medium containing multiple inexcitable obstacles. It was demonstrated that waves propagating in such media can induce an electrogram characteristic for discontinuous propagation occurring in fibrotic cardiac tissue. However, this paper dealt with the introduction of a new model rather than its detailed study and was limited to several important but illustrative examples.

In this article we perform a detailed study on the influence of randomly distributed small obstacle on several important aspects of wave propagation. We study the effect of obstacles on planar wave propagation speed and on the eikonal curvature relation in 2D media. We investigate the influence of obstacles on the vulnerability for spiral wave generation in two-dimensional and three-dimensional media. Finally, we study the effect of obstacles on the onset of spatiotemporal chaos through spiral wave breakup in 2D and 3D media. We study in detail how the effect of nonexcitable obstacles differs between 2D and 3D excitable media. Note that because the nonexcitable cells are just obstacles (heterogeneities) for propagating waves, the problem which we study here is also relevant for other types of excitable media with heterogeneities, for example the Belousov-Zhabotinsky system (Manz *et al.*, 2002).

3.2 Model

The excitable medium is described by the Aliev-Panfilov model (Aliev & Panfilov, 1996b):

$$\frac{\partial e}{\partial t} = -ke(e-a)(e-1) - er + \Delta_{2,3}e \tag{3.1}$$

$$\frac{\partial r}{\partial t} = (\epsilon + \frac{\mu_1 r}{\mu_2 + e})(-r - ke(e-b-1)) \tag{3.2}$$

Here the variable e stands for the transmembrane potential; Δ is a 2D ($\Delta_2 = \partial^2/\partial x^2 + \partial^2/\partial y^2$) or 3D ($\Delta_3 = \partial^2/\partial x^2 + \partial^2/\partial y^2 + \partial^2/\partial z^2$) Laplace operator; and the variable r stands for the conductance of the slow inward current. The expression $-ke(e-a)(e-1)$ in (3.1) determines the fast processes, such as the upstroke of the action potential. The dynamics of the recovery phase of the action potential are determined by the time course of the variable r, mainly by the expression $(\epsilon + (\mu_1 r)/(\mu_2 + e))$. The parameters of the model do not have a clear physiological meaning but can be adjusted to reproduce key characteristics of cardiac tissue such as the shape of the action potential, refractoriness and restitution of action potential duration. The parameter values used in this study are $a = 0.1, \mu_2 = 0.3, k = 8, \epsilon = 0.01, b = 0.1$, while parameter μ_1 is varied. The most relevant dynamical change (for spiral wave stability) as μ_1 is varied is the steepness of the APD restitution curve, where maximum slope increases as μ_1 is decreased.

In two dimensions Laplacians were numerically approximated using 4-point centered difference Euler schemes; in three dimensions 6-point centered difference schemes were used. Computations were performed using an explicit time integration scheme with a time integration step of $\Delta t = 0.2$ and space integration step of $\Delta x = 0.6$ (both dimensionless units), as in previous publications (Panfilov, 2002). No-flux boundary conditions were imposed. In two dimensions a 200×200 sheet was used; in three dimensions $100 \times 100 \times 40$, $100 \times 100 \times 60$ or $200 \times 200 \times 76$ slabs were used. Obstacles were modeled as 1×1 inexcitable cells with Neumann boundary conditions, similar to (Pertsov, 1997; Agladze *et al.*, 1994), and were randomly distributed over the medium. To quantitatively investigate the effect of the obstacles, we varied the percentage of grid points in the medium occupied by obstacles, and refer to this as the % obstacles. The size of the obstacles, scaled on the basis of a spiral wave length of $30mm$ in human cardiac tissue, was $1 \times 1mm^2$. To initiate the first spiral wave we used initial data corresponding to a broken wave front, the break being located at the middle of the excitable medium. If a spiral persisted for 80 cycles without fragmentation we considered breakup to be absent for these parameter values.

3.3 Wave propagation in 2D media

3.3.1 Plane wave propagation in 2D

First we study the effect of randomly distributed nonexcitable obstacles on planar wave conduction velocity (CV) in 2D excitable media. For that we stimulated an excitable medium along the left vertical boundary and measured the velocity of the initiated wave. In an excitable medium without obstacles the wave front will be along a straight vertical line, and conduction velocity can be evaluated from simple 1D computations. However, the presence of obstacles will disturb the wave front shape (Fig. 3.1A) and therefore conduction velocity should be measured as an average along the vertical axis. Fig.3.1B shows the dependence of average planar CV on the percentage of obstacles. It can be seen that CV decreases as a function of the percentage of nonexcitable obstacles present in the medium. We also see that this dependence can be well approximated by a straight line. When the percentage of obstacles exceeded 38%, we observed failure of wave propagation.

3.3.2 Curvature effects on wave speed in 2D

As a next step we investigate how the presence of randomly distributed small obstacles influences the eikonal curvature relation in 2D excitable media. As was shown in (Zykov, 1980), the speed-curvature relation in a 2D excitable medium

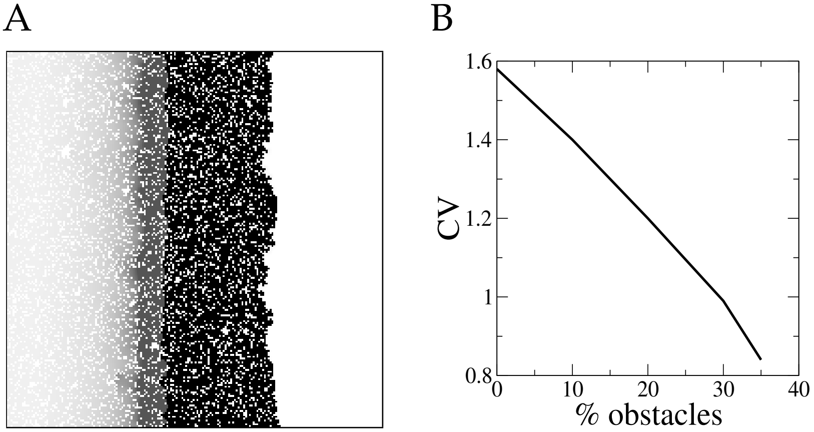

Figure 3.1: **A** Planar wave front propagating from left to right in a medium with 20% obstacles. The black area represents the excited state ($e > 0.6$), and intermediate shading from gray to white shows different levels of recovery.**B** Dependence of planar wave conduction velocity (CV) on the percentage of obstacles. Results are for $\mu_1 = 0.13$.

is given by the following formula, valid for small curvatures:

$$CV = CV_0 - DK, \tag{3.3}$$

where CV_0 is the conduction velocity of a planar wave, D is the diffusion coefficient of the medium, and K is the wave front curvature. We studied the relation between wave speed and wave front curvature for different percentages of obstacles.

There are two possible ways of computing the eikonal curvature relation. One method is the direct measurement of propagation velocity in a 2D computation of an expanding radial wave. Because the velocity of the wave changes continuously with the wave front curvature (which changes because of the expansion of the radial front), this method requires high accuracy. However, a single simulation results in the complete curvature relation. The other method is to determine the curvature relation from waves propagating with constant curvature and velocity, which mathematically can be studied as waves propagating in a medium with a modified diffusion term: $\frac{\partial^2}{\partial x^2}$ in (3.1) is replaced by $\frac{\partial^2}{\partial x^2} + K\frac{\partial}{\partial x}$, where K is the constant wave front curvature (Keener, 1991; Marée & Panfilov, 1997). Because wave front curvature and speed stay constant during a single simulation, this method requires much less accuracy. The complete curvature relation can be obtained by varying K and determining constant wave speed.

In Figure 3.2A we can see a snapshot of an expanding radial wave in an excitable medium with obstacles, initiated by applying a point stimulus in the center of the medium. We see that the wave has an approximately circular-shaped wave front, however, the presence of obstacles causes substantial local disturbances of the wave front shape. These local disturbances will cause inevitable errors in determining wave speed, which should be determined instantly for each position of

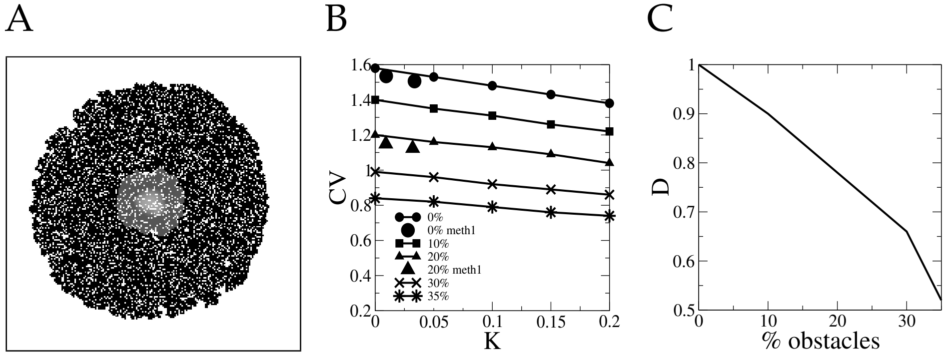

Figure 3.2: **A** A circular wave front in a medium with 30% obstacles. **B** Dependence of conduction velocity (CV) on wave front curvature (K) for different percentages of obstacles present. Most data are obtained using the second method described; for 0% and 20% obstacles some data are also obtained using the first method and are added for comparison. **C** Dependence of the (effective) diffusion coefficient on the percentage of obstacles. Results are for $\mu_1 = 0.13$. For further explanation, see text.

the wave front when using the first method for determining the eikonal curvature relation. We therefore decided to use the second method.

In Figure 3.2B we show the dependence of CV on curvature for different percentages of obstacles found using this second method. For comparison purposes, for 0 and 20% obstacles a few data points obtained using the first method are also shown. Two observations can be made from this figure. First, an increase in the percentage of obstacles leads to a decrease of CV, both in the absence and presence of curvature. Second, an increase in the wave front curvature leads to a linear decrease in wave front propagation speed, both in the absence and presence of obstacles, thus the linear dependence in the eikonal curvature equation (3.3) also holds in the presence of obstacles. In addition, it can be seen that the data points obtained using the first method have similar values to those obtained using the first method. Finally, we determined the effective diffusion coefficient, which determines the slope of the CV versus K curve. In Figure 3.2C we plot this diffusion coefficient as a function of the percentage of obstacles. It can be seen that the diffusion coefficient decreases almost linearly with the percentage of obstacles. This decrease can be explained by the effective decrease of coupling between excitable cells in the presence of obstacles.

Note that the linear decrease of the effective diffusion coefficient alone (Fig. 3.2C) cannot explain the linear decrease in wave velocity in (Fig. 3.1B), since the velocity of a wave in an excitable medium is proportional to the square root of the diffusion coefficient. This indicates that the obstacles also change the effective reaction rate of the medium. These effects can possibly be studied analytically using homogenization theory of excitable media (Keener, 2000) as was shown in (Bär *et al.*, 2002) for the case of small periodic obstacles that are nonreactive, but allow for diffusion.

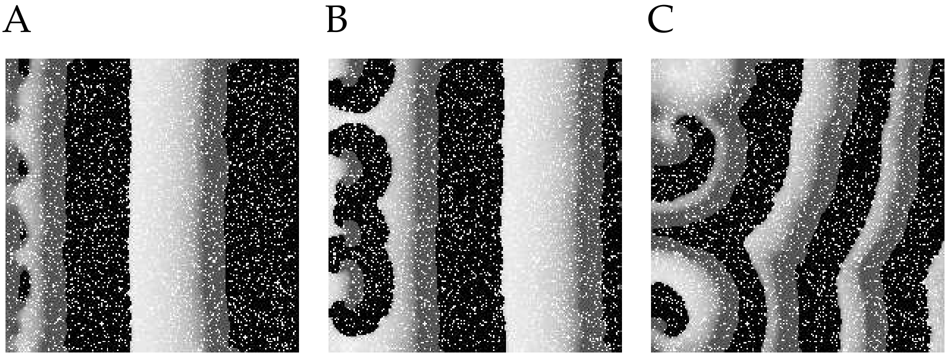

Figure 3.3: Development of initial wave breaks (**A**), and subsequent spiral wave formation (**B**), and presence of stable spiral activity (**C**) after applying three stimuli with a short stimulus period. Results are for a medium with 10% obstacles, $\mu_1 = 0.14$ and a stimulation period of 28 time units.

3.3.3 Vulnerability in the presence of obstacles in 2D

When extra stimuli are applied in the heart in the interval between heart beats, there is a window of time during which life-threatening arrhythmias can be induced. This window is called the vulnerable period or the vulnerable window. The vulnerable period can be readily demonstrated in any model of an excitable medium that is heterogeneous with respect to the refractory period (Krinsky, 1978). In such models, the extra stimulation can induce wave breaks that evolve into rotating spiral waves of excitation, which are believed to underlie particular types of cardiac arrhythmias called tachycardias. In addition, it has been shown that high frequency stimulation can also lead to spiral wave formation in the presence of inexcitable obstacles (Panfilov & Keener, 1993a; Agladze *et al.*, 1994; Cabo *et al.*, 1994, 1996; Pertsov, 1997).

Here we study the vulnerability of 2D excitable media that are homogeneous in their properties of excitability and refractoriness, but contain randomly distributed obstacles. To do so we apply three stimuli with varying short interstimulus intervals along the left vertical boundary of the medium, and study whether they will induce wave breaks and spiral waves. In a homogeneous excitable medium without obstacles this method of stimulation will lead either to normal wave propagation, or, if the period of stimulation is too low and cells have not recovered yet, to the propagation block of one or several waves. However, in the presence of obstacles, there is a third possibility, namely, that wave propagation blocks locally and progresses in other places, thus leading to the formation of wave breaks, which than evolve into spiral waves.

The reasons why the presence of obstacles may lead to localized conduction block are twofold. First, narrow gaps present between nearby obstacles lead to a so-called source-sink mismatch: in the gap the wave consists of only a few excited points that serve as a current source, whereas for the wave to progress after the gap a much larger number of points that serve as current sink need to

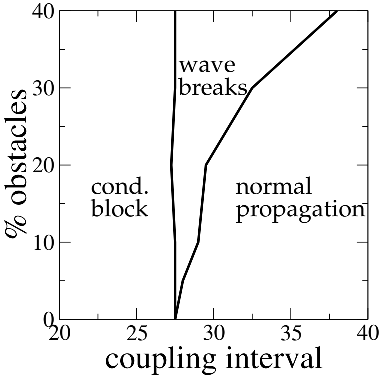

Figure 3.4: Dependence of the vulnerable window in stimulation coupling interval space on the percentage of obstacles present. Results are for $\mu_1 = 0.14$.

be excited. This may lead to local conduction block after the gap. In addition, clumps of small obstacles may form a larger obstacle interrupting the wave front as discussed in (Panfilov & Keener, 1993a; Agladze *et al.*, 1994; Cabo *et al.*, 1994, 1996). Figure 3.3 shows an example of the successful induction of spiral waves after application of three stimuli with a short coupling interval. In Fig. 3.3A we can see that the third stimulus gives rise to a locally propagating and locally blocked wave. In Fig. 3.3B we can see how these broken wave fronts immediately curl around to form spiral waves. In Fig. 3.3C the wave pattern is shown after 256 units of time (time is in dimensionless units) after the third stimulus. It can be seen that of the five spirals originally formed (Fig. 3.3B), two are remaining, the others have disappeared through collisions with each other or the boundary of the medium. Note also that the spirals stay in the area of the medium where they originated.

In Figure 3.4 we show the dependence of the vulnerable window of coupling intervals that lead to wave breaks and spiral formation on the percentage of obstacles. We see that the lower border of the vulnerable window, below which the interval between stimuli is too short and wave propagation blocks, is independent of the number of obstacles present in the medium. It can also be seen that the upper border of the vulnerable window, above which normal wave propagation occurs, is strongly dependent on the percentage of obstacles. If the number of obstacles increases, the upper border of the vulnerable window goes up, increasing the width of the vulnerable window.

3.3.4 Effect of obstacles on spiral wave rotation in 2D

In this section we study the effect of obstacles on spiral wave rotation. Spirals are created by initializing the medium with a broken wave front that curls around to form a single spiral wave. Figure 3.5 shows stable spiral wave patterns for media with no obstacles (A), 10% obstacles (B), and 30% obstacles (C). From Figure 3.5 it can be seen that increasing the percentage of obstacles leads to a less regularly shaped spiral wave with local disturbances in the wave front, wavelength, however, does not seem to be affected by the percentage of obstacles.

To study in more detail the effect of randomly distributed obstacles on spiral

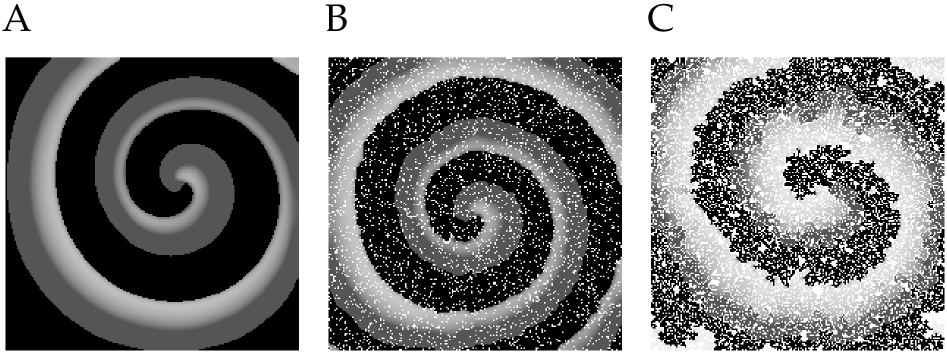

Figure 3.5: Spiral wave rotation in a medium with 0% (**A**), 10% (**B**), or 30% (**C**) obstacles. Results are for $\mu_1 = 0.13$.

wave dynamics, we computed how the main characteristics of spiral waves, namely CV, action potential duration (duration of the excited state) (APD), diastolic interval (the interval between two successive action potentials) (DI) and period (APD+DI) of spiral wave rotation depend on the percentage of obstacles. The results of these computations are shown in Figure 3.6. It can be seen that conduction velocity decreases approximately linearly as a function of the percentage of obstacles, whereas period, DI, and APD all increase in a similar, nonlinear manner as a function of the percentage of obstacles. From these results it can also be understood why wavelength stays approximately the same for percentages of obstacles in the range from 0 to 30%: wavelength is the product of period and CV. For 0% obstacles, period is approximately 26.5 and CV is 1.24, resulting in a wavelength of 32.9, for 30% obstacles period is 38.6 and CV 0.87, resulting in a wavelength of 33.6, which is approximately the same as for 0% obstacles. In other words, the decrease in conduction velocity is compensated by an equally sized increase in period, leading to similar wavelengths. For 35% obstacles and more, this effect no longer holds: CV keeps decreasing linearly with the percentage of obstacles, whereas period increases more than linearly with the percentage of obstacles, causing wavelength to increase: for 35% obstacles, period is 64.2, CV is 0.82, and therefore wavelength is 52.6, which is significantly more than for 0 and 30% obstacles.

Note that Figure 3.6 shows average values of spiral wave characteristics. Individual values of spiral wave characteristics vary, depending on the particular pattern in which the obstacles are distributed over the excitable medium. This variation of spiral wave characteristics as a function of obstacle pattern can have important consequences for spiral wave dynamics, and will be further illustrated in section 3.4.2.

3.3.5 Effect of obstacles on spiral breakup in 2D

Now we investigate the influence of randomly distributed small obstacles on spiral wave breakup in 2D media. Spiral wave breakup is the process of frag-

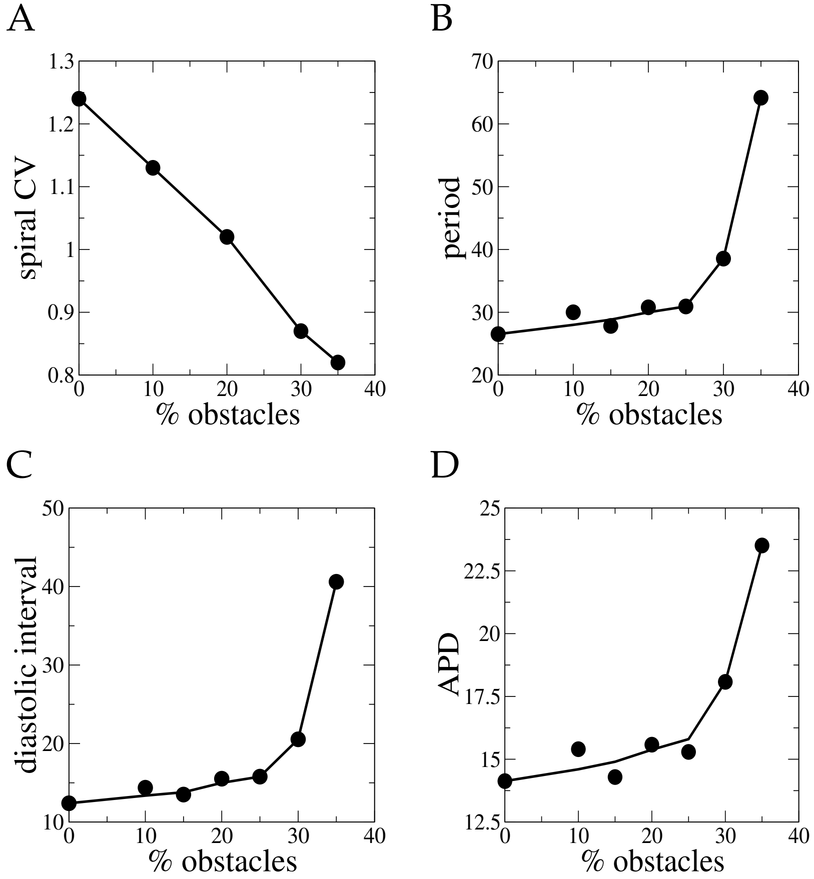

Figure 3.6: Dependence of spiral conduction velocity (**A**), period (**B**), diastolic interval (**C**), and action potential duration (APD) (**D**) on the percentage of obstacles present. Results are for $\mu_1 = 0.13$.

mentation of a single spiral wave into a spatiotemporally chaotic wave pattern (Panfilov & Holden, 1990; Courtemanche & Winfree, 1991; Ito & Glass, 1991; Karma, 1993; Garfinkel *et al.*, 2000), which is thought to underlie another type of dangerous cardiac arrhythmia called fibrillation. To study the effect of obstacles on the occurrence of spiral breakup, we used parameter values for which spiral breakup is observed in a homogeneous medium without obstacles and studied how the presence of obstacles affect the breakup phenomenon. We started our simulations with a broken wave front that curls around to form a single spiral wave. In Fig. 3.7 we see the time evolution of spiral wave patterns in two-dimensional media with 0% (top row), 10% (middle row), and 30% (bottom row) obstacles for a parameter value of $\mu_1 = 0.09$. In all three cases, at time $T = 160$ (first column) an intact spiral wave is present. In the top row, the first wave break occurs at time $T = 428$ (second column), and after that we can see a turbulent wave pattern develop (third and fourth columns). In the middle row, at time

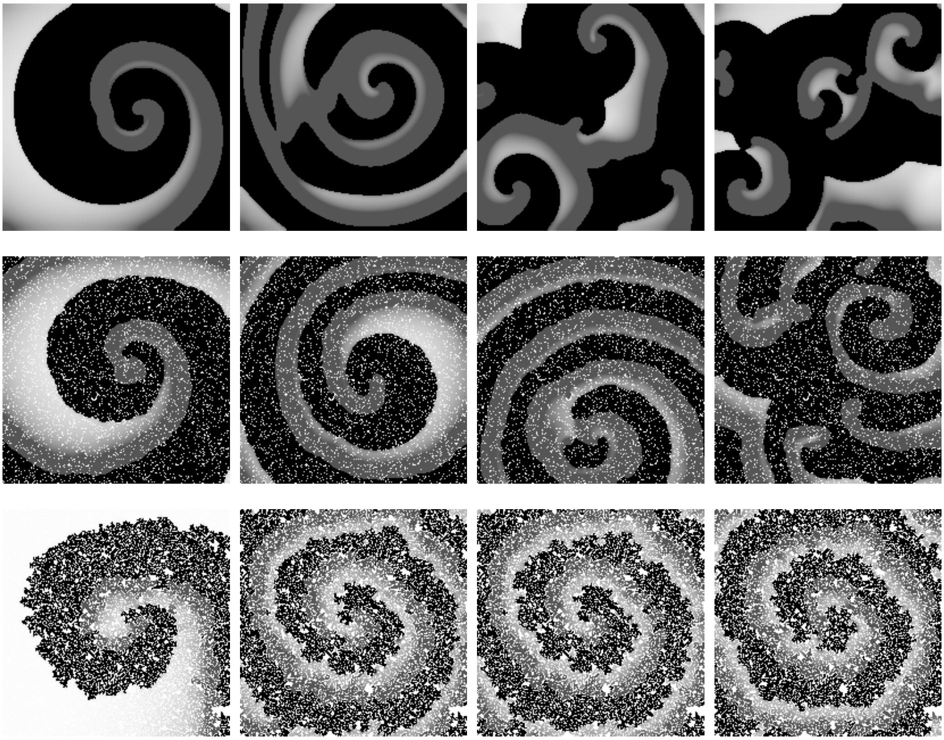

Figure 3.7: Time evolution of 2D spiral wave patterns. **Top row** medium with no obstacles present. **Middle row** medium with 10% obstacles. **Bottom row** medium with 30% obstacles. **First column** wave patterns at time T=160. **Second column** Wave patterns at time T=428. **Third column** wave patterns at time T=832. **Fourth column** wave patterns at time T=1600. Results are for $\mu_1 = 0.09$.

$T = 428$ (second column) the spiral wave is still intact, but at time $T = 832$ (third column) the first wave break occurs, and this wave break also develops into a chaotic wave pattern (fourth column). In the bottom row, no wave breaks occur, and the spiral wave is still stable at time $T = 1600$ (fourth column). These results suggest that increasing the percentage of obstacles suppresses spiral wave breakup: 10% obstacles postponed the occurrence of the first wave break, and 30% obstacles completely suppressed spiral breakup.

In the Aliev-Panfilov model the occurrence of spiral breakup is linked to the value of parameter μ_1. If μ_1 is below some critical value, spiral breakup occurs, above the critical value spiral waves are stable. Therefore, we further investigate whether increasing the percentage of obstacles indeed suppresses spiral wave breakup, by performing a series of simulations for different values of μ_1 in combination with different percentages of obstacles. Figure 3.8 displays the dependence of the critical value of μ_1 on the percentage of obstacles. We can indeed see that increasing the percentage of obstacles decreases the window in parameter space for which spiral breakup occurs.

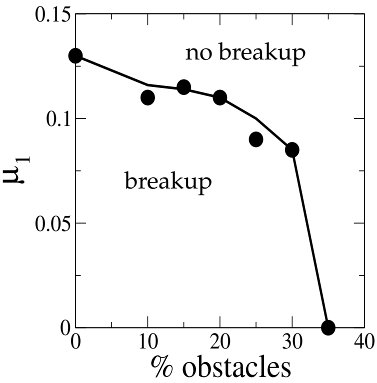

Figure 3.8: Dependence of the critical value of μ_1 on the percentage of obstacles present in 2D media.

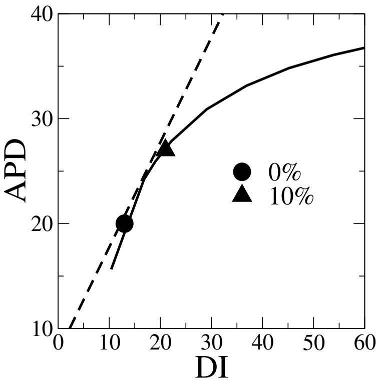

Figure 3.9: APD restitution curve for $\mu_1 = 0.09$. For an explanation see text.

Now we would like to find out why spiral breakup disappears if the percentage of obstacles increases. The mechanism of spiral breakup in this model is the presence of a steep restitution curve (Panfilov, 2002). The restitution curve describes the relationship between action potential duration and the duration of the preceding diastolic interval. Typically, APD decreases if DI is shorter and cells have had less time to recover. It can be mathematically proven that if the restitution relation has a slope steeper than 1, a flip bifurcation or period doubling bifurcation occurs, leading to alternations of long and short action potentials and long and short diastolic intervals. In Figure 3.9 a typical restitution curve is shown for $\mu_1 = 0.09$; for comparison, a line with a slope 1 is added. It can be seen that the restitution slope is steepest for short DIs and hence high excitation frequencies. Spiral waves typically rotate with a high frequency, and if for this excitation frequency the restitution slope exceeds 1, a flip bifurcation occurs, APDs alternate, and if locally a very short action potential arises, localized conduction block and spiral wave breakup can occur.

In the previous section on the influence of obstacles on spiral wave rotation, we showed that increasing the percentage of obstacles leads to an increase of spiral wave period, DI, and APD. In Figure 3.9 we show how these effects lead to the suppression of spiral wave breakup. On the restitution curve two points are drawn. The circle is for a spiral rotating in a medium with no obstacles, the spiral has a short DI and lies on the part of the restitution curve that has a slope steeper than 1: spiral breakup will occur. The triangle is for a spiral rotating in a medium with 30% obstacles, the spiral therefore has a longer DI and lies on the part of the restitution curve that has a slope less than 1: the spiral wave will stay stable. From this we can derive the following mechanism for spiral wave breakup suppression by obstacles: increasing the percentage of obstacles leads to an increase in period, APD and DI that causes a shift along the restitution curve, away from the steep part where breakup occurs.

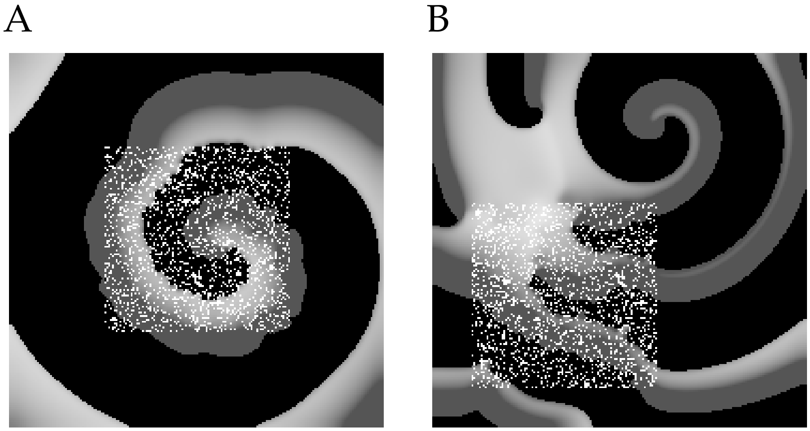

Figure 3.10: 2D media in which 30% obstacles are present only in a localized patch. **A** Spiral tip rotates inside the area with obstacles and is stable. **B** Spiral tip rotates outside the area with obstacles and undergoes breakup. In both cases $\mu_1 = 0.11$.

In Figure 3.10 we show 2D media for which obstacles are present in only part of the medium. Parameters are the same in the two figures: $\mu_1 = 0.11$ and locally 30% obstacles, the only difference being the location of the patch with obstacles relative to the tip of the spiral. In Fig. 3.10A the spiral tip, which is the organizing center of a spiral wave and determines the rotation speed of the spiral, resides in the area with obstacles; as a consequence, the obstacles slow down rotation and the spiral stays stable. In Fig. 3.10B, the spiral tip is outside the area with obstacles, therefore the obstacles cannot slow down spiral wave dynamics, and spiral breakup occurs. These results indicate that for obstacles to stabilize spiral wave dynamics they do not need to be present in the whole medium, instead, it is important that the tip of the spiral is inside the region where the obstacles are present.

3.4 Wave propagation in 3D media

Next, we would like to investigate the effect of obstacles on 3D wave propagation. However, since there are many similarities between 2D and 3D wave propagation, we will not study all aspects that were studied in 2D, but rather study the influence of obstacles on vulnerability and scroll wave (three-dimensional spiral wave) breakup in 3D. We find both differences and similarities in 2D and 3D media, and explain the mechanism behind the differences.

3.4.1 Vulnerability in the presence of obstacles in 3D

In this section we study whether the presence of obstacles also leads to an increased vulnerability to spiral wave formation in 3D excitable media. Two series of simulations were performed. In the first series, coupling between excitable

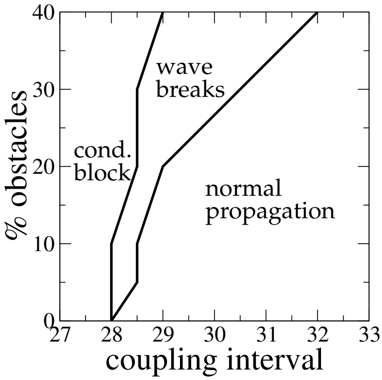

Figure 3.11: Dependence of the vulnerable window in stimulation coupling interval space on the percentage of obstacles present in 3D media. Results are for $\mu_1 = 0.14$ and a coupling strength in the z direction that is 1/9 of that in the x and y directions.

cells was equal in the x, y and z direction. In the second series, coupling strength in the z direction is 1/9 of that in the x and y direction, reflecting the layer structure of cardiac tissue (LeGrice *et al.*, 1997) but ignoring many other details of cardiac tissue structure in order to keep the problem close to that considered in two dimensions. In the first series of experiments we did not observe the formation of wave breaks or spiral waves. In the second series of experiments (with less strong coupling in the z direction) spiral waves could be induced. The dependence of the vulnerable window on the percentage of obstacles for this particular case is shown in Figure 3.11. From a comparison of Figures 3.11 and 3.4 it can be seen that the vulnerable window for scroll wave formation is much smaller than in 2D media and is shifted toward higher percentages of obstacles.

Both the fact that scroll waves could not be induced in the first series of experiments and that in the second series the vulnerable window was much narrower than in two dimensions can be explained as follows: in two dimensions, when a wave is locally blocked by a clump of obstacles or a small gap, a wave break always occurs. However, in three dimensions, the random pattern of obstacles is different in the different layers of the medium. Therefore, often when conduction is blocked in one layer of the medium it can still propagate in the adjacent layers. As a consequence, wave front disturbances get quickly restored from other layers, due to the electrotonic interaction between the layers. We found that for conduction block to arise in three dimensions, the coupling between layers should be less strong than within layers, in order for wave front defects not to be restored immediately from other layers. In addition, we found that higher percentages of obstacles are required than in two dimensions to get the same amount of vulnerability, also indicating that sustained wave breaks are harder to create in three dimensions. Higher percentages of obstacles result in larger clumps, leading to larger wave breaks that can less easily be restored, and lead to larger numbers of gaps and wave breaks, which might not all be restored, and increase the likelihood of conduction block co-occurring in neighboring layers, again making wave front deformations less easy to restore.

It should be noted that the combined effect of anisotropy and obstacles on wave propagation is a complex issue that requires further investigation, however,

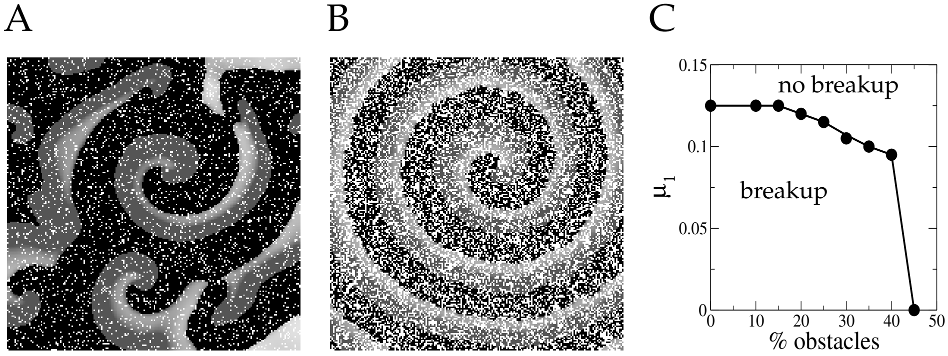

Figure 3.12: **A** Wave patterns at time T=2600 for $\mu_1 = 0.11$ and 10% or **B** 40% obstacles. The shown wave patterns are from a 2D cross-section at the middle layer of the 3D medium. **C** Dependence of the critical value of μ_1 below which breakup occurs on the percentage of obstacles in 3D.

this is not the goal of the present study.

3.4.2 Effect of obstacles on spiral breakup in 3D

Finally, we investigate whether randomly distributed small obstacles also suppress spiral wave breakup in 3D media. In Fig. 3.12A and B 2D cross sections of 3D wave patterns are shown. In Fig. 3.12A we see a turbulent wave pattern that arises after spiral breakup in a 3D medium with 10% obstacles. In Fig. 3.12B we see a stable spiral wave in a 3D medium for the same parameter settings as in Fig. 3.12A but with 40% obstacles. Figure 3.12C displays the dependence of the critical value of μ_1 below which spiral breakup occurs on the percentage of obstacles. We can see that increasing the percentage of obstacles decreases the window in parameter space for which spiral breakup occurs, similarly to what was observed for 2D media. However, from a comparison of Figures 3.12C and 3.8, it can be seen that in three dimensions a larger percentage of obstacles is required to obtain the same decrease in the critical value of μ_1: the 2D curve for the critical value of μ_1 decreases faster as a function of the percentage of obstacles than the 3D curve, in addition, in three dimensions the critical value for μ_1 goes to zero for 45% obstacles, whereas in two dimensions the critical value for μ_1 already goes to zero for 35% obstacles.

To investigate why the effect of obstacles on spiral breakup is less pronounced in three than in two dimensions, we measured the dependence of scroll wave period, diastolic interval and action potential duration on the percentage of obstacles in 3D excitable media. Fig. 3.13 shows the dependence of period on the percentage of obstacles in three dimensions. It can be seen that period increases in a nonlinear fashion as a function of the percentage of obstacles, similar to the case in two dimensions. However, from a comparison of Figures 3.13 and 3.6B, it can be seen that the increase in period is much less pronounced in 3D than in 2D excitable media: for 35% of obstacles, in two dimensions the period has

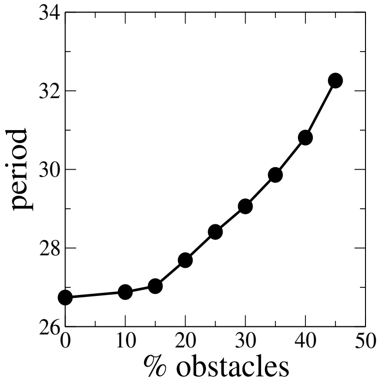

Figure 3.13: Scroll wave period as a function of the percentage of obstacles in three dimensions. Results are for $\mu_1 = 0.13$.

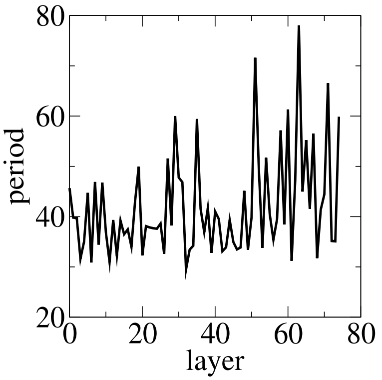

Figure 3.14: Spiral wave period as a function of layer for $\mu_1 = 0.13$ and 30% obstacles.

increased from approximately 26.5 (for 0% of obstacles) to 64.2, whereas in three dimensions the period has increased from the same 26.5 to only 29.9. Similar results were obtained for DI and APD (data not shown). Thus, to get the same increase in DI and shift a spiral wave to the part of the restitution curve with a slope less than 1, a larger percentage of obstacles is needed. The next question now is why a certain percentage of obstacles leads to much less increase in period, DI, and APD in 3D than in 2D media.

To explain this difference, we repeated the 3D simulation for a value of $\mu_1 = 0.13$ and 30% obstacles, but now we decoupled the layers of the 3D slab in the z direction. This results in 76 independent 2D simulations that have an obstacle pattern corresponding to those of the different layers in the 3D medium that we simulated previously. We determined the average period of spiral wave rotation in each of the 76 layers and found that there was a large variability in spiral wave period between layers (Fig. 3.14), with a lowest period of 29.47 (layer 32), a highest period of 78.05 (layer 63), a mean period of 41.85, and a standard deviation of 9.98. These results suggest that due to different spatial distribution of obstacles in the different layers, the spiral waves have substantially different periods. As was shown in (Panfilov, 1991; Panfilov & Keener, 1993c), if different layers with different periods of spiral rotation are coupled into a heterogeneous 3D medium, the medium will be driven by the layer with the fastest spiral, due to the electrotonic interactions between the different layers.

In order to check whether this effect also holds for media with inexcitable obstacles, we simulated spiral wave rotation for $\mu_1 = 0.13$ in a $100 \times 100 \times 60$ medium consisting of three different but fully coupled regions each of 20 layers in height, with the outer two regions containing no obstacles and the inner region containing 0%, 10%, 20%, 30%, or 40% obstacles. In Figure 3.15 it can be seen that the period of spiral wave rotation in these media is independent of the percent-

Figure 3.15: Period of scroll wave rotation as a function of the percentage of obstacles in the middle region of a 3D excitable medium that has no obstacles in the outer two regions of the medium. To illustrate that periods do not differ significantly for different percentages of obstacles, mean values and standard deviations are shown. Results are for $\mu_1 = 0.13$.

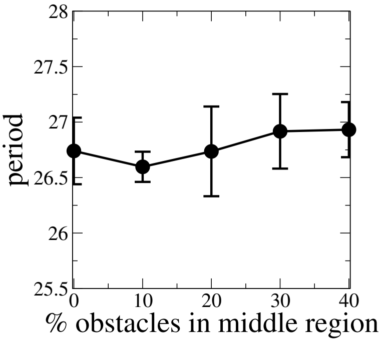

age of obstacles in the middle region of the medium and equal to the spiral wave period in a medium without obstacles (0% obstacles in middle region), confirming that the effect also holds in the case of obstacles.

Going back to our experiment with the uncoupled layers, we can indeed see that in the completely coupled 3D simulation the scroll wave period is 29.06, which is very close to the lowest spiral wave period recorded in our uncoupled 3D simulation.

The fact that the 3D spiral period approximately equals the minimum period of the 2D layers constituting the 3D medium allows for the following statistical interpretation (Ten Tusscher & Panfilov, 2003a): if $f(x)$ is the density distribution function of 2D spiral wave periods, and $F(x) = \int_{-\infty}^{x} f(u)du$ is the distribution function for the probability that a period is less than x, then the probability that at least one in N randomly selected patterns has a period less than x is $\Phi(x) = 1 - (1 - F(x))^N$. Therefore, the density distribution function for the minimum period out of N periods and hence for the expected period of a 3D scroll wave in a medium with N layers is $\phi(x) = \frac{d\Phi(x)}{dx} = N(1 - F(x))^{N-1} f(x)$. Since it is not possible to derive the density distribution function $f(x)$ analytically, we estimated the density distributions $f(x)$ and $\phi(x)$ by Monte Carlo simulation. For that we did 2477 simulations with different random obstacle patterns for $\mu_1 = 0.13$ and 30% obstacles. Fig. 3.16A shows the relative frequency distribution (estimate of $f(x)$) of spiral wave periods found in these simulations. Again, we see a large variability in spiral wave period: the distribution has a mean of 42.77 and a variance of 9.96. To mimic our 3D simulation consisting of 76 layers, with the fastest layer determining scroll wave period, we randomly drew 76 simulations from the total of 2477, determined the minimum period and repeated this experiment 2000 times. From this we obtained a relative frequency distribution for the minimum (out of 76) period (estimate of $\phi(x)$) (Fig. 3.16B). This distribution has a mean of 30.93 and a variance of 0.81. From a comparison of Figures 3.16A and B we can see that the expected value for the period of a 3D scroll wave (the mean of the minimum period distribution) is almost 30 % shorter than that of a 2D spiral wave (the mean of the normal period distribution). We can also see that the variance of the 3D period is much smaller than that of the 2D period. Note that we found a period of 38.48 for the 2D spiral wave and a

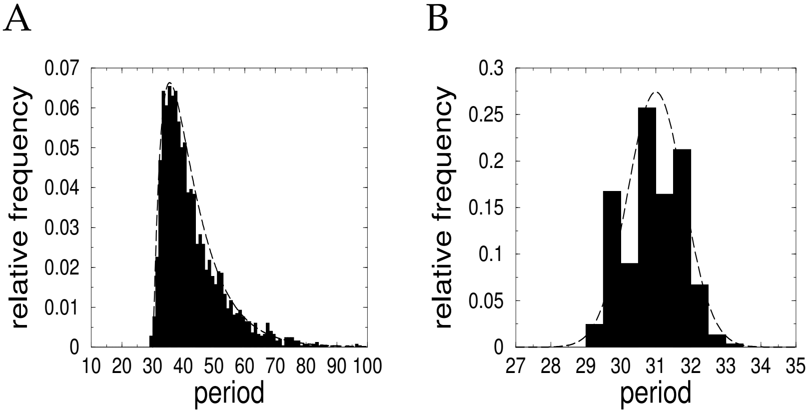

Figure 3.16: **A** Relative frequency distribution of the spiral wave period for 2477 simulations. **B** Relative frequency distribution of the minimum period out of 76 periods for 2000 experiments. For clarity fitted idealized frequency distributions are also shown. Results are for $\mu_1 = 0.13$ and 30% obstacles.

period of 29.06 for the 3D scroll wave, close to the mean values of the normal and minimum period distributions, respectively (Fig. 3.16A and B). Concluding, the difference in spiral wave period between 2D and 3D media with obstacles can be explained by the fact that in three dimensions, scroll wave period is determined by the minimum period of multiple 2D layers, which, as follows from our statistical analysis, will on average be smaller than a single, normal 2D period. Note, that real cardiac tissue does not consist of discrete layers. However, a "virtual" number of layers can be estimated as $N = L/l$, where L is the thickness of the tissue and l is the characteristic (liminal) correlation length of cardiac tissue, which is on the order of 1-2mm (Weidmann, 1952).

3.5 Discussion

We studied the effects of randomly distributed small nonexcitable obstacles on wave propagation in excitable media. In 2D media, we showed that increasing the percentage of obstacles leads to a linear decrease in conduction velocity, which can be explained simply by the smaller number of excitable cells contributing to the propagating wave front. We also investigated the effect of obstacles on the eikonal curvature relation for excitable media. We found that the linear dependence of wave speed on curvature also holds in the presence of obstacles, but that the effective diffusion coefficient decreases with an increase in the percentage of obstacles.

We showed that the vulnerability of the medium for wave breaks and spiral wave formation increases as a function of the percentage of obstacles. This agrees well with clinical data on the increased occurrence of cardiac arrhythmias in the presence of increased amounts of fibrotic tissue in the heart (De Bakker *et al.*, 1988;

Hsia & Marchlinski, 2002). In addition, we showed that an increase in the percentage of randomly distributed obstacles suppresses restitution induced spiral breakup. This result, which at first may seem counterintuitive, we explained by showing that an increased number of obstacles slows down spiral wave dynamics, leading to longer period, action potential duration, and diastolic interval, causing an upward shift along the restitution curve away from the steep part, thus suppressing steep restitution breakup. The finding that small obstacles suppress steep restitution spiral breakup is similar to results obtained in a previous study (Panfilov, 2002), where we showed a similar effect of a decreased gap junctional coupling. Together, these results suggest that discontinuous conduction caused by small obstacles or depressed gap junctional coupling (small scale discontinuities) suppresses *restitution induced* spiral breakup.

The result that small obstacles suppress steep restitution mediated spiral breakup might agree less well with clinical data, as increased amounts of fibrosis are correlated both with arrhythmias caused by the rotation of a single spiral wave (tachycardia) as with arrhythmias generated by the chaotic excitation patterns that arise after spiral wave fragmentation (fibrillation) (Wu *et al.*, 1998; Hayashi *et al.*, 2002). In this context, it is important to realize that obstacles suppress spiral breakup caused by the steep restitution mechanism, but that this need not be the case for other possible mechanisms of spiral wave fragmentation (Jalife, 2000; Marée & Panfilov, 1997; Bär & Or-Guil, 1999; Sandstede & Scheel, 2000). Indeed, the variation of spiral wave periods induced by different percentages and patterns of obstacles through the thickness of a 3D excitable medium may potentially result in alternative mechanisms of scroll wave breakup involving filament twist induced by transversal heterogeneity, as shown in (Panfilov & Keener, 1993c). However, we did not observe such dynamics in our current study, probably because either spiral wave period differences were to small or particular periods extended over only one or a few layers, thus not inducing substantial filament twist. In addition, it is important to note that the disease states that lead to extensive fibrosis in the heart often also lead to changes in both the excitable properties of cardiac cells and their coupling to other cells (Swynghedauw, 1999; Jongsma & Wilders, 2000), which are not captured in our simple model of excitable media but that may very well lead to breakup mechanisms unique to cardiac excitable tissue. Indeed, Bub *et al.* (Bub *et al.*, 2002; Bub & Shrier, 2002) show that the combination of decreased cell-cell coupling, heterogeneity and the presence of obstacles promotes wave break both in experiments and model simulations. The model presented by Bub *et al.* has no APD rate dependence and therefore has a flat restitution curve, in addition, they use a much lower excitability and much larger obstacles than we used in our models. These differences indicate that the mechanism of breakup in their model is clearly not dynamical instability caused by steep restitution, instead the large obstacles and low excitability used in (Bub *et al.*, 2002; Bub & Shrier, 2002) lead to site dependent localized conduction block. Summarizing, our results do not imply that fibrosis always suppresses fibrillation, but only that small nonexcitable objects in an otherwise normally excitable medium suppress steep restitution mediated breakup.

We extended our study to 3D excitable media. We showed that obstacles also lead to vulnerability for wave breaks and scroll wave formation in three dimensions, but that this effect is less strong than in two dimensions. For wave breaks and spiral waves to be induced, coupling in the z direction had to be less strong than in the x and y direction, and higher percentages of obstacles were required for the same amount of vulnerability as in two dimensions. This difference can be explained by the fact that in three dimensions the wave front can also progress in the direction of the third dimension, causing wave breaks in one layer to be repaired by normally progressing wave fronts in neighboring layers. Based on these results, we can hypothesize that the effect of fibrose tissue on the initiation of cardiac arrhythmias should be more pronounced in the atria (thin, semi-2D) than in the ventricles (thick, 3D) of the heart. Note, however, that these results should be verified in more detailed, electrophysiologically and anatomically adequate models of cardiac tissue, before they can be reliably extended to a clinical context.

Finally, we demonstrated that the stabilizing effect of obstacles on spiral wave dynamics also occurs in 3D media, but again this effect is less pronounced than in two dimensions. We demonstrated that this difference is caused by the fact that in three dimensions scroll wave period is determined by the minimum period of multiple 2D spirals in the different layers of the 3D medium. We confirmed this finding by a statistical study. This result may indicate that, in the presence of fibrotic tissue, the period of arrhythmias might be shorter in thin sections of the heart than in thick sections.

It should be noted that the effects we studied here are relevant not only for cardiac tissue but also for wave propagation in other excitable media. As a few examples, research has been performed on the influence of patterned heterogeneities and obstacles on wave propagation both in the Belousov-Zhabotinsky reaction (Manz *et al.*, 2002; Steinbock *et al.*, 1995) and in CO oxidation on Pt surfaces (Bär *et al.*, 1996), including the influence of heterogeneities on spiral wave formation and stability.

Acknowledgments

We are grateful to Dr. J. de Bakker and Dr. E. Belitser for valuable discussions and help in this research. This research is funded by the Netherlands Organization for Scientific Research (NWO) through grant number 620061351 of the Research Council for Physical Sciences (EW) (K.H.W.J. ten Tusscher).

4

Eikonal formulation of the minimal principle for scroll wave filaments

K. H. W. J. Ten Tusscher and A. V. Panfilov
Department of Theoretical Biology, Utrecht University
Padualaan 8, 3584 CH Utrecht, The Netherlands.

Phys Rev Lett **93**: 108106 (2004)

Abstract

Recently, Wellner *et al.* (2002) proposed a principle for predicting stable scroll wave filament shape as a geodesic in a 3D space with a metric determined by the inverse diffusivity tensor of the medium. Using the Hamilton-Jacobi theory we show that this geodesic is the shortest path for a wave propagating through the medium. This allows the use of shortest path algorithms to predict filament shapes, which we confirm numerically for a medium with orthotropic anisotropy. Our method can be used in cardiac tissue experiments since it does not require knowledge of the tissue anisotropy.

4.1 Introduction

Scroll waves have been reported in chemical systems, such as the Belousov-Zhabotinsky reaction (Winfree, 1973), in biological systems, such as aggregations of the slime mould *Dictyostelium discoideum* (Siegert & Weijer, 1992) and cardiac tissue (Chen *et al.*, 1988; Efimov *et al.*, 1999), where they underlie life threatening cardiac arrhythmias (Gray & Jalife, 1998). Theoretical studies of scroll waves (Panfilov & Rudenko, 1987; Keener, 1988; Setayeshgar & Bernoff, 2002) have shown that their dynamics are governed by filament curvature and twist. In the case of positive filament tension, scroll rings contract and disappear, whereas non-closed filaments attain a stable shape (Panfilov & Rudenko, 1987). These stable configurations have the shape of a straight line in isotropic media, but can have much more complex shapes in anisotropic media (Berenfeld & Pertsov, 1999; Wellner *et al.*, 2000; Berenfeld *et al.*, 2001). Predicting stable filament shapes in anisotropic media is of great importance for understanding the 3D organization of cardiac arrhythmias.

Recently, Wellner *et al.* (2002) proposed a 'minimal principle for rotor filaments'. They showed that the stable filament shape of a scroll wave in a 3D anisotropic medium is described by a geodesic in a 3D space with a metric given by the inverse diffusivity tensor of the medium, thus providing an elegant analytical formulation for predicting filament shapes. Its practical application, however, has some limitations: First, to predict filament shape, the method requires a priori knowledge of the diffusivity tensor of the medium. Furthermore, to specify boundary conditions for the geodesic equation, a priori knowledge of the position of filament ends on boundaries is required. Therefore, Wellner *et al.* (2002) suggest that future research in this direction should make use of variational principles in geometric contexts.

In this Letter, we propose an alternative geometrical formulation of the minimal principle for scroll wave filaments, based on the Hamilton-Jacobi variational approach. We show that the geodesic describing the stable scroll wave filament between two given points is the path of shortest travel time of a wave propagating between these two points in the same medium as in which the scroll wave rotates. We show that this shortest wave path can be found using standard shortest path wave algorithms, with wave propagation computed using the same set of equations as for scroll wave dynamics. Our method predicts global filament position and shape, without requiring either a priori knowledge of the position of filament ends on boundaries or of the anisotropic diffusion tensor of the medium, provided that wave arrival times can be found. This makes our method more practically suited for experiments on cardiac tissue.

4.2 Reformulation of the minimal principle

Let us consider the following reaction diffusion model:

$$\frac{\partial u}{\partial t} = \frac{\partial}{\partial x_i} D_{ij} \frac{\partial u}{\partial x_j} + \Phi(u, \vec{v}); \quad \frac{\partial \vec{v}}{\partial t} = \vec{\Psi}(u, \vec{v}) \tag{4.1}$$

where $D_{ij}(\vec{x})$ is the diffusivity tensor, which may depend on the local coordinates $\vec{x} = (x_1, x_2, x_3)$, and $\Phi(u, \vec{v}), \vec{\Psi}(u, \vec{v})$ are non-linear functions that do not depend on $\vec{x}$ explicitly.

As stated in (Wellner *et al.*, 2002), the configuration of the filament of a stable 3D vortex in equations (4.1) will be along a geodesic in a Riemannian space with a metric:

$$ds = (G_{ij} dx_i dx_j)^{1/2}; \quad G_{ij} = D_{ij}^{-1} \tag{4.2}$$

where $G_{ij}(\vec{x})$ is the metric tensor (summation convention is assumed).

Note that in the formulation of (4.2) the dimension of the 'path element' ds is $[time]^{1/2}$ and its physical meaning is not obvious. To reformulate the dimension of the path length, first let us introduce a dimensionless metric tensor: $g_{ij} = \hat{D}_{ij}^{-1} = \frac{D_{ij}^{-1}}{D_0}$ where $D_0 = 1\frac{[space]^2}{[time]}$. Second, we introduce v_0, the velocity of wave propagation in equations (4.1) with $D_{ij} = D_0 \delta_{ij}$ (δ_{ij} is the unitary tensor). Note, that the choice of the value of D_0 is arbitrary, however v_0 should be evaluated at the chosen value of D_0. Using these two new quantities, we can rewrite (4.2) as:

$$dt = \frac{1}{v_0}(g_{ij} dx_i dx_j)^{1/2}; \quad g_{ij} = \hat{D}_{ij}^{-1}, \tag{4.3}$$

The 'path length' dt now has the physical dimension of $[time]$, and as we will demonstrate, it describes the activation time of the medium. Note that, because the governing equations of a geodesic are invariant under a constant scaling (see page 8016 of (Wellner *et al.*, 2002)), metric (4.3) is equivalent to metric (4.2).

The geodesic $x_i(t)$ between two points $\vec{x_0}$ and $\vec{x_1}$ in a Riemannian space (4.3) minimizes the functional:

$$I = \frac{1}{v_0} \int_{\vec{x_0}}^{\vec{x_1}} (g_{ij} \dot{x}_i \dot{x}_j)^{1/2} dt; \quad (\dot{} = d/dt), \tag{4.4}$$

Following the standard Hamilton-Jacobi theory (Smirnov, 1964), consider (4.4) with an arbitrary upper limit, i.e. introduce a function $T(\vec{X})$, which is the value of I (4.4) *along the geodesics* from point $\vec{x_0}$ to an arbitrary point $\vec{X}$:

$$T(\vec{X}) = \frac{1}{v_0} \int_{\vec{x_0}}^{\vec{X}} (g_{ij} \dot{x}_i \dot{x}_j)^{1/2} dt = \int_{\vec{x_0}}^{\vec{X}} F(\vec{x}, \dot{\vec{x}}) dt, \tag{4.5}$$

A general variation of (4.5) is given (see e.g. (Smirnov, 1964)) as:

$$\delta T = \frac{\partial F}{\partial \dot{x}_i} \delta x_i + \int_{\vec{x_0}}^{\vec{X}} \left(\frac{\partial F}{\partial x_i} - \frac{d}{dt}\frac{\partial F}{\partial \dot{x}_i}\right) \delta x_i dt \tag{4.6}$$

Since we have integrated along a geodesic, the second term in (4.6) equals zero. Using the symmetry of the metric tensor ($g_{ij} = g_{ji}$), we obtain:

$$\frac{\partial T}{\partial x_i} = \frac{\partial F}{\partial \dot{x}_j} = \frac{1}{v_0} \frac{g_{ij} \dot{x}_i}{(g_{kl} \dot{x}_k \dot{x}_l)^{1/2}} \tag{4.7}$$

Substituting (4.7) and (4.3) in the following equation yields:

$$\hat{D}_{ij}\frac{\partial T}{\partial x_i}\frac{\partial T}{\partial x_j} \equiv g_{ij}^{-1}\frac{\partial T}{\partial x_i}\frac{\partial T}{\partial x_j} = \frac{1}{v_0^2}\frac{g_{ij}\dot{x}_i\dot{x}_j}{g_{kl}\dot{x}_k\dot{x}_l} = \frac{1}{v_0^2} \tag{4.8}$$

Equation (4.8) is known as the zero-order eikonal equation for wave propagation in the reaction-diffusion system (4.1) (Franzone *et al.*, 1990; Keener & Sneyd, 1998), where T stands for the arrival time of the wave. Now we see that the value of function (4.4) can be interpreted as the travel time of a wave propagating from point $\vec{x_0}$ to $\vec{x_1}$. Furthermore, the geodesic, and hence the stable filament shape (Wellner *et al.*, 2002), is the path of shortest travel time of a wave propagating from point $\vec{x_0}$ to point $\vec{x_1}$.

In conclusion, we have shown that the physical interpretation of the 'path element' of the metric space introduced in (Wellner *et al.*, 2002) is the wave travel time, and hence that the 'minimal path' principle can be seen as a 'shortest travel time' principle. In addition, we have shown that the eikonal equation can be used to find the shortest wave path, and hence the stable filament shape. Since the eikonal equation (4.8) is the zero-order approximation for wave propagation in eq.(4.1), we can use (4.1) rather than (4.8) to find the shortest wave path. The wave algorithms used for finding the shortest wave path are discussed below.

4.3 Shortest path wave algorithms

To solve the shortest path problem, we use two algorithms similar to the classical Lee-Moore algorithms for finding the shortest path in a maze (Moore, 1959; Krinsky *et al.*, 1991). The principle is illustrated in Fig. 4.1A. Let us denote the vertical direction in the plane with the y coordinate and refer to a horizontal line of points as a y layer. To find the path of shortest travel time from point A to the upper boundary of the plane, we initiate a wave at point A and find the point with the earliest arrival time at the upper boundary (point B). The shortest wave path is determined by stepwise tracing back from point B to point A and finding the point of earliest arrival time (black circles) in each y layer and connecting these points.

To find a global shortest wave path between the lower and the upper boundaries, we modify the algorithm as follows. We initiate a wave at the whole lower boundary of the medium, rather than at a single point and find the arrival times (Fig. 4.1B, continuous lines). Then we do the same for a planar wave initiated at the upper boundary (Fig. 4.1B, broken lines). The global shortest wave path of the medium is the line connecting the points that have the minimum summed arrival time in each y layer (Fig. 4.1C).

4.4 Numerical results

We illustrate the predictive value of our wave algorithms by numerical simulations in a two variable FitzHugh-Nagumo model for excitable media of the form

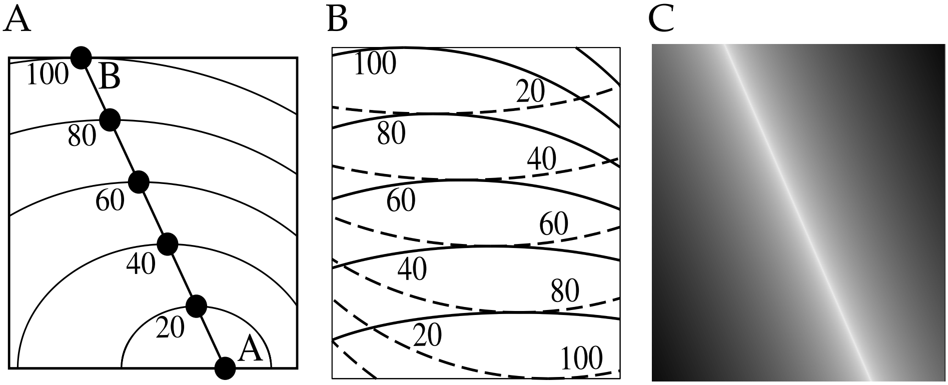

Figure 4.1: Illustration of the first (**A**) and second (**B** and **C**) shortest path wave algorithm. In A and B lines with numbers are iso-arrival time lines. In B the continuous lines are for an upward and the broken lines for a downward propagating wave. In C gray-scale indicates summed arrival time (white is short, black is long). For an explanation of the algorithms see text.

(4.1) with

$$\Phi(u,\vec{v}) = -ku(u-a)(u-1) - uv; \quad \vec{\Psi}(u,\vec{v}) = \epsilon(ku - v) \tag{4.9}$$

Parameter values are: $a = 0.07$, $k = 8$ and $\epsilon = 0.066$.

We study three different cases of anisotropy. In the first case we use a conductivity tensor D_1 with parallel curved fiber organization similar to that of (Berenfeld *et al.*, 2001), but extended to the orthotropically anisotropic case (LeGrice *et al.*, 1997): $D_{xx} = D_T; D_{yy} = D_L\cos(\alpha)^2 + D_{TT}\sin(\alpha)^2; D_{yz} = D_{zy} = (D_L - D_{TT})\cos(\alpha)\sin(\alpha); D_{zz} = D_L\sin(\alpha)^2 + D_{TT}\cos(\alpha)^2; D_{xy} = D_{xz} = D_{yx} = D_{zx} = 0$, where D_L, D_T and D_{TT} are the conductivities parallel and transversal to the fibers, and transversal to the plane in which the fibers are organized, respectively. We choose $D_L = 1$, $D_T = 1/4$ and $D_{TT} = 1/16$. α is a function of position in the y direction: $\tan(\alpha) = \frac{2\pi A}{N} cos(\frac{2\pi y}{N})$, $A = 20$.

For the second and third case we performed the following transformations of the original conductivity tensor:

$$D_2 = \mathbf{A}^T D_1 \mathbf{A}; \quad D_3 = \mathbf{B}^T D_2 \mathbf{B} \tag{4.10}$$

Matrix **A** performs a rotation in the yz plane with an angle β, with $\beta = 2(N/2 - z)$. Matrix **B** performs a rotation in the xy plane by an angle $\gamma = 2(N/2 - x)$.

Computations were performed using an explicit time integration scheme on an $N \times N \times N$ array, with $N = 120$ and using Neumann boundary conditions. The time integration step was dt=0.02, the space integration step was dx=0.01. We used initial data corresponding to a broken wave front to create scroll waves.

We start with a medium described by conductivity tensor D_1. Fig. 4.2A shows a stable scroll wave rotating in this medium. The scroll wave filament, together

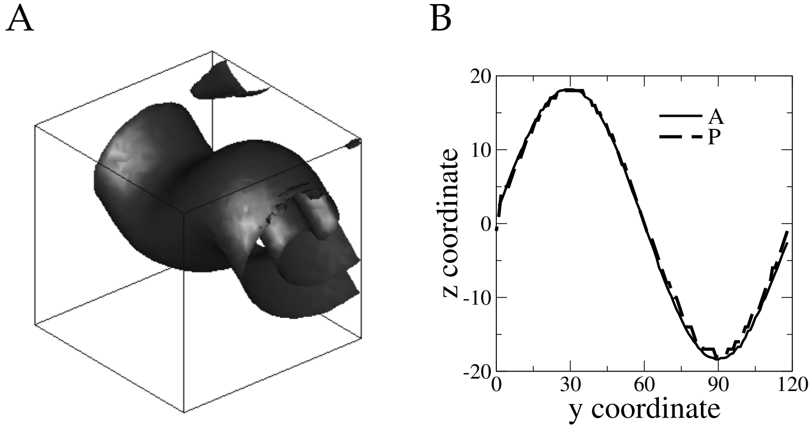

Figure 4.2: **A** Scroll wave in a medium with conductivity tensor D_1. **B** Actual (A) and predicted (P) filament shape.

with the prediction we found using the first wave algorithm (Fig. 4.1A), by initiating a wave at the point were the scroll filament touches the $y = 0$ boundary, are shown in Fig. 4.2B. We see that our algorithm's prediction agrees well with the actual filament shape (note that the resolution of our algorithm is restricted to the space step of the simulation grid).

Because of the translational symmetry of D_1 in the xz plane, filaments with similar shapes can be obtained starting from almost any point at the $y = 0$ boundary, provided it is not too close to the other boundaries. To unfold this degeneracy, we performed simulations in a medium with conductivity tensor D_2, obtained via a non-uniform rotation of tensor D_1 in the yz plane. To determine the global shortest wave path of this medium we applied the second wave algorithm (Fig. 4.1B), with plane waves initiated at the $y = 0$ and $y = N$ boundaries.

We found a family of shortest wave paths making up a shortest path surface (Fig. 4.3 gray) that is translationally invariant in the x direction. We tested the prediction from the wave algorithm by initiating two scroll waves at different initial positions. Fig. 4.3A to D shows that the two scroll wave filaments (both in black) align with the predicted shortest wave path surface in the course of time, each at a different x position.

To unfold the symmetry of conductivity tensor D_2 in the x direction, we performed simulations in a medium with conductivity tensor D_3 (obtained via a non-uniform rotation of tensor D_2 in the xy plane). Fig. 4.4 shows the shortest wave path (gray) predicted by the second wave algorithm, which now is a single curve that will act as a global attractor for all filaments running from $y = 0$ to $y = N$. Fig. 4.4A to D shows that the filament (black) of a scroll wave initiated at an arbitrary initial position indeed aligns with the predicted shortest wave path curve in the course of time.

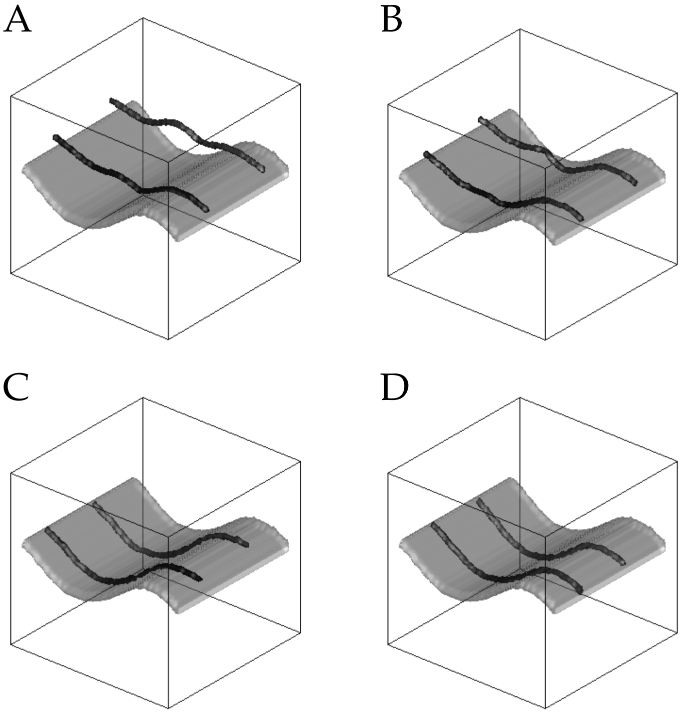

Figure 4.3: Convergence of two filaments (both in black) to the shortest wave path predicted by our algorithm (gray). Snapshots were taken at time (dimensionless units) 23.5 (A), 50 (B), 850 (C) and 3100 (D).

4.5 Discussion

The original Wellner *et al.* (2002) principle and our reformulation imply that the filament shape of a stable scroll wave in a 3D anisotropic reaction-diffusion medium is solely defined by the diffusion tensor and does not depend on the reaction kinetics of the medium. In our view this is similar to previous observations that filaments in rectangular isotropic media minimize their length and attain a straight shape independent of the medium's reaction kinetics. In the anisotropic case, where shortest length is not clearly defined, the minimal principle states that filaments will attain the shape of the path of shortest travel time. We demonstrated that this shortest travel time path can be found with wave algorithms that use the same equations for wave propagation as those used for the actual scroll wave simulations. Note that this by no means implies any similarity between equations describing filament dynamics (which are still unknown for general anisotropic media) and equations describing wave propagation.

Note, however, that these explanations are only qualitative. Further research is needed to establish why stable filament shape does not depend on reaction kinetics, and to determine why the filament of a scroll wave in an anisotropic

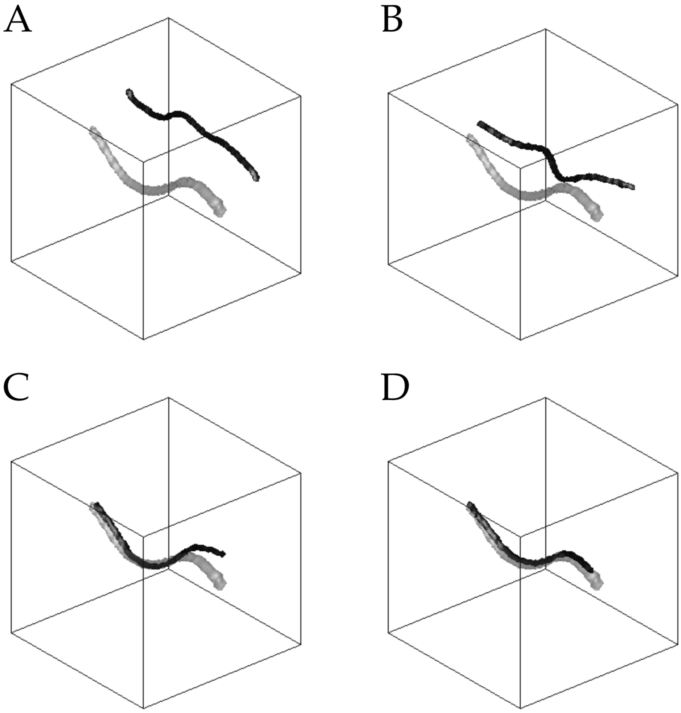

Figure 4.4: Convergence of a scroll wave filament (black) to the shortest wave path predicted by our algorithm (gray). Snapshots were taken at time 23.5 (A), 100 (B), 850 (C) and 3100 (D).

medium follows the path of shortest travel time of a wave propagating through the medium.

In this Letter, we propose an eikonal formulation of the minimal principle for scroll wave filaments that allows the application of shortest path wave algorithms to find stable filament configurations. An important feature of this method is that it allows the prediction of stable filament shapes without a priori knowledge of the anisotropic conductivity tensor of the medium and of the filament end positions on the tissue boundaries. The only information that is required are the arrival times of a planar wave front initiated at the tissue boundaries. The method can be applied to any tissue anisotropy and boundary geometry. Since arrival times may be obtained for 3D wave propagation in cardiac tissue, using, for example, the transillumination technique (Baxter *et al.*, 2001), our method can thus be applied to real cardiac tissue.

The original formulation of the minimal principle (Wellner *et al.*, 2002) was proposed for the case of isotropic transversal anisotropy. Here, we extended the numerical verification of this principle to media with orthotropic anisotropy, which is extremely relevant for cardiac tissue (LeGrice *et al.*, 1995).

Our method has several limitations that should be addressed in future studies: First, our wave algorithm, as well as the original geodesic formulation, is proposed for the case of homogeneously excitable media and non-meandering scroll waves. Second, our wave algorithm finds a global shortest wave path, while filaments can potentially be stable at local minima that may exist for particular anisotropy configurations. Third, our method is precise only if one uses the eikonal equation (4.8) in the shortest path wave algorithms. The approximation used in this paper (equations (4.1)) is accurate provided that the effect of curvature on wave propagation is small.

In conclusion, we propose an eikonal formulation of the minimal principle for stable filament shapes that allows us to effectively predict filament configurations in complex anisotropic excitable media.

Acknowledgments

We are grateful to Dr. S. Fomel and Dr. R. Hinch, for valuable discussions on important aspects of our Letter. This research is funded by the Netherlands Organization for Scientific Research (NWO) through Grant No. 620061351 of the Research Council for Physical Sciences (EW) (K.H.W.J.t.T.).

Part II

Reentrant arrhythmias in human ventricular tissue

5

A model for human ventricular tissue

K. H. W. J. Ten Tusscher[1], D. Noble[2], P. J. Noble[2], and A. V. Panfilov[1,3]
[1]*Department of Theoretical Biology, Utrecht University,*
Padualaan 8, 3584 CH Utrecht, The Netherlands.
[2]*University Laboratory of Physiology, University of Oxford,*
Parks Road, Oxford OX1 3PT, United Kingdom.
[3]*Division of Mathematics, University of Dundee,*
23 Perth Road, Dundee DD1 4HN, United Kingdom.

Am J Physiol Heart Circ Physiol **286**: H1573–H1589 (2004)

Abstract

The experimental and clinical possibilities for studying cardiac arrhythmias in human ventricular myocardium are very limited. Therefore, the use of alternative methods such as computer simulations is of great importance. In this article we introduce a mathematical model of the action potential of human ventricular cells that, while including a high level of electrophysiological detail, is computationally cost-effective enough to be applied in large-scale spatial simulations for the study of reentrant arrhythmias. The model is based on recent experimental data on most of the major ionic currents: the fast sodium, L-type calcium, transient outward, rapid and slow delayed rectifier, and inward rectifier currents. The model includes a basic calcium dynamics, allowing for the realistic modeling of calcium transients, calcium current inactivation, and the contraction staircase.

We are able to reproduce human epicardial, endocardial and M cell action potentials and show that differences can be explained by differences in the transient outward and slow delayed rectifier currents. Our model reproduces the experimentally observed data on action potential duration restitution, which is an important characteristic for reentrant arrhythmias. The conduction velocity restitution of our model is broader than in other models and agrees better with available data. Finally, we model the dynamics of spiral wave rotation in a two-dimensional sheet of human ventricular tissue and show that the spiral wave follows a complex meandering pattern and has a period of 265*ms*.

We conclude that the proposed model reproduces a variety of electrophysiological behaviors and provides a basis for studies of reentrant arrhythmias in human ventricular tissue.

5.1 Introduction

Cardiac arrhythmias and sudden cardiac death are among the most common causes of death in the industrialized world. Despite decades of research their causes are still poorly understood. Theoretical studies into the mechanisms of cardiac arrhythmias form a well-established area of research. One of the most important applications of these theoretical studies is the simulation of the human heart, which is important for a number of reasons. First, the possibilities for doing experimental and clinical studies involving human hearts are very limited. Second, animal hearts used for experimental studies may differ significantly from human hearts (heart size, heart rate, action potential (AP) shape, duration, and restitution, vulnerability to arrhythmias, etc.). Finally, cardiac arrhythmias, especially those occurring in the ventricles, are three-dimensional phenomena whereas experimental observations are still largely constrained to surface recordings. Computer simulations of arrhythmias in the human heart can overcome some of these problems.

To perform simulation studies of reentrant arrhythmias in human ventricles we need a mathematical model that on the one hand reproduces detailed properties of single human ventricular cells, such as the major ionic currents, calcium transients, and AP duration (ADP) restitution (APDR), and important properties of wave propagation in human ventricular tissue, such as conduction velocity (CV) restitution (CVR). On the other hand, it should be computationally efficient enough to be applied in the large-scale spatial simulations needed to study reentrant arrhythmias.

Currently, the only existing model for human ventricular cells is the Priebe-Beuckelman (PB) model and the reduced version of this model constructed by Bernus *et al.* (Priebe & Beuckelmann, 1998; Bernus *et al.*, 2002). The PB model is largely based on the phase 2 Luo-Rudy (LR) model for guinea pig ventricular cells (Luo & Rudy, 1994). Although the model incorporates some data on human cardiac cells and successfully reproduces basic properties of APs of normal and failing human ventricular cells, it has several limitations. First, several major ionic currents are still largely based on animal data, and second, the APD is $360ms$, which is much longer than the values typically recorded in tissue experiments ($\sim 270ms$ (Li *et al.*, 1998)). The aim of this work was to formulate a new model for human ventricular cells that is based on recent experimental data and that is efficient for large-scale spatial simulations of reentrant phenomena.

We formulated a model in which most major ionic currents (fast Na^+ current (I_{Na}), L-type Ca^{2+} current (I_{CaL}), transient outward current (I_{to}), rapid delayed rectifier current (I_{Kr}), slow delayed rectifier current (I_{Ks}), and inward rectifier current (I_{K1})) are based on recent experimental data. The model includes a simple calcium dynamics that reproduces realistic calcium transients and a positive human contraction staircase and allows us to realistically model calcium-dominated I_{CaL} inactivation, while at the same time maintaining a low computational load.

The model fits experimentally measured APDR properties of human myocardium (Morgan *et al.*, 1992). In addition, the CVR properties of our model agree better with experimental data −which are currently only available for dog and guinea pig (Cao *et al.*, 1999; Girouard *et al.*, 1996)− than those of existing ionic models. Both APD and CV restitution are very important properties for the occurrence and stability of reentrant arrhythmias (Karma, 1994; Qu *et al.*, 1999; Cao *et al.*, 1999; Garfinkel *et al.*, 2000; Watanabe *et al.*, 2001). Our model is able to reproduce the different AP shapes corresponding to the endo-, epi-, and midmyocardial regions of the ventricles and their different rate dependencies (Drouin *et al.*, 1995, 1998; Li *et al.*, 1998). Finally, we model spiral wave dynamics in a two-dimensional (2D) sheet of human ventricular tissue and study the dynamics of its rotation, the ECG manifestation of the spiral wave, and membrane potential recordings during spiral wave rotation. In conclusion, we propose a new model for human ventricular tissue that is feasible for large-scale spatial computations of reentrant sources of cardiac arrhythmias.

5.2 Materials and Methods

5.2.1 General

The cell membrane is modeled as a capacitor connected in parallel with variable resistances and batteries representing the different ionic currents and pumps. The electrophysiological behavior of a single cell can hence be described with the following differential equation (Hodgkin & Huxley, 1952):

$$\frac{dV}{dt} = -\frac{I_{ion} + I_{stim}}{C_m} \tag{5.1}$$

where V is voltage, t is time, I_{ion} is the sum of all transmembrane ionic currents, I_{stim} is the externally applied stimulus current, and C_m is cell capacitance per unit surface area.

Similarly, ignoring the discrete character of microscopic cardiac cell structure, a 2D sheet of cardiac cells can be modeled as a continuous system with the following partial differential equation (Hodgkin & Huxley, 1952):

$$\frac{\partial V}{\partial t} = -\frac{I_{ion} + I_{stim}}{C_m} + \frac{1}{\rho_x S_x C_m}\frac{\partial^2 V}{\partial x^2} + \frac{1}{\rho_y S_y C_m}\frac{\partial^2 V}{\partial y^2} \tag{5.2}$$

where ρ_x and ρ_y are the cellular resistivity in the x and y directions, S_x and S_y are the surface-to-volume ratio in the x and y directions, and I_{ion} is the sum of all transmembrane ionic currents given by the following equation:

$$\begin{aligned} I_{ion} = {} & I_{Na} + I_{K1} + I_{to} + I_{Kr} + I_{Ks} + I_{CaL} + I_{NaCa} + I_{NaK} \\ & + I_{pCa} + I_{pK} + I_{bCa} + I_{bNa} \end{aligned} \tag{5.3}$$

where I_{NaCa} is Na^+/Ca^{2+} exchanger current, I_{NaK} is Na^+/K^+ pump current, I_{pCa} and I_{pK} are plateau Ca^{2+} and K^+ currents, and I_{bCa} and I_{bNa} are background Ca^{2+} and Na^+ currents.

Physical units used in our model are as follows: time (t) in milliseconds, voltage (V) in millivolts, current densities (I_X) in picoamperes per picofarad, conductances (G_X) in nanosiemens per picofarad, and intracellular and extracellular ionic concentrations (X_i, X_o) in millimoles per liter. The equations for the ionic currents are specified in *Membrane Currents*.

For one-dimensional (1D) computations cell capacitance per unit surface area is taken as $C_m = 2.0\mu F/cm^2$ and surface-to-volume ratio is set to $S = 0.2\mu m^{-1}$, following Bernus *et al.* (2002). To obtain a maximum planar conduction velocity (CV) of $70cm/s$, the velocity found for conductance along the fiber direction in human myocardium by Taggart *et al.* (2000), a cellular resistivity $\rho = 162\Omega cm$ was required. This is comparable to the $\rho = 180\Omega cm$ used by Bernus *et al.* (2002) and the $\rho = 181\Omega cm$ used by Jongsma & Wilders (2000), and it results in a "diffusion" coefficient $D = 1/(\rho S C_m)$ of $0.00154cm^2ms^{-1}$. Because in 2D we did not intend to study the effects of anisotropy, we use the same values for ρ_x and ρ_y, and for S_x and S_y. Parameters of the model are given in Table 5.1.

Table 5.1: Model parameters.

Parameter	Definition	Value
R	Gas constant	$8.3143JK^{-1}mol^{-1}$
T	Temperature	$310K$
F	Faraday constant	$96.4867Cmmol^{-1}$
C_m	cell capacitance per unit surface area	$2.\mu Fcm^{-2}$
S	surface to volume ratio	$0.2\mu m^{-1}$
ρ	cellular resistivity	$162\Omega cm$
V_C	cytoplasmic volume	$16,404\mu m^3$
V_{SR}	sarcoplasmic reticulum volume	$1,094\mu m^3$
K_o	Extracellular K^+ concentration	$5.4mM$
Na_o	Extracellular Na^+ concentration	$140mM$
Ca_o	Extracellular Ca^{2+} concentration	$2mM$
G_{Na}	Maximal I_{Na} conductance	$14.838nSpF^{-1}$
G_{K1}	Maximal I_{K1} conductance	$5.405nSpF^{-1}$
G_{to}, epi, M	Maximal epicardial I_{to} conductance	$0.294nSpF^{-1}$
G_{to}, endo	Maximal endocardial I_{to} conductance	$0.073nSpF^{-1}$
G_{Kr}	Maximal I_{Kr} conductance	$0.096nSpF^{-1}$
G_{Ks}, epi, endo	Maximal epi and endocardial I_{Ks} conductance	$0.245nSpF^{-1}$
G_{Ks}, M	Maximal M cell I_{Ks} conductance	$0.062nSpF^{-1}$
p_{KNa}	Relative I_{Ks} permeability to Na^+	0.03
G_{CaL}	Maximal I_{CaL} conductance	$1.75^{-4}cm^3\mu F^{-1}s^{-1}$
k_{NaCa}	Maximal I_{NaCa}	$1000pApF^{-1}$
γ	Voltage dependence parameter of I_{NaCa}	0.35
K_{mCa}	Ca_i half saturation constant for I_{NaCa}	$1.38mM$
K_{mNai}	Na_i half saturation constant for I_{NaCa}	$87.5mM$
k_{sat}	Saturation factor for I_{NaCa}	0.1
α	Factor enhancing outward nature of I_{NaCa}	2.5

Continued on next page

Continued from previous page

Parameter	Definition	Value
P_{NaK}	Maximal I_{NaK}	$1.362 pApF^{-1}$
K_{mK}	K_o half saturation constant of I_{NaK}	$1 mM$
K_{mNa}	Na_i half saturation constant of I_{NaK}	$40 mM$
G_{pK}	Maximal I_{pK} conductance	$0.0146 nSpF^{-1}$
G_{pCa}	Maximal I_{pCa} conductance	$0.825 pApF^{-1}$
K_{pCa}	Half saturation constant of I_{pCa}	$0.0005 mM$
G_{bNa}	Maximal I_{bNa} conductance	$0.00029 nSpF^{-1}$
G_{bCa}	Maximal I_{bCa} conductance	$0.000592 nSpF^{-1}$
V_{maxup}	Maximal I_{up}	$0.000425 mMms^{-1}$
K_{up}	Half saturation constant of I_{up}	$0.00025 mM$
a_{rel}	Maximal Ca_{SR} dependent I_{rel}	$16.464 mMs^{-1}$
b_{rel}	Ca_{SR} half saturation constant of I_{rel}	$0.25 mM$
c_{rel}	Maximal Ca_{SR} independent I_{rel}	$8.232 mMs^{-1}$
V_{leak}	Maximal I_{leak}	$0.00008 ms^{-1}$
Buf_c	Total cytoplasmic buffer concentration	$0.15 mM$
K_{bufc}	Ca_i half saturation constant for cytoplasmic buffer	$0.001 mM$
Buf_{sr}	Total sarcoplasmic buffer concentration	$10 mM$
K_{bufsr}	Ca_{SR} half saturation constant for sarcoplasmic buffer	$0.3 mM$

For 1D and 2D computations, the forward Euler method was used to integrate Eq. 5.1. A space step of $\Delta x = 0.1\text{-}0.2 mm$ and a time step of $\Delta t = 0.01\text{-}0.02 ms$ were used. To integrate the Hodgkin-Huxley-type equations for the gating variables of the various time-dependent currents (m, h and j for I_{Na}, r and s for I_{to}, x_{r1} and x_{r2} for I_{Kr}, x_s for I_{Ks}, d, f and f_{Ca} for I_{CaL}, and g for I_{rel}) the Rush and Larsen scheme (Rush & Larsen, 1978) was used.

We test the accuracy of our numerical simulations in a cable of cells by varying both the time and space steps of integration. The results of these tests are shown in Table 5.2. From Table 5.2 it follows that, with a $\Delta x = 0.2 mm$, decreasing Δt from 0.02 to $0.0025 ms$ leads to a 3.7% increase in CV. Similarly, with $\Delta t = 0.02 ms$, decreasing Δx from 0.2 to $0.1 mm$ leads to an increase in CV of 4.6%. The changes in CV occurring for changes in space and time integration steps are similar to those occurring in other models (see, for example (Qu *et al.*, 1999)). The time and space steps used in most computations are $\Delta t = 0.02 ms$ and $\Delta x = 0.2 mm$, similar to values used in other studies (Qu *et al.*, 1999; Cao *et al.*, 1999; Xie *et al.*, 2001a; Bernus *et al.*, 2002). Major conclusions of our model were tested for smaller space and time steps; the results were only slightly different.

Action potential duration (APD) is defined as action potential duration at 90% repolarization (APD_{90}). Two different protocols were used to determine APD restitution ($APDR$). The S1-S2 restitution protocol, typically used in experiments, consists of 10 S1 stimuli applied at a frequency of 1Hz and a strength of two times the threshold value, followed by a S2 extra-stimulus delivered at some diastolic interval (DI) after the AP generated by the last S1 stimulus. The APDR curve is generated by decreasing DI and plotting APD generated by the S2 stimulus against DI. The second restitution protocol is called the dynamic restitution

Table 5.2: Numerical accuracy of CV for different Δt and Δx.

Conduction velocity (cm/s)				
Δx, cm	$\Delta t = 0.0025$ ms	$\Delta t = 0.005$ ms	$\Delta t = 0.01$ ms	$\Delta t = 0.02$ ms
0.010	75.4	75.0	74.2	72.5
0.015	74.4	73.8	73.0	71.5
0.020	71.9	71.5	70.8	69.3
0.030	67.8	67.4	66.8	65.7
0.040	63.2	63.0	62.6	61.7

protocol. It was first proposed by Koller *et al.* (1998) as being a more relevant determinant of spiral wave stability than S1-S2 restitution. The protocol consists of a series of stimuli at a certain cycle length until a steady-state APD is reached; after that, cycle length is decreased. The APDR curve is obtained by plotting steady-state APDs against steady-state DIs. CV restitution (CVR) was simulated in a linear strand of 400 cells by pacing it at one end at various frequencies and measuring CV in the middle of the cable.

Spiral waves were initiated in 2D sheets of ventricular tissue with the S1-S2 protocol. We first applied a single S1 stimulus along the entire length of one side of the tissue, producing a planar wave front propagating in one direction. When the refractory tail of this wave crossed the middle of the medium, a second S2 stimulus was applied in the middle of the medium, parallel to the S1 wave front but only over three-quarters of the length of the medium. This produces a second wave front with a free end around which it curls, thus producing a spiral wave. Stimulus currents lasted for 2 (S1) and 5 (S2) ms and were two times diastolic threshold. The trajectory of the spiral tip was traced with an algorithm suggested by Fenton & Karma (1998). It is based on the idea that the spiral tip is defined as the point where excitation wave front and repolarization wave back meet. This point can be found as the intersection point of an isopotential line (in our case $-35mV$) and the $dV/dt = 0$ line.

Electrograms of spiral wave activity were simulated in 2D by calculating the dipole source density of the membrane potential V in each element, assuming an infinite volume conductor (Plonsey & Barr, 1989). The electrogram was recorded with a single electrode located $10cm$ above the center of the sheet of tissue.

All simulations were written in C^{++}. Single cell and cable simulations were run on a PC Intel Pentium III 800-MHz CPU; 2D simulations were run on 32 500-MHz processors of a SGI Origin 3800 shared-memory machine, using OpenMP for parallelization.
(Source code available on: **http://www-binf.bio.uu.nl/khwjtuss/HVM**)

A description of the membrane currents of the model and the experimental data on which they are based is given in *Membrane Currents*. For most currents a comparison is made with the formulations used in existing models for human ventricular myocytes by Priebe & Beuckelmann (1998) −for the rest of the text referred to as the PB model− and for human atrial myocytes by Courtemanche *et al.* (1998) −for the rest of the text referred to as the CRN model. For the fast Na^+ current a comparison is made to the widely used I_{Na} formulation first used in phase 1 of the Luo-Rudy (LR) model (Luo & Rudy, 1991) that is used in both the PB and CRN model. The LR I_{Na} formulation is largely based on the I_{Na} formulation by Ebihara & Johnson (1980), which is fitted to data from embryonic chicken heart cells, to which a slow inactivation gate j, as first proposed by Beeler & Reuter (1977), was added. A detailed listing of all equations can be found in the Appendix.

5.2.2 Membrane Currents

Fast Na^+ current: I_{Na}

We use the three gates formulation of I_{Na} first introduced by Beeler & Reuter (1977)

$$I_{Na} = G_{Na} m^3 h j (V - E_{Na}) \tag{5.4}$$

where m is an activation gate, h is a fast inactivation gate, and j is a slow inactivation gate. Each of these gates is governed by Hodgkin-Huxley-type equations for gating variables and characterized by a steady-state value and a time constant for reaching this steady-state value, both of which are functions of membrane potential (See Appendix).

The steady-state activation curve (m_∞^3) is fitted to data on steady-state activation of wild-type human Na^+ channels expressed in HEK-293 cells from Nagatomo *et al.* (1998). Experimental data were extrapolated to 37°. Because there is no equivalent to the Q_{10} values used to extrapolate time constants to different temperatures, a linear extrapolation was used based on a comparison of values obtained at 23° and 33°. Note that similar Na^+ channel activation data were obtained by others (Wan *et al.*, 2001; Makita *et al.*, 2000; Sakakibara *et al.*, 1992). Figure 5.1A shows the steady-state activation curve used in our model. For comparison temperature-corrected experimental data are added.

The steady-state curve for inactivation ($h_\infty \times j_\infty$) is fitted to steady-state inactivation data from Nagatomo *et al.* (1998). Again, data were extrapolated to 37°. Similar inactivation data were obtained by others (Wan *et al.*, 2001; Sakakibara *et al.*, 1992). Figure 5.1B shows the steady-state inactivation curve used in our model together with temperature-corrected experimental data. Note that for resting membrane potentials the h and j gates are partially inactivated.

The time constants τ_h and τ_j are derived from current decay (typically V greater than $-50mV$) and current recovery experiments (typically V less than $-80mV$) (Nagatomo *et al.*, 1998; Schneider *et al.*, 1994; Sakakibara *et al.*, 1992; Makita *et al.*, 2000; Wan *et al.*, 2001; Viswanathan *et al.*, 2001; Wang *et al.*, 2000). In both types of experiments a double-exponential fit is made to the data, allowing interpretation of the fast and slow inactivation time constants as τ_h and τ_j, respectively. To convert all data to 37° a $Q_{10} = 2.79$ (derived from a comparison of fast inactivation time constants obtained at 23° and 33° by Nagatomo *et al.*) was used. Figure 5.1D shows our fit for the fast inactivation time constants,

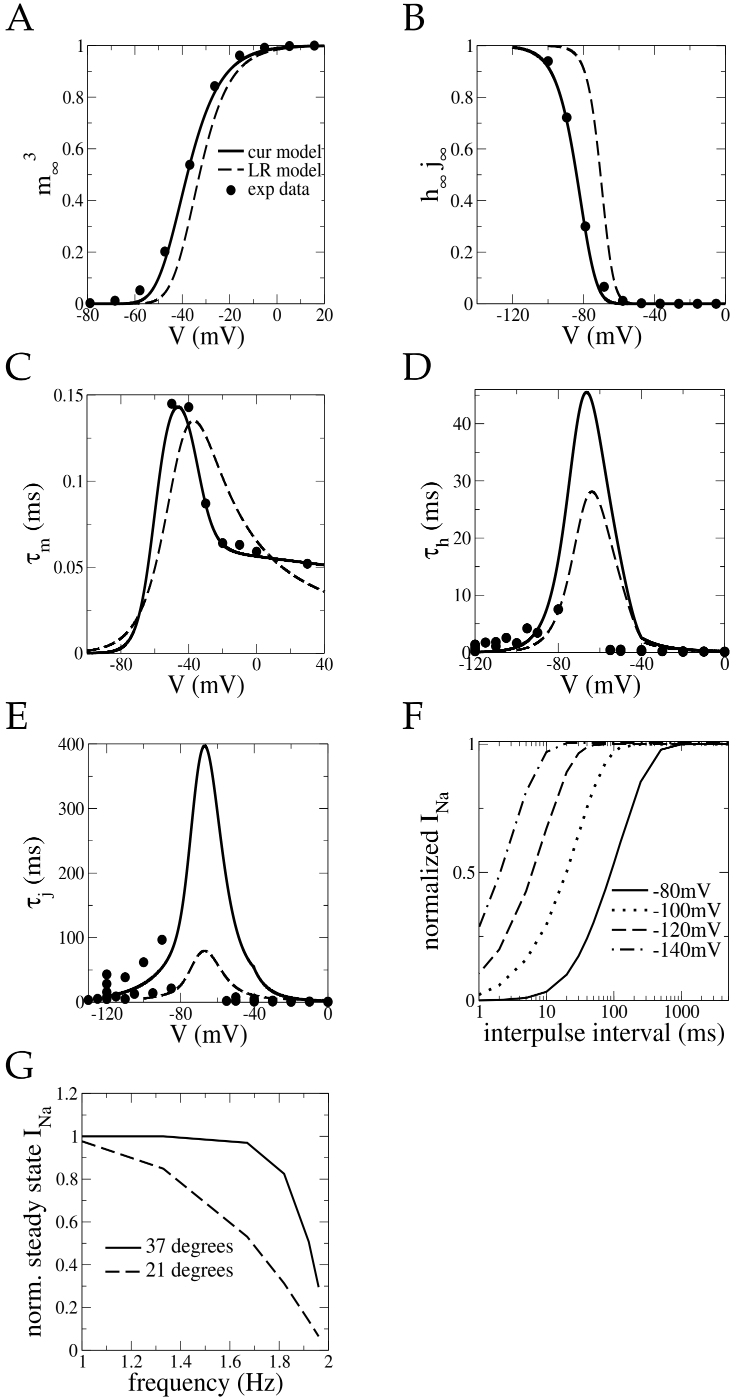
A
m_∞^3
V (mV)
cur model
LR model
exp data
B
$h_\infty j_\infty$
V (mV)
C
τ_m (ms)
V (mV)
D
τ_h (ms)
V (mV)
E
τ_j (ms)
V (mV)
F
normalized I_{Na}
interpulse interval (ms)
-80mV
-100mV
-120mV
-140mV
G
norm. steady state I_{Na}
frequency (Hz)
37 degrees
21 degrees

Figure 5.1: Steady-state and time constant curves describing the gating of the fast sodium current. Model curves of our model (cur model) and the Luo-Rudy (LR) model are shown together with experimental data. **A** steady-state activation curves. Experimental data are from Nagatomo *et al.* (1998) and are extrapolated to 37°. **B** steady-state inactivation curves. Experimental data are from Nagatomo *et al.* **C** activation time constants. Experimental activation time constants are derived from time to peak data from Nagatomo *et al.* Experimental data are converted to 37° ($Q_{10} = 2.79$). **D** fast inactivation constants. **E** slow inactivation constants. Fast and slow experimental inactivation time constants are taken from Nagatomo *et al.* (1998), Schneider *et al.* (1994), Sakakibara *et al.* (1992), Makita *et al.* (2000), Wan *et al.* (2001), Viswanathan *et al.* (2001) and Wang *et al.* (2000). Experimental time constants are converted to 37° ($Q_{10} = 2.79$). **F** recovery from inactivation for different recovery potentials. The time course of recovery from inactivation was established using a double-pulse protocol: from the holding potential a first 1-s duration pulse to $-20mV$ was applied to fully inactivate I_{Na}, then voltage was stepped back to the holding potential to allow recovery for periods ranging from $1ms$ to $5s$, and finally a second 30-ms pulse to $-20mV$ was applied to measure the amount of recovery. I_{Na} elicited by the second pulse was normalized to the I_{Na} elicited by the first pulse and is shown as a function of recovery time. **G** frequency dependence of I_{Na}. From a holding potential of $-100mV$, 500-ms pulses to $-10mV$ are given with interpulse intervals of 10, 20, 50, 100, 250, and 500ms, corresponding to stimulus frequencies of 1.96, 1.92, 1.82, 1.67, 1.3, and 1Hz. The steady-state I_{Na} obtained for the different frequencies is normalized to the I_{Na} current elicited by the first pulse. Frequency dependence was determined for 37° and 21 °. For the 21° experiments gate dynamics were adapted with a $Q_{10} = 2.79$.

and Fig. 5.1E shows our fit for the slow inactivation time constants of the model. Temperature-adjusted experimental data points are added for comparison.

Activation time constants are derived from time to peak data from Nagatomo *et al.*, converted as discussed above to 37°. τ_m can be calculated from the peak time (where $dI_{Na}/dt = 0$), assuming that j is constant, and knowing m_∞, h_∞ and τ_h. Figure 5.1C shows our fit of τ_m together with experimentally derived, temperature-corrected time constants.

In Fig. 5.1F the time course of recovery from inactivation for our I_{Na} is shown. Recovery from inactivation was established by applying a double-pulse protocol: from the holding potential, a 1-s duration pulse to $-20mV$ was applied to fully inactivate I_{Na}, the voltage was then stepped back to the holding potential to allow I_{Na} to recover for variable durations, and finally a second 30-ms pulse to $-20mV$ was applied. The I_{Na} elicited during the second pulse is normalized relative to the I_{Na} elicited during the first pulse to establish the amount of recovery. Figure 5.1F shows normalized I_{Na} as a function of the duration of the recovery interval between the two pulses for various values of the holding potential. Similar to experimental observations by Viswanathan *et al.* (2001), Nagatomo *et al.* (1998), Schneider *et al.* (1994), and Makita *et al.* (2000), recovery is slower for higher recovery potentials and has a sigmoid shape when plotted on a logarithmic scale. Note that in experiments I_{Na} recovery is often slower than observed in our model, because our model is at physiological temperature whereas most experiments are performed at room temperature.

Figure 5.1G displays the rate dependence of the I_{Na} current. Rate dependence was tested by applying 500-ms pulses to $-10mV$ from a holding potential of $-100mV$ with different interpulse intervals. Steady-state current was normalized to the current elicited by the first pulse. The graph shows that for increasing frequency (decreasing interpulse interval) I_{Na} decreases and that this decrease is considerably faster for 21° than for 37°. Experiments performed by Wang *et al.* (2000) at 32° using an interpulse interval of $20ms$ ($1.92Hz$) show a reduction to 0.17 of the original current level, which lies between the reduction to 0.5 we measure at 37° and the reduction to 0.13 we measure at 21°.

For comparison purposes we also added LR m_∞, h_∞, τ_m, τ_h, and τ_j curves to Fig. 5.1, A−E. The following observations can be made. Our steady-state activation curve lies $8mV$ to more negative potentials (Fig. 5.1A). Our steady-state inactivation curve lies $12mV$ to more negative potentials (Fig. 5.1B). Activation time constants are in the same range of values (Fig. 5.1C). Our τ_h curve has a similar shape, but for voltages smaller than $-40mV$ time constants are a factor of 1.6 larger, resulting in slower recovery dynamics (Fig. 5.1D). Similarly, our τ_j is a factor of 3−5 larger for voltages smaller than $-30mV$, leading to a considerably slower recovery from inactivation (Fig. 5.1E). G_{Na} was fitted to reproduce a $\dot{V}_{max} = 288mV/ms$, which is in the range of experimental data found by Drouin *et al.* (1998).

L-type Ca^{2+} current: I_{CaL}

The L-type calcium current is described by the following equation

$$I_{CaL} = G_{CaL} d f f_{Ca} 4 \frac{VF^2}{RT} \frac{Ca_i e^{2VF/RT} - 0.341 Ca_o}{e^{2VF/RT} - 1} \tag{5.5}$$

where d is a voltage-dependent activation gate, f is a voltage-dependent inactivation gate, f_{Ca} is an intracellular calcium-dependent inactivation gate, and driving force is modeled with a Goldmann-Hodgkin-Katz equation.

The steady-state activation d_∞ and steady-state voltage inactivation curve f_∞ are fitted to I_{CaL} steady-state data from human ventricular myocytes reported by Benitah *et al.* (1992), Mewes & Ravens (1994), Pelzmann *et al.* (1998), and Magyar *et al.* (2002). Figure 5.2A shows the steady-state activation, and Fig. 5.2B shows the steady-state inactivation curve of our model together with experimental data from Pelzmann *et al.* (1998).

Experimental data show that calcium-mediated inactivation is rapid, increases with calcium concentration, but is never complete (Sun *et al.*, 1997; Grantham & Cannell, 1996). More quantitative data about the precise dependence of amount and speed of inactivation on calcium concentration are unavailable and hard to obtain because intracellular calcium cannot be clamped to a constant value. As shown in Fig. 5.2C our $f_{ca\infty}$ curve has a switch-like shape, switching from no inactivation to considerable but incomplete inactivation if calcium concentration exceeds a certain threshold. For supra-threshold concentrations the amount of inactivation depends mildly on calcium concentration.

There are hardly any experimental data on activation times of I_{CaL} in human myocytes. Therefore, as was done in the CRN model, we used the curve from the phase 2 LR model. Limited data on I_{CaL} activation times from Pelzmann *et al.*

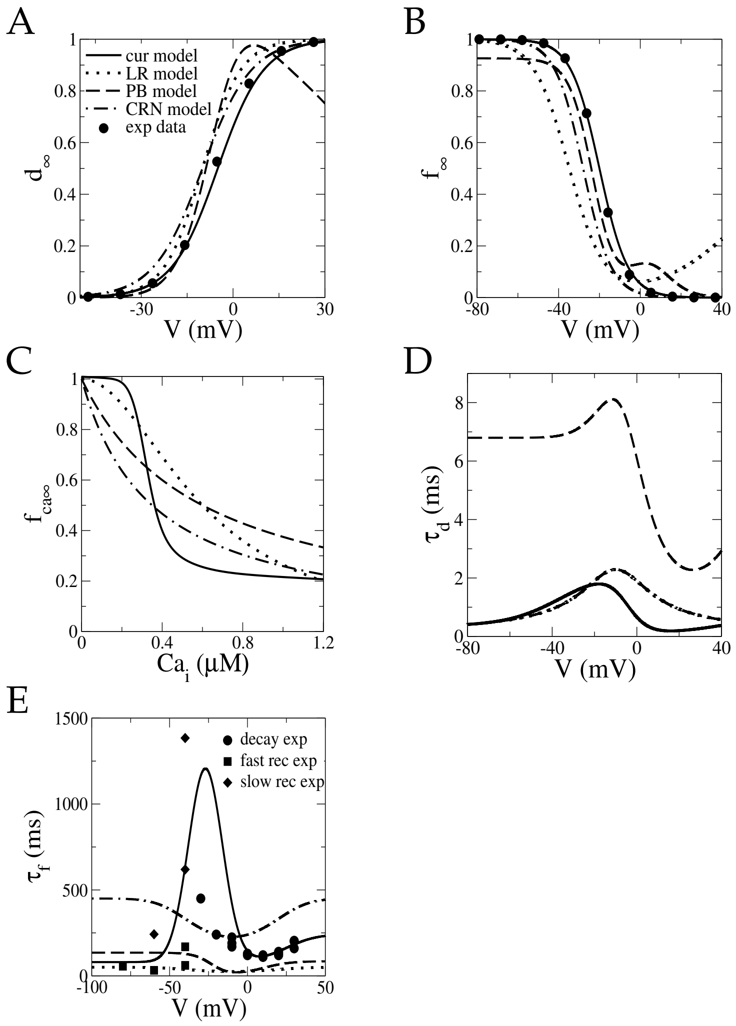

Figure 5.2: Steady-state and time constant curves describing the gating of the L-type calcium current. Model curves of our model (cur model), the LR model, the PB model, and the CRN model are shown together with experimental data. **A** steady-state voltage activation curves. Experimental steady-state activation data are from Pelzmann *et al.* (1998). **B** steady-state voltage inactivation curves. Experimental steady-state inactivation data are from Pelzmann *et al.* **C** steady-state calcium inactivation curves. **D** voltage activation time constants. Note that the LR and CRN model have the same time constant formulation: curves are overlapping. **E** voltage inactivation time constants. Experimental inactivation time constants are taken from Beuckelmann *et al.* (1991), Benitah *et al.* (1992), Mewes & Ravens (1994), Sun *et al.* (1997), Li & Nattel (1997), Pelzmann *et al.* (1998) and Magyar *et al.* (2002). Experimental data are converted to 37° ($Q_{10} = 2.1$). In addition, time constants derived from current decay experiments (V greater than $-30mV$) are also corrected for the presence of extracellular calcium (correction factor 2.2). For an explanation of the latter, see text.

(1998) were used to adjust the shape of the τ_d curve of the LR model. Figure 5.2D displays the voltage-dependent activation time constant of our model.

The time constant for τ_{fca} is derived from experiments performed by Sun *et al.* (1997). They show that during current decay experiments a fast and a slow time constant can be distinguished, with the fast time constant being independent of voltage and depending only on calcium, allowing interpretation as τ_{fca}. Sun *et al.* (1997) find a time constant of $\sim 12ms$ at 23°; no data on the concentration dependence of the time constant is available. We assumed a single time constant of $2ms$ to be reasonable at 37°, comparable to the immediate inactivation used in the PB model and the $2ms$ time constant used in the CRN model.

The time constant τ_f is derived from experiments on calcium current decay and recovery in human ventricular and atrial myocytes by Beuckelmann *et al.* (1991), Benitah *et al.* (1992), Mewes & Ravens (1994), Sun *et al.* (1997), Li & Nattel (1997), Pelzmann *et al.* (1998), and Magyar *et al.* (2002). Sun *et al.* (1997) show that during current decay experiments the slow inactivation time constant depends both on voltage and extracellular calcium. After removal of extracellular calcium, an even slower, purely voltage-dependent inactivation time constant arises. It is this time constant that should be interpreted as τ_f. Therefore, slow inactivation time constants found in current decay experiments were not only converted to 37° using a $Q_{10} = 2.1$ (based on a comparison of time constants obtained by Li *et al.* and Pelzmann *et al.* at physiological temperatures and data obtained by Benitah *et al.* at 21°) but were also corrected for the presence of extracellular Ca^{2+} using a slowing-down correction factor of 2.2 (based on a comparison of time constants obtained under normal conditions and under conditions in which extracellular Ca^{2+} was replaced by Sr^{2+} performed by Sun *et al.*).

In current recovery experiments also two time constants are derived. However, assuming that recovery from calcium inactivation is fast and given the clear voltage dependence of both fast and slow recovery time constants, both can be considered as voltage-dependent time constants. Because our formulation of I_{CaL} incorporates only a single voltage-dependent inactivation gate, our τ_f is constructed to form an intermediate between these fast and slow recovery time constants (-40<V<-80mV). Figure 5.2E displays the voltage-dependent inactivation time constant of our model. For comparison, experimentally found inactivation time constants are added.

For comparison purposes we also added LR phase 2, PB, and CRN model curves for d_∞, f_∞, $f_{ca\infty}$, τ_d and τ_f to Fig. 5.2, A−E. From this the following observations can be made. Our steady-state activation curve is similar to the curves used in the LR and CRN model. The PB model has, for unknown reasons, a curve with a somewhat different shape (Fig. 5.2A). Our steady-state inactivation curve inactivates completely, similar to the curve used in the CRN model, whereas the LR and PB model use incompletely inactivating curves (Fig. 5.2B). In experiments, inactivation is more complete if prepulse duration is longer or temperature is higher (Li & Nattel, 1997; Sun *et al.*, 1997), implying that inactivation is slow rather than incomplete.

Our $f_{ca\infty}$ curve has a switch shape, with a high level of inactivation beyond the threshold, whereas the LR, PB, and CRN curves are gradually declining functions of calcium (Fig. 5.2C). The high level of calcium inactivation, together with slow voltage inactivation, causes calcium to be the dominant mechanism of I_{CaL} inactivation in our model. This agrees well with experimental data. Incorporating calcium-dominated inactivation in models without local control may easily result in action potential instability: in a local control model (Rice *et al.*, 1999; Greenstein & Winslow, 2002) −in which individual I_{CaL} and calcium-induced calcium release (CICR) channels interact in subspaces− a smaller I_{CaL} current implies fewer open channels and hence fewer local calcium transients (sparks); the individual sparks still have the same effectiveness in closing nearby calcium channels. However, in a non-local control model, a smaller I_{CaL} generates a smaller global calcium transient that might be less effective in inactivating the I_{CaL} current. By using a switch-shape for $f_{ca\infty}$, we ensure effective calcium inactivation for a wide range of systolic calcium levels in our model.

The τ_d curve of our model has a similar shape as that used in the PB model, but with a factor of $2-3$ shorter time constants, and is a minor adaptation of the curves used in the LR and CRN model (Fig. 5.2D). Our τ_f curve, which is fitted to the experimental data, has a maximum between -50 and $0mV$, whereas the curves used in the LR, PB, and CRN models have a minimum in this voltage region, in strong contrast with the experimental data (Fig. 5.2E). The f gate inactivation in our model is much slower than in the LR and PB model; f gate inactivation in the CRN model is even slower. The slow f gate inactivation in our model and the CRN model is important for making calcium the dominant mechanism of I_{CaL} inactivation. The f gate recovery in our model is similar to that in the LR and PB model and a factor of 4 faster than in the CRN model. It plays an important role in determining APDR, which in our model agrees well with experimental data (See Fig. 5.8). P_{CaL} is fitted to reproduce peak current values found by Li & Nattel (1997) under physiological temperatures.

We modeled the driving force of the calcium current with the Goldmann-Hodgkin-Katz equation. For simplicity, we ignored the small permeability the channel also has for sodium and potassium ions. In the Luo-Rudy phase-2 model, a Goldmann-Hodgkin-Katz like equation for calcium, sodium and potassium is used. In the PB and CRN models a constant-valued reversal potential is used.

Transient outward current: I_{to}

For I_{to} the following formulation is used

$$I_{to} = G_{to} rs(V - E_K) \tag{5.6}$$

where r is a voltage-dependent activation gate and s is a voltage-dependent inactivation gate.

The steady-state activation curve (r_∞) is fitted to data on steady-state activation of I_{to} current in human ventricular myocytes of epicardial and endocardial origin at 35° from Nabauer *et al.* (1996). Because no significant difference between activation in epicardial and endocardial cells was found, a single formulation was used. Figure 5.3A shows the steady-state activation curve used in the model together with experimental data. A 10-mV positive shift was performed on the experimental data to account for the use of Cd^{2+} to block I_{CaL} current, similar to the approach taken by Courtemanche *et al.* (1998). The greater steepness of the

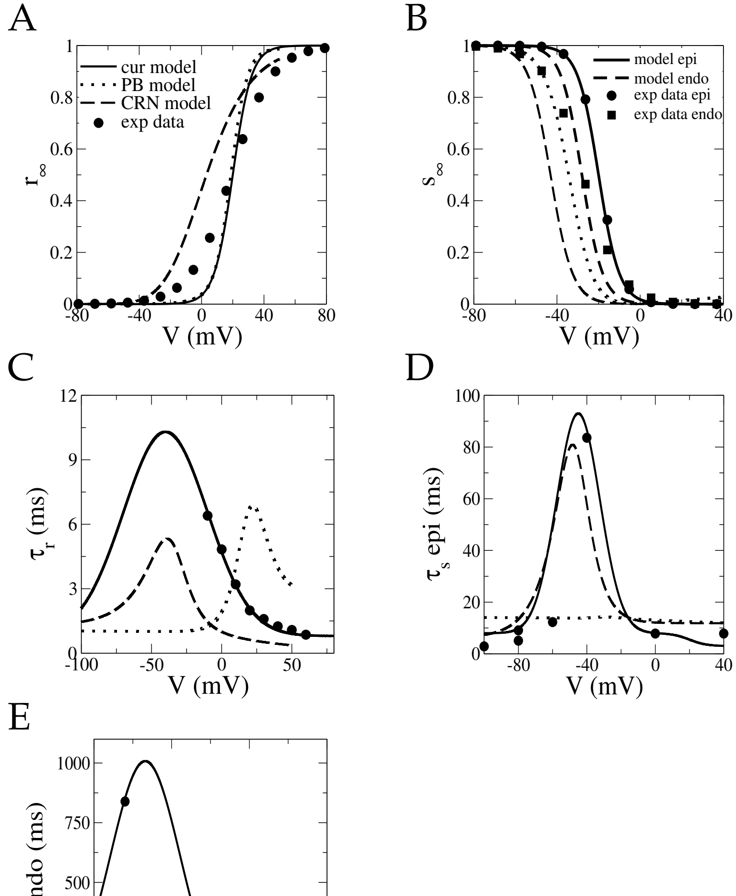

Figure 5.3: Steady-state and time constant curves describing the gating of the transient outward current. Model curves of our model (cur model), the PB, and the CRN model are shown together with experimental data. **A** steady-state activation curves. Experimental steady-state data are from Nabauer *et al.* (1996). A 10-mV positive shift was performed on the experimental curve to account for the use of Cd^{2+}. **B** steady-state inactivation curves. Cd^{2+}-corrected experimental data are from Nabauer *et al.* **C** activation time constants. Experimental activation time constants are derived from time to peak data by Greenstein *et al.* (2000). **D** epicardial inactivation time constants. Experimental inactivation time constants are from Nabauer *et al.* and are obtained at physiological temperatures. **E** endocardial inactivation time constants. Experimental data are from Nabauer *et al.*

model curve relative to the experimental curve was necessary to make sure that no significant reactivation of I_{to} occurs on repolarization.

The steady-state inactivation curve (s_∞) is fitted to data on steady-state inactivation from Nabauer *et al.* Because of significant differences between curves obtained for epicardial and endocardial cells, two separate model formulations were used. Figure 5.3B shows the steady-state inactivation curves used in the model together with Cd^{2+}-corrected experimental data.

Inactivation time constants are fitted to data from Nabauer *et al.* (1996) and Wettwer *et al.* (1994). Current decay experiments show similar time constants for epicardial and endocardial I_{to}, whereas current recovery experiments show much slower recovery from inactivation for endocardial than epicardial I_{to}, thus making two separate formulations for τ_s necessary. Figure 5.3D shows our fit for epicardial τ_s, and Fig. 5.3E shows our fit for endocardial τ_s. For comparison, experimental inactivation time constants are added.

Activation time constants are derived from time to peak data from expression of hKv4.3-2 −encoding an epicardial type transient outward channel− in mouse fibroblast cells by Greenstein *et al.* (2000) in a manner similar to the derivation of τ_m. Figure 5.3C shows our τ_r curve together with experimentally derived time constants.

For comparison purposes we also added PB and CRN model curves for r_∞, s_∞, τ_r, and τ_s to Fig. 5.3, A-D. From this the following observations can be made. The steady-state activation of our model almost coincides with that of the PB model and has a steeper slope and more positive half-activation point than that of the CRN model (Fig. 5.3A). In our model we distinguish epicardial and endocardial steady-state inactivation, whereas the PB and CRN model only have a single steady-state inactivation curve. The epicardial steady-state inactivation curve of our model lies 15 and 25 mV to more positive potentials than the curves used in the PB and CRN model, respectively. For the endocardial steady-state inactivation of our model these numbers are 8 and 18 mV, respectively (Fig. 5.3B).

The activation time constant of our model results in faster activation and slower deactivation than that of the PB model, whereas it is a factor of 2 slower than the CRN model time constant (Fig. 5.3C). However, in the CRN model three activation gates are used (r^3), causing net activation to be slower and net deactivation to be faster than that of a single gate and thus complicating the comparison. In our model we distinguish epicardial and endocardial inactivation time constants, whereas the PB and CRN model only have a single inactivation time constant. The inactivation time constant of the PB model resembles our epicardial inactivation time constant in magnitude but has hardly any voltage dependence. The inactivation time constant of the CRN model is similar to our epicardial inactivation time constant (Fig. 5.3D).

G_{to} is fitted to experimental data on current density from Wettwer *et al.* (1994) and Nabauer *et al.* (1996). Both show large differences in I_{to} size between epicardial and endocardial cells. We use $G_{to} = 0.294nS/pF$ for epicardial and $G_{to} = 0.073nS/pF$ for endocardial cells (25% of the value for epicardial cells). Figure 5.4 shows the current voltage (*I-V*) relationships for epicardial (Fig. 5.4A) and endocardial (Fig. 5.4B) I_{to} together with experimental data from Nabauer *et al.*

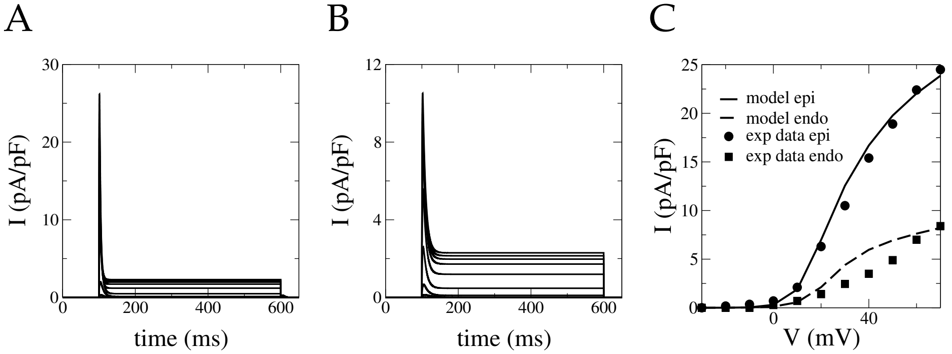

Figure 5.4: A and B: epicardial (**A**) and endocardial (**B**) I_{to} current traces generated by the model during simulated voltage clamp experiments. Currents are recorded during 500-ms voltage steps to potentials ranging from -30 to $80mV$ from a holding potential of $-80mV$ and an intermittent 100-ms prepulse to $-60mV$. Note that during simulation both the I_{to} and I_{pK} currents where switched on. The sustained part of the current traces is generated by I_{pK}. **C** epicardial and endocardial I_{to} current-voltage (*I-V*) curves obtained from the series of experiments shown in **A** and **B**, respectively. Peak current minus maintained current was measured. Experimental *I-V* curves from Nabauer *et al.* (1996), obtained using a similar voltage-clamp protocol, are added for comparison. The experimental curves are rescaled by a factor of 1.4. We choose I_{to} current density to be somewhat larger than experimentally found to obtain a realistic notch in epicardial action potential morphology.

(1996).

We assume that I_{to} is specific for potassium ions and used the reversal potential E_K. A similar approach is taken in the CRN model, whereas in the PB model it is assumed that the channel is also permeable to sodium ions.

Slow delayed rectifier current: I_{Ks}

For the slow delayed rectifier the following formulation is used

$$I_{Ks} = G_{Ks} x_s^2 (V - E_{Ks}) \tag{5.7}$$

where x_s is an activation gate and E_{Ks} is a reversal potential determined by a large permeability to potassium and a small permeability to sodium ions (See Appendix).

The steady-state activation curve ($x_{s\infty}^2$) is fitted to I_{Ks} activation data obtained for human ventricular myocytes at 36° from Li *et al.* (1996). In Figure 5.5A the steady-state activation curve used in the model is shown together with the experimental data.

Activation time constants are based on data from Virag *et al.* (2001) and Wang *et al.* (1994). Both sets of data were obtained in human ventricular myocytes at physiological temperatures. Figure 5.5B shows our fit of τ_{xs}. Experimentally obtained activation time constants are added for comparison.

Fitting G_{Ks} to experimentally obtained current densities would result in a small I_{Ks} current that has little effect on APD: simulating M cells by a 75% reduction in I_{Ks} current density (the principal difference with epicardial cells) would

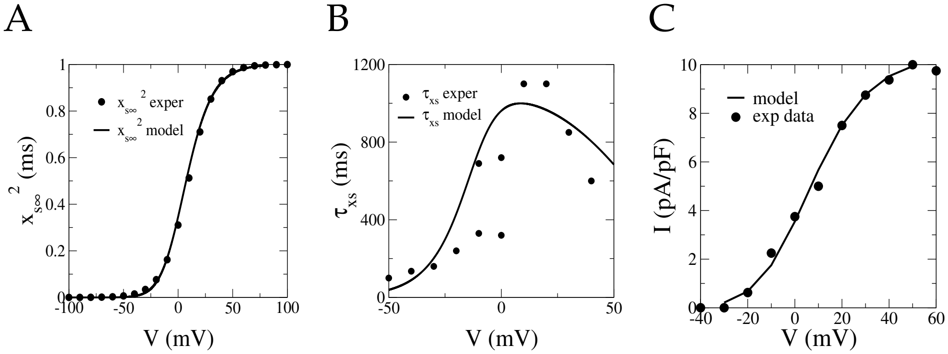

Figure 5.5: Steady-state and time constant curves describing the gating of the slow delayed rectifier current. **A** steady-state activation curve. Experimental steady-state data are from Li *et al.* (1996). **B** activation time constants. Experimental activation time constants are from Virag *et al.* (2001) (for voltages ranging from -50 to $0mV$) and Wang *et al.* (1994) (for voltages ranging from $-10mV$ to $40mV$) and are obtained at physiological temperatures. **C** *I-V* relationship for I_{Ks}. Tail currents are measured during 5,000-ms voltage steps to potentials ranging from -10 to $50mV$ from a holding potential of $-40mV$. Experimental *I-V* curves obtained using a similar protocol by Li *et al.* (1996) were included for comparison. Experimental data are rescaled by a factor of 12.5. See text for an explanation of why our model I_{Ks} is much larger than the experimentally measured I_{Ks}.

result in M cell APD being only $10ms$ longer than epicardial APD, in strong contrast with the 100-ms difference in APD found experimentally (Drouin *et al.*, 1995; Li *et al.*, 1998). Thus there is a discrepancy between current density measured in voltage-clamp experiments and the apparent contribution of the current to APD. This discrepancy is probably due to sensitivity of I_{Ks} channels to the cell isolation procedures used for voltage-clamp experiments (Yue *et al.*, 1996), resulting in considerable degradation of I_{Ks} channels before current density measurements. Therefore, instead of fitting G_{Ks} to voltage-clamp data, we based it on APD measurements: by using a $G_{Ks} = 0.245nSpF^{-1}$ for epicardial cells and a $G_{Ks} = 0.062nSpF^{-1}$ in M cells, we get an epicardial APD at 1Hz of $276ms$ and an M cell APD of $336ms$, resulting in an APD difference of $60ms$, which is in the range of experimental values (Drouin *et al.*, 1995; Li *et al.*, 1998). This approach of basing a conductance value on electrophysiological properties rather than measured current density is also used in the development of other models; e.g., in the CRN model, G_{Na} is fitted to get the right $\dot{V}_{max}$, G_{to} to get the right AP morphology and G_{Kr} and G_{Ks} to get the right APD (Courtemanche *et al.*, 1998) and in a later version of the LR model in which I_K was replaced by I_{Kr} and I_{Ks}, G_{Ks} was fitted to get the right APD prolongation if I_{Ks} current is blocked (Zeng *et al.*, 1995). In addition, the values used for G_{Ks} and G_{Kr} in the CRN model and the LR model are similar to the values we use in our model. In Figure 5.5 C the *I-V* relationship of I_{Ks} is shown together with rescaled experimental data from Li *et al.*

We use a sodium-to-potassium permeability ratio of $p_{KNa} = 0.03$, resulting in a reversal potential E_{Ks} that forms a compromise between reversal potentials found experimentally (Li *et al.*, 1996; Virag *et al.*, 2001). In the PB model a permeability ratio of 0.018 is used, whereas in the CRN model it is assumed that I_{Ks} is permeable to potassium ions only. Our steady-state activation curve lies 5 and $15mV$ to more positive potentials than the curves used in the CRN and PB models, respectively. Compared with the τ_{xs} formulations used by both of these models, our I_{Ks} displays slower activation and more rapid deactivation.

Rapid delayed rectifier current: I_{Kr}

The rapid delayed rectifier current is described by the following equation

$$I_{Kr} = G_{Kr}\sqrt{\frac{K_o}{5.4}}x_{r1}x_{r2}(V - E_K) \tag{5.8}$$

where x_{r1} is an activation gate and x_{r2} is an inactivation gate. $\sqrt{K_o/5.4}$ represents the K_o dependence of the current. Note that since no data are available on the K_o dependence of human ventricular I_{Kr}, a similar dependence as measured in and implemented for animal myocytes is assumed (Luo & Rudy, 1994).

The steady-state activation curve ($x_{r1\infty}$) is fitted to activation data on the expression of HERG channels in HEK 293 cells by Zhou *et al.* (1998), in Chinese hamster ovary cells by Johnson *et al.* (1999), and in *Xenopus* oocytes by Smith & Yellen (2002). Steady-state inactivation ($x_{r2\infty}$) is fitted to data from Johnson *et al.* (1999) and Smith & Yellen (2002). Figure 5.6A shows steady-state curves of the model together with experimental data.

Activation time constants (τ_{xr1}) are fitted to data from Zhou *et al.* (1998) obtained at physiological temperatures. τ_{xr2} is fitted to inactivation time constants obtained at physiological temperatures by Johnson *et al.* (1999). Figure 5.6B shows our fit of τ_{xr1} and Fig. 5.6C shows our fit of τ_{xr2}. Experimentally obtained time constants are added for comparison.

Fitting G_{Kr} to experimentally obtained current densities would result in an I_{Kr} that has a lower contribution to APD than suggested by experiments in which I_{Kr} is blocked (Li *et al.*, 1996). Therefore, similar to our approach for G_{Ks}, we used such a value for G_{Kr} ($0.096nSpF^{-1}$) that a complete blocking of I_{Kr} current leads to $44ms$ of APD prolongation, which is in the range of values found experimentally by Li *et al.* (1996). The *I-V* relationship of I_{Kr} is shown in Fig. 5.6D. For comparison, rescaled experimental data from Iost *et al.* (1998) and Li *et al.* (1996) are added. Note that our model curve is shifted toward more negative potentials relative to the experimental curves. This difference may be due to the fact that we fitted I_{Kr} to data from expression experiments in hamster and *Xenopus* cells, whereas the experimental *I-V* curves are from experiments on human cardiac cells.

The steady-state activation curve of our I_{Kr} lies 10 and $20mV$ to more negative potentials than the curves used in the PB and CRN model, respectively. τ_{xr1} has a size and shape similar to those used in these two models. We modeled inward rectification as a time-dependent inactivation gate, whereas the PB and the CRN model implemented this inactivation as being instantaneous. Our steady-state inactivation curve lies 50 and $60mV$ to more negative potentials than the inward rectification curves used in the PB and CRN models, which seem to have no clear experimental basis.

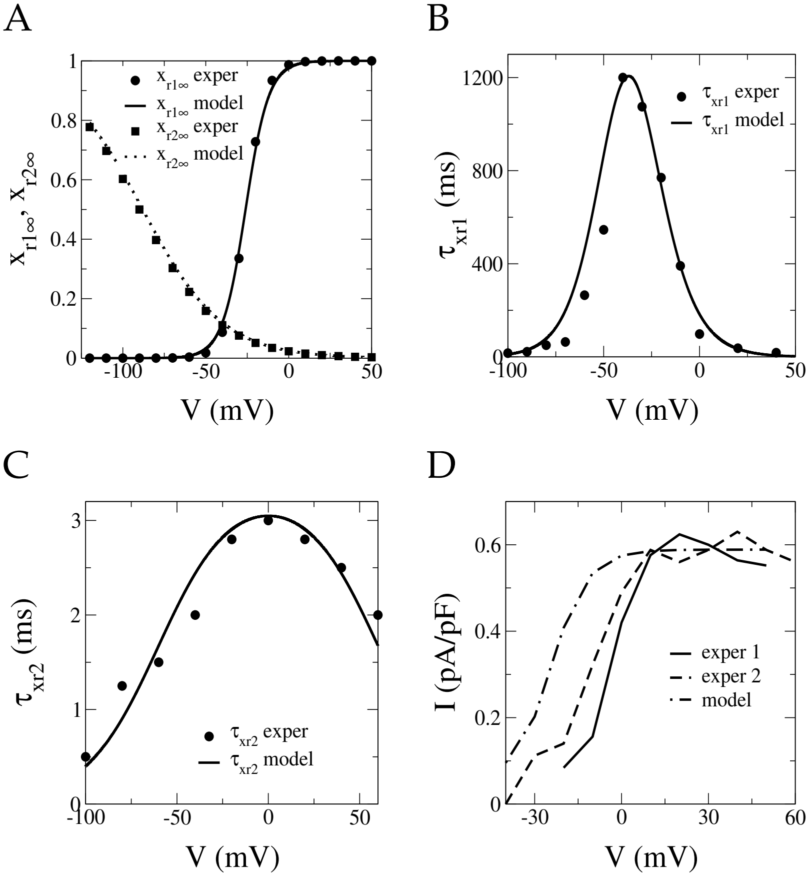

Figure 5.6: Steady-state and time constant curves describing the gating of the rapid delayed rectifier current. **A** steady-state activation and inactivation curves. Experimental data on steady-state activation are from Zhou *et al.* (1998), experimental data on inactivation are from Johnson *et al.* (1999) and Smith & Yellen (2002). **B** activation time constants. Experimental activation time constants are from Zhou *et al.* (1998). **C** inactivation time constants. Experimental inactivation time constants are from Johnson *et al.* (1999). Experimental time constants are obtained at physiological temperatures. **D** *I-V* relationship for I_{Kr}. Tail currents are measured during 3,000-ms voltage steps to potentials ranging from -40 to $60mV$ from a holding potential of $-60mV$. For comparison experimental *I-V* curves obtained using a similar protocol by Iost *et al.* (1998) (exper 1) and Li *et al.* (1996) (exper 2) are added. Experimental curves are rescaled by factors of 2.4 and 1.4, respectively. See text for an explanation of why our model I_{Kr} is larger than the experimentally measured I_{Kr}.

Inward rectifier K^+ *current:* I_{K1}

For I_{K1} the following formulation is used

$$I_{K1} = G_{K1}\sqrt{\frac{K_o}{5.4}}x_{K1\infty}(V - E_K) \tag{5.9}$$

where $x_{K1\infty}$ is a time-independent inward rectification factor that is a function of voltage. $\sqrt{K_o/5.4}$ represents the K_o dependence of the current. As for I_{Kr}, because of a lack of data on K_o dependence of human I_{K1} we assumed a dependence similar to that in animal myocytes.

Experimental data on I_{K1} current size are highly variable, as previously discussed by Courtemanche *et al.* (1998). We used the formulation for I_{K1} used in the PB model but increased G_{K1} by a factor of 2 to account for the larger current densities found by Koumi *et al.* (1995) in the for I_{K1} relevant voltage range ($-90mV$ to $-40mV$). This results in a value for G_{K1} that is approximately five times larger than in the CRN model, which agrees with data from Koumi *et al.* (1995) showing that I_{K1} is a factor of 5.6 higher in human ventricular than in atrial myocytes.

Na^+/Ca^{2+} exchanger current, Na^+/K^+ pump current, and plateau and background currents

For I_{NaCa} the following equation is used

$$I_{NaCa} = k_{NaCa} \frac{e^{\frac{\gamma VF}{RT}} Na_i^3 Ca_o - e^{\frac{(\gamma-1)VF}{RT}} Na_o^3 Ca_i \alpha}{(K_{mNai}^3 + Na_o^3)(K_{mCa} + Ca_o)(1 + k_{sat} e^{\frac{(\gamma-1)VF}{RT}})} \tag{5.10}$$

This formulation is similar to the equation used in the LR model, except for the extra factor α ($= 2.5$) that accounts for the higher concentration of calcium in the subspace close to the sarcolemmal membrane where the Na^+/Ca^{2+} exchanger actually is operating. Our approach is similar to that used in the Noble *et al.* model with diadic subspace (Noble *et al.*, 1998), where I_{NaCa} was made dependent on diadic calcium rather than bulk cytoplasmic calcium. Otherwise, during the AP plateau phase the increase in bulk cytoplasmic calcium is not enough to counteract the increase in voltage and I_{NaCa} current becomes outward oriented during a long period of the plateau phase, which is unrealistic (Janvier & Boyett, 1996).

For I_{NaK} we use the following formulation

$$I_{NaK} = P_{NaK} \frac{K_o}{K_o + K_{mK}} \frac{Na_i}{Na_i + K_{mNa}} \frac{1}{1 + 0.1245 e^{-0.1VF/RT} + 0.0353 e^{-VF/RT}} \tag{5.11}$$

This formulation is similar to the formulations used in the LR, PB, and CRN models.

For I_{pCa} the following commonly applied equation is used

$$I_{pCa} = G_{pCa} \frac{Ca_i}{Ca_i + K_{pCa}} \tag{5.12}$$

For I_{pK} the following equation is used:

$$I_{pK} = G_{pK} \frac{V - E_K}{1. + e^{(25-V)/5.98}} \tag{5.13}$$

This is similar to the equation used by Luo and Rudy.

The background sodium and calcium leakage currents are given by the following equations

$$\begin{aligned} I_{bNa} &= G_{bNa}(V - E_{Na}) && (5.14)\\ I_{bCa} &= G_{bCa}(V - E_{Ca}) && (5.15) \end{aligned}$$

For P_{NaCa}, P_{NaK}, G_{pCa}, G_{pK}, G_{bNa} and G_{bCa} values were chosen such that a frequency change results in Na_i, K_i and Ca_i transients with a timescale of $\sim$ 10 minutes, similar to experimental recordings (Boyett & Fedida, 1988) and which result in equilibrium concentrations −for different frequencies− that lie in the range of experimental observations (Pieske *et al.*, 2002). The values used lie in the range of values used in the PB and CRN models (for parameter values see Table 5.1).

Intracellular ion dynamics

The calcium dynamics of our model are described using the following set of equations

$$\begin{aligned} I_{leak} &= V_{leak}(Ca_{SR} - Ca_i) && (5.16)\\ I_{up} &= \frac{V_{maxup}}{1 + K_{up}^2/Ca_i^2} && (5.17)\\ I_{rel} &= (a_{rel}\frac{Ca_{SR}^2}{b_{rel}^2 + Ca_{SR}^2} + c_{rel})dg && (5.18)\\ Ca_{ibufc} &= \frac{Cai \times Buf_c}{Cai + K_{bufc}} && (5.19)\\ \frac{dCa_{itotal}}{dt} &= -\frac{I_{CaL} + I_{bCa} + I_{pCa} - 2I_{NaCa}}{2V_cF} + I_{leak} - I_{up} + I_{rel} && (5.20)\\ Ca_{srbufsr} &= \frac{Ca_{sr} \times Buf_{sr}}{Ca_{sr} + K_{bufsr}} && (5.21)\\ \frac{dCa_{srtotal}}{dt} &= \frac{V_c}{V_{sr}}(-I_{leak} + I_{up} - I_{rel}) && (5.22) \end{aligned}$$

where I_{leak} is a leakage current from the sarcoplasmic reticulum to the cytoplasm, I_{up} is a pump current taking up calcium in the SR, I_{rel} is the calcium-induced calcium release (CICR) current, d is the activation gate of I_{CaL}, here reused as the activation gate of I_{rel}, following a similar approach as in Chudin *et al.* (1999), and g is the calcium dependent inactivation gate of I_{rel}. Ca_{itotal} is the total calcium in the cytoplasm, it consists of Ca_{ibufc}, the buffered calcium in the cytoplasm, and Ca_i, the free calcium in the cytoplasm. Similarly, $Ca_{srtotal}$ is the total calcium in the SR, it consists of $Ca_{srbufsr}$, the buffered calcium in the SR, and Ca_{sr}, the free calcium in the SR. Ratios between free and buffered calcium are analytically computed assuming a steady-state for the buffering reaction (Eqs. 19 and 21), following the same approach as first used by Zeng *et al.* (1995). (For a description and values of the parameters see Table 5.1) Our model for calcium dynamics has a complexity similar to that of most of the current models that are used to study the dynamics of wave propagation in cardiac tissue (LR, CRN and PB models). Recently, complex models for intracellular calcium handling have been developed that model individual L-type calcium and ryanodine channels, discrete calcium release subunits, and sparks (Rice *et al.*, 1999; Greenstein & Winslow, 2002). Because of their huge computational demands these models for calcium dynamics have not yet been incorporated in models for cardiac wave propagation.

The changes in the intracellular sodium (Na_i) and potassium (K_i) concentrations are governed by the following equations

$$\frac{dNa_i}{dt} = -\frac{I_{Na} + I_{bNa} + 3I_{NaK} + 3I_{NaCa}}{V_c F} \tag{5.23}$$

$$\frac{dK_i}{dt} = -\frac{I_{K1} + I_{to} + I_{Kr} + I_{Ks} - 2I_{NaK} + I_{pK} + I_{stim} - I_{ax}}{V_c F} \tag{5.24}$$

To avoid the model being overdetermined, as is the case for a lot of second-generation electrophysiological models (Endresen *et al.*, 2000; Endresen & Skarland, 2000; Hund *et al.*, 2001), we followed the approach suggested by Hund *et al.* (2001) and accounted for the external stimulus current (I_{stim}) and the axial current flow (I_{ax}) in the equation for K_i dynamics. As mentioned before, conductances of background leakage, plateau and pump currents were chosen such that transient timescales and equilibrium concentrations lie in the range of experimental observations.

5.3 Results

5.3.1 Single Cell

Figure 5.7 shows an AP, calcium transient and the major ionic currents generated by the model under 1-Hz pacing for a parameter setting corresponding to a human epicardial ventricular cell. The AP shows the characteristic spike notch dome architecture found for epicardial cells. Resting potential is $-87.3mV$, maximum plateau potential is $21.7mV$, and $\dot{V}_{max} = 288mV/ms$, all in agreement with experimental data (Li *et al.*, 1998; Drouin *et al.*, 1998). The calcium transient shows the characteristic rounded-off triangular shape found in experiments. Diastolic calcium level is $0.07\mu M$ and maximum systolic calcium level under 1-Hz pacing is $1.0\mu M$, comparable to values in the PB model and experimentally obtained values by Beuckelmann *et al.* (1992). The ionic currents presented in Fig. 5.7 have shapes and values similar to those recorded experimentally. Note that the initial spike-like increase of I_{Kr} in our model is absent in the PB and CRN models. This initial increase is also observed in experiments (Zhou *et al.*, 1998; Gintant, 2000) and is achieved by modeling the inward rectification as a time dependent process.

Fig. 5.8 shows the APDR curve for a single epicardial cell obtained using the S1-S2 restitution protocol (see Materials and Methods) with a basic cycle length (BCL) of $1,000ms$. For comparison, experimental data found by Morgan and coworkers (Morgan *et al.*, 1992) are added. It can be seen that the APDR curve of our model in a wide range closely matches the experimentally measured curve.

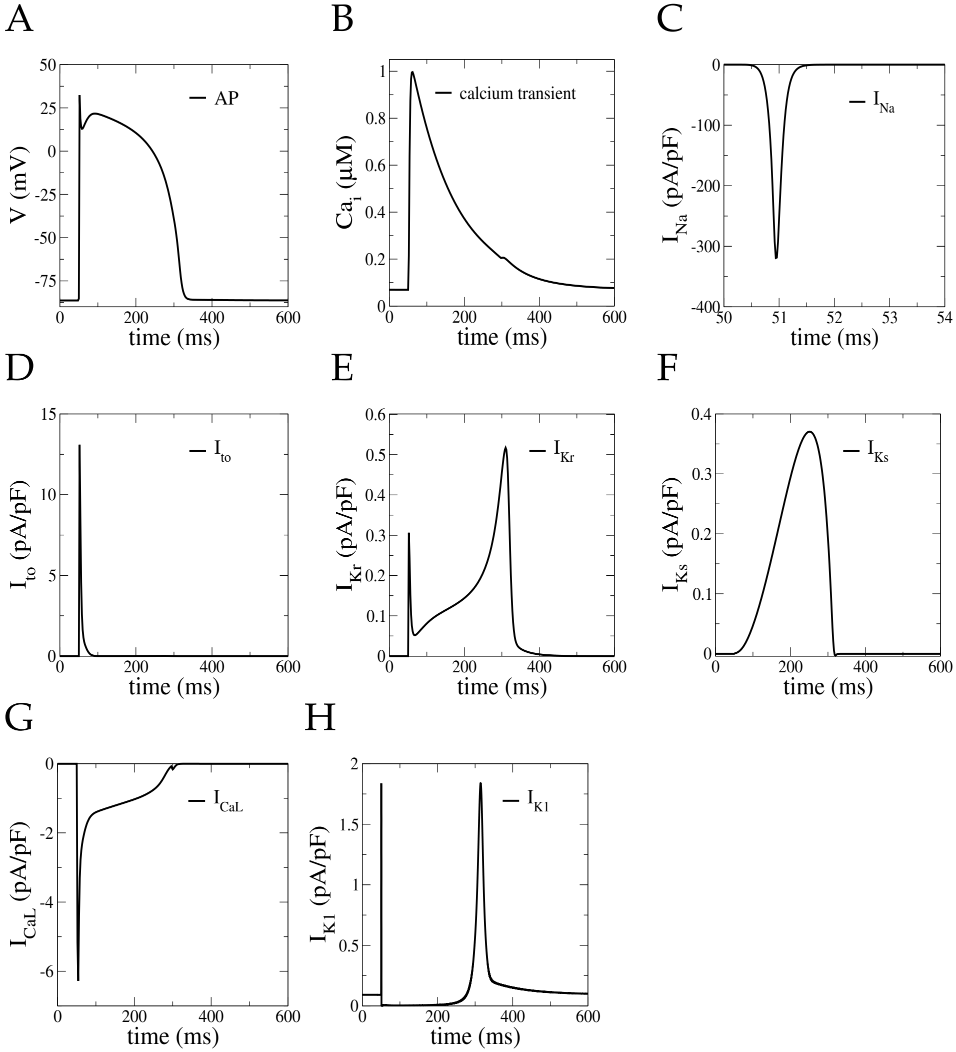

Figure 5.7: Steady-state action potential, calcium transient and major ionic currents under 1-Hz pacing. **A** action potential. **B** calcium transient. **C** fast sodium current (note the difference in timescale used here). **D** transient outward current. **E** rapid delayed rectifier current. **F** slow delayed rectifier current. **G** L-type calcium current. **H** inward rectifier current.

Fig. 5.9A shows the change in diastolic and systolic calcium levels when pacing frequency is increased in a stepwise fashion from 0.25 to 0.5 to 1 to 1.5 to 2 to 2.5 to 3Hz. From the figure it can be seen that systolic calcium level first increases substantially up to a frequency of 2Hz, saturates, and than starts to decrease. In Fig. 5.9B the corresponding increase in intracellular sodium levels with increasing pacing frequency are shown. It can be seen that sodium keeps

Figure 5.8: Action potential duration (APD) restitution curve obtained by using the S1-S2 protocol with a basic cycle length of $1,000 ms$. For comparison, experimental data from Morgan *et al.* (1992) are included. DI, diastolic interval.

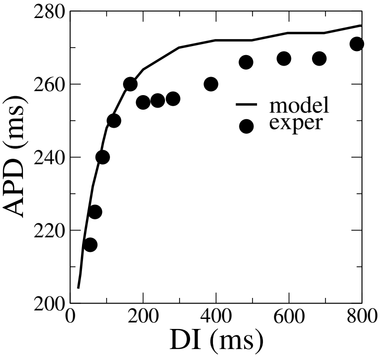

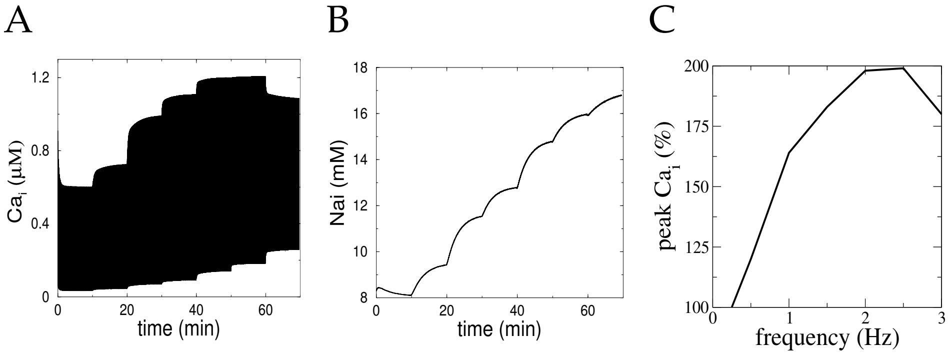

Figure 5.9: Changes in calcium dynamics under increasing pacing frequencies. Pacing frequency is varied from 0.25 to 3Hz; each frequency is maintained for 10 min. **A** positive contraction staircase: increase in calcium transient amplitude when pacing frequency is increased from 0.25 to 0.5 to 1 to 1.5 to 2 to 2.5Hz. For the transition from 2.5 to 3Hz a mild decrease of systolic calcium level occurs. **B** concurrent increase in intracellular sodium when pacing frequency is increased **C** normalized systolic calcium as a function of pacing frequency. Normalization relative to level at 0.25 Hz.

increasing but the speed of increase decreases for higher frequencies. Sodium concentrations for different frequencies are in the range of values measured by Pieske *et al.* (2002). Figure 5.9C shows the normalized systolic calcium level as a function of pacing frequency. Assuming that generated force is linearly dependent on systolic calcium, the calcium frequency staircase of our model is similar to the force-frequency relationship obtained experimentally for human myocardial cells by Pieske *et al.* (1999, 2002) and Schmidt *et al.* (1998).

5.3.2 Different Cell types

The parameter setting in *Single Cell* reproduces the AP of an epicardial cell. By changing a few parameters, our model is capable of reproducing the AP shapes of the two other ventricular cell types: endocardial and M cells.

In our model, endocardial cells differ from epicardial cells in their lower I_{to}

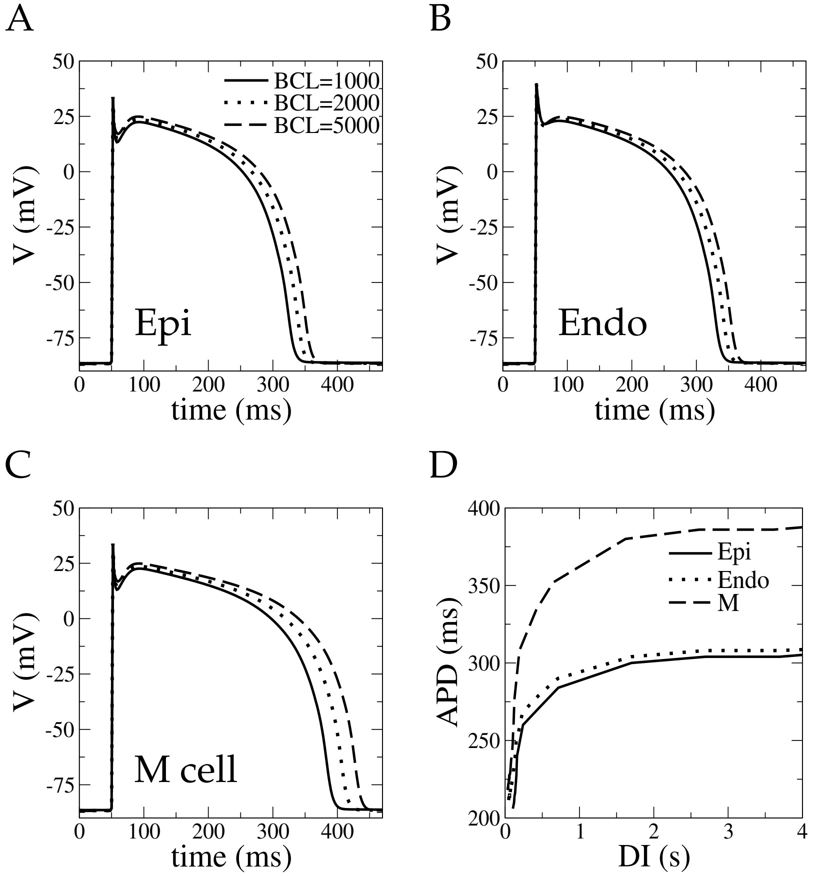

Figure 5.10: Different behavior of epicardial, endocardial, and midmyocardial cell types. Steady-state action potentials for BCL of 1,000, 2,000 and 5,000 ms for epicardial (**A**), endocardial (**B**), and M (**C**) cells. **D** APD restitution curves of the three cell types obtained with the dynamic restitution protocol.

density ($G_{to} = 0.073nSpF^{-1}$ instead of $0.294nSpF^{-1}$, factor 4 difference) and in their slower recovery from inactivation (different τ_s, see Appendix). These differences are based on data from Nabauer *et al.* (1996) and Wettwer *et al.* (1994). According to Pereon *et al.* (2000), I_{Ks} of epicardial and endocardial cells are similar. In our model, M cells differ from epicardial and endocardial cells by having an I_{Ks} density of $0.062nS/pF$ instead of $0.245nS/pF$ (factor 4 difference). This is based on data from Pereon *et al.* (2000). M cells have I_{to} density and dynamics similar to those of epicardial cells (Li *et al.*, 1998).

Fig. 5.10 shows APs recorded under steady-state conditions at BCLs of 1,000, 2,000 and 5,000 ms for epicardial (Fig. 5.10A), endocardial (Fig. 5.10B), and M (Fig. 5.10C) cells. From a comparison of Fig. 5.10, A and B it follows that the smaller I_{to} current of endocardial cells results in the virtual absence of the notch that is clearly present in the APs of epicardial and M cells. From a comparison

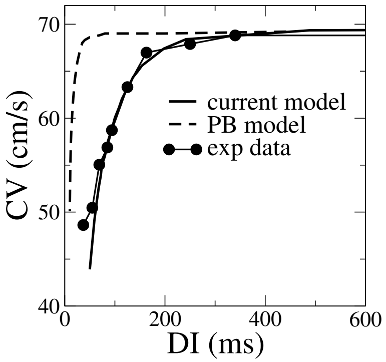

Figure 5.11: Model conduction velocity restitution (CVR) curves for both the current model and the PB model obtained by pacing 1 end of a cable of a length of 400 cells with the dynamic restitution protocol. For comparison, experimental guinea pig CVR data measured by Girouard *et al.* (1996) are added. The experimental data are rescaled by a factor 0.92 to get the same maximum conduction velocity level as measured in human tissue.

of Fig. 5.10, A and C it follows that the smaller I_{Ks} of M cells results in a longer APD relative to epicardial and endocardial cells ($336ms$ in M cells vs. $276ms$ in epicardial and $282ms$ in endocardial cells for $BCL = 1,000ms$) and in a stronger rate dependence of M cell APD.

Note that simulated APD and rate dependence differences between M cells and epi- and endocardial cells are a bit smaller than the experimentally observed differences (Drouin *et al.*, 1995; Li *et al.*, 1998). This is probably due to the fact that M cells differ from the other cell types not only in their I_{Ks} density but also with respect to other current densities. Currently, differences in the late component of I_{Na} have been described for guinea pig (Sakmann *et al.*, 2000) and canine myocardium (Zygmunt *et al.*, 2001), with guinea pig M cells having a smaller and canine M cells having a larger I_{Nalate} than the other cell types, and differences in the density of I_{NaCa} have been described for canine myocardium (Zygmunt *et al.*, 2000), with M cells having a larger exchanger current. Because of the partially contradictory nature of the data and the lack of data for human myocardium, we decided not to incorporate any of these other differences in our M cell description in the current version of our model.

Fig. 5.10D shows restitution curves for epicardial, endocardial and M cells obtained using the dynamic restitution protocol. Again, the longer APD and stronger rate dependence of M cells can be observed. In addition, we can see that the APD of endocardial cells is slightly longer than that of epicardial cells, because of the lower I_{to} density, and their APD rate dependence is slightly different, because of the slower I_{to} recovery dynamics. Results are very similar to experimentally obtained restitution curves by Drouin *et al.* (1998).

5.3.3 1-D propagation

Fig. 5.11 shows conduction velocity restitution curves for a cable of 400 cells. We plotted results for our model and for the PB model, which uses the LR formulation of I_{Na} dynamics. For comparison, we also added experimental CV data. Because no experimental data on human CVR are available, guinea pig CV data measured by Girouard *et al.* (1996) were used. It can be seen that the CV restitution of our model agrees much better with experimental data; it declines less

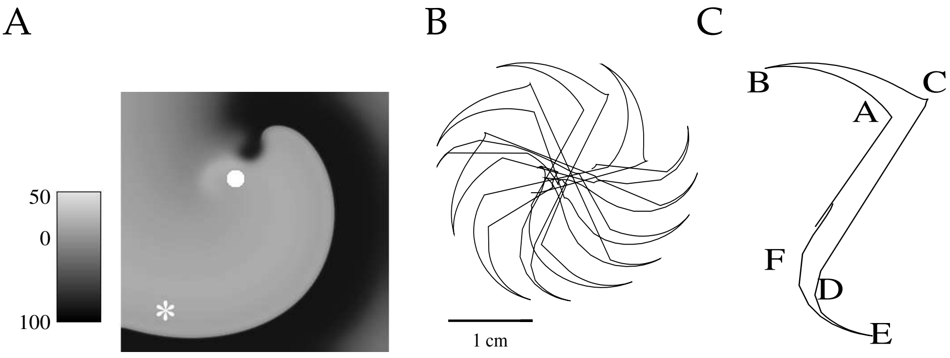

Figure 5.12: **A** spiral wave pattern. The star denotes a measurement electrode at position (100,100) and the circle denotes a measurement electrode at position (200,375). **B** spiral tip trajectory during 1*s* of rotation 8*s* after the S2 stimulus. **C** tip trajectory for a single full rotation showing 'Z' type core.

steeply and over a much broader range of diastolic intervals than is the case with the LR I_{Na} formulation.

Essential for the shape of the CVR curve is the recovery of I_{Na} current, which is mainly determined by the recovery time constant of the slow inactivation gate j. Slowing down the dynamics of the j gate in the LR I_{Na} formulation makes CVR less steep and similar to that of our model (Cao *et al.*, 1999). Note, however, that our CVR curve was not obtained by rescaling of a time constant but is based on our τ_j formulation, which fits experimental data on human I_{Na}.

5.3.4 Spiral waves

The 2D simulations were performed on a 600 × 600 square lattice of epicardial ventricular cells with $\Delta x = 200\mu m$. Spiral waves were initiated with the S1-S2 stimulation protocol described in Materials and Methods. The results of these computations are shown in Fig. 5.12. Fig. 5.12A shows a typical spiral wave pattern after an initial period of spiral formation and stabilization (at 1.38s after the S2 stimulus). The average period of the spiral wave is $264.71ms \pm 10.49ms$, with an average APD of $217.36ms \pm 9.19ms$ and an average diastolic interval of $47.21ms \pm 6.13ms$. The spiral wave meanders with a typical tip trajectory shown in Fig. 5.12B; the size of the core is $\sim 3cm$; the rotation type is similar to the 'Z'-core (see Fig. 5.12C) described by Fast *et al.* (1990) and Efimov *et al.* (1995), which combines regions of fast rotation of the tip (see Fig. 5.12C, A-B-C and D-E-F), typical of a circular core, with regions of laminar motion (See Fig. 5.12C, C-D) typical of a linear core.

Figure 5.13A shows an ECG recorded during spiral wave rotation. The ECG is similar to ECGs recorded during ventricular tachycardia. Figure 5.13,B and C, show recordings of membrane voltage in a point far away from the spiral core (star in Fig. 5.12A) and close to the spiral core (circle in Fig. 5.12B), respectively.

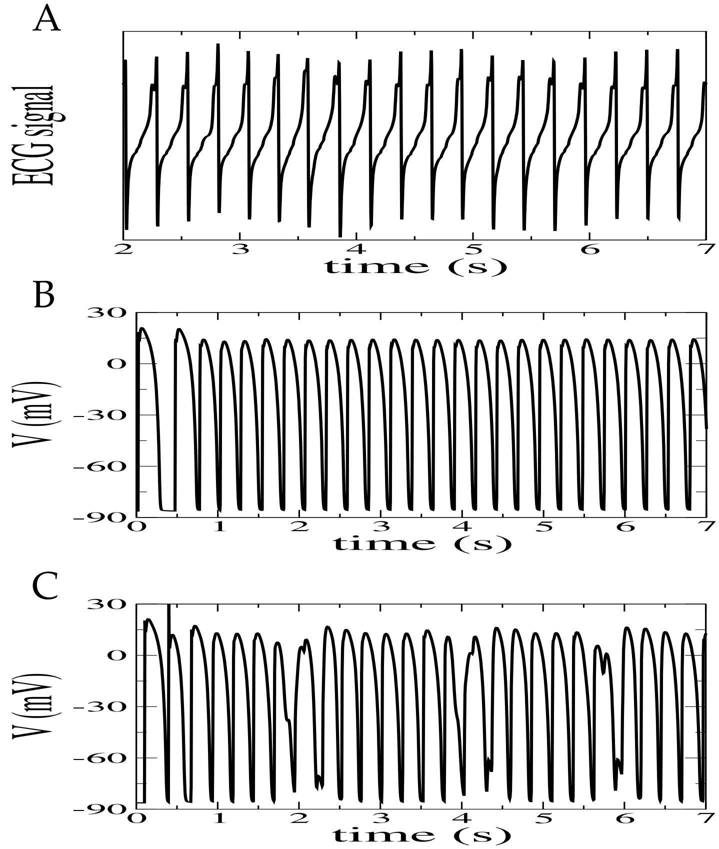

Figure 5.13: **A** ECG recorded during the spiral wave activity shown in Fig. 5.12A. **B** membrane potential (V) recorded at point (100,100) and **C** point (200,375) during 7s after the application of S1. Point (100,100) corresponds to the star and point (200,375) corresponds to the circle in Fig. 5.12A.

Note the regular AP pattern in the point far from the core and the irregular pattern recorded close to the spiral core.

Similar results were obtained for simulations of sheets of endocardial and M cells. Wave patterns, tip trajectories, and ECG and membrane potential recordings were very similar (data not shown), the only real difference being the period of spiral wave rotation, which is $264.23ms \pm 10.37ms$ for endocardial and $285.60ms \pm 6.70ms$ for M cell tissue.

Table 5.3: Summary of most important differences in major currents between our model and original LR phase 2, PB and CRN models and electrophysiological properties for which they are relevant.

Current	Our model	LR model	PB model	CRN model
I_{Na}	Slow τ_j recovery from inactivation Gradual CV restitution	Faster τ_j recovery from inactivation Steep CV restitution	Same as in LR model	Same as in LR model
G_{Na}	$14.838 nSpF^{-1}$	$16 nSpF^{-1}$	$16 nSpF^{-1}$	$7.8 nSpF^{-1}$
I_{CaL}	Typical τ_f shape Slow f gate inactivation Switchlike $f_{ca\infty}$, large calcium inactivation Calcium dominated inactivation GHK current model	Atypical τ_f shape Fast f gate inactivation $f_{ca\infty}$ gradually declining Voltage dominated inactivation GHK current model	Similar to LR model Linear current model	Atypical τ_f shape Slow f gate inactivation $f_{ca\infty}$ gradually declining Calcium dominated inactivation Linear current model
G_{CaL}	$1.75^{-4} cm^3 \mu F^{-1} s^{-1}$	$5.4^{-4} cm^3 \mu F^{-1} s^{-1}$	$0.064 nSpF^{-1}$	$0.1238 nSpF^{-1}$
I_{to}	Different G_{to} and recovery dynamics for epi- and endocardial cells	No I_{to} current	Only epicardial I_{to}	Only epicardial I_{to}
G_{to}	$0.294 nSpF^{-1}$(epi) $0.073 nSpF^{-1}$(endo)		$0.3 nSpF^{-1}$	$0.1652 nSpF^{-1}$
I_{Ks}	Slower activation and faster inactivation	No I_{Ks} current	Faster activation and slower inactivation	Similar to PB model
G_{Ks}	$0.245 nSpF$1(epi/endo) $0.062 nSpF^{-1}$(M cell)		$0.02 nSpF$1	$0.129 nSpF^{-1}$
I_{Kr}	Time dependent inactivation gate Initial peak of current during AP	No I_{Kr} current	Immediate inactivation gate No initial peak	Similar to PB model
G_{Kr}	$0.096 nSpF^{-1}$		$0.015 nSpF^{-1}$	$0.0294 nSpF^{-1}$

5.4 Discussion

In this paper we propose a model for human ventricular tissue. An important feature of our model is that all major ionic currents are fitted to recent data on human ventricular myocytes and expression experiments of human cardiac channels. This results in several important differences between our and previous models, the most important of which are the following: slower recovery dynamics of the fast sodium current, leading to a more gradual CVR that agrees better with available experimental data; differentiated formulations for epicardial and endocardial transient outward current, allowing the modeling of these different cell types; and an L-type calcium current with a fast, dominant and stable calcium inactivation and slow voltage inactivation dynamics. In Table 5.3 the most important differences between the major ionic currents in our model and the LR, PB, and CRN model are summarized together with their electrophysiological consequences. In addition, conductance parameters used for these currents in our model and the other models are compared.

Our model reproduces three different cell types: endocardial, epicardial, and M cells with different characteristic action potential morphologies and rate dependencies. The APDR of our model closely matches experimentally obtained APDR curves. In addition, the CVR of our model resembles experimentally obtained CVR curves, which are currently only available for animal cardiac tissue, much closer than CVR curves generated with models using the Luo-Rudy I_{Na} formulation. Both APDR and CVR are very important determinants for the stability of reentrant arrhythmias. Our calcium dynamics formulation is of a complexity comparable to that of the LR, PB, and CRN models and allows us to simulate a realistic calcium transient and a typical positive human contraction staircase.

The feasibility of spatial simulations is demonstrated with a simulation of a reentrant spiral wave in a 2D sheet of epicardial tissue. The period of spiral wave rotation is $265 ms$, versus $304 ms$ in the reduced PB model (Bernus *et al.*, 2002), because of the shorter APD in our model. The spiral wave tip trajectory is somewhat different from the linear tip trajectory found by Bernus *et al.* (2002), because of the larger horizontal parts of the Z-type core. Another difference is that in the model by Bernus *et al.* (2002) the core pattern has a cross section of $\sim 5cm$, whereas in our model, the core pattern has a cross section of $\sim 3cm$, again because of the shorter APD in our model.

Limitations

A limitation of our model is that differences in APD and rate dependence between M cells and epicardial and endocardial cells in our model are smaller than the experimentally observed differences. This is because of the limited current knowledge of basic electrophysiological differences between M cells and the other cell types causing these differences. If these differences are further characterized they can be easily incorporated in our model in terms of different current densities and/or dynamics for M cells, similar to what already has been done for I_{Ks} density differences.

We put considerable effort in obtaining, evaluating, rescaling to physiological conditions, and fitting of experimental data to get a model closely resembling true human ventricular cells. However, limitations are unavoidable because of the limited availability of data, the extensive variability among experimental data, the considerable variation in experimental conditions, and the potentially deleterious effects of cell isolation procedures used in voltage-clamp experiments.

There were no data available on I_{CaL} activation time constants, so formulations from another model based on animal experiments had to be used. The precise nature of calcium-mediated inactivation of the L-type calcium current is unknown. We used a simple description with a constant-valued time constant and a dependence on intracellular calcium only, although data suggest that extracellular calcium also plays a role in inactivation (Sun *et al.*, 1997). Finally, no data were available on the nature of calcium dynamics under high frequencies. We assumed calcium dynamics to stay stable under high frequencies. In addition, we assumed CICR to depend in a saturating manner on sarcoplasmic reticulum calcium content.

There is no agreement of experimental data on steady-state inactivation of I_{Na}. Some researchers give a value of $-85mV$ for the voltage of half-inactivation (Nagatomo *et al.*, 1998; Wan *et al.*, 2001; Sakakibara *et al.*, 1992), whereas others give a value of around $-65mV$ (Makita *et al.*, 2000; Kambouris *et al.*, 2000; Schneider *et al.*, 1994). Rather than making a compromise, we decided to base our steady-state inactivation curves on data from Nagatomo *et al.* (1998) because we also used their data for steady-state activation and time constants and wanted to maintain consistency.

Experiments are often performed at different temperatures. This is especially true for I_{Na} voltage-clamp experiments, where the temperature is usually below the physiological temperature to slow dynamics and limit current size. We derived a single Q_{10} factor and used this to rescale all I_{Na} time constants to 37°. As it is not clear how steady-state curves change with temperature, we performed a linear extrapolation of the half-(in)activation voltages and slopes.

Experiments are also performed in the presence of different combinations of pharmacological agents used to suppress other currents. It is known that some of these chemicals have an impact on the dynamics of the measured current, e.g., Cd^{2+} used to block L-type calcium current is known to influence steady-state curves of I_{to} current. We corrected experimental steady-state curves of I_{to} for the presence of Cd^{2+} by shifting them $10mV$ in the positive direction.

To perform single-cell voltage-clamp experiments, cells must be isolated. These isolation procedures can have profound effects on the density of particular currents. Clear examples of this are the I_{Ks} and I_{Kr} currents. I_{Ks} and I_{Kr} current densities found during voltage-clamp experiments are in sharp contrast with the clear relevance of these currents for action potential duration and restitution and the different behavior of M cells. We therefore decided to apply current densities for I_{Ks} and I_{Kr} that are substantially larger than experimentally measured densities, and that allow us to realistically simulate the consequences of I_{Kr} block and the behavior of M cells.

In conclusion, we propose a new model for human ventricular epicardial, endocardial and M cells based on ionic currents measured in human ventricular cells or measured in expression experiments using human cardiac channels. The model reproduces a number of experimental observations, ranging from voltage-clamp current traces and *I-V* curves, to AP morphology, as well as APD and CV restitution curves and the contraction staircase. Because of its relative computational simplicity, the model is suitable for application in large-scale spatial simulations, which are necessary for investigating the dynamics of reentrant arrhythmias. The latter is illustrated with the simulation of a reentrant spiral wave in a 2D sheet of epicardial ventricular tissue.

5.5 Appendix

Reversal potentials

$$E_X = \frac{RT}{zF} log \frac{X_o}{X_i} \quad \text{for} \quad X = Na^+, K^+, Ca^{2+} \tag{5.25}$$

$$E_{Ks} = \frac{RT}{F} log \frac{K_o + p_{KNa} Na_o}{K_i + p_{KNa} Na_i} \tag{5.26}$$

Fast Na^+ current

$$I_{Na} = G_{Na} m^3 h j (V - E_{Na}) \tag{5.27}$$

$$m_\infty = \frac{1}{(1. + e^{(-56.86 - V)/9.03})^2} \tag{5.28}$$

$$\alpha_m = \frac{1}{1. + e^{(-60. - V)/5.}} \tag{5.29}$$

$$\beta_m = \frac{0.1}{1. + e^{(V + 35.)/5.}} + \frac{0.1}{1. + e^{(V - 50.)/200.}} \tag{5.30}$$

$$\tau_m = \alpha_m \beta_m \tag{5.31}$$

$$h_\infty = \frac{1}{(1. + e^{(V + 71.55)/7.43})^2} \tag{5.32}$$

$$\alpha_h = \begin{cases} 0 & \text{if } V \geq -40, \\ 0.057 e^{-(V+80.)/6.8} & \text{otherwise.} \end{cases} \tag{5.33}$$

$$\beta_h = \begin{cases} \frac{0.77}{0.13(1.+e^{-(V+10.66)/11.1})} & \text{if } V \geq -40, \\ 2.7 e^{0.079V} + 3.1 \times 10^5 e^{0.3485V} & \text{otherwise.} \end{cases} \tag{5.34}$$

$$\tau_h = \frac{1}{\alpha_h + \beta_h} \tag{5.35}$$

$$j_\infty = \frac{1}{(1. + e^{(V + 71.55)/7.43})^2} \tag{5.36}$$

$$\alpha_j = \begin{cases} 0 & \text{if } V \geq -40, \\ \frac{(-2.5428 \times 10^4 e^{0.2444V} - 6.948 \times 10^{-6} e^{-0.04391V})(V+37.78)}{1.+e^{0.311(V+79.23)}} & \text{otherwise.} \end{cases} \tag{5.37}$$

$$\beta_j = \begin{cases} \frac{0.6 e^{0.057V}}{1.+e^{-0.1(V+32.)}} & \text{if } V \geq -40, \\ \frac{0.02424 e^{-0.01052V}}{1.+e^{-0.1378(V+40.14)}} & \text{otherwise.} \end{cases} \tag{5.38}$$

$$\tau_j = \frac{1}{\alpha_j + \beta_j} \tag{5.39}$$

L-type Ca^{2+} current

$$I_{CaL} = G_{CaL} d f f_{Ca} 4 \frac{VF^2}{RT} \frac{Ca_i e^{2VF/RT} - 0.341 Ca_o}{e^{2VF/RT} - 1} \tag{5.40}$$

$$d_\infty = \frac{1}{1. + e^{(-5.-V)/7.5}} \tag{5.41}$$

$$\alpha_d = \frac{1.4}{1. + e^{(-35-V)/13}} + 0.25 \tag{5.42}$$

$$\beta_d = \frac{1.4}{1. + e^{(V+5)/5}} \tag{5.43}$$

$$\gamma_d = \frac{1}{1. + e^{(50-V)/20}} \tag{5.44}$$

$$\tau_d = \alpha_d \beta_d + \gamma_d \tag{5.45}$$

$$f_\infty = \frac{1}{1. + e^{(V+20.)/7.}} \tag{5.46}$$

$$\tau_f = 1125 e^{-(V+27)^2/240} + 80 + \frac{165}{1 + e^{(25-V)/10}} \tag{5.47}$$

$$\alpha_{fca} = \frac{1.}{1. + (Cai/0.000325)^8} \tag{5.48}$$

$$\beta_{fca} = \frac{0.1}{1. + e^{(Cai-0.0005)/0.0001}} \tag{5.49}$$

$$\gamma_{fca} = \frac{0.2}{1. + e^{(Cai-0.00075)/0.0008}} \tag{5.50}$$

$$f_{Ca\infty} = \frac{\alpha_{fca} + \beta_{fca} + \gamma_{fca} + 0.23}{1.46} \tag{5.51}$$

$$\tau_{fCa} = 2. \tag{5.52}$$

$$\dot{f_{Ca}} = k \frac{f_{Ca\infty} - f_{Ca}}{\tau_{fCa}} \tag{5.53}$$

$$k = \begin{cases} 0 & \text{if } f_{Ca\infty} > f_{Ca} \text{ and } V > -60mV, \\ 1 & \text{otherwise.} \end{cases} \tag{5.54}$$

Transient outward current

$$I_{to} = G_{to} r s (V - E_K) \tag{5.55}$$

For all cell types:

$$r_\infty = \frac{1}{1. + e^{(20-V)/6.}} \tag{5.56}$$

$$\tau_r = 9.5 e^{-(V+40)^2/1800} + 0.8 \tag{5.57}$$

For epicardial and M cells:

$$s_\infty = \frac{1}{1. + e^{(V+20)/5}} \tag{5.58}$$

$$\tau_s = 85.e^{-(V+45)^2/320} + \frac{5}{1. + e^{(V-20.)/5.}} + 3 \tag{5.59}$$

For endocardial cells:

$$s_\infty = \frac{1}{1. + e^{(V+28)/5.}} \tag{5.60}$$

$$\tau_s = 1000e^{-(V+67)^2/1000} + 8 \tag{5.61}$$

Slow delayed rectifier current

$$I_{Ks} = G_{Ks}x_s^2(V - E_{Ks}) \tag{5.62}$$

$$x_{s\infty} = \frac{1}{1. + e^{(-5.-V)/14.}} \tag{5.63}$$

$$\alpha_{xs} = \frac{1100.}{\sqrt{1. + e^{(-10.-V)/6}}} \tag{5.64}$$

$$\beta_{xs} = \frac{1}{1. + e^{(V-60.)/20.}} \tag{5.65}$$

$$\tau_{xs} = \alpha_{xs}\beta_{xs} \tag{5.66}$$

Rapid delayed rectifier current

$$I_{Kr} = G_{Kr}\sqrt{\frac{K_o}{5.4}}x_{r1}x_{r2}(V - E_K) \tag{5.67}$$

$$x_{r1\infty} = \frac{1}{1. + e^{(-26.-V)/7.}} \tag{5.68}$$

$$\alpha_{xr1} = \frac{450.}{1. + e^{(-45.-V)/10.}} \tag{5.69}$$

$$\beta_{xr1} = \frac{6.}{1. + e^{(V+30.)/11.5}} \tag{5.70}$$

$$\tau_{xr1} = \alpha_{xr1}\beta_{xr1} \tag{5.71}$$

$$x_{r2\infty} = \frac{1}{1. + e^{(V+88.)/24.}} \tag{5.72}$$

$$\alpha_{xr2} = \frac{3.}{1. + e^{(-60.-V)/20.}} \tag{5.73}$$

$$\beta_{xr2} = \frac{1.12}{1. + e^{(V-60.)/20.}} \tag{5.74}$$

$$\tau_{xr2} = \alpha_{xr2}\beta_{xr2} \tag{5.75}$$

Inward rectifier K^+ current

$$I_{K1} = G_{K1}\sqrt{\frac{K_o}{5.4}}\,x_{K1\infty}(V - E_K) \tag{5.76}$$

$$\alpha_{K1} = \frac{0.1}{1. + e^{0.06(V-E_K-200)}} \tag{5.77}$$

$$\beta_{K1} = \frac{3.e^{0.0002(V-E_K+100)} + e^{0.1(V-E_K-10)}}{1. + e^{-0.5(V-E_K)}} \tag{5.78}$$

$$x_{K1\infty} = \frac{\alpha_{K1}}{\alpha_{K1} + \beta_{K1}} \tag{5.79}$$

Na^+/Ca^{2+} exchanger current

$$I_{NaCa} = k_{NaCa}\frac{e^{\frac{\gamma VF}{RT}}Na_i^3Ca_o - e^{\frac{(\gamma-1)VF}{RT}}Na_o^3Ca_i\alpha}{(K_{mNai}^3 + Na_o^3)(K_{mCa} + Ca_o)(1 + k_{sat}e^{\frac{(\gamma-1)VF}{RT}})} \tag{5.80}$$

Na^+/K^+ pump current

$$I_{NaK} = P_{NaK}\frac{K_o}{K_o + K_{mK}}\frac{Na_i}{Na_i + K_{mNa}}\frac{1}{1 + 0.1245e^{-0.1VF/RT} + 0.0353e^{-VF/RT}} \tag{5.81}$$

I_{pCa} current

$$I_{pCa} = G_{pCa}\frac{Ca_i}{Ca_i + K_{pCa}} \tag{5.82}$$

I_{pK} current

$$I_{pK} = G_{pK}\frac{V - E_K}{1. + e^{(25-V)/5.98}} \tag{5.83}$$

Background currents

$$I_{bNa} = G_{bNa}(V - E_{Na}) \tag{5.84}$$

$$I_{bCa} = G_{bCa}(V - E_{Ca}) \tag{5.85}$$

Calcium dynamics

$$I_{leak} = V_{leak}(Ca_{SR} - Ca_i) \tag{5.86}$$

$$I_{up} = \frac{V_{maxup}}{1 + K_{up}^2/Ca_i^2} \tag{5.87}$$

$$I_{rel} = (a_{rel}\frac{Ca_{SR}^2}{b_{rel}^2 + Ca_{SR}^2} + c_{rel})dg \tag{5.88}$$

$$g_\infty = \begin{cases} \frac{1}{1.+(Cai/0.00035)^6} & \text{if } Ca_i <= 0.00035, \\ \frac{1}{1.+(Cai/0.00035)^{16}} & \text{otherwise.} \end{cases} \tag{5.89}$$

$$\tau_g = 2ms \tag{5.90}$$

$$\dot{g} = k\frac{g_\infty - g}{\tau_g} \tag{5.91}$$

$$k = \begin{cases} 0 & \text{if } g_\infty > g \text{ and } V > -60mV, \\ 1 & \text{otherwise.} \end{cases} \tag{5.92}$$

$$Ca_{ibufc} = \frac{Cai \times Buf_c}{Cai + K_{bufc}} \tag{5.93}$$

$$\frac{dCa_{itotal}}{dt} = -\frac{I_{CaL} + I_{bCa} + I_{pCa} - 2I_{NaCa}}{2V_cF} + I_{leak} - I_{up} + I_{rel} \tag{5.94}$$

$$Ca_{srbufsr} = \frac{Ca_{sr} \times Buf_{sr}}{Ca_{sr} + K_{bufsr}} \tag{5.95}$$

$$\frac{dCa_{SRtotal}}{dt} = \frac{V_c}{V_{sr}}(-I_{leak} + I_{up} - I_{rel}) \tag{5.96}$$

Sodium and potassium dynamics

$$\frac{dNa_i}{dt} = -\frac{I_{Na} + I_{bNa} + 3I_{NaK} + 3I_{NaCa}}{V_cF} \tag{5.97}$$

$$\frac{dK_i}{dt} = -\frac{I_{K1} + I_{to} + I_{Kr} + I_{Ks} - 2I_{NaK} + I_{pK} + I_{stim} - I_{ax}}{V_cF} \tag{5.98}$$

Acknowledgments

We are thankful to Dr. O. Bernus and Dr. R. Wilders for valuable discussions. This work was funded by the Netherlands Organization for Scientific Research (NWO) through Grant 620061351 of the Research Council for Physical Sciences (EW) (to K. H. W. J. ten Tusscher), the Netherlands National Computer Facilities Foundation (NCF) through Grant SG-095, the British Heart Foundation, the British Medical Research Council, the Welcome Trust, and Physiome Sciences (to D. Noble and P. J. Noble)

6

Dynamics of reentrant arrhythmias in the human ventricles

K. H. W. J. Ten Tusscher[1], R. Hren[2], and A. V. Panfilov[1]
[1] *Department of Theoretical Biology, Utrecht University*
Padualaan 8, 3584 CH Utrecht, The Netherlands.
[2] *Institute of Mathematics, Physics & Mechanics*
University of Ljubljana, Ljubljana, Slovenia

preliminary version

Abstract

We study reentrant arrhythmias in an anatomically detailed model of the human ventricles using our recently developed human ventricular myocyte model. We show that for the standard parameter setting of our model, which corresponds to normal healthy human myocardium, premature stimulation leads to stable ventricular tachycardia. We study the dynamics of the scroll waves underlying ventricular tachycardia. We find that a scroll wave in the right ventricle is stationary, whereas a scroll wave in the left ventricle meanders.

We demonstrate scroll wave fragmentation for modified parameter settings of our model, resulting in dynamics similar to ventricular fibrillation. We analyze the dynamics of fibrillation in terms of ECG, activation frequency, types of epicardial surface wave patterns, number of on the surface observable reentries, and the number of scroll wave filaments present during fibrillation. We compare the types and sizes of surface wave patterns and the number of observable surface reentries with recent data from Nanthakumar *et al.* (2004) who performed surface recordings during in vivo fibrillation in the human heart. We find a good agreement between our simulated and their experimental results. We find that in some cases fibrillation may be organized by a much lower number of reentrant sources than previously thought.

6.1 Introduction

Cardiac arrhythmias are caused by deviations in the timing, sequence and synchrony of the excitation process triggering cardiac contraction. A frequently occurring, dangerous category of cardiac arrhythmias are reentrant ventricular arrhythmias, namely ventricular tachycardia (VT) and ventricular fibrillation (VF). Ventricular tachycardia is thought to be caused by a reentrant, spiral-shaped, excitation wave pattern that circulates and re-excites the same tissue again and again, as opposed to the normal waves emitted by the sinus node that each excite all tissue only once. Experimental evidence of the presence of spiral waves in cardiac tissue was first provided by Allessie *et al.* (1973) for thin slices of atrial cardiac tissue. These results were confirmed by Davidenko *et al.* (1990, 1992) and Pertsov *et al.* (1993) and extended to three-dimensional tissue slabs by Frazier *et al.* (1989). Because the spiral waves typically rotate at a frequency that is substantially higher than normal sinus rhythm, VT results in less time for ventricular filling and a loss of cardiac output.

Ventricular tachycardia often deteriorates into ventricular fibrillation. VF is characterized by a complete loss in coherence of ventricular contraction, resulting in almost zero cardiac output. Sudden cardiac death is the most common cause of death in the industrialized world and in 80% of the cases it is caused by ventricular fibrillation (Zevitz, 2004). In recent years, ideas on the organization of fibrillation wave patterns have changed substantially. Traditionally, fibrillation was thought to be organized by large numbers of small, randomly wandering wavelets (Moe *et al.*, 1964; Krinsky, 1966). Extensive experimental mapping studies of ventricular fibrillation in animal hearts have made it clear that fibrillation is much less chaotic and much more organized than previously thought (Gray *et al.*, 1995a, 1998; Witkowski *et al.*, 1998; Zaitsev *et al.*, 2000).

Until recently it was not known in how far this was also true for VF in the human heart. Walcott *et al.* (2002) performed the first in vivo mapping study of activation patterns during induced fibrillation in human hearts, using a 36-electrode catheter to record endocardial activation. Their data suggested that activation consisted of a few large wave fronts that were tracing a few recurring activation paths. More recently, Nanthakumar *et al.* (2004) performed a detailed epicardial surface activation mapping of induced ventricular fibrillation in patients undergoing cardiac surgery using a $20cm^2$ plaque with 504 electrodes. They also found that activation consisted of a few large wave fronts that follow repeatable activation paths. In addition, they showed that only 6-10% of the time during ventricular fibrillation reentrant activity could be observed in the recording area.

However, the data from the Nanthakumar *et al.* study has several limitations. First, the recordings were made with a $20cm^2$ plaque electrode covering a part of the left ventricular epicardium. As a consequence, no data are available for activation patterns occurring in the rest of the ventricles. Furthermore, the recordings were made on the surface of the heart only, whereas the underlying excitation sources are three-dimensional. Therefore, to gain more insight in the three-dimensional excitation processes that underlie the observed surface patterns, modeling studies are a valuable and widely used tool. In this study we will use a model of the human ventricles to study the basic dynamics of ventricular tachycardia and fibrillation in the human heart. We will characterize the simulated episodes of ventricular tachycardia and fibrillation in terms of global three-dimensional wave patterns, ECG patterns and activation frequencies. In addition, we will perform a detailed analysis of epicardial surface wave patterns occurring during fibrillation and compare them to the observations from Nanthakumar *et al.* (2004).

For our model we will combine a recently developed model for human ventricular myocytes (Ten Tusscher *et al.*, 2004) that includes a description of intracellular calcium handling with an anatomically detailed human ventricular geometry that incorporates fiber direction anisotropy (Hren, 1996). For the standard parameter setting of our model, which corresponds to normal healthy human myocardium, we find that premature stimulation leads to stable scroll wave dynamics resulting in a dynamics similar to stable ventricular tachycardia. We show that for modified parameter settings of our model that result in a steep APD restitution curve we obtain scroll wave fragmentation resulting in dynamics similar to ventricular fibrillation. We will demonstrate a good agreement in terms of ECG patterns, activation frequencies, surface wave patterns, activation paths and amount of on the surface observable reentries between our simulations and the clinical data.

We will investigate the number of reentrant wave sources organizing ventricular fibrillation in our model, and compare the number of scroll wave filaments to results from previous modeling studies (Panfilov, 1999; Clayton & Holden, 2004; Xie *et al.*, 2004). Our preliminary results indicate that for the fibrillation parameter setting resulting in an ECG pattern, activation frequency and epicardial surface wave patterns closely resembling the clinical data, fibrillation can be organized by as few as ~ 6 reentrant sources. These results further underline the high degree of organization that may be present during VF.

6.2 Methods

Mathematical modeling

The excitable behavior of individual cardiac muscle cells was described using a recently developed model for human ventricular myocytes that is based on detailed voltage clamp data for all major ionic currents and that incorporates an intracellular calcium handling (Ten Tusscher *et al.*, 2004). Important characteristics of the model are an action potential duration and conduction velocity restitution that fit the experimental data and stability of the intracellular calcium dynamics for high stimulation frequencies under the standard parameter setting of the model. Because of the short time scale of spatial simulations, dynamic changes occurring in intracellular sodium and potassium concentrations that are modeled in the original formulation of the model are negligible. Therefore, to save computational time, intracellular sodium and potassium concentrations were treated as constant valued parameters rather than variables.

Action potential propagation in cardiac tissue was described using the following parabolic reaction diffusion equation:

$$C_m \frac{\partial V}{\partial t} = \frac{\partial}{\partial x_i} D_{ij} \frac{\partial}{\partial x_j} V - I_{ion} \tag{6.1}$$

where C_m is the cellular membrane capacitance, V is the transmembrane potential, I_{ion} is the sum of all transmembrane ionic currents (for a description see (Ten Tusscher *et al.*, 2004)) and D_{ij} (with $i, j = 1, 2, 3$) is the conductivity tensor that describes the anisotropic properties of the cardiac tissue.

In two dimensions, isotropic tissue sheets were modeled ($D_{ij} = D_L \delta_{ij}$, where δ_{ij} is the unitary tensor). In simulations involving the human ventricles, muscle fiber direction anisotropy was taken into account. Assuming that transverse conductivity is the same in all directions orthogonal to the direction of the muscle fiber axis, we described the ventricular conductivity tensor using the following equation:

$$D_{ij} = D_L * \delta_{i,j} + (D_L - D_T)\alpha_i \alpha_j \tag{6.2}$$

where α is the muscle fiber direction, and D_L is the conductivity in the longitudinal and D_T the conductivity in the transversal fiber direction, respectively. We use a ratio of 2:1 for the anisotropy of action potential conduction velocities and hence a ratio of 4:1 for $D_L : D_T$. For D_L we used $162\Omega cm$, which results in a longitudinal conduction velocity of approximately $70cm/s$ as was experimentally reported by Jongsma & Wilders (2000).

In all simulations the tissue consisted entirely of cells of the epicardial type, as described in (Ten Tusscher *et al.*, 2004).

Data describing human ventricular geometry and muscle fiber direction field were obtained by Hren (1996) from a structurally normal human heart. The conductivity tensor at each position was derived from the local muscle fiber direction field using equation 6.2. The geometry and conductivity data were validated by Hren (1996) against experimental data on the normal excitation sequence in the human heart (Durrer *et al.*, 1970).

Numerical approach

For two-dimensional isotropic tissue sheets a field size of 1200×1200 was used with a space step of $\Delta x = 0.2mm$ and a time step of $\Delta t = 0.02ms$. Simple Euler forward integration was used to integrate equation 6.1. To integrate the Hodgkin-Huxley type equations of the various gating variables the Rush and Larsen integration scheme was used (Rush & Larsen, 1978).

For the human ventricular geometry a $434 \times 434 \times 434$ voxel grid with a space step of $\Delta x = 0.25mm$ encompassing the human ventricles was used. Equation 6.1 was integrated using the operator splitting method for reaction diffusion equations, resulting in an ordinary differential equation (ODE) for the reaction part (transmembrane ionic currents) and a partial differential equation (PDE) for the diffusion part (action potential propagation). The ODE was integrated using a time-adaptive Euler forward scheme with a short ($\Delta t_{min} = 0.02ms$) and long ($\Delta t_{max} = 0.1ms$) time step. Standard, in each heart grid point the ODE was integrated using the long time step; if the integration result satisfied the condition

$dV_m/dt \leq 1mV/ms$ the result was considered valid; otherwise the ODE was integrated five ($\Delta t_{max}/\Delta t_{min}$) times with the short time step. As a consequence, the short time step is only used if voltage changes are large: during the steep upstroke phase of the action potential. In space this means that the short time step is only used along the wave front. The PDE was integrated using the long time step, ensuring spatial synchrony of the grid points. To compensate for the fact that diffusion occurs after a five times longer time step and ensure normal propagation speed, the PDE was applied to the average of the voltage that served as input to the ODE integration and the voltage that is the result of the ODE integration. The correctness of this approach was checked in a previous study (Ten Tusscher & Panfilov, 2003b).

To integrate the PDE, we need to evaluate at each point of the ventricular geometry the following Laplacian:

$$\Delta(i,j,k) = \frac{\partial}{\partial x_i} D_{ij} \frac{\partial}{\partial x_j} V_m \tag{6.3}$$

This Laplacian can be discretized to the following equation:

$$L(i,j,k) = \sum_{l=0}^{18} w_l V_m(l) \tag{6.4}$$

where l is an index running over the 18 neighbors of the point (i,j,k) and the point itself and w_l is the weight with which the voltage of a particular neighbor grid point contributes to the Laplacian of the point (i,j,k). The weights w_l are computed based on the local conductivity tensor and the local boundary situation in the point (i,j,k). No flux boundary conditions are imposed to ensure a zero axial-current flow from heart points to non-heart points. To accomplish this, a neighbor l that lies outside the heart geometry receives a weight $w_l = 0$. Given that in a non-contracting heart model conductivity tensors and boundary conditions stay constant over time, these weights can be precomputed and stored, and used in simulations as an efficient means to evaluate the Laplacian and automatically handle boundary conditions.

Two-dimensional spiral waves and three-dimensional scroll waves were initiated using a S1-S2 stimulus protocol, with the S2 stimulus applied in the refractory tail of the S1 wave. Stimulus currents strengths were at twice the diastolic threshold. Electrograms were obtained by assuming an infinite volume conductor and calculating the dipole source density of the membrane potential V_m in all node points of the medium using the following equation (Plonsey & Barr, 1989):

$$ECG = \int_V \frac{D\nabla V_m \cdot \vec{r}}{r^3} dV \tag{6.5}$$

where V is the volume (for the ventricles) or area (for the two-dimensional tissue sheets) over which is integrated, and $\vec{r}$ is the vector from the recording electrode to a point in the tissue. For the two-dimensional tissue we placed the recording electrode $10cm$ above the middle of the sheet, for the ventricles it was placed $10cm$ from the center of the ventricles in the transverse plane.

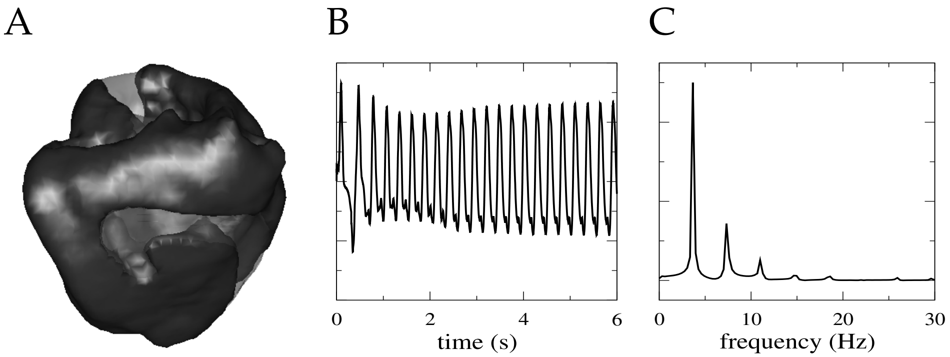

Figure 6.1: **A** Snapshot of scroll wave dynamics in the right ventricular wall 1.6 seconds after the application of the S2 extra-stimulus. See also the color plate on page 131. **B** ECG recording of the scroll wave activity shown in A. **C** Fourier transform of the ECG shown in B.

In the ventricular simulations, scroll wave filaments were detected using an algorithm proposed by Fenton & Karma (1998). It is based on the idea that the tip or singular point of a spiral wave is defined as the point where excitation wave front and repolarization wave back meet. This point can be found as the intersection point of an isopotential line (in our case $-60mV$) and the $dV/dt = 0$ line. Intersection points thus found were stored as voxel data. Individual filaments were detected by iteratively joining neighboring voxels that contained filament points and giving all voxels belonging to a single filament a unique identifier.

The two-dimensional tissue sheet simulations were coded in C++ and run on a single processor of a Dell 650 Precision Workstation (dual Intel xeon 2.66 GHz). The three-dimensional ventricular simulations were coded in C++ and MPI and were run on 8 processors of a Beowulf cluster consisting of four Dell 650 Precision Workstations (dual Intel xeon 2.66 GHz). With this approach, simulating 1 second of wave propagation in the ventricles took about 17 hours of computational time. Ventricular geometry, wave patterns and scroll wave filaments were visualized using the marching cube algorithm for isosurface detection in voxel data and OpenGL for isosurface drawing.

Movies of all the simulations described in this article are available at
http://www-binf.bio.uu.nl/khwjtuss/ThChapter6

6.3 Results

6.3.1 Monomorphic and Polymorphic Ventricular Tachycardia

First, we study spiral wave dynamics for the standard parameter setting of our human ventricular cell model (Ten Tusscher *et al.*, 2004), corresponding to conditions in normal healthy human myocardium. In two-dimensional tissue sheets, we demonstrated stable spiral wave dynamics for the standard parameter set-

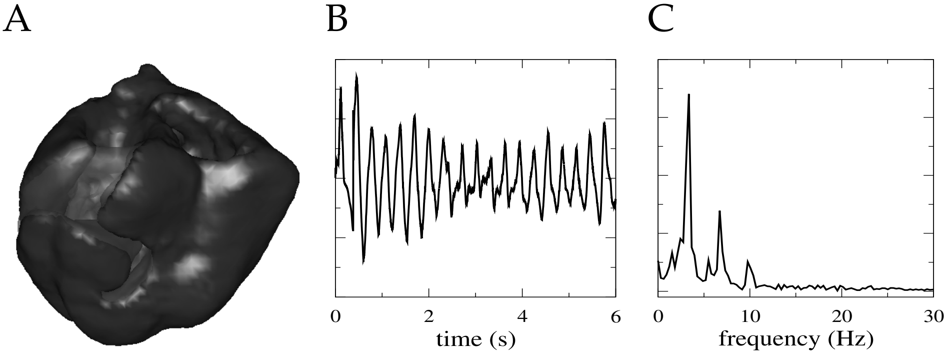

Figure 6.2: **A** Snapshot of scroll wave dynamics in the left ventricular wall 1.96 seconds after the application of the S2 extra-stimulus. See also the color plate on page 131. **B** ECG recording of the scroll wave activity shown in A. **C** Fourier transform of the ECG shown in B.

ting of our model (Ten Tusscher *et al.*, 2004). Here we will study the effect of the complex anatomy and fiber rotation anisotropy of the human ventricles on this dynamics. Figure 6.1A shows a snapshot of a scroll wave induced with a S1-S2 protocol in the right ventricle. The snapshot was obtained 1.6 seconds after spiral wave initialization. Similar stable spiral wave dynamics were observed throughout the simulation. Figure 6.1B shows the ECG corresponding to the spiral wave in Fig. 6.1A. It can be seen that the stable spiral wave dynamics result in a periodic ECG pattern, similar to ECGs obtained clinically under conditions of monomorphic ventricular tachycardia (Clayton *et al.*, 1995b). Figure 6.1C shows the Fourier transform of the ECG of Fig. 6.1B. The largest peak lies around a frequency of 3.7Hz, which corresponds to the period of 267ms of scroll wave rotation.

Figure 6.2A shows a snapshot of a scroll wave induced in the left ventricle. The snapshot was taken 1.96 seconds after scroll wave formation. The ECG corresponding to the scroll wave activity in the left ventricle is shown in Figure 6.2B. It can be seen that the ECG pattern of the scroll wave in the left ventricle is much less regular than that of the scroll wave in the right ventricle shown in Fig. 6.1B, probably due to meandering of the scroll wave. The scroll wave in the left ventricle results in an ECG pattern that resembles polymorphic rather than monomorphic ventricular tachycardia (Clayton *et al.*, 1995b). Figure 6.2C shows the Fourier transform of the ECG in Fig. 6.2B. The largest peak lies around a frequency of 3.6Hz, which corresponds to the period of 278ms of scroll wave rotation.

6.3.2 Ventricular Fibrillation

For the standard parameter setting of our model, which corresponds to normal healthy human myocardium, we have an action potential duration (APD) restitution curve with a maximum slope less than one (0.76). As a consequence, prema-

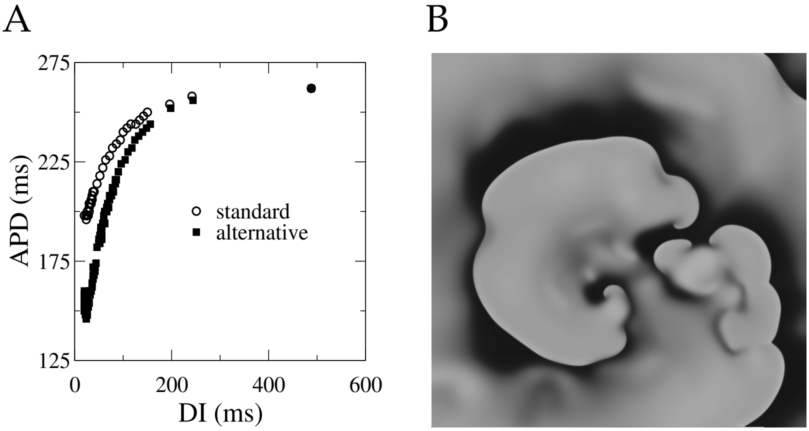

Figure 6.3: **A** Action potential duration (ADP) versus diastolic interval (DI). Restitution data were obtained using a dynamic restitution protocol in a single cell. Restitution data are for the standard parameter setting of our model, as published in (Ten Tusscher *et al.*, 2004), and for an alternative parameter setting in which recovery of the I_{Ks} x_s gate is slowed by a factor of 30 and the I_{Na} j gate is clamped to 0.77. **B** Snapshot of wave dynamics after spiral breakup for the alternative parameter setting.

ture stimulation leads to stable spiral wave dynamics in two-dimensional tissue sheets, and stable scroll wave dynamics in the human ventricular geometry. To simulate fibrillation dynamics, we looked for alternative parameter settings of our model that result in an APD restitution curve with a maximum slope steeper than one and spiral breakup. We found that the major currents of importance for obtaining a steep restitution slope are I_{Ks} and I_{Kr}. In addition, we found that a clamping of the I_{Na} j gate was necessary to obtain APD alternans and breakup in multicellular settings. For normal sodium current dynamics, electrotonic interactions tended to dampen APD alternans and suppress spiral breakup.

We found that one way to obtain an action potential duration restitution curve with a slope exceeding one was to slow down the recovery dynamics of the x_s gate of the slow delayed rectifier current. This results in a stronger accumulation of not yet deactivated I_{Ks} current when pacing frequency is increased and hence enhances action potential duration shortening. Figure 6.3A shows action potential duration restitution curves obtained using the dynamic restitution protocol for both the standard parameter setting of our model and for an alternative parameter setting in which I_{Ks} x_s gate recovery dynamics was slowed and the I_{Na} j gate was clamped. The alternative parameter setting results in an increase of the maximum slope of the restitution curve from a value of 0.76 under the standard parameter setting to a value of 1.4. In Figure 6.3B snapshots of wave dynamics occurring after the formation of an initial spiral wave in an isotropic epicardial tissue sheet described by the alternative parameter setting is shown. We can see that the steep restitution curve leads to spiral breakup and subsequent fibrillation like dynamics.

In Figure 6.4 we show snapshots of wave dynamics occurring after a scroll

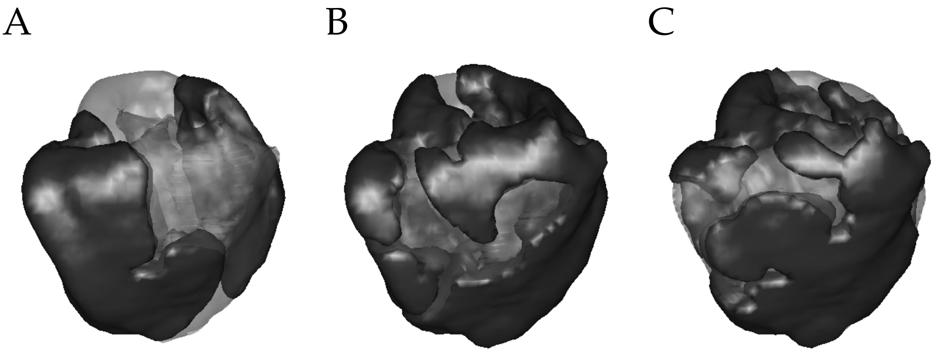

Figure 6.4: Snapshots of wave dynamics 0.08 (**A**), 0.7 (**B**) and 5.6 (**C**) seconds after application of an S2 extra-stimulus leading to scroll wave formation in the right ventricle. Results are for the alternative parameter setting with slowed I_{Ks} x_s gate recovery and clamped I_{Na} j gate. See also the color plate on page 131.

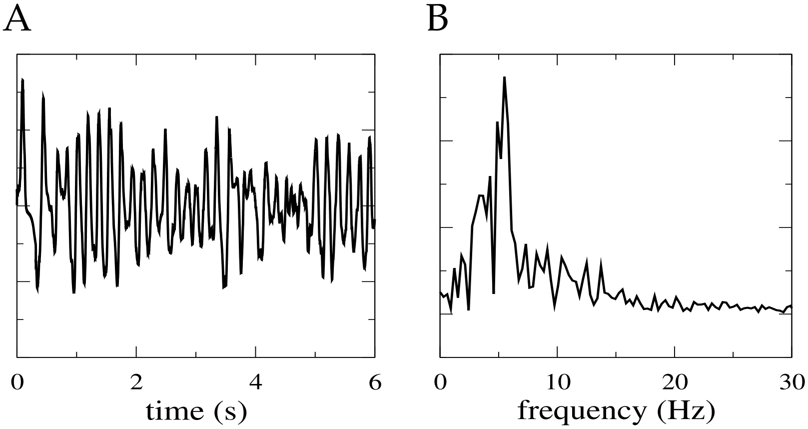

Figure 6.5: **A** ECG of the wave dynamics shown in Figure 5. **B** Fourier transform of the ECG shown in A.

wave was initialized in the right ventricle for the alternative parameter setting of slowed I_{Ks} x_s gate recovery and clamped I_{Na} j gate dynamics. The snapshots were taken 0.08, 0.7 and 5.6 seconds after scroll wave initialization. We can see that, similar to the two-dimensional case (Fig. 6.3B), scroll wave dynamics soon turns unstable, leading to scroll wave fragmentation and a subsequent dynamics similar to fibrillation. In Figure 6.5A we show the ECG corresponding to this wave dynamics, which after some time develops into a pattern similar to ventricular fibrillation (Clayton *et al.*, 1995b). Figure 6.5B shows the Fourier transform of the ECG pattern of Fig. 6.5A, which shows a dominant activation frequency of approximately 5.2Hz.

Another way of obtaining an APD restitution curve with a slope steeper than one is to reduce the density of the slow delayed rectifier current and increase the

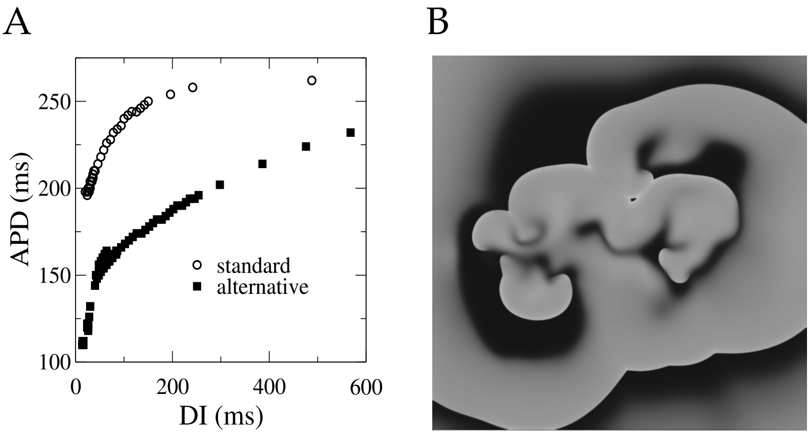

Figure 6.6: **A** Action potential duration versus diastolic interval. Restitution data were obtained using a dynamic restitution protocol in a single cell. Restitution data are for the standard parameter setting of our model and for a second alternative parameter setting in which I_{Kr} density is increased by a factor of 2.5, I_{Ks} density is put to zero, I_{CaL} f gate recovery is slowed by a factor of 4.8, and I_{Na} j gate is clamped to 0.77. **B** Snapshot of wave dynamics after spiral breakup for the second alternative parameter setting.

density of the rapid delayed rectifier current. This effect most likely arises because the recovery dynamics of I_{Ks}, if not slowed down, is much faster than the recovery dynamics of the I_{Kr} current. Increasing the I_{Kr} to I_{Ks} ratio hence leads to increased potassium current accumulation and action potential shortening under high frequencies. Figure 6.6A shows action potential duration restitution curves for the standard parameter setting of our model and for a second alternative parameter setting in which I_{Kr} current density is increased, I_{Ks} current density is decreased, the I_{Na} j gate is clamped and I_{CaL} f gate recovery is slowed. Calcium current recovery was slowed to obtain a restitution curve with a substantially different shape. For this second alternative parameter setting APD starts decaying earlier, for longer diastolic intervals, resulting in a flat restitution curve with a slope of 0.2. For diastolic intervals between 40 and 80ms this slope increases to a value of 0.5, and for a small range of diastolic intervals shorter than 40ms the slope increases to a value of 1.6. Figure 6.6B shows a snapshot of wave dynamics occurring after the formation of an initial spiral wave in a homogeneous, isotropic tissue sheet described by the second alternative parameter setting. We can see that the steep restitution curve results in spiral breakup and a subsequent fibrillation like dynamics.

In Figure 6.7 we show snapshots of wave dynamics occurring after a scroll wave was initialized in the right ventricle for the alternative parameter setting of increased I_{Kr} density, reduced I_{Ks} density, slowed I_{CaL} f gate recovery and clamped I_{Na} j gate. The snapshots were taken 0.2, 0.6 and 5.4 seconds after scroll wave initialization. It can be seen that the initial scroll wave rapidly breaks down into a fibrillatory wave pattern. In Figure 6.8A the ECG generated by this wave activity is shown. Compared to the ECG shown in Figure 6.5A and to clinically

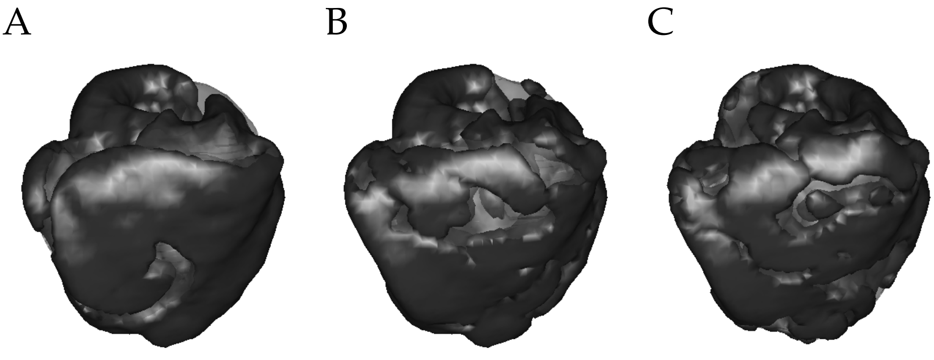

Figure 6.7: Snapshots of wave dynamics 0.2 (**A**), 0.6 (**B**) and 5.4 (**C**) seconds after application of an S2 extra-stimulus leading to scroll wave formation in the right ventricle. Results are for the second alternative parameter setting with increased I_{Kr} density, decreased I_{Ks} density, slowed I_{CaL} f gate recovery and clamped I_{Na} j gate. See also the color plate on page 131.

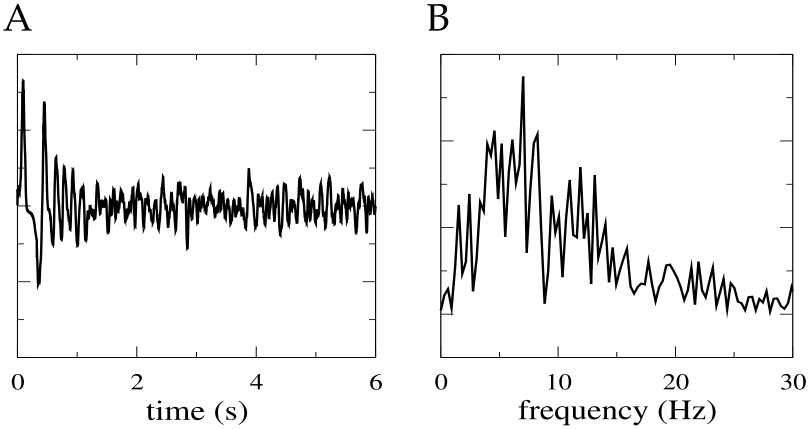

Figure 6.8: **A** ECG of the wave dynamics shown in Figure 9. **B** Fourier transform of the ECG shown in A.

observed ECGs during ventricular fibrillation (Clayton *et al.*, 1995b), the signal is much more fragmented. Figure 6.8B shows the Fourier transform of the ECG of Figure 6.8A. Compared to the frequency spectrum in Figure 6.5B and clinically observed spectra (Clayton *et al.*, 1995b), the frequency spectrum is rather broad and ill-defined. The dominant activation frequency of the spectrum is approximately 6.7Hz.

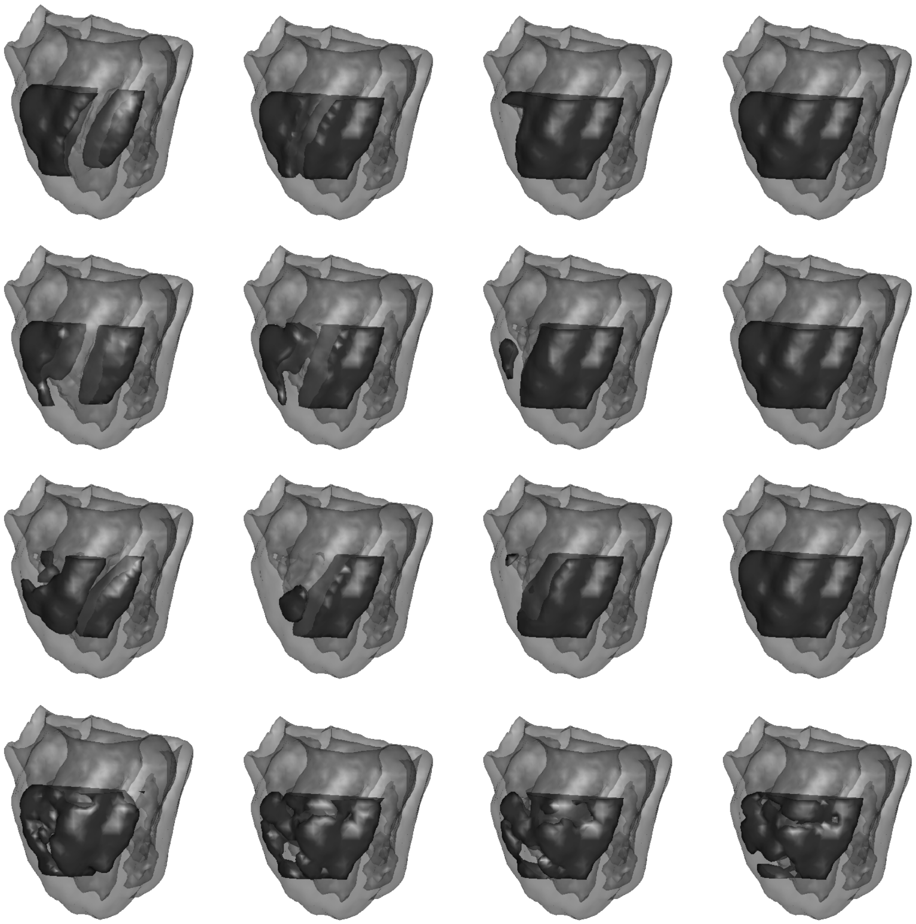

Figure 6.9: Top three rows: Snapshots of three consecutive episodes of large wave fronts entering the recording area at the right border and sweeping across the entire recording area from right to left following a similar path. Wave patterns are from fibrillation under the first alternative parameter setting. Bottom row: Snapshots of fragmented wave fronts during fibrillation under the second alternative parameter settings. See also the color plate on page 132.

6.3.3 Organization of Ventricular Fibrillation

Wave Patterns

In this section we will compare the surface activation wave patterns occurring during the two episodes of simulated ventricular fibrillation discussed in the previous sections to recent clinical data on the organization of in vivo human ventricular fibrillation obtained by Nanthakumar *et al.* (2004). Note that we use a S1-S2 stimulus protocol to induce scroll wave dynamics. The mechanism leading

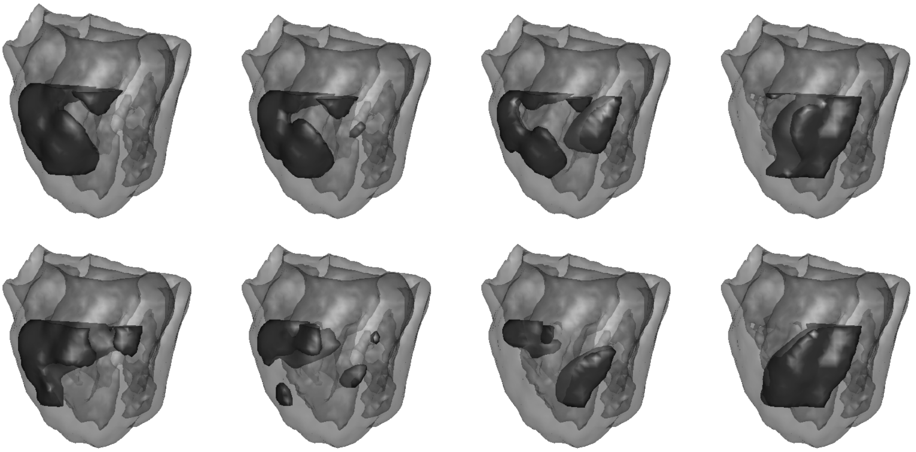

Figure 6.10: Snapshots of two consecutive episodes with the occurrence of an epicardial breakthrough wave that develops into a large propagating wave front. The episodes are from fibrillation under the first alternative parameter setting. See also the color plate on page 133.

to fibrillation dynamics is steep restitution spiral breakup. In contrast, Nanthakumar *et al.* use a rapid burst pacing protocol. The mechanism by which this leads to fibrillation is unknown. However, here our primary interest is not in the mechanism of fibrillation, but in its subsequent dynamics and organization. Given that activation frequencies and wave lengths observed during our simulated episodes of fibrillation agree well with data from clinical studies on human ventricular fibrillation, we consider it reasonable to also compare our fibrillation wave dynamics with fibrillation wave dynamics clinically observed by Nanthakumar *et al.*

To obtain a fair comparison between our data and the data from Nanthakumar *et al.* we only considered surface excitation patterns occurring in an approximately $20cm^2$ region in the anterior left ventricular epicardium that corresponds in size and position with the recording electrode plaque used by Nanthakumar *et al.* Therefore, all pictures in this section only show activation patterns in this particular region of the ventricles, although obviously activation is also occurring in the other parts of the ventricles. Note also that, compared to the activation pattern pictures shown in the article by Nanthakumar *et al.*, we show the entire activation wave rather than just the wave front.

The top three rows of Figure 6.9 show snapshots of a sequence of three large activation fronts traveling from the right to the left and sweeping across the entire recording area. The same activation path was followed six times in a row, without interruption by other wave patterns, but is shown here only three times to save space. Both the size of the wave patterns and the repeatability of the trajectories followed by the wave patterns are very similar to characteristics of wave patterns observed by Nanthakumar *et al.* (see Fig. 2 of their article). We observed these large waves following similar paths frequently during fibrillation under the first alternative parameter setting. However, we seldom observed these wave patterns during fibrillation under the second alternative parameter setting. The bottom row of Figure 6.9 shows frequently occurring fragmented wave patterns observed during fibrillation under the second alternative parameter setting. These wave patterns are very similar to wave patterns observed by Nanthakumar *et al.* during fibrillation in a patient using calcium channel blockers (see Fig. 4 of their article, bottom row). Note that in the second alternative parameter setting L-type calcium current recovery is slowed down, hence effectively reducing I_{CaL} current density.

In Figure 6.10 a series of snapshots is shown that display breakthrough patterns that lead to propagating large wave fronts. Both the position of the breakthrough pattern and the subsequent propagation path show repeatability. Breakthrough patterns were regularly observed in both cases of fibrillation, but are displayed only for the first parameter setting because the larger wave patterns occurring under these conditions make the initially small breakthrough waves easier to observe. These wave patterns are very similar to the breakthrough waves found in the mapping study of Nanthakumar *et al.* (see Fig. 3 of their article).

In Figure 6.11 snapshots of three episodes of reentry are shown. Episodes of reentry were observed for both cases of simulated fibrillation studied in this paper. Again, these wave patterns are very similar to the reentrant wave patterns observed by Nanthakumar *et al.* (See Fig. 5 of their article). Similar to their findings, the number of cycles performed by the reentrant wave patterns was always less than 2. We most frequently observed reentrant waves completing between 1/2 to 3/4 cycles of rotation.

Quantification of Reentry

In this section we will look at the role of reentrant excitation sources in maintaining the two episodes of simulated fibrillation. First, we quantified the occurrence of on the epicardial surface observable reentrant waves in the same surface area in which we studied wave patterns in the previous section and in which Nanthakumar *et al.* (2004) performed their mapping of in vivo human ventricular fibrillation. We compared our results with the data from Nanthakumar *et al.* For fibrillation under the first alternative parameter setting we found 12 short episodes of reentry, lasting between 1/4 to 3/4 reentry cycles, and taking up 8.2% of the total time during which fibrillation was recorded. For fibrillation under the second alternative parameter setting we found 20 short episodes of reentry, lasting between 1/4 to 3/4 reentry cycles, and taking up 10.4% of the total fibrillation time. All recorded episodes of reentry ended by a collision of the reentrant wave front with another wave front or by propagation of the reentrant wave front outside the recording area. Our findings are consistent with the $9.5 \pm 6.6\%$ of the time during which reentrant activity was recorded by Nanthakumar *et al.*

Next, we determined the actual number of reentrant sources present in the ventricles by counting the number of scroll wave filaments (Winfree & Strogatz, 1984). In Figure 6.12 we show snapshots of scroll wave filaments present during

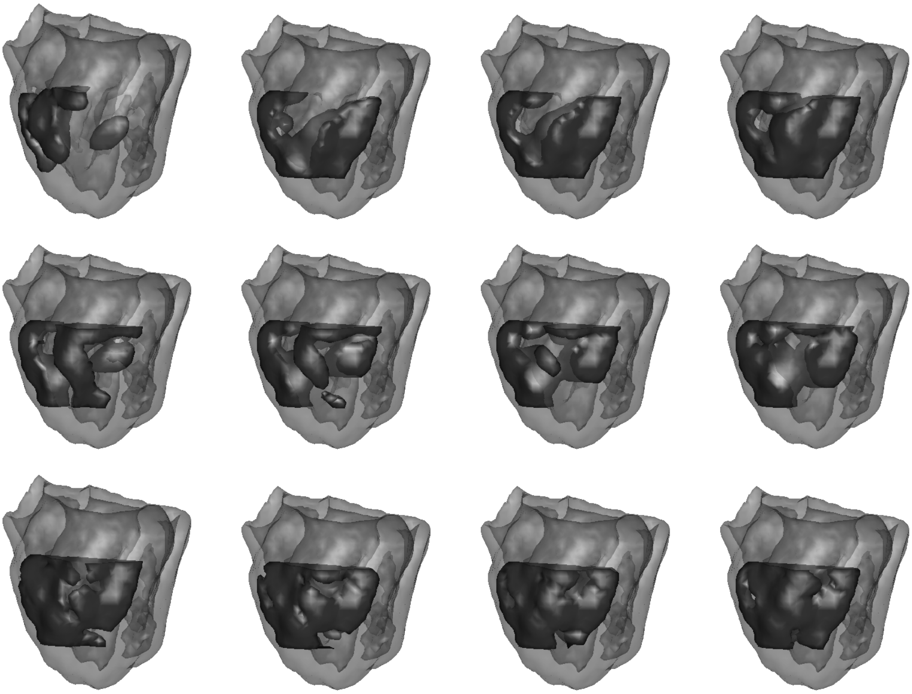

Figure 6.11: Two top rows: Snapshots of two episodes of reentry during fibrillation under the first alternative parameter setting. Bottom row: Snapshots of episode of reentry during fibrillation under the second alternative parameter setting. All shown episodes of reentry ended by a collision with another wave front. See also the color plate on page 133.

the two episodes of simulated fibrillation. In the top row, the development of filaments present during fibrillation under the first alternative parameter setting is shown. In the bottom row, the development of filaments present during fibrillation under the second alternative parameter setting is shown. From Fig. 6.12, two important observations can be made. First, in both cases, multiple filaments and hence scroll waves are present at each moment in time during fibrillation. This confirms results from previous modeling studies simulating ventricular fibrillation that observable surface reentries strongly underestimate the amount of reentrant sources underlying fibrillation (Panfilov, 1999; Clayton & Holden, 2004; Xie *et al.*, 2004). For both cases we can see illustrations of why scroll waves often cannot be observed as reentrant waves on surface recordings. We can see circular, closed filaments and filaments with both ends on inner boundaries of the ventricles. Scroll waves corresponding to such filaments will appear as breakthrough patterns rather than reentrant waves on surface recordings. In addition, we can see that a large proportion of the filaments is present in the ventricular septum. Scroll waves corresponding to these filaments are also invisible for surface recordings. The second important observation that can be made is that the

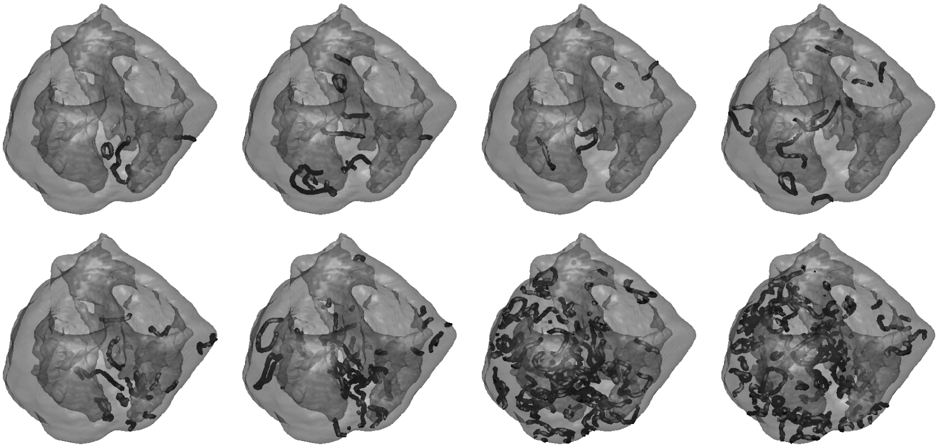

Figure 6.12: Top row: Snapshots of scroll wave filaments present during fibrillation under the first alternative parameter setting at times 1.2, 2.8, 4.2 and 4.5 seconds. Bottom row: Snapshots of scroll wave filaments present during fibrillation under the second alternative parameter setting at times 0.6, 0.8, 3.8 and 5 seconds. See also the color plate on page 134.

number of filaments and hence scroll waves present during fibrillation under the first alternative parameter setting is much smaller than for the second alternative parameter setting.

Figure 6.13A shows the time evolution of the number of filaments present during fibrillation for the first alternative parameter setting. Filament numbers progressively increase during the first 2.6 seconds of fibrillation. After this time, a phase arises in which filament numbers strongly fluctuate, with a minimum of 1, a maximum of 15, and an average of 6.0 filaments. Figure 6.13B shows the corresponding time evolution of the total summed filament length. After the first 2.6 seconds, summed filament length varies between 5.3 and 350.0mm, with an average of 119.4mm. In Figure 6.13C the time-averaged length frequency distribution of the filaments is shown. The distribution is obtained by dividing the filament length range in a number of categories, count the filaments falling into the different categories, and time-average these data. We only used data after the first 2.6 seconds of initial increase in filament numbers. We can see from Fig. 6.13C that most filaments have a length of 0−10mm or a length of 10−20mm. These lengths are close to the thickness of the left and right ventricular wall and therefore probably correspond to simple semi-straight filaments spanning the ventricular walls. Similar observations were made by (Clayton & Holden, 2004).

Figures 6.13D, E and F show the time evolution of filament numbers, the time evolution of total summed filament length, and the length frequency distribution of the filaments for fibrillation under the second alternative parameter setting. Again, we can see that filament numbers increase progressively over the first 2.6 seconds of fibrillation. However, in this case, after this initial phase, filament numbers reach a much higher level and stay relatively much more constant, with

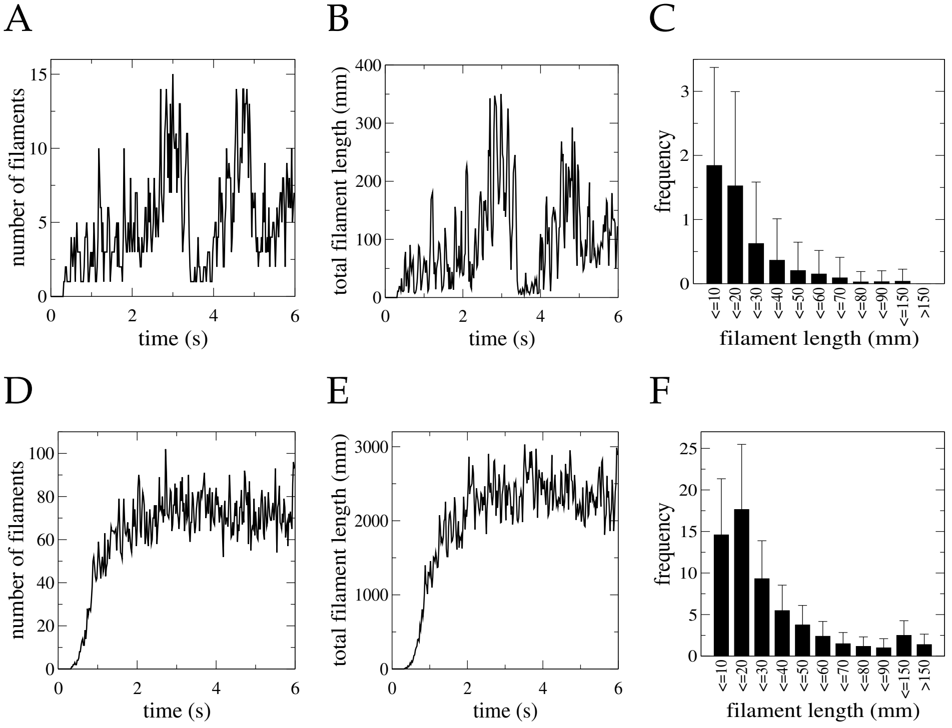

Figure 6.13: **A**, **B**, and **C** Filament characteristics for fibrillation under the first alternative parameter settings. **D**, **E**, and **F** Filament characteristics for fibrillation under the second alternative parameter settings. **A** and **D** Number of filaments present during fibrillation as a function of time. **B** and **E** Total summed length of all filaments present as a function of time. **C** and **F** Averaged length frequency distribution of filaments.

a minimum of 52, a maximum of 102, and an average of 73.0 filaments. Total summed filament length varies between a minimum of 1811.3 and a maximum of 3029.8mm, with an average of 2374.6mm. From the length frequency distribution we can see that again most filaments have a length of 0−10mm or a length of 10−20mm. In addition, we can also see that whereas for the first alternative parameter setting hardly any very long filaments occur (Fig. 6.13C), for the second alternative parameter setting a few very long filaments (on average 2.5 filaments with a length of 90−150mm and on average 1.39 filaments with a length of more than 150mm) are present at all times during fibrillation.

From a comparison of filament numbers and lengths for the two parameter settings, we find that filament numbers are on average a factor of 12.1 lower and total summed filament length is on average a factor of 19.9 lower for the first alternative parameter setting.

6.4 Discussion

In this study we investigated the dynamics of simulated reentrant arrhythmias in the human ventricles using a detailed ionic model for human ventricular cells (Ten Tusscher *et al.*, 2004) combined with a detailed model for human ventricular anatomy including a description for fiber direction anisotropy (Hren, 1996). For the standard parameter setting of the ionic model, which corresponds to normal healthy human myocardium, we found that premature stimulation led to stable scroll wave dynamics. The scroll wave induced in the right ventricle gave rise to a dynamics similar to monomorphic ventricular tachycardia. The scroll wave induced in the left ventricle gave rise to a dynamics similar to polymorphic ventricular tachycardia. It remains to be investigated whether similar differences in right and left ventricular scroll wave dynamics will be found if scroll waves are initiated at a lot of different initial positions in the left and right ventricle. A possible explanation of the difference is the greater wall thickness in the left ventricles, given that three-dimensionality and larger wall thickness is known to increase scroll wave instability (Panfilov & Hogeweg, 1996; Panfilov & Keener, 1995). We found activation frequencies of 3.7Hz for scroll wave dynamics in the right ventricle, and of 3.6Hz for scroll wave dynamics in the left ventricle, close to the clinically observed values of 3.8 and 3.7Hz for monomorphic and polymorphic ventricular tachycardia by Clayton *et al.* (1995b).

We studied two alternative parameter settings of our ionic model for which the action potential duration restitution curve has a maximum slope steeper than one. The first parameter setting resulted in a mere increase of the restitution slope relative to that of the standard parameter setting to a value exceeding one. The second parameter setting led to a restitution curve that was shallow over a broad range of diastolic intervals but that had a slope exceeding one for a small range of short diastolic intervals. In both cases action potential duration alternans occurred under high frequency pacing in a cable. In addition, spiral breakup was observed for both settings in homogeneous two-dimensional tissue sheets and in the ventricular geometry. It is interesting that in the second parameter setting only a small range of DIs for which restitution is steep can still lead to alternans and spiral breakup. This may imply that experimentally obtained curves that appear shallow and hence seem to imply stable scroll wave rotation, can have a final steep part that cannot be determined in restitution experiments and that leads to scroll wave breakup.

We further studied simulated ventricular fibrillation under these two parameter settings. For the first parameter setting we found an ECG pattern and frequency spectrum that closely resembles clinically recorded ECGs and spectra (Clayton *et al.*, 1995b,a). We found a dominant activation frequency of 5.2H, close to the clinically found values of 4.8 and 5.2Hz by Clayton *et al.* (1995b,a) and the values of 5.8Hz found by Nanthakumar *et al.* (2004) and Wu *et al.* (1998). For the second parameter settings we found a much more fragmented ECG, a broader frequency spectrum, and a activation frequency of 6.7Hz. These characteristics less closely resemble the clinically recorded fibrillation characteristics.

We performed a detailed comparison of the epicardial surface activation patterns occurring during the two simulated episodes of fibrillation with the experimental observations of Nanthakumar *et al.* (2004), who recently performed the first detailed mapping of the organization of in vivo human ventricular fibrillation. For the first parameter setting we found large wave fronts sweeping the entire mapping area and following repeatable paths, breakthrough patterns, and rare occurrences of reentry. The types and sizes of the wave patterns and the repeatability of followed wave paths are all in good agreement with the observations from Nanthakumar *et al.* For the second parameter setting, in which L-type calcium recovery is slowed and hence calcium current availability is reduced, we found smaller wave fronts and more wave fragmentation. This closely resembles results from Nanthakumar *et al.*, who found smaller wave fronts and more wave breaks during ventricular fibrillation in the hearts of patients using calcium channel blockers. The percentage of time during which reentrant activity could be observed on the epicardial surface mapping area was 8.2% for the first parameter setting and 10.4% for the second parameter setting, which both agree nicely with the value of 9.5 ± 6.6% found by Nanthakumar *et al.*

Finally, we established the actual number of reentrant sources present during the two cases of fibrillation by determining the number of scroll wave filaments (Winfree & Strogatz, 1984). In previous modeling studies using a canine ventricular geometry with a size similar to our human ventricles, numbers of 38 to 110 filaments were found (Panfilov, 1999; Clayton & Holden, 2004; Xie *et al.*, 2004), indicating that the rare observation of surface reentries in experiments strongly underestimates the number of reentrant sources underlying fibrillation. Here we show for both parameter settings that multiple scroll waves are present at all times during fibrillation, thus confirming these previous results. However, for the second parameter setting we find an average of 73 filaments, in the range of the previously found numbers, whereas for the first parameter setting we find an average of only 6 filaments. This difference may have a number of causes. First, in the second parameter setting I_{CaL} recovery is slowed, leading to a smaller calcium current and hence shorter APD and wave length, which allows a larger number of scroll waves to fit in the ventricles. Second, the maximum restitution slope is slightly higher for the first parameter setting, which may lead to larger instability and an increased rate of wave break formation leading to a larger number of reentrant sources. The differences in filament numbers are consistent with the other observed differences. For the first parameter setting, which results in fibrillation with a small number of filaments, we observed larger waves and less wave fragmentation, consistent with a smaller number of sources of larger size. In addition, the ECG pattern was somewhat more regular and of higher amplitude, consistent with the fact that a few large scroll waves lead to larger areas excited synchronously than a large number of small scroll waves. Finally, the frequency spectrum was less broad, consistent with a smaller number of frequency sources.

It should be noted that our results are preliminary, and that it will be necessary to establish whether these low filament numbers also occur for more clinically realistic model settings leading to fibrillation. However, given the much better agreement of the ECG pattern, frequency spectrum, dominant activation frequency and surface wave patterns of fibrillation under the first parameter setting with the clinical data, we hypothesize that this simulated fibrillation, organized by only a few scroll waves, more closely resembles clinically occurring ventricular fibrillation than simulated fibrillation under the second parameter setting.

Limitations There are a number of limitations to the human ventricle model used in this study.

Our current model does not include a Purkinje system. However, clinical studies suggest that the Purkinje network may play an important role in arrhythmogenesis, both as a source of premature ectopic activations (Haïssaguerre *et al.*, 2002) and by offering extra routes for the propagating excitation wave (Ouyang *et al.*, 2002). Indeed, a modeling study by Berenfeld & Jalife (1998), using FitzHugh-Nagumo dynamics in a canine ventricular geometry, showed that the Purkinje fibers could offer a route for the first rounds of semi one-dimensional reentry before a three-dimensional scroll wave is formed. We therefore plan to incorporate the Purkinje system in a future version of our model.

Because cardiac muscle fibers are organized into laminar tissue sheets that are separated by connective tissue, conductivity transversal to the tissue planes is less strong than conductivity transversal to the muscle fibers but in the tissue sheets (LeGrice *et al.*, 1995; Hunter *et al.*, 1997; Hooks *et al.*, 2002). However, in our current human ventricle model these two transversal conductivities are still assumed to be equal. Given the small differences found between the two transversal conductivities in a modeling study investigating the effect of laminar sheets on wave propagation by Hooks *et al.* (2002), we do not expect to obtain very different results when this orthotropic anisotropy is incorporated into our model.

Our human ventricular model consists entirely of identical, epicardial type, myocytes. However, in the real heart, heterogeneities such as the transmural epicardial-M cell- endocardial, the base-apex and the left-right ventricular gradient are present. Given that modeling studies have shown that transmural APD gradients may enhance scroll wave fragmentation (Clayton & Holden, 2003) and that gradients in the plane of spiral rotation may induce considerable spiral drift (Ten Tusscher & Panfilov, 2003b), we expect that including these gradients in our model will affect scroll wave dynamics and stability.

Apart from being homogeneous, our model consists of cells typical of healthy human myocardium. However, clinically, ventricular tachycardia and fibrillation occur in people with diseases such as ischemic heart disease, cardiomyopathies, and heart failure, in which formation of fibrotic, non-conducting tissue and changes in ionic currents, calcium handling, gap junctional coupling and nervous innervation occur (Pinto & Boyden, 1999; Hill, 2003; Swynghedauw, 1999; Kanno & Saffitz, 2001; Severs, 2002; Chen *et al.*, 2001), and in people with diseases such as the Brugada and long QT syndromes in which ion channel mutations cause an increase in transmural APD differences (Wehrens *et al.*, 2000, 2002; Grant *et al.*, 2002; Clancy & Rudy, 2002). The increased anatomical and functional heterogeneity occurring in these diseases plays a crucial role in initiating arrhythmias, and is also expected to influence subsequent arrhythmia dynamics and stability.

Finally, in this study we only take into account the cardiac excitation process.

However, excitation is tightly coupled to contraction and metabolism via intracellular calcium and metabolites (Bers, 2002; Guatimosim *et al.*, 2002; Csordas *et al.*, 2001), and processes influencing metabolism such as acute ischemia are highly pro-arrhythmic. In addition, mechano-electrical feedback can lead to stretch activated ectopic activity and enhanced vulnerability (Rice *et al.*, 1998; Kohl *et al.*, 1999). Finally, autonomic nervous innervation regulates heart rate and performance by influencing ionic currents and calcium dynamics (Chandra *et al.*, 1999; Bers, 2002; Taggart *et al.*, 1973) and the increased heterogeneity in this innervation that occurs after an infarction is also thought to be highly arrhythmogenic (Chen *et al.*, 2001).

It is important to note that, despite these limitations −some of which we plan to overcome in a future version of our model−, the characteristics of ventricular tachycardia and fibrillation simulated with our model agree well with data on in vivo human VT and VF (Clayton *et al.*, 1995b,a; Wu *et al.*, 1998; Nanthakumar *et al.*, 2004). Our model is the first that reproduces surface activation wave patterns of in vivo human ventricular fibrillation, and subsequently demonstrates that these activation patterns are most compatible with a very limited number of reentrant sources that is much lower than the numbers found in previous modeling studies of VF. In addition, our model is the first that uses a detailed second-generation ionic model including intracellular calcium handling in a complete ventricular geometry. It should be considered a first but important step in performing detailed studies of simulated arrhythmias in the human ventricles. One promising direction for future work could be to adapt the calcium dynamics of our model to be able to generate calcium alternans, and compare the dynamics of calcium alternans and electrical restitution alternans induced fibrillation.

Acknowledgments

This research was supported by the Netherlands Organization for Scientific Research (NWO) through grant number 620061351 of the Research Council for Physical Sciences (EW).

Color Plates

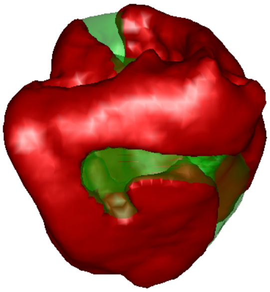

Figure 6.1 A on page 114

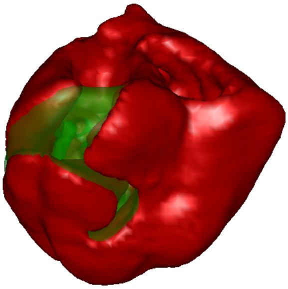

Figure 6.2 A on page 115

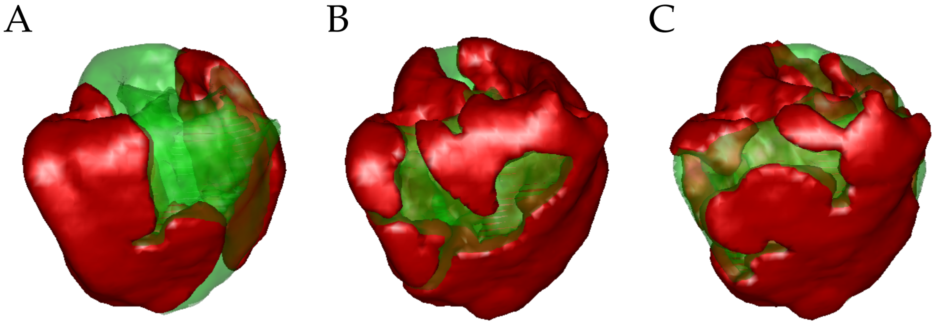

Figure 6.4 on page 117

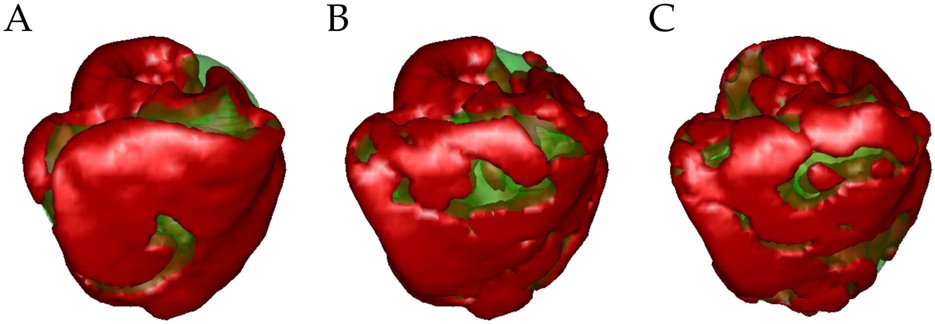

Figure 6.7 on page 119

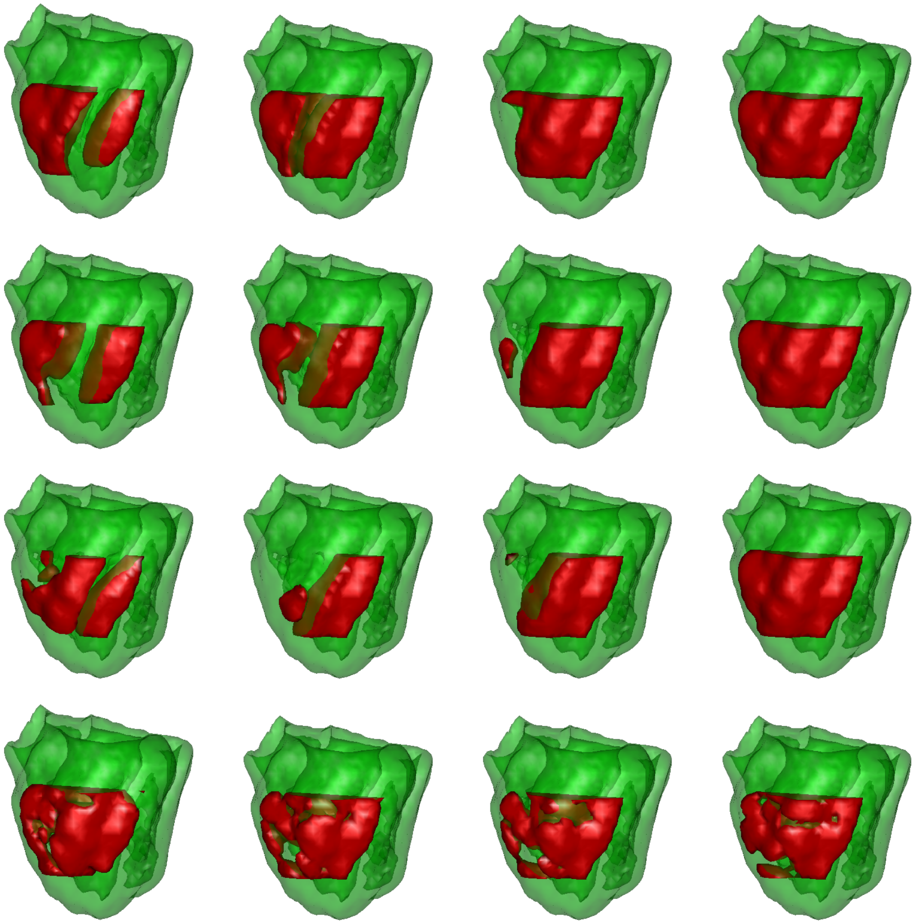

Figure 6.9 on page 120

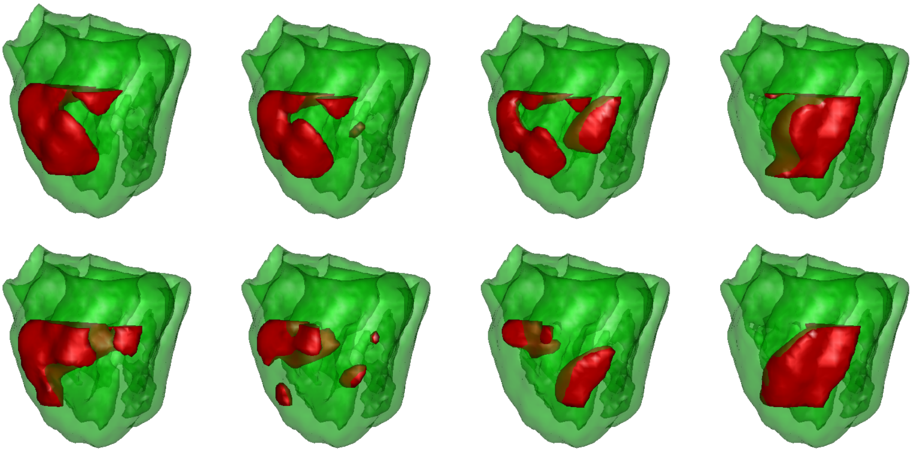

Figure 6.10 on page 121

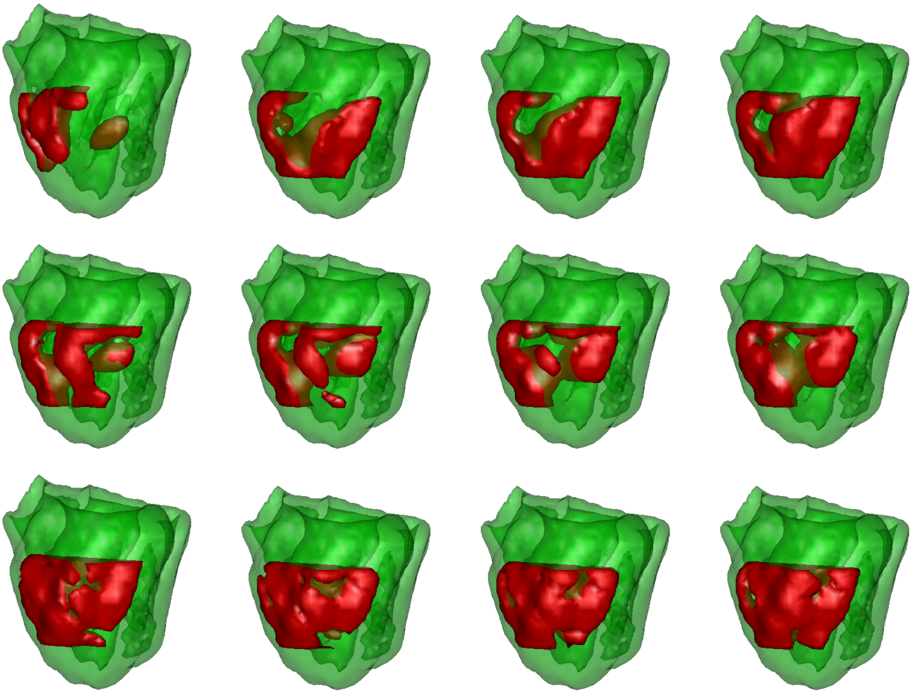

Figure 6.11 on page 123

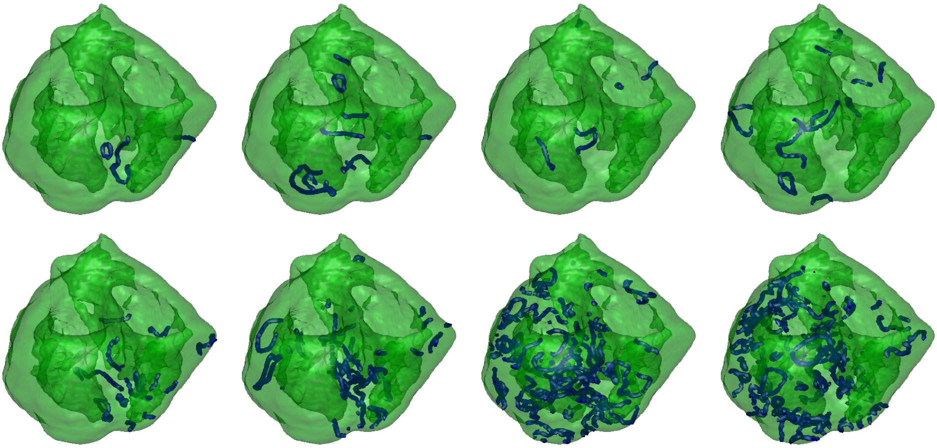

Figure 6.12 on page 124

7

Summarizing Discussion

7.1 A Review

This thesis consists of two parts. In part I, which consists of chapters 2, 3, and 4, we investigated general, basic properties of the dynamics of spiral waves as a model for reentrant cardiac arrhythmias and how these are influenced by different sorts of heterogeneities. The types of heterogeneities that were studied are: heterogeneity caused by a linear gradient in the density of an ionic current, heterogeneity caused by fibrosis of cardiac tissue, and heterogeneity caused by the presence of complex fiber direction anisotropy in three-dimensional tissue slabs.

In part II, which consists of chapters 5 and 6, we studied specific properties of reentrant cardiac arrhythmias occurring in the human ventricles. For this, in chapter 5 we first developed a detailed model for human ventricular cardiomyocytes based on recent data for all major ionic currents. In chapter 6 we used this model to study the dynamics of ventricular tachycardia and fibrillation in an anatomically accurate model of the human ventricles.

Part I

In **chapter 2** we studied the influence of gradients in ionic currents densities on the dynamics of spiral wave rotation in the Luo-Rudy phase 1 ionic model. We investigated the influence of gradients in inward rectifier potassium current (I_{K1}), and (normal) potassium current (I_K). Both currents influence action potential duration (APD) and spiral wave rotation period. We found that both gradients lead to a net displacement of the spiral wave center. This net displacement is called spiral wave drift. We showed that spiral drift consisted of a longitudinal (parallel to the gradient) and a transverse (perpendicular to the gradient) component. Independent of the parameter used to create the gradient, the longitudinal component was always directed toward the region with the longest spiral wave rotation period (where I_{K1} or I_K was lowest and hence APD was longest). We demonstrate that the direction of the transverse drift component depends on the direction of spiral wave rotation. This could be shown to follow from simple symmetry arguments. We demonstrated that the longitudinal drift speed was linearly dependent on the size of the effective spiral wave rotation period gradient induced by the I_K or I_{K1} gradient.

Our finding that spiral waves display gradient induced drift with one component of the drift in the direction of longer spiral wave rotation period and the other component perpendicular to this direction, is similar to results from a previous modeling study using a FitzHugh-Nagumo type model by Rudenko & Panfilov (1983) and to experimental results in a light-sensitive Belousov-Zhabotinsky reaction by Markus *et al.* (1992). In contrast, Boerlijst & Hogeweg (1995) find that in the presence of gradients spiral waves drift toward regions with faster spiral wave rotation (shorter spiral wave period). Note however that there are large differences in excitable media properties and spiral wave dynamics between the different above-mentioned studies. For example, in our study and those of Rudenko & Panfilov (1983) and Markus *et al.* (1992) slower spiral wave rotation is coupled to a larger spiral core, whereas in the study of Boerlijst & Hogeweg (1995) faster spiral wave rotation is coupled to a larger spiral core. As was shown by Mikhailov *et al.* (1994) and Wellner *et al.* (1999), differences in medium excitability and amount of wave front wave tail interactions during spiral wave rotation may change the direction of spiral wave drift.

The drift velocities found in our computations are on the order of $2mm$ per second for period gradients of $0.2ms/mm$. Such drift speeds could induce a significant Doppler-shift in the rotation frequency of spiral waves, causing a spiral wave to appear on the ECG as Torsade de Pointes or polymorphic tachycardia rather than stable monomorphic tachycardia (Davidenko *et al.*, 1992; Pertsov *et al.*, 1993; Gray *et al.*, 1995a).

It is important to note that we only investigated gradients of parameters that mainly influence action potential duration. It would be interesting to investigate the effect of other types of gradients, such as gradients in fast sodium current density that influence excitability, or gradients in L-type calcium current, that may influence both excitability and action potential duration. Another interesting extension of the work performed in chapter 2 would be to study the influence of a current density gradient in a ventricular geometry and to see how the gradient induced drift interacts with the effect that the complex ventricular geometry and anisotropy have on the spiral dynamics.

In **chapter 3** we studied the influence of large numbers of small inexcitable obstacles as a model for diffuse fibrosis on wave propagation, curvature effects, vulnerability to spiral wave formation and spiral wave stability in a FitzHugh-Nagumo type model. We showed that increasing the percentage of obstacles leads to a linear decrease in planar wave conduction velocity and effective diffusion coefficient. We demonstrated that an increased number of obstacles leads to an increased vulnerability of the medium for spiral wave formation. This finding is consistent with previous findings that other forms of increased heterogeneity lead to an increased vulnerability to spiral wave formation and arrhythmias (Moe *et al.*, 1964; Krinsky, 1966; Antzelevitch *et al.*, 1999). However, we found that this effect is less strong in three-dimensional than in two-dimensional excitable media. This difference is caused by the fact that the different layers of a 3D medium have different obstacle distributions. Therefore, a localized conduction block occurring in one layer is unlikely to occur at the same location in the neighboring layers, allowing their undisturbed wave fronts to invade and repair the wave break.

As a next step we studied the effect of obstacles on spiral breakup and fibrillation. In contrast to the obstacle induced increase in vulnerability to spiral wave formation, we found that obstacles suppressed steep restitution induced spiral breakup. We explained this as follows. The presence of obstacles does not change the restitution curve, but leads to a lengthening of spiral wave rotation period, action potential duration and diastolic interval (DI). The stability of spiral wave dynamics is determined by whether the restitution curve is steeper than one for the DI and APD corresponding to the spiral wave dynamics. Without obstacles, the spiral wave has a short APD and DI, corresponding to a point on the steep part of the restitution curve. The obstacle induced lengthening of APD and DI causes the point on the restitution curve to which the spiral wave corresponds to shift away from this steep part where breakup occurs. Again, the effect was less strong in three-dimensions, where a larger percentage of obstacles was required to suppress breakup. We showed that this difference could be explained by the fact that in three-dimensional media the period of scroll wave rotation is equal to the minimum period of all the two-dimensional spiral waves of the separate layers of the medium.

Our model study was inspired by the clinical finding that people with large amounts of fibrotic tissue, occurring after infarctions or in particular diseases, suffer substantially more often from ventricular tachycardia and fibrillation (De Bakker *et al.*, 1988; Wu *et al.*, 1998; Swynghedauw, 1999). We found that large numbers of small obstacles, similar to a diffuse type of fibrosis, lead to an increased vulnerability for spiral wave formation. This result agrees nicely with the clinical findings. However, we also found that small obstacles suppress spiral wave fragmentation into a fibrillatory state. This seems to disagree with the clinical data. This discrepancy might imply a number of different things. One possibility is that diffuse fibrosis in fact does not lead to an increased incidence of fibrillation. In a clinical study, Saumarez & Grace (2000) found a strong correlation between fractionated electrograms and the occurrence of ventricular fibrillation in patients. In an experimental study on human ventricular tissue with different types of fibrosis, Kawara *et al.* (2001) showed that this electrogram fractionation only occurs in the case of strand-like fibrosis but not in the case of diffuse fibrosis. Together these findings may suggest that only strand-like fibrosis leads to an increased incidence of fibrillation.

Another possible explanation is that in cardiac diseases with increased fibrotic tissue another mechanism for fibrillation than steep restitution induced spiral breakup is at work. The increased amounts of fibrotic tissue often co-occur with other changes in tissue properties, such as excitability and calcium handling, which substantially increase tissue heterogeneity. The fibrotic tissue and other changes in tissue properties may occur more in some layers of the ventricular wall than in others. This may lead to transmural gradients in excitability and action potential duration that could lead to a substantial scroll wave filament twist and subsequent breaking of transmural scroll waves.

Based on the previous, an interesting direction for future work would be to investigate whether larger, more elongated obstacles, representing stringy rather than diffuse fibrosis, or small obstacles combined with factors such as lowered excitability and increased tissue anisotropy can lead to an increased vulnerability to both tachycardia and fibrillation.

In **chapter 4** we developed an efficient method for predicting position and shape of scroll wave filaments in complex anisotropic media. Our prediction method is based on the minimum length principle derived by Wellner *et al.* (2002). Wellner *et al.* showed that the filament of a stable 3D scroll wave rotating in a medium is given by a geodesic in a 3D space with a metric given by the inverse diffusion tensor of the medium. We showed that this metric space can be interpreted as a wave arrival time space and that the geodesic, and hence the stable filament shape, is the path of shortest travel time for a wave propagating in the medium in which the scroll wave rotates. In addition, we showed that for finding the shortest wave path, the same equations that are used to simulate scroll wave dynamics can be used to compute wave propagation. Standard shortest path wave algorithms can then be used to determine the path of shortest travel time for wave propagation.

A major advantage of our method is that no a priori knowledge of the medium's diffusion tensor and of the filament's end position on the medium boundaries is needed. As a consequence our method can be applied to any type of anisotropy and any type of medium geometry. The only information that our method requires are the wave front arrival times. This means that, provided that arrival times can be recorded experimentally using for example plunge needle electrodes or transmural optical recordings, our method can be applied in electrophysiological experiments on cardiac tissue.

We tested the predictive quality of shortest path wave algorithms for finding stable filament shapes by performing numerical simulations of both actual scroll wave dynamics and planar wave propagation in anisotropic three-dimensional media described by a FitzHugh-Nagumo model. We studied two media with diffusivity tensors designed such that one results in a medium with a translationally invariant family of shortest wave paths, and one results in a medium with a single unique shortest wave path. In the first medium our wave algorithm indeed found a collection of shortest wave paths forming a curved shortest wave path surface. To check this prediction, we initiated scroll waves at different initial conditions. We found that the filaments of these scroll waves aligned with the shortest path surface at different positions. In the second medium our shortest path wave algorithm indeed found a single unique shortest wave path in the form of a curved line. To check this prediction, we initiated a single scroll wave at an arbitrary initial position in the medium. We showed that the filament of this scroll wave aligned with the shortest wave path curve over the course of time. We thus demonstrated that our prediction method works and that it does so for media with different complex anisotropic diffusion tensors. We showed that our method can predict filament shape and global filament position, provided that the medium has a unique shortest wave path.

The research described in this chapter was performed using a FitzHugh-Nagumo model with parameter settings resulting in spirals with a small and stable core. Therefore, further research using ionic models in which parameters can be varied to vary spiral core meander pattern is required to determine how well our prediction method works for larger and more irregular spiral core patterns. An interesting extension of the work presented in this chapter would be to try to predict filament shapes in complex anisotropic ventricular geometries to see what are the most likely positions for scroll waves.

Part II

In **chapter 5** we developed a new model for human ventricular cardiomyocytes. We decided a new model was needed since most available models are based on animal myocyte data. Animal hearts can differ substantially from the human heart in factors such as heart size, heart rates, action potential duration and restitution, and currents contributing to the action potential, which are all considered important for if, how and which arrhythmias may occur. The only existing human ventricular cell model is the Priebe & Beuckelmann (1998) model. This model is based on a limited set of human data, but is still largely based on the Luo-Rudy phase 2 guinea pig model (Luo & Rudy, 1994). In addition, it results in unrealistically long action potential duration.

Voltage clamp data for all major ionic currents were collected from experiments on human ventricular cardiomyocytes or from experiments in which human cardiac channels were cloned and expressed in other cell types. The obtained data were converted to physiological conditions and fitted to obtain new Hodgkin-Huxley type formulations for the fast sodium (I_{Na}), L-type calcium (I_{CaL}), transient outward (I_{to}), inward rectifying potassium (I_{K1}) and slow (I_{Ks}) and rapid delayed rectifier potassium (I_{Kr}) currents. Different model formulations were constructed for epicardial, endocardial and M cells. These formulations are based on experimentally found differences in transient outward current between endocardial cells and the other cell types, and in slow delayed rectifier current between M cells and the other cell types. The different cell type formulations could largely reproduce the differences in action potential shape, duration and restitution found experimentally between the three cell types. We validated the individual current behavior and complete model behavior against a broad set of experimental data on current-voltage curves, action potential, calcium transient and current shapes, and action potential duration restitution.

An important aspect of our model is our new fast sodium current formulation. Our formulation has a much slower j gate recovery dynamics than the widely used Luo-Rudy I_{Na} formulation. This results in a substantially more gradual and shallow CV restitution that agrees much better with the experimental data. Note that CV restitution is considered to be an important determinant of the stability of reentrant arrhythmias (Qu *et al.*, 1999; Watanabe *et al.*, 2001; Wu *et al.*, 2002; Cherry & Fenton, 2004).

To keep our model computationally efficient for large-scale spatial simulations, we formulated a simple intracellular calcium dynamics with a complexity comparable to that of other ionic models used for spatial simulations. In addition, we included a description of intracellular sodium and potassium dynamics. We validated the ion dynamics of our model by simulating a force-frequency staircase. We showed that sodium levels and systolic calcium levels increase with increasing stimulation frequencies in a manner similar to what is observed in experiments. The feasibility of spatial simulations using our model was demonstrated by simulating spiral wave dynamics in a large 2D sheet of epicardial cells.

In **chapter 6** we used our new human ventricular cell model to study reentrant arrhythmias in two-dimensional human ventricular tissue sheets and in an anatomically detailed human ventricular geometry including fiber direction anisotropy.

In the previous chapter we demonstrated that for the standard parameter settings of our model, which correspond to normal healthy human myocardium, premature stimulation leads to stable spiral wave dynamics in two-dimensional tissue sheets. Here we investigated scroll wave dynamics under these standard parameter settings in the human ventricular geometry. We found persistent scroll wave dynamics and no scroll wave fragmentation for scroll waves initiated in the right and left ventricle. However, the scroll wave dynamics in the left ventricle appeared to be less stable than those in the right ventricle. It remains to be investigated whether similar results will be found if scroll waves are initiated at various initial positions in the left and right ventricle. A possible explanation of the difference is the greater wall thickness in the left ventricles, since three-dimensionality and larger wall thickness is known to increase scroll wave instability (Panfilov & Hogeweg, 1996; Panfilov & Keener, 1995). The activation frequencies we found for the scroll waves agree with the clinically observed activation frequencies for ventricular tachycardia reported by Clayton *et al.* (1995b).

We found two alternative parameter settings of our model for which spiral breakup and subsequent ventricular fibrillation like dynamics occurred. The first parameter setting led to a 'traditional' steep action potential duration restitution curve with a maximum slope exceeding one. The second parameter setting led to an APD restitution curve that has a shallow slope for most diastolic intervals and a steep slope exceeding one for a small range of very short diastolic intervals. Both parameter settings lead to the occurrence of action potential duration alternans in a cable under high frequency pacing. In two-dimensional tissue sheets and in the ventricles this alternans instability led to spiral wave fragmentation and a subsequent fibrillatory state. It is interesting that the very small range of DIs during which restitution is steep for the second parameter setting can still lead to alternans and spiral breakup. This suggests that experimentally measured curves that appear shallow and hence seem to imply stable scroll wave dynamics may have a final steep part that is easily missed in restitution experiments and that leads to unstable scroll wave dynamics. The ECG pattern, frequency spectrum and dominant activation frequency occurring during fibrillation for the first parameter setting agree nicely with clinical data on human ventricular fibrillation (Clayton *et al.*, 1995b,a; Nanthakumar *et al.*, 2004; Wu *et al.*, 1998). For fibrillation under the second parameter setting, the ECG pattern is much more fragmented. In addition, the frequency spectrum is broader and has a relatively high dominant activation frequency. These characteristics agree less well with the clinical data.

Recently, Nanthakumar *et al.* (2004) performed the first detailed mapping of in vivo human ventricular fibrillation in patients undergoing cardiac surgery. They mapped surface activation patterns during fibrillation in a 20cm^2 area on the anterior left ventricular epicardium. We analyzed surface activation patterns occurring during the two cases of fibrillation in a similar surface area of our model's ventricular geometry. We performed a detailed comparison of simulated and experimentally observed wave patterns and demonstrated a good correspondence with regard to repeatability of wave paths followed, and types and sizes of wave patterns. In addition, we found that the percentage of time during which on the surface observable reentries occurred agreed with the percentage found experimentally by Nanthakumar et al. and lies around 10%.

Finally, we determined the number of scroll wave filaments as a measure for the number of reentrant wave sources present during fibrillation. We showed that multiple filaments and hence scroll waves are present at all times during fibrillation, in contrast with the rare observation of reentries in surface wave patterns (only $\sim$10% of the time). This agrees with results from previous modeling studies (Panfilov, 1999; Clayton & Holden, 2004; Xie *et al.*, 2004), indicating that the number of on the surface observable reentries also underestimates the actual number of reentries present during fibrillation in the human heart. However, interestingly, our preliminary results also show that for fibrillation under the first parameter setting, which resulted in the 'traditional' steep restitution curve, and a realistic ECG, frequency spectrum and activation frequency, fibrillation may be organized by as few as $\sim$ 6 reentrant sources. This number is much lower than the numbers found in previous modeling studies.

7.2 Model complexity

In this thesis models with different levels of complexity were used for modeling cardiac tissue excitability and for modeling cardiac tissue geometry.

In part I of this thesis (chapters 2,3 and 4), low-dimensional relatively general models for tissue excitability -either a FitzHugh-Nagumo type model or the Luo-Rudy phase 1 model- were used. In addition, rectangular two-dimensional planes and three-dimensional cubes were used for tissue geometry. This approach has several advantages. First, the use of low-dimensional excitability models combined with simple geometries makes these models computationally very efficient. Second and most importantly, because of the simplicity of excitability model and geometry, these models are very suitable for studying the influence of factors in isolation, without other complexities such as anisotropy or a complex geometry obscuring their effects. Therefore, use of these types of models is an essential first step for unraveling the roles of different factors that are thought to potentially play a role in arrhythmia dynamics. Third, even though the investigated heterogeneities were chosen with conditions in healthy and diseased cardiac tissue in mind, the found results can be applied to excitable media in general. However, the approach has the disadvantage that when the models are interpreted specifically as models for (human) cardiac tissue, results should be considered in a qualitative rather than quantitative manner. Incorporation of more details of human ventricular tissue excitability and anatomy in models will lead to changes in wave length, spiral wave rotation period, spiral wave core pattern, effective tissue size, shape and anisotropy, influencing the quantitative effect of these heterogeneities.

In part II of this thesis (chapters 5 and 6) we used a detailed ionic model for human ventricular cells including intracellular calcium dynamics combined with an anatomically accurate human ventricular geometry. The clear advantage of this approach is that the dynamics and organization of ventricular arrhythmias can be investigated in a quantitative manner, specific for the human heart. We demonstrated this by showing a good agreement between ECGs, frequency spectra, activation frequencies and surface wave patterns of simulated and clinically recorded human ventricular tachycardia and fibrillation. Note that similar quantitative results may be obtained by using computationally more efficient low-dimensional excitable tissue models fitted to action potential shape, duration and restitution characteristic for human ventricular tissue in a human ventricular geometry. However, using this approach new model fits should be constructed for each effect that one wants to investigate: blocking a current with a drug, an ion channel mutation, a current density gradient, nervous innervation acting on particular currents, etcetera. In contrast, in our detailed ionic model incorporating a particular effect only requires the straightforward adjustment of current properties. Furthermore, these low-dimensional models do not include accurate intracellular ion dynamics. As a consequence, these models can only fit and describe a single static APD restitution curve, whereas in reality restitution behavior dynamically depends on the applied pacing protocol and intracellular ion concentrations. In addition, these models are not suitable for investigating the role of calcium dynamics in arrhythmogenesis. Since we plan to investigate the role of factors such as ion channel mutations, natural and disease induced current density heterogeneities, and calcium dynamics on the dynamics and stability of reentrant human ventricular arrhythmias, we decided that a detailed ionic cell model combined with the human ventricular geometry would be most appropriate to use.

7.3 Model limitations

There are of course a number of limitations to the modeling approach taken in this thesis. Limitations to our modeling approach that we plan to overcome in the near future are discussed in section 7.4. Issues that can only be dealt with in the longer term, for example because of excessive computational demands, are discussed in this section.

First, there are limitations to how we modeled the cardiac excitation process. We described the excitability of single cardiac cells using ionic models with Hodgkin-Huxley type current equations or an even simpler FitzHugh-Nagumo type model. In recent years, Markov state chain models combined with Monte Carlo simulations have been used to simulate the summed stochastic behavior of collections of individual ion channels. This approach has thus far been applied mainly to L-type calcium and ryanodine channels (Rice *et al.*, 1999; Greenstein & Winslow, 2002) interacting in local subspaces, and could successfully explain graded calcium release, calcium sparks and calcium waves, which could not be explained using Hodgkin-Huxley type equations. These results point out that the summed stochastic behavior of locally acting individual channels can differ significantly from the deterministic globally acting behavior of Hodgkin-Huxley type currents. However, this approach is computationally unfeasible for the large-scale spatial models used to study reentrant arrhythmias. Therefore, rather than using this approach, averaged, phenomenological descriptions of new processes and mechanisms found in these detailed single cell models should be incorporated in spatial models (see for example (Shiferaw *et al.*, 2003)).

Second, there are some limitations to how we modeled the propagation of excitation in multicellular cardiac tissue. Throughout this thesis we used a so-called mono-domain approach to model action potential generation and propagation. In the mono-domain modeling formalism, only transmembrane current flow and intracellular axial current flow are described. Resistance in the extracellular fluid is assumed to be zero, and, as a consequence, extracellular axial current flow is also assumed to be zero. Another possible approach is to use a bi-domain model in which transmembrane current flow and both the intracellular and extracellular axial current flow are described (Roth & Wikswo, 1986). Bi-domain models therefore provide a more accurate description of the current flow in cardiac tissue. Bi-domain models are essential for computations in which the assumption of zero or very small extracellular axial current flow does not hold. As a consequence, they are extensively used in computations in which the influence of large external stimulus currents and phenomena such as virtual electrode formation are studied (Sepulveda *et al.*, 1989; Roth & Wikswo, 1994). However, bi-domain models are computationally much more costly to solve. Given the fact that we were interested in normal wave propagation rather than in specific effects induced by large external stimulus currents, we considered it reasonable to use the computationally much more efficient mono-domain modeling approach in this thesis.

A third limitation to our modeling approach is that only the cardiac excitation process is modeled. Excitation, contraction and metabolism are tightly coupled via intracellular calcium, ATP and creatinephosphate dynamics (Bers, 2002; Guatimosim *et al.*, 2002; Csordas *et al.*, 2001). These interactions can be important for understanding arrhythmias, given the important role of calcium dynamics in arrhythmogenesis, and the fact that processes influencing metabolism, such as acute ischemia, are highly arrhythmogenic. Cardiac mechanics feeds back to the excitation process via stretch activated ion channels, changes in calcium handling, or interaction with other mechano-sensitive cells such as fibroblasts (Rice *et al.*, 1998; Kohl *et al.*, 1999). Modeling studies have shown that stretch activation in an infarcted region of the heart with delayed contraction may lead to ectopic beats triggering arrhythmias and increased vulnerability. Regulation of heart rate and performance by the autonomic nervous system occurs by influencing intracellular calcium dynamics, ion channel conductances and dynamics (Chandra *et al.*, 1999; Bers, 2002), and action potential duration restitution (Taggart *et al.*, 1973). In a research by Chen *et al.* (2001), it was found that the increased amount and heterogeneity in distribution of nerves innervating the heart that occurs after an infarction played an important role in arrhythmogenesis.

The interaction of these processes with excitation lies outside the scope of this thesis.

7.4 Future Directions

We ended this thesis with a study of the dynamics of reentrant arrhythmias in a model that combines a detailed description of human ventricular myocyte behavior with a realistic geometry of the human ventricles incorporating rotational muscle fiber anisotropy. We think that this is a large step forward from using phenomenological FitzHugh-Nagumo type models or animal myocyte ionic models for the excitable behavior of cardiac tissue and from using animal ventricular geometries. However, there are still a number of important details missing from our model that we would like to include in future work.

In our current human ventricular model, only fiber direction anisotropy is incorporated. However, it is now well known that the ventricles have a laminar structure, with the muscle fibers being organized in planes separated by interstitial connective tissue, causing the ventricular conductivity tensor to be orthotropically anisotropic (LeGrice *et al.*, 1995; Hunter *et al.*, 1997; Hooks *et al.*, 2001). Currently, the only model including this orthotropic anisotropy in a ventricular geometry is by Colli-Franzone *et al.* (2004). However, they used a truncated ellipsoid as a simplified model of only the left ventricle and computed wave propagation using eikonal equations. In addition, they only studied the effect of orthotropic anisotropy on normal wave propagation. Now that orthotropic anisotropy data have become available for the human heart, we would like to incorporate it in a future version of our human ventricles model. This will allow us to study the effect of orthotropic anisotropy on scroll wave dynamics and stability and the organization of ventricular fibrillation.

Our human ventricle model does not include a Purkinje fiber system. However, Purkinje fibers may play an important role in arrhythmias, both as a potential source of ectopic beats that may trigger reentry (Haïssaguerre *et al.*, 2002), and by offering extra routes to the excitation waves (Ouyang *et al.*, 2002). Indeed, a modeling study by Berenfeld & Jalife (1998), using a FitzHugh-Nagumo model in a canine ventricular geometry, suggests that the Purkinje network may serve as an initial semi one-dimensional route for reentry before a 3D scroll wave arises in the ventricular mass. We plan to incorporate a Purkinje network in a future version of our model to investigate how it can be involved in the initiation of reentry, how it influences the character of wave patterns, and whether it influences the transition from tachycardia to fibrillation.

In our current human ventricle model, all cells are of the same epicardial cell type. However, in reality, there are three distinct cell types −epicardial, endocardial and midmyocardial− present in the ventricular wall, leading to substantial heterogeneity (Burton & Cobbe, 2001; Liu & Antzelevitch, 1995; Zygmunt *et al.*, 2000). This heterogeneity is further increased by the presence of gradients in particular ionic currents across the ventricles, such as the base-apex gradient and the left-right ventricle gradient (Burton & Cobbe, 2001). In a future version of our model we would like to include these naturally present heterogeneities to study their influence on the dynamics of reentrant waves. As a basis for this we can use the in chapter 5 formulated parameter settings for epicardial, endocardial and M cells, and the in chapter 2 obtained insights on the influence of current density gradients on spiral wave behavior.

Furthermore, the parameter setting used to describe cardiac cell behavior corresponds to healthy human myocardium. However, clinically, arrhythmias occur in people with particular heart diseases. The occurrence of ventricular tachycardia and fibrillation is strongly coupled to diseases such as myocardial infarction, cardiomyopathies, and heart failure. In these diseases extensive fibrosis formation, and ion, calcium handling, gap junctional and nervous innervation remodeling take place (Pinto & Boyden, 1999; Hill, 2003; Swynghedauw, 1999; Kanno & Saffitz, 2001; Severs, 2002; Chen *et al.*, 2001), dramatically enhancing cardiac heterogeneity. In addition, these arrhythmias often occur in people with inherited diseases such as the Brugada and long QT syndromes. In these diseases mutations that cause a preferential shortening of epicardial action potential (Brugada) or lengthening of M cell action potential (LQT) enhance the epicardial-endocardial action potential duration gradient (Wehrens *et al.*, 2002, 2000; Grant *et al.*, 2002; Clancy & Rudy, 2002). In a future version of our model we would like to include, on top of the naturally present heterogeneities mentioned above, the additional heterogeneities occurring in these diseases. This would allow us to study the dynamics of reentrant arrhythmias under the conditions in which they occur clinically. Moreover, this would allow us to not only study the dynamics of artificially induced arrhythmias, but also study the mechanisms involved in initiating these arrhythmias.

7.5 Conclusion

The most important insights obtained in part I of this thesis are the following: Tissue heterogeneity in the form of a gradient in ion current density can lead to substantial spiral wave drift. Measured drift velocities may potentially cause a spiral wave to appear on the ECG as polymorphic rather than monomorphic tachycardia. Diffuse fibrosis, modeled by the presence of large numbers of small inexcitable obstacles, increases tissue vulnerability to spiral wave formation. However, these small obstacles suppress steep restitution mediated spiral wave breakup. This indicates that the general concept of increased heterogeneity being pro-arrhythmic needs refinement and that heterogeneity may play different roles in initiating an arrhythmia and in influencing it's subsequent dynamics and stability. Finally, the position and shape of scroll wave filaments in complex anisotropic 3D media can be interpreted as the path of shortest wave travel time and can be found using simple shortest path wave algorithms that can also be applied to real cardiac tissue.

Note that these effects were investigated mainly in low-dimensional generalized models of excitable media applied in rectangular 2D and 3D geometries. This means that results should be interpreted in a qualitative rather than quantitative manner.

Therefore, to be able to quantitatively investigate the dynamics and organization of human ventricular arrhythmias, we developed in part II of this thesis an ionic model for human ventricular myocytes and combined it with a human ventricular geometry. We demonstrated that it is feasible to simulate reentrant ventricular arrhythmias using this detailed ionic model in a ventricular geometry consisting of $\sim$ 14 million grid points on a modest size Beowulf cluster. We found a good agreement between simulated and clinically observed arrhythmias in terms of ECG patterns, frequency spectra, activation frequencies, and surface wave patterns. An interesting outcome of our study is the prediction that ventricular fibrillation in the human heart can be organized by as few as $\sim$ 6 reentrant sources.

In a future version of our human ventricle model we plan to incorporate the heterogeneities present in healthy (current density gradients, complex anisotropy) and diseased (enhanced current density gradients, fibrosis) hearts, thus combining the research performed in the two parts of this thesis. This will improve the realism of our human ventricle model, allowing us to study the dynamics of reentrant arrhythmias under clinically more realistic conditions, and to investigate the effects of these heterogeneities quantitatively and specific for human ventricular arrhythmias.

Bibliography

Agladze, K. I., Keener, J. P., Müller, S. C. & Panfilov, A. V. Rotating spiral waves created by geometry. *Science* 264: 1746–1748 (1994).

Akar, F. G., Yan, G., Antzelevitch, C. & Rosenbaum, D. S. Unique Topographical Distribution of M Cells Underlies Reentrant Mechanism of Torsade de Pointes in the Long-QT Syndrome. *Circulation* 105: 1247–1253 (2002).

Aliev, R. R. & Panfilov, A. V. Modeling of Heart Excitation Patterns caused by a Local Inhomogeneity. *J. theor. Biol.* 181: 33–40 (1996a).

Aliev, R. R. & Panfilov, A. V. A simple two-variable model of cardiac excitation. *Chaos, Solitons and Fractals* 7: 293–301 (1996b).

Allessie, M. A., Bonke, F. I. M. & Schopman, F. J. G. Circus movement in rabbit atrial muscle as a mechanism of tachycardia. *Circ. Res.* 33: 54–62 (1973).

Antzelevitch, C. & Fish, J. Electrical heterogeneity within the ventricular wall. *Basic Res. Cardiol.* 96: 517–527 (2001).

Antzelevitch, C., Yan, G. X., Shimizu, W. & A., Burashnikov. Electrical heterogeneity, the ECG, and cardiac arrhythmias. In *Cardiac electrophysiology. From cell to bedside, 3rd edition*, edited by D. P. Zipes & J. Jalife, pp. 222–238. Saunders, Philadelphia (1999).

Banville, I. & Gray, R. A. Effect of action potential duration and conduction velocity restitution and their spatial dispersion on alternans and the stability of arrhythmias. *J. Cardiovasc. Electrophysiol.* 13: 1141–1149 (2002).

Bär, M., Bangia, A. K., Kevrekidis, I. G., Haas, G., Rotermund, H. H. & Ertl, G. Composite catalyst surfaces: Effect of inert and active heterogeneities on pattern formation. *J. Phys. Chem.* 100: 19106–19117 (1996).

Bär, M., Meron, E. & Utzny, C. Pattern formation on anisotropic and heterogeneous catalytic surfaces. *Chaos* 12: 204–214 (2002).

Bär, M. & Or-Guil, M. Alternative scenarios of spiral breakup in a reaction-diffusion model with excitable and oscillatory dynamics. *Phys. Rev. Lett.* 82: 1160–1163 (1999).

Baxter, W. T., Mironov, S. F., Zaitsev, A. V., Jalife, J. & Pertsov, A. M. Visualizing Excitation Waves inside Cardiac Muscle Using Transillumination. *Biophys. J.* 80: 516–530 (2001).

Beeler, G. W. & Reuter, H. Reconstruction of the action potential of ventricular myocardial fibers. *J. Physiol. (Lond.)* 268: 177–210 (1977).

Behrens, S., Li, C. & Franz, M. R. Effects of myocardial ischemia on ventricular fibrillation inducibility and defibrillation efficiency. *J. Am. Coll. Cardiol.* 29: 817–824 (1997).

Bendall, J. K., Heymes, C., Ratajczak, P. & Samuel, J. L. Extracellular matrix and cardiac remodeling. *Arch. Mal. Coeur* 95: 1226–1229 (2002).

Benitah, J., Bailly, P., D'Agrosa, M., Da Ponte, J., Delgado, C. & Lorente, P. Slow inward current in single cells isolated from adult human ventricles. *Pflugers Arch.* 421: 176–187 (1992).

Berenfeld, O. & Jalife, J. Purkinje-Muscle Reentry as a Mechanism of Polymorphic Ventricular Arrhythmias in a 3-Dimensional Model of the Ventricles. *Circ. Res.* 82: 1063–1077 (1998).

Berenfeld, O. & Pertsov, A. M. Dynamics of intramural scroll waves in a 3-dimensional continuous myocardium with rotational anisotropy. *J. theor. Biol* 199: 383–394 (1999).

Berenfeld, O., Wellner, M., Jalife, J. & Pertsov, A. M. Shaping of a scroll wave filament by cardiac fibers. *Phys. Rev. E* 63: 061901 (2001).

Berne, R. M. & Levy, M. N. *Physiology*, chapter 24: The Cardiac Pump. Mosby Year Book (1993).

Bernus, O., Verschelde, H. & Panfilov, A. V. Reentry in an anatomical model of the human ventricles. *Int. J. Bif. Chaos* 13: 3693–3702 (2003).

Bernus, O., Wilders, R., Zemlin, C. W., Verschelde, H. & Panfilov, A. V. A computationally efficient electrophysiological model of human ventricular cells. *Am. J. Physiol. Heart Circ. Physiol.* 282: H2296–H2308 (2002).

Bers, D. M. Cardiac excitation-contraction coupling. *Nature* 415: 198–205 (2002).

Bers, D. M., Pogwizd, S. M. & Schlotthauer, K. Upregulated Na/Ca exchange is involved in both contractile dysfunction and arrhythmogenesis in heart failure. *Basic Res. Cardiol.* 97: S36–S42 (2002).

Beuckelmann, D. J., Nabauer, M. & Erdmann, E. Characteristics of Calcium-Current in Isolated Human Ventricular Myocytes from Patients with Terminal Heart Failure. *J. Mol. Cell. Cardiol.* 23: 929–937 (1991).

Beuckelmann, D. J., Nabauer, M. & Erdmann, E. Intracellular calcium handling in isolated ventricular myocytes from patients with terminal heart failure. *Circulation* 94: 992–1002 (1992).

Biktashev, V. N., Holden, A. V. & Zhang, H. Tension of organizing filaments of scroll waves. *Phil. Trans. R. Soc. Lond. A* 347: 611–630 (1994).

Boerlijst, M. C. & Hogeweg, P. Spatial gradients enhance persistence of hypercycles. *Physica D* 88: 29–39 (1995).

Boyett, M. R. & Fedida, D. A Computer Simulation of the Effect of Heart Rate on Ion Concentrations in the Heart. *J. theor. Biol.* 132: 15–27 (1988).

Bub, G. & Shrier, A. Propagation through heterogeneous substrates in simple excitable media models. *Chaos* 12: 747–753 (2002).

Bub, G., Shrier, A. & Glass, L. Spiral Wave Generation in Heterogeneous Excitable Media. *Phys. Rev. Lett.* 88: 058101–1–058101–4 (2002).

Burton, F. L. & Cobbe, S. M. Dispersion of ventricular repolarization and refractory period. *Cardiovasc. Res.* 50: 10–23 (2001).

Byars, J. L., Smith, W. M., Ideker, R. E. & Fast, V. G. Development of an Optrode for Intramural Multisite Optical Recordings of V_m in the Heart. *J. Cardiovasc. Electrophysiol.* 14: 1196–1202 (2003).

Cabo, C., Pertsov, A. M., Baxter, W. T., Davidenko, J. M., Gray, R. A. & Jalife, J. Wavefront curvature as a cause of slow conduction and block in isolated cardiac muscle. *Circ. Res.* 75: 1014–1028 (1994).

Cabo, C., Pertsov, A. M., Davidenko, J. M., Baxter, W. T., Gray, R. A. & Jalife, J. Vortex shedding as a precursor of turbulent electrical activity in cardiac muscle. *Biophys. J.* 70: 1105–1111 (1996).

Cao, J., Qu, Z., Kim, Y., Wu, T., Garfinkel, A., Weiss, J. N., Karagueuzian, H. S. & Chen, P. Spatiotemporal Heterogeneity in the Induction of Ventricular Fibrillation by Rapid Pacing, Importance of Cardiac Restitution Properties. *Circ. Res.* 84: 1318–1331 (1999).

Chandra, R., Chauhan, V. S., Starmer, C. F. & Grant, A. O. β-adrenergic action on wild-type and KPQ mutant human cardiac Na^+ channels: shift in gating but no change in Ca^{2+}:Na^+ selectivity. *Cardiovasc. Res.* 42: 490–502 (1999).

Chen, J., Mandapati, R., Berenfeld, O., Skanes, A. C. & Jalife, J. High-Frequency Periodic Sources Underlie Ventricular Fibrillation in the Isolated Rabbit Heart. *Circ. Res.* 86: 86–89 (2000).

Chen, P., Chen, L. S., Cao, J., Sharifi, B., Karagueuzian, H. S. & Fishbein, M. C. Sympathetic nerve sprouting, electrical remodeling and the mechanisms of sudden cardiac death. *Cardiovasc. Res.* 50: 409–416 (2001).

Chen, P., Garfinkel, A., Weiss, J. N. & Karagueuzian, H. S. Computerized mapping of fibrillation in normal ventricular myocardium. *Chaos* 8 (1998).

Chen, P. S., Wolf, P., Dixon, E. G., Danieley, N. D., Frazier, D. W., Smith, W. M. & Ideker, R. E. Mechanism of ventricular vulnerability to single premature stimuli in open-chest dogs. *Circ. Res.* 62: 1191–1209 (1988).

Cherry, E. M. & Fenton, F. H. Suppression of alternans and conduction blocks despite steep APD restitution: Electrotonic, memory and conduction velocity effects. *Am. J. Physiol. Heart Circ. Physiol.* 286: H2332–H2341 (2004).

Choi, B., Burton, F. & Salama, G. Cytosolic Ca^{2+} triggers early afterdepolarizations and torsade de pointes in rabbit hearts with type 2 long QT syndrome. *J. Physiol.* 543: 615–631 (2002a).

Choi, B., Nho, W., Liu, T. & Salama, G. Life span of ventricular fibrillation frequencies. *Circ. Res.* 91: 339–345 (2002b).

Chudin, E., Goldhaber, J., Garfinkel, A. Weiss, J. & Kogan, B. Intracellular Ca^{2+} Dynamics and the Stability of Ventricular Tachycardia. *Biophys. J.* 77: 2930–2941 (1999).

Chung, M. K., Pogwizd, S. M., Miller, D. P. & Cain, M. E. Three-dimensional mapping of the initation of nonsustained ventricular tachycardia in the human heart. *Circulation* 95: 2517–2527 (1997).

Clancy, C. E. & Rudy, Y. Na^{+} Channel Mutation That Causes Both Brugada and Long-QT Syndrome Phenotypes, A Simulation Study of Mechanism. *Circulation* 105: 1208–1213 (2002).

Clayton, R. H. & Holden, A. V. Effect of regional differences in cardiac cellular electrophysiology on the stability of ventricular arrhythmias: a computational study. *Phys. Med. Biol.* 48: 95–111 (2003).

Clayton, R. H. & Holden, A. V. Filament Behaviour in a Computational Model of Ventricular Fibrillation in the Canine Heart. *IEEE Trans. Biom. Eng.* 51: 28–34 (2004).

Clayton, R. H., Murray, A. & Campbell, R. W. Analysis of the body surface ECG measured in independent leads during ventricular fibrillation in humans. *Pacing Clin. Electrophysiol.* 18: 1876–1881 (1995a).

Clayton, R. H., Murray, A. & Campbell, R. W. Objective features of the surface electrocardiogram during ventricular tachyarrhythmias. *Eur. Heart J.* 16: 1115–1119 (1995b).

Colli-Franzone, P., Guerri, L. & Taccardi, B. Modeling ventricular excitation: axial and orthotropic anisotropy effects on wavefronts and potential. *Math. Biosci.* 188: 191–205 (2004).

Compton, S. Ventricular Tachycardia [online] <www.emedicine.com/med/topic2367.html> (2002).

Courtemanche, M., Glass, L. & Keener, J. P. Instabilities of a propagating pulse in a ring of excitable media. *Phys. Rev. Lett.* 70: 2182–2185 (1993).

Courtemanche, M., Keener, J. P. & Glass, L. A delay equation representation of pulse circulation on a ring of excitable media. *SIAM J. Appl. Math.* 56: 119–142 (1996).

Courtemanche, M., Ramirez, R. J. & Nattel, S. Ionic mechanisms underlying human atrial action potential properties: insights from a mathematical model. *Am. J. Physiol. Heart Circ. Physiol.* 275: H301–H321 (1998).

Courtemanche, M. & Winfree, A. T. Re-entrant rotating waves in a Beeler-Reuter based model of two-dimensional cardiac activity. *Int. J. Bif. Chaos* 1: 431–444 (1991).

Csordas, G., Thomas, A. P. & Hajnoczky, G. Calcium Signal Transmission between Ryanodine Receptors and Mitochondria in Cardiac Muscle. *Trends Cardiovasc. Med.* 11: 269–275 (2001).

Davidenko, J. M., Kent, P. F., Chialvo, D. R., Michaels, D. C. & Jalife, J. Sustained vortex-like waves in normal isolated ventricular muscle. *Proc. Natl. Acad. Sci. U.S.A.* 87:

8785–8789 (1990).

Davidenko, J. M., Pertsov, A. M., Salomonsz, R., Baxter, W. & Jalife, J. Stationary and drifting spiral waves of excitation in isolated cardiac muscle. *Nature* 355: 349–351 (1992).

De Bakker, J. M. T., Van Capelle, F. J. L & Janse, M. J. Reentry as a cause of ventricular tachycardia in patients with chronic ischemic heart disease: electrophysiologic and anatomic correlation. *Circulation* 68: 518–533 (1988).

Di Diego, J. M., Cordeiro, J. M., Goodrow, R. J., Fish, J. M., Zygmunt, A. C., Perez, G. J., Scornik, F. S. & Antzelevitch, C. Ionic and Cellular Basis for the Predominance of the Brugada Syndrome Phenotype in Males. *Circulation* 106: 2004–2011 (2002).

Diaz, M. E., O'Neill, S. C. & Eisner, D. A. Sarcoplasmic reticulum calcium content fluctuation is the key to cardiac alternans. *Circ. Res.* 94: 650–656 (2004).

DiFrancesco, D. & Noble, D. A model of cardiac electrical activity incorporating ionic pumps and concentration changes. *Phil. Trans. R. Soc. Lond.* B 307: 353–398 (1985).

Drouin, E., Charpentier, F., Gauthier, C., Laurent, K. & Le Marec, H. Electrophysiologic characteristics of cells spanning the left ventricular wall of human heart: evidence for the presence of M cells. *J. Am. Coll. Cardiol.* 26: 185–192 (1995).

Drouin, E., Lande, G. & Charpentier, F. Amiodarone Reduces Transmural Heterogeneity of Repolarization in the Human Heart. *J. Am. Coll. Cardiol.* 32: 1063–1067 (1998).

Durrer, D., Van Dam, R. T., Freud, G. E., Janse, M. J., Meijler, F. L. & Arzbaecher, R. C. Total excitation of the isolated human heart. *Circulation* 41: 899–912 (1970).

Ebihara, L. & Johnson, E. A. Fast Sodium Current in Cardiac Muscle, A Quantitative Description. *Biophys. J.* 32: 779–790 (1980).

Ebihara, L., Shigeto, N., Lieberman, M. & Johnson, E. A. The Initial Inward Current in Spherical Clusters of Chick Embryonic Heart Cells. *J. Gen. Physiol.* 75: 437–456 (1980).

Eckert, R., Randall, D. & Augustine, G. *Animal Physiology, Mechanisms and Adaptations*, chapter 13: Circulation of the blood. W. H. Freeman and Company (1988).

Efimov, I. R., Krinsky, V. I. & Jalife, J. Dynamics of Rotating Vortices in the Beeler-Reuter Model of Cardiac Tissue. *Chaos, Solitions and Fractals* 5: 513–526 (1995).

Efimov, I. R., Sidorov, V. Y., Cheng, Y. & Wollenzier, B. Evidence of 3D scroll waves with ribbon-shaped filament as a mechanism of ventricular tachycardia in the isolated rabbit heart. *J. Cardiovasc. Electrophysiol.* 10: 1452–1462 (1999).

El-Sherif, N., Chinushi, M., Caref, E. B. & Restivo, M. Electrophysiological Mechanism of the Characteristic Electrocardiographic Morphology of Torsade de Pointes Tachyarrhythmias in the Long-QT Syndrome. *Circulation* 96: 4392–4399 (1997).

Endresen, L. P., Hall, K., Hoye, J. S. & Myrheim, J. A theory for the membrane potential of living cells. *Eur. Biophys. J.* 29: 90–103 (2000).

Endresen, L. P. & Skarland, N. Limit cycle oscillations in pacemaker cells. *IEEE Trans. Biomed. Eng.* 47: 1134–1137 (2000).

Fast, V. G., Efimov, I. R. & Krinsky, V. I. Transition from circular to linear cores in excitable media. *Phys. Lett. A* 151: 157–161 (1990).

Fast, V. G. & Kléber, A. G. Role of wavefront curvature in propagation of cardiac impulse. *Cardiovasc. Res.* 33: 258–271 (1997).

Fast, V. G. & Pertsov, A. M. Drift of a vortex in the myocardium. *Biophysics* 35: 489–494 (1990).

Fenton, F., Evans, S. J. & Hastings, H. M. Memory in an excitable medium: A mechanism for spiral wave breakup in the low-excitability limit. *Phys. Rev. Lett.* 83: 3964–3967 (1999).

Fenton, F. & Karma, A. Vortex dynamics in three-dimensional continuous myocardium with fiber rotation: Filament instability and fibrillation. *Chaos* 8: 20–47 (1998).

FitzHugh, R. Thresholds and plateaus in the Hodgkin-Huxley nerve equations. *J. Gen.*

Physiol. 43: 867–896 (1960).

FitzHugh, R. Impulses and physiological states in theoretical models of nerve membrane. *Biophys. J.* 1: 445–466 (1961).

Franzone, P. C., Guerri, L. & Tentoni, S. Mathematical modeling of the excitation process in myocardial tissue: influence of fiber rotation on wavefront propagation and potential field. *Math. Biosci.* 101: 155–235 (1990).

Frazier, D. W., Wolf, P. D., Wharton, J. M., Tang, A. S. L., Smith, W. M. & Ideker, R. E. Stimulus-induced critical point. Mechanism for electrical initiation of reentry in normal canine myocardium. *J. Clin. Invest.* 83: 1039–1052 (1989).

Garfinkel, A., Kim, Y. H., Voroshilovsky, O., Qu, Z., Kil, J. R., Lee, M. H., Karagueuzian, H. S., Weiss, J. N. & Chen, P. S. Preventing ventricular fibrillation by flattening cardiac restitution. *Proc. Natl. Acad. Sci. U.S.A.* 97: 6061–6066 (2000).

Garfinkel, A. & Qu, Z. Nonlinear dynamics of excitation and propagation in cardiac tissue. In *Cardiac electrophysiology. From cell to bedside, 3rd edition*, edited by D. P. Zipes & J. Jalife, pp. 315–320. Saunders, Philadelphia (1999).

Gerisch, G. Standienspezifische aggregationsmuster bei Dictyostelium discoideum. *Wilhelm Roux Arch. Entwick. Org.* 156: 127–144 (1965).

Gettes, L. S. & Reuter, H. Slow recovery from inactivation of inward currents in mammalian myocardial fibres. *J. Physiol.* 240: 703–724 (1974).

Gintant, G. A. Characterization and functional consequences of delayed rectifier current transient in ventricular repolarization. *Am. J. Physiol. Heart Circ. Physiol.* 278: H806–H817 (2000).

Girouard, S. D., Pastore, J. M., Laurita, K. R., Gregory, K. W. & Rosenbaum, D. S. Optical Mapping in a New Guinea Pig Model of Ventricular Tachycardia Reveals Mechanisms for Multiple Wavelengths in a Single Reentrant Circuit. *Circulation* 93: 603–613 (1996).

Gopalakrishnan, M. & Malkin, R. A. Two-dimensional Analysis of Ventricular Fibrillation in the Guinea Pig. *J. Electrocardiol.* 36: 147–153 (2003).

Gorelova, N. A. & Bures, J. J. Spiral waves of spreading depression in the isolated chicken retina. *J. Neurobiol.* 14: 353–363 (1983).

Gourdie, R. G., Harris, B. S., Bond, J., Justus, C., Hewett, K. W., O'Brien, T. X., Thompson, R. P. & Sedmera, D. Development of the cardiac pacemaking and conduction system. *Birth Defects Research* 69: 46–57 (2003).

Grant, A. O., Carboni, M. P., Neplioueva, V., Starmer, C. F., Memmi, M., Napolitano, C. & Priori, S. Long QT syndrome, Brugada syndrome, and conduction system disease are linked to a single sodium channel mutation. *J. Clin. Invest.* 110: 1201–1209 (2002).

Grantham, C. J. & Cannell, M. B. Ca^{2+} Influx During the Cardiac Action Potential in Guinea Pig Ventricular Myocytes. *Circ. Res.* 79: 194–200 (1996).

Gray, R. A. & Jalife, J. Ventricular fibrillation and atrial fibrillation are two different beasts. *Chaos* 8: 65–78 (1998).

Gray, R. A., Jalife, J., Panfilov, A., Baxter, W. T., Cabo, C., Davidenko, J. M. & Pertsov, A. M. Nonstationary vortexlike reentrant activity as a mechanism of polymorphic ventricular tachycardia in the isolated rabbit heart. *Circulation.* 91: 2454–2469 (1995a).

Gray, R. A., Jalife, J., Panfilov, A. V., Baxter, W. T., Cabo, C., Davidenko, J. M. & Pertsov, A. M. Mechanisms of cardiac fibrillation. *Science* 270: 1222–1223 (1995b).

Gray, R. A., Pertsov, A. M. & Jalife, J. Spatial and temporal organization during cardiac fibrillation. *Nature* 392: 75–78 (1998).

Greenstein, J. L. & Winslow, R. L. An Integrative Model of the Cardiac Ventricular Myocyte Incorporating Local Control of Ca^{2+} Release. *Biophys. J.* 83: 2918–2945 (2002).

Greenstein, J. L., Wu, R., Po, S., Tomaselli, G. F. & Winslow, R. L. Role of the Calcium-Independent Transient Outward Current I_{to1} in Shaping Action Potential Morphology and Duration. *Circ. Res.* 87: 1026–1033 (2000).

Grindrod, P. *Patterns and waves: The theory and application of reaction-diffusion equations.* Claredon Press, Oxford (1991).

Guatimosim, S., Dilly, K., Santana, L. F., Jafri, M. S., Sobie, E. A. & Lederer, W. J. Local Ca^{2+} Signalling and EC Coupling in Heart: Ca^{2+} Sparks and the Regulation of the $[Ca^{2+}]_i$ Transient. *J. Mol. Cell. Cardiol.* 34: 941–950 (2002).

Guevara, M.R., Ward, A., Shrier, A. & Glass, L. Electrical alternans and period doubling bifurcations. *IEEE Comp. Cardiol.* 562: 167–170 (1984).

Haïssaguerre, M., Shah, D. C., Jaïs, P., Shoda, M., Kautzner, J., Arentz, T., Kalushe, D., Kadish, A., Griffith, M., Gaïta, F., Yamane, T., Garrigue, S., Hocini, M. & Clémente, J. Role of Purkinje conducting system in triggering of idiopathic ventricular fibrillation. *The Lancet* 359: 677–678 (2002).

Hayashi, H., Wang, C., Miyauchi, Y., Omichi, C., Pak, H. N., Zhou, S., Ohara, T., Mandel, W. J., Lin, S. F., Fishbein, M. C., Chen, P. C. & Karagueuzian, H. S. Aging-related increase to inducible atrial fibrillation in the rat model. *J. Cardiovasc Electrophysiol* 13: 801–808 (2002).

Hein, S., Arnon, E., Kostin, S., Schönburg, M., Elsässer, A., Polyakova, V., Bauer, E. P., Klövekorn, W. P. & Schaper, J. Progression from compensated hypertrophy to failure in the pressure overloaded human heart. *Circulation* 107: 984–991 (2003).

Henry, H. & Rappel, W. J. The role of M cells in the long QT syndrome in cardiac arrhythmias: Simulation studies of reentrant excitations using a detailed electrophysiological model. *Chaos* 14: 172–182 (2004).

Hill, J. A. Electrical Remodeling in Cardiac Hypertrophy. *Trends Cardiovasc. Med.* 13: 316–322 (2003).

Hill, R. W. & Wyse, G. A. *Animal Physiology*, chapter Circulation. Harper & Row (1989).

Hodgkin, A. L. & Huxley, A. F. A quantitative description of membrane current and its application to conduction and excitation in nerve. *J. Physiol.* 117: 500–544 (1952).

Hooks, D. A., LeGrice, I. J., Harvey, J. D. & Smaill, B. H. Intramural Multisite Recording of Transmembrane Potential in the Heart. *Biophys. J.* 81: 2671–2680 (2001).

Hooks, D. A., Tomlinson, K. A., Marsden, S. G., LeGrice, I. J., Smaill, B. H., Pullan, A. J. & Hunter, P. Cardiac microstructure: implications for electrical propagation and defibrillation in the heart. *Circ. Res.* 23: 331–338 (2002).

Hort, W. Untersuchungen über die muskelfaserdehnung und das gefuge des myokards in der rechten herzkammerwand des meerschweinchens. *Virchows. arch* 329: 694–731 (1957).

Hren, R. *A realistic model of the human ventricular myocardium: Application to the study of ectopic activation.* PhD thesis, Dalhouse University, Halifax (1996).

Hsia, H. H. & Marchlinski, F. E. Characterization of the electroanatomic substrate for Monomorphic Ventricular Tachycardia in Patients with Nonischemic Cardiomyopathy. *Pacing Clin. Electrophysiol.* 25: 1114–1127 (2002).

Huang, J., Rogers, J. M., Killingsworth, C. R., Walcott, G. P., KenKnight, B. H., Smith, W. M. & Ideker, R. E. Improvement of Defibrillation Efficiency and Quantification of Activation Patterns During Ventricular Fibrillation in a Canine Heart Failure Model. *Circulation* 103: 1473–1478 (2001).

Huang, J., Skinner, J. L., Rogers, J. M., Smith, W. M., Holman, W. L. & Ideker, R. E. The Effects of Acute and Chronic Amiodarone on Activation Patterns and Defibrillation Threshold During Ventricular Fibrillation in Dogs. *J. Am. Coll. Cardiol.* 40: 375–383 (2002).

Hund, T. J., Kucera, J. P., Otani, N. F. & Rudy, Y. Ionic Charge Conservation and Long-Term Steady State in the Luo-Rudy Dynamic Cell Model. *Biophys. J.* 81: 3324–3331

(2001).

Hunter, P. J., Smail, B. H., Nielson, P. M. F. & LeGrice, I. J. A mathematical model of cardiac anatomy. In *Computational Biology of the Heart*, edited by A. V. Panfilov & A. V. Holden, pp. 171–215. Wiley, Chichester (1997).

Ideker, R. E., Huang, J., Fast, V. & Smith, W. M. Recent fibrillation studies, Attempts to wrest order from disorder. *Circ. Res.* 89: 1089–1091 (2001).

Ikeda, T., Czer, L., Trento, A., Hwang, C., Ong, J. J. C., Hough, D., Fishbein, M. C., Mandel, W. J., Karagueuzian, H. S. & Chen, P. Induction of Meandering Functional Reentrant Wave Front in Isolated Human Atrial Tissues. *Circulation* 96: 3013–3020 (1997).

Imbihl, R. & Ertl, G. Oscillatory kinetics in heterogeneous catalysis. *Chem. Rev.* 95: 697–733 (1995).

Iost, N., Virag, L., Opincariu, M., Szecsi, J., Varro, A. & Papp, J. G. Delayed rectifier potassium current in undiseased human ventricular myocytes. *Cardiovasc. Res.* 40: 508–515 (1998).

Ito, H. & Glass, L. Spiral breakup in a new model of discrete excitable media. *Phys. Rev. Lett.* 66: 671–674 (1991).

Ivanitsky, G. R., Krinsky, V. I., Panfilov, A. V. & Tsyganov, M. A. Two Regimes of Drift of Reverberators in Heterogeneous Active Media. *Biophysics.* 34: 319–322 (1989).

Jalife, J. Ventricular fibrillation: mechanisms of initiation and maintenance. *Annu. Rev. Physiol.* 62: 25–50 (2000).

Jalife, J. Experimental and clinical AF mechanisms: Bridging the divide. *J. Interv. Card. Electrophysiol.* 9: 85–92 (2003).

Jalife, J., A., Gray. R., Morley, G. E. & Davidenko, J. M. Self-organization and the dynamical nature of ventricular fibrillation. *Chaos* 8: 79–93 (1998).

Janvier, N. C. & Boyett, M. R. The role of the Na-Ca exchange current in the cardiac action potential. *Cardiovasc. Res.* 32: 69–84 (1996).

Johnson, J. P., Mullins, F. M. & Bennet, P. B. Human Ether-a-go-go-related Gene K^+ Channel Gating Probed with Extracellular Ca^{2+}, evidence for Two Distinct Voltage Sensors. *J. Gen. Physiol.* 113: 565–580 (1999).

Jongsma, H. J. & Wilders, R. Gap junctions in cardiovascular disease. *Circ. Res.* 86: 1193–1197 (2000).

Joyner, R. W. Modulation of repolarization by electrotonic interactions. *Jpn. Heart J.* Suppl 1: 167–183 (1986).

Jugdutt, B. I. Remodelling of the myocardium and potential targets in the collagen synthesis pathways. *Curr. Drug Targets Cardiovasc. Haematol. Disord.* 3: 1–30 (2003).

Kambouris, N. G., Nuss, H. B., Johns, D. C., Marban, E., Tomaselli, G. F. & Balser, J. R. A revised view of cardiac sodium channel 'blockade' in the long-QT syndrome. *J. Clin. Invest.* 105: 1133–1140 (2000).

Kanno, S. & Saffitz, J. E. The role of myocardial gap junctions in electrical conduction and arrhythmogenesis. *Cardiovasc. Pathol.* 10: 169–177 (2001).

Karma, A. Spiral breakup in model equations of action potential propagation in cardiac tissue. *Phys. Rev. Lett.* 71: 1103–1106 (1993).

Karma, A. Electrical alternans and spiral wave breakup in cardiac tissue. *Chaos* 4: 461–472 (1994).

Kawara, T., Derksen, R., De Groot, J. R., Coronel, R., Tasseron, S., Linnenbank, A. C., Hauer, R. N. W., Kirkels, H., J., Janse M. & De Bakker, J. M. T. Activation Delay After Premature Stimulation in Chronically Diseased Human Myocardium Relates to the Architecture of Interstitial Fibrosis. *Circulation* 104: 3069–3075 (2001).

Keener, J. & Sneyd, J. *Mathematical physiology*. Springer-Verlag, New York, Heidelberg, Berlin (1998).

Keener, J. P. The dynamics of three-dimensional scroll waves in excitable media. *Physica D* 31: 269–276 (1988).

Keener, J. P. An eikonal equation for action potential propagation in myocardium. *J. Math. Biol.* 29: 629–651 (1991).

Keener, J. P. Propagation of waves in an excitable medium with discrete release sites. *SIAM J. Appl. Math.* 61: 317–334 (2000).

Kim, D. T., Kwan, Y., Lee, J. L., Ikeda, T., Uchida, T., Kamjoo, K., Kim, Y., Ong, J. J. C., Athill, C. A., Wu, T., Czer, L., Karagueuzian, H. S. & Chen, P. Patterns of spiral tip motion in cardiac tissue. *Chaos* 8: 137–148 (1998).

Kim, Y., Yashima, M., Wu, T., Doshi, R., Chen, P. & Karagueuzian, H. R. Mechanism of Procainamide-Induced Prevention of Spontaneous Wave Break During Ventricular Fibrillation, Insight Into the Maintenance of Fibrillation Wave Fronts. *Circulation* 100: 666–674 (1999a).

Kim, Y., Yashima, M., Wu, T., Doshi, R., Chen, P. & Karagueuzian, H. R. Role of Papillary Muscle in the Generation and Maintenance of Reentry During Ventricular Tachycardia and Fibrillation in Isolated Swine Right Ventricle. *Circulation* 100: 1450–1459 (1999b).

Kirchhof, P. F., Fabritz, C. L., Zabel, M. & Franz, M. R. The vulnerable period for low and high energy T-wave shocks: Role of dispersion of repolarisation and effect of *d*-solatol. *Cardiovasc. Res.* 31: 953–962 (1996).

Kogan, B. Y., Karplus, W. J., Billett, B. S., Pang, A. T., Karagueuzian, H. S., & Khan, S. S. The simplified FitzHugh-Nagumo model with action potential duration restitution: effects on 2D wave propagation. *Physica D* 50: 327–340 (1991).

Kohl, P., Hunter, P. J. & Noble, D. Stretch-induced changes in heart rate and rhythm: clinical observations, experiments and mathematical models. *Prog. Biophys. Mol. Biol.* 71: 91–138 (1999).

Koller, M. L., Riccio, M. L. & Gilmour Jr., R. F. Dynamic restitution of action potential duration during electrical alternans and ventricular fibrillation. *Am. J. Physiol. Heart Circ. Physiol.* 275: H1635–H1642 (1998).

Koumi, S., Backer, C. L. & Arentzen, C. E. Characterization of Inwardly Rectifying K^+ Channel in Human Cardiac Myocytes. *Circulation* 92: 164–174 (1995).

Krinsky, V. I. Spread of excitation in an inhomogeneous medium (state similar to cardiac fibrillation). *Biophysics* 11: 776–784 (1966).

Krinsky, V. I. Mathematical models of cardiac arrhythmias (spiral waves). *Pharm. Ther. B.* 3: 539–555 (1978).

Krinsky, V. I., Biktashev, V. N. & Efimov, I. R. Autowave principles for parallel image processing. *Physica D* 49: 247–253 (1991).

Krinsky, V.I. Autowaves: Results, problems, outlooks. In *Self-Organization. Autowaves and Structures far from equilibrium*, edited by V. I. Krinsky, pp. 9–18. Springer-Verlag, Heidelbeg (1984).

Lechleiter, J., Girard, S., Peralta, E. & Clapham, D. Spiral calcium wave propagation and annihilation in Xenopus laevis oocytes. *Science* 252: 123–126 (1991).

Lee, J. J., Kamjoo, K., Hough, D., Hwang, C., Fan, W., Fishbein, M. C., Bonometti, C., Ikeda, T., Karagueuzian, H. S. & Chen, P. S. Reentrant wave fronts in Wiggers' stage II ventricular fibrillation. Characteristics and mechanisms of termination and spontaneous regeneration. *Circ. Res.* 78: 660–675 (1996).

LeGrice, I. J., Hunter, P. J. & Smaill, B. H. Laminar structure of the heart a mathematical model. *Am. J. Physiol. Heart Circ. Physiol.* 272: H2466–H2476 (1997).

LeGrice, I. J., Smaill, B. H., Chai, L. Z., Edgar, S. G., Gavin, J. B. & Hunter, P. J. Laminar structure of the heart: ventricular myocyte arrangement and connective tissue architecture in the dog. *Am. J. Physiol. Heart Circ. Physiol.* 269: H571–H582 (1995).

Lemery, R. Atrial fibrillation: Mechanistic insights from biatrial (and triatrial) mapping. *J. Cardiovasc. Electrophysiol.* 14: 1248–1251 (2003).

Li, G. R., Feng, J., Yue, L. & Carrier, M. Transmural heterogeneity of action potentials and I_{to1} in myocytes isolated from the human right ventricle. *Am. J. Physiol. Heart Circ. Physiol.* 275: H369–H377 (1998).

Li, G. R., Feng, J., Yue, L., Carrier, M. & Nattel, S. Evidence for Two Components of Delayed Rectifier K^+ Current in Human Ventricular Myocytes. *Circ. Res.* 78: 689–696 (1996).

Li, G. R. & Nattel, S. Properties of human atrial I_{Ca} at physiological temperatures and relevance to action potential. *Am. J. Physiol. Heart Circ. Physiol.* 272: H227–H235 (1997).

Liu, D. W. & Antzelevitch, C. Characteristics of the delayed rectifier current (I_{Kr} and I_{Ks}) in canine ventricular epicardial, midmyocardial, and endocardial myocytes. A weaker I_{Ks} contributes to the longer action potential of the M cell. *Circ. Res.* 76: 351–365 (1995).

Liu, Y., Wu, C., Lu, L., Su, M., Lin, C., Lin, S., Chen, L. S., Fishbein, M. C., Chen, P. & Lee, Y. Sympathetic nerve sprouting, electrical remodelling, and increased vulnerability to ventricular fibrillation in hypercholesterolemic rabbits. *Circ. Res.* 92: 1145–1152 (2003).

Luo, C. & Rudy, Y. A Model of the Ventricular Cardiac Action Potential, Depolarization, Repolarization, and Their Interaction. *Circ. Res.* 68: 1501–1526 (1991).

Luo, C. & Rudy, Y. A Dynamic Model of the Cardiac Ventricular Action Potential I Simulations of Ionic Currents and Concentration Changes. *Circ. Res.* 74: 1071–1096 (1994).

Magyar, J., Szentandrassy, N., Banyasz, T., Fulop, L., Varro, A. & Nanasi, P. P. Effects of thymol on calcium and potassium currents in canine and human ventricular cardiomyocytes. *Br. J. Pharmacol.* 136: 330–338 (2002).

Makita, N., Shirai, N., Wang, D. W., Sasaki, K., George, A. L., Kanno, M. & Kitabatake, A. Cardiac Na^+ Channel Dysfunction in Brugada Syndrome Is Aggravated by β_1-Subunit. *Circulation* 101: 54–60 (2000).

Mandapati, R., Asano, Y., Baxter, W. T., Gray, R., Davidenko, J. & Jalife, J. Quantification of Effects of Global Ischemia on Dynamics of Ventricular Fibrillation in Isolated Rabbit Heart. *Circulation* 98: 1688–1696 (1973).

Manz, N., Davydov, V. A., Zykov, V. S. & Müller, S. C. Excitation fronts in a spatially modulated light-sensitive Belousov-Zhabotinsky system. *Phys. Rev. E* 66: 036207–1–036207–5 (2002).

Marée, A. F. M. & Panfilov, A. V. Spiral breakup in excitable tissue due to lateral instability. *Phys. Rev. Lett.* 78: 1819–1822 (1997).

Markus, M., Nagy-Ungvarai, Z. & Hess, B. Phototaxis of spiral waves. *Science* 257: 225–227 (1992).

Meron, E. Pattern formation in excitable media. *Phys. Rep.* 218: 1–66 (1992).

Mewes, T. & Ravens, U. L-type Calcium Currents of Human Myocytes from Ventricle of Non-Failing and Failing Hearts and Atrium. *J. Mol. Cell. Cardiol.* 26: 1307–1320 (1994).

Mikhailov, A. S., Davydov, V. A. & Zykov, V. S. Complex dynamics of spiral waves and motion of curves. *Physica D* 70: 1–39 (1994).

Mines, G. R. On dynamic equilibrium in the heart. *J. Physiol. (London)* 46: 349–382 (1913).

Moe, G. K., Rheinboldt, W. C. & Abildskov, J. A. A computer model of atrial fibrillation. *Am. Heart J.* 67: 200–220 (1964).

Moore, E. Shortest path through a maze. *Annals Comp. Lab. Harvard Univ.* 30: 285–292 (1959).

Moorman, A. F. M. & Christoffels, V. M. Cardiac Chamber Formation: Development, Genes, and Evolution. *Phys. Rev.* 83: 1223–1267 (2003).

Morgan, J. M., Cunningham, D. & Rowland, E. Dispersion of monophasic action potential duration: demonstrable in humans after premature ventricular extrastimulation but not in steady state. *J. Am. Coll. Cardiol.* 19: 1244–1253 (1992).

Moubarak, J. B., Karasik, P. E., Fletcher, R. D. & Franz, M. R. High Dispersion of Ventricular Repolarization After an Implantable Defibrillator Shock Predicts Induction of Ventricular Fibrillation As Well As Unsuccessful Defibrillation. *J. Am. Coll. Cardiol.* 35: 422–427 (2000).

Nagatomo, T., Fan, Z., Ye, B., Tonkovich, G. S., January, C. T., Kyle, J. W. & Makielski, J. C. Temperature dependence of early and late currents in human cardiac wild-type and long-QT ΔKPQ Na^+ channels. *Am. J. Physiol. Heart Circ. Physiol.* 275: H2016–H2024 (1998).

Nabauer, M., Beuckelmann, D. J., Uberfuhr, P. & Steinbeck, G. Regional Differences in Current Density and Rate-Dependent Properties of the Transient Outward Current in Subepicardial and Subendocardial Myocytes of Human Left Ventricle. *Circulation* 93: 168–177 (1996).

Nagumo, J. S., Arimoto, S. & Yoshizawa, S. An active pulse transmission line simulating nerve axon. *Proc. IRE* 50: 2061–2071 (1962).

Nanthakumar, K., Walcott, G. P., Melnick, S., Rogers, J. M., Kay, M. W., Smith, W. M., Ideker, R. E. & Holman, W. Epicardial organization of human ventricular fibrillation. *Heart Rhythm* 1: 14–23 (2004).

Nash, M. P., Bradley, C. P. & Paterson, D. J. Imaging electrocardiographic dispersion of depolarization and repolarization during ischemia: simultaneous body surface and epicardial mapping. *Circulation* 107: 2257–2263 (2003).

Noble, D. A modification of the Hodgkin-Huxley equations applicable to Purkinje fibres action and pacemaker potential. *J. Physiol. (Lond.)* 160: 317–352 (1962).

Noble, D., Varghese, A., Kohl, P. & Noble, P. Improved guinea-pig ventricular cell model incorporating a diadic space, I_{Kr} and I_{Ks}, and length- and tension-dependent processes. *Can. J. Cardiol.* 14: 123–134 (1998).

Nolasco, J.B. & Dahlen, R.W. A graphic method for the study of alternation in cardiac action potentials. *J. Appl. Physiol.* 25: 191–196 (1968).

Obel, O. A. & Camm, A. J. Supraventricular tachycardia. ECG diagnosis and anatomy. *Eur. Heart J.* 18: C2–C11 (1997).

Ohtani, K., Yutani, C., Nagata, S., Koretsune, Y., Hori, M. & Kamada, T. High prevalence of atrial fibrosis in patients with dilated cardiomyopathy. *J. Am. Coll. Cardiol.* 25: 1162–1169 (1995).

Omichi, C., Lamp, S. T., Lin, S., Yang, J., Baher, A., Zhou, S., Attin, M., Lee, M., Karagueuzian, H. S., Kogan, B., Qu, Z., Garfinkel, A., Chen, P. & Weiss, J. N. Intracellular Ca Dynamics in Ventricular Fibrillation. *Am. J. Physiol. Heart Circ. Physiol.* 286: H1836–H1844 (2004).

Ouyang, F., Cappato, R., Ernst, S., Goya, M., Volkmer, M., Hebe, J., Antz, M., Vogtmann, T., Schaumann, A., Fotuhi, P., Hoffman-Riem, M. & Kuck, K. Electroanatomic substrate of idiopathic left ventricular tachycardia, Unidirectional block and macroreentry within the Purkinje network. *Circulation* 105: 462–469 (2002).

Panfilov, A. V. Three-dimensional vortices in active media. In *Nonlinear wave processes in excitable media*, edited by A. V. Holden, M. Markus & H. G. Othmer, pp. 361–382. Plenum Press, New York (1991).

Panfilov, A. V. Modelling of reentrant patterns in an anatomical model of the heart. In *Computational Biology of the Heart*, edited by A. V. Panfilov & A. V. Holden, pp. 259–276. Wiley, Chichester (1997).

Panfilov, A. V. Three-dimensional organization of electrical turbulence in the heart. *Phys. Rev. E* 59: R6251–R6254 (1999).

Panfilov, A. V. Spiral breakup in an array of coupled cells: the role of the intercellular conductance. *Phys. Rev. Lett.* 88: 118101–1–118101–4 (2002).

Panfilov, A. V., Aliev, R. R. & Mushinsky, A. V. An integral invariant for scroll rings in a reaction-diffusion system. *Physica D* 36: 181 188 (1989).

Panfilov, A. V. & Hogeweg, P. Spiral break-up in a modified FitzHugh−Nagumo model. *Phys. Lett. A* 176: 295–299 (1993).

Panfilov, A. V. & Hogeweg, P. Scroll breakup in a three-dimensional excitable medium. *Phys. Rev. E* 53: 1740–1743 (1996).

Panfilov, A. V. & Holden, A. V. Self-generation of turbulent vortices in a two-dimensional model of cardiac tissue. *Phys. Lett. A* 147: 463–466 (1990).

Panfilov, A. V. & Keener, J. P. Effects of high frequency stimulation on cardiac tissue with an inexcitable obstacle. *J. theor. Biol.* 163: 439–448 (1993a).

Panfilov, A. V. & Keener, J. P. Re-entry generation in anisotropic twisted myocardium. *J. Cardiovasc. Electrophys.* 4: 412–421 (1993b).

Panfilov, A. V. & Keener, J. P. Twisted scroll waves in heterogeneous excitable media. *Int. J. Bif. Chaos* 3: 445–450 (1993c).

Panfilov, A. V. & Keener, J. P. Re-entry in three-dimensional Fitzhugh-Nagumo medium with rotational anisotropy. *Physica D* 84: 545–552 (1995).

Panfilov, A. V. & Pertsov, A. M. Ventricular fibrillation: evolution of the multiple wavelet hypothesis. *Phil. Trans. R. Soc. Lond. A* 359: 1315–1325 (2001).

Panfilov, A. V. & Rudenko, A. N. Two regimes of the scroll ring drift in the three dimensional active media. *Physica D* 28: 215–218 (1987).

Panfilov, A. V. & Vasiev, B. N. Vortex initiation in a heterogeneous excitable medium. *Physica D* 49: 107–113 (1991).

Pelzmann, B., Schaffer, P., Bernhart, E., Lang, P., Machler, H., Rigler, B. & Koidl, B. L-type calcium current in human ventricular myocytes at a physiological temperature from children with tetralogy of Fallot. *Cardiovasc. Res.* 38: 424–432 (1998).

Pereon, Y., Demolombe, S., Baro, I., Drouin, E., Charpentier, F. & Escande, D. Differential expression of KvLQT1 isoforms across the human ventricular wall. *Am. J. Physiol. Heart Circ. Physiol.* 278: H1908–H1915 (2000).

Pertsov, A. Scale of Geometric Structures Responsible for Discontinuous Propagation in Myocardial Tissue. In *Discontinuous Conduction in the Heart.*, edited by P.M. Spooner, R. W. Joyner & J. Jalife. Futura Publishing Company, Armonk, NY (1997).

Pertsov, A. M., Davidenko, J. M., Salomonsz, R., Baxter, W. T. & Jalife, J. Spiral waves of excitation underlie reentrant activity in isolated cardiac muscle. *Circ. Res.* 72: 631–650 (1993).

Pertsov, A. M. & Jalife, J. Scroll waves in three-dimensional cardiac muscle. In *Cardiac electrophysiology. From cell to bedside, 3rd edition*, edited by D. P. Zipes & J. Jalife, pp. 336–344. Saunders, Philadelphia (1995).

Pieske, B., Maier, L. S., Bers, D. M. & Hasenfuss, G. Ca^{2+} Handling and Sarcoplasmic Reticulum Ca^{2+} Content in Isolated Failing and Non-Failing Human Myocardium. *Circ. Res.* 85: 38–46 (1999).

Pieske, B., Maier, L. S., Piacentino, V., Weisser, J., Hasenfuss, G. & Houser, S. Rate Dependence of $[Na^{+}]_i$ and Contractility in Nonfailing and Failing Human Myocardium. *Circ. Res.* 106: 447–453 (2002).

Pinto, J. M. B. & Boyden, P. A. Electrical remodeling in ischemia and infarction. *Cardiovasc. Res.* 42: 284–297 (1999).

Plonsey, R. & Barr, R.C. *Bioelectricity*. Plenum Publishing Corporation, NY (1989).

Pogwizd, S. M., McKenzie, J. P. & Cain, M. E. Mechanisms underlying spontaneous and induced ventricular arrhythmias in patients with idiopathic dilated cardiomyopathy.

Circulation 98: 2404–2414 (1998).

Priebe, L. & Beuckelmann, D. J. Simulation Study of Cellular Electric Properties in Heart Failure. *Circ. Res.* 82: 1206–1223 (1998).

Pruvot, E. J., Katra, R. P., Rosenbaum, D. S. & Laurita, K. R. Role of calcium cycling versus restitution in the mechanism of repolarization alternans. *Circ. Res.* 94: 1083–1090 (2004).

Qu, Z., Kil, J., Xie, F., Garfinkel, A. & Weiss, J. N. Scroll wave dynamics in a three-dimensional cardiac tissue model: Roles of restitution, thickness, and fiber rotation. *Biophys. J.* 78: 2761–2775 (2000).

Qu, Z., Weiss, J. N. & Garfinkel, A. Cardiac electrical restitution properties and stability of reentrant spiral waves: a simulation study. *Am. J. Physiol. Heart Circ. Physiol* 276: H269–H283 (1999).

Riccio, M.L., Koller, M.L. & Gilmour Jr, R.F. Electrical restitution and spatiotemporal organization during ventricular fibrillation. *Circ. Res.* 84: 955–963 (1999).

Rice, J. J., Jafri, M. S. & Winslow, R. L. Modeling gain and gradedness of Ca^{2+} release in the functional unit of the cardiac diadic space. *Biophys. J.* 77: 1871–1884 (1999).

Rice, J. J., Winslow, R. L., Dekanski, J. & McVeigh, E. Model Studies of the Role of Mechano-sensitive Currents in the Generation of Cardiac Arrhythmias. *J. theor. Biol.* 190: 295–312 (1998).

Rogers, J. M., Huang, J., Melnick, S. B. & Ideker, R. E. Sustained reentry in the left ventricle of fibrillating pig hearts. *Circ. Res.* 92: 539–545 (2003).

Rogers, J. M., Huang, J., Smith, W. M. & Ideker, R. E. Incidence, Evolution, and Spatial Distribution of Functional Reentry During Ventricular Fibrillation in Pigs. *Circ. Res.* 84: 945–954 (1999).

Roth, B. J. & Wikswo, J. P. A bidomain model for the extracellular potential and magnetic field of cardiac tissue. *IEEE Trans. Biomed. Eng.* 33: 467–469 (1986).

Roth, B. J. & Wikswo, J. P. Electrical stimulation of cardiac tissue: a bidomain model with active membrane properties. *IEEE Trans. Biomed. Eng.* 41: 232–240 (1994).

Rudenko, A. N. & Panfilov, A. V. Drift and interaction of vortices in two-dimensional heterogeneous active medium. *Studia Biophysica* 98: 183–188 (1983).

Rush, S. & Larsen, H. A practical algorithm for solving dynamic membrane equations. *IEEE Trans. Biomed. Eng.* 25: 389–392 (1978).

Sakakibara, Y., Wasserstrom, J. A., Furukawa, T., Jia, H., Arentzen, C. E., Hartz, R. S. & Singe, D. H. Characterization of the Sodium Current in Single Human Atrial Myocytes. *Circ. Res.* 71: 535–546 (1992).

Sakmann, B. F. A. S., Spindler, A. J., Bryant, S. M., Linz, K. W. & D., Noble. Distribution of a Persistent Sodium Current Across the Ventricular Wall in Guinea Pig. *Circ. Res.* 87: 910–914 (2000).

Samie, F. H., Berenfeld, O., Anumonwo, J., Mironov, S. F., Udassi, S., Beaumont, J., Taffet, S., Pertsov, A. M. & Jalife, J. Rectification of the background potassium current: a determinant of rotor dynamics in ventricular fibrillation. *Circ. Res.* 89: 1216–1223 (2001).

Sandstede, B. & Scheel, A. Absolute versus convective instability of spiral waves. *Phys. Rev. E* 62: 7708–7714 (2000).

Saumarez, R. C. & Grace, A. A. Paced ventricular electrogram fractionation and sudden death in hypertrophic cardiomyopathy and other non-coronary heart diseases. *Cardiovasc. Res.* 47: 11–22 (2000).

Schmidt, U., J., Hajjar. R., Helm, P. A., Kim, C. S., Doye, A. A. & Gwathmey, J. K. Contribution of Abnormal Sarcoplasmic Reticulum ATPase Activity to Systolic and Diastolic Dysfunction in Human Heart Failure. *J. Mol. Cell. Cardiol.* 30: 1929–1937 (1998).

Schneider, M., Proebstle, T., Hombach, V., Hannekum, A. & Rudel, R. Characterization of the sodium currents in isolated human cardiocytes. *Pflugers Arch.* 428: 84–90 (1994).

Schram, G., Pourrier, M., Melnyk, P. & Nattel, S. Differential Distribution of Cardiac Ion Channel Expression as a Basis for Regional Specialization in Electrical Function. *Circ. Res.* 90: 939–950 (2002).

Selfridge, O. Studies on flutter and fibrillation V. Some notes on the theory of flutter. *Arch. Inst. Cardiol. de Mexico* 18: 177–187 (1948).

Sepulveda, N. G., Roth, B. J. & Wikswo, J. P. Current injection into a two-dimensional anisotropic bidomain. *Biophys. J.* 55: 987–999 (1989).

Setayeshgar, S & Bernoff, AJ. Scroll waves in the presence of slowly varying anisotropy with application to the heart. *Phys. Rev. Lett.* 88: 028101 (2002).

Severs, N. J. Gap Junction Remodeling in Heart Failure. *J. Card. Fail.* 8: S293–S299 (2002).

Shepard, R. K., Wood, M. A., Dan, D., Clemo, H. F., Gilligan, D. M. & Ellenbogen, K. A. Induction of Ventricular Fibrillation by T Wave Shocks: Observations from Monophasic Action Potential Recordings. *J. Interv. Card. Electrophysiol.* 3: 335–340 (1999).

Shiferaw, Y., Watanabe, M. A., Garfinkel, A., Weiss, J. N. & Karma, A. Model of intracellular calcium cycling in ventricular myocytes. *Biophys. J.* 85: 3666–3686 (2003).

Shimizu, H., Ohnishi, Y., Inoue, T. & Yokoyama, M. QT and JT Dispersion in Patients With Monomorphic or Polymorphic Ventricular Tachycardia/Ventricular Fibrillation. *J Electrocard.* 34: 119–125 (2001).

Shimizu, W. & Antzelevitch, C. Cellular and ionic basis for T-wave alternans under long-QT conditions. *Circulation* 99: 1499–1507 (1999).

Siegert, F. & Weijer, C. J. Three dimensional scroll waves organize dictyostelium slugs. *Proc. Natl. Acad. Sci. U.S.A.* 89: 6433–6437 (1992).

Smirnov, V. I. *A course on higher mathematics*. Pergamon Press, New York (1964).

Smith, P. L. & Yellen, G. Fast and Slow Voltage Sensor Movements in HERG Potassium Channels. *J. Gen. Physiol.* 119: 275–293 (2002).

Starmer, C. F., Lastra, A. A., Nesterenko, V. V. & Grant, A. O. Proarrhythmic response to sodium channel blockade. Theoretical model and numerical experiments. *Circulation.* 84: 1364–1377 (1991).

Steinbock, O., Kettunen, P. & Showalter, K. Anisotropy and spiral organizing centers in patterned excitable media. *Science* 269: 1857–1860 (1995).

Stellbrink, C., Mischke, K., Stegemann, E., Killmann, R., Minkenberg, R., Lu, X., Schutt, H. & Hanrath, P. Spatial features in body surface potential maps of patients with ventricular tachyarrhythmias with or without coronary artery disease. *Int. J. Cardiol.* 70: 109–118 (1999).

Streeter, D. D., Spotnitz, M. M., Patel, D. P., Ross, J. & Sonnenblick, E. H. Fiber orientation in the canine left ventricle during diastole and systole. *Circ. Res.* 24: 339–347 (1969).

Streeter, D. D. Jr. Gross morphology and fiber geometry of the heart. In *Handbook of physiology. - Section 2: The cardiovascular system, Volume I: The heart*, pp. 61–112. Am. Physiol. Soc., Bethesda, MD (1979).

Sun, H., Leblanc, N. & Nattel, S. Mechanisms of inactivation of L-type calcium channels in human atrial myocytes. *Am. J. Physiol. Heart Circ. Physiol.* 272: H1625–H1635 (1997).

Swynghedauw, B. Molecular mechanisms of myocardial remodeling. *Physiol. Rev.* 79: 215–262 (1999).

Taggart, P., Sutton, P., Chalabi, Z., Boyett, M. R., Simon, R., Elliott, D. & Gill, J. S. Effect of Adrenergic Stimulation on Action Potential Duration Restitution in Humans. *Circ. Res.* 33: 54–62 (1973).

Taggart, P., Sutton, P. M. I., Opthof, T., Coronel, R., Trimlett, R., Pugsley, W. & Kallis, P.

Inhomogeneous transmural conduction during early ischemia in patients with coronary artery disease. *J. Mol. Cell. Cardiol.* 32: 621–639 (2000).

Ten Tusscher, K. H. W. J., Noble, D., Noble, P. J. & Panfilov, A. V. A model for human ventricular tissue. *Am. J. Physiol. Heart Circ. Physiol.* 286: H1573–H1589 (2004).

Ten Tusscher, K. H. W. J. & Panfilov, A. V. Influence of nonexcitable cells on spiral breakup in two-dimensional and three-dimensional excitable media. *Phys. Rev. E* 68: 062902–1–062902–4 (2003a).

Ten Tusscher, K. H. W. J. & Panfilov, A. V. Reentry in heterogeneous cardiac tissue described by the Luo-Rudy ventricular action potential model. *Am. J. Physiol. Heart Circ. Physiol.* 284: H542–H548 (2003b).

Thomas, C. E. The muscular architecture of the ventricles of hog and dog hearts. *Am. J. Anat.* 101: 17–57 (1957).

Tolkacheva, E. G., Schaeffer, D. G., Gauthier, D. J. & Krassowska, W. Condition for alternans and stability of the 1:1 response pattern in a 'memory' model of paced cardiac dynamics. *Phys. Rev. E* 67: 031904–1–031904–10 (2003).

Ujhelyi, M. R., Sims, J. J. & Winecoff Miller, A. Induction of electrical heterogeneity impairs ventricular defibrillation. *Circulation* 100: 2534–2540 (1999).

Valderrabano, M., Lee, M. H., Ohara, T., Lai, A. C., Fishbein, M. C., Lin, S. F., Karagueuzian, H. S. & Chen, P. S. Dynamics of intramural and transmural reentry during ventricular fibrillation in isolated swine ventricles. *Circ. Res.* 88: 839–848 (2001).

Valderrabano, M., Yang, J., Omichi, C., Kil, J., Lamp, S. T., Qu, Z., Lin, S., Karagueuzian, H. S., Garfinkel, A., Chen, P. & Weiss, J. N. Frequency analysis of ventricular fibrillation in swine ventricles. *Circ. Res.* 90: 213–222 (2002).

Varnava, A. M., Elliott, P. M., Mahon, N., Davies, M. J. & McKenna, W. J. Relation between Myocyte Disarray and Outcome in Hypertrophic Cardiomyopathy. *Am. J. Cardiol.* 88: 275–279 (2001).

Virag, L., Iost, N., Opincariu, M., Szolnoky, J., Szecsi, J., Bogats, G., Szenohradszky, P., Varro, A. & Papp, J. G. The slow component of the delayed rectifier potassium current in undiseased human ventricular myocytes. *Cardiovasc. Res.* 49: 790–797 (2001).

Viswanathan, P. C., Bezzina, C. R., George, A. L., Roden, D. M., Wilde, A. A. M. & Balser, J. R. Gating-Dependent Mechanism for Flecainide Action in SCN5A-Linked Arrhythmia Syndromes. *Circulation* 104: 1200–1205 (2001).

Viswanathan, P. C. & Rudy, Y. Cellular arrhythmogenic effects of congenital and acquired long-QT syndrome in the heterogeneous myocardium. *Circulation* 101: 1192–1198 (2000).

Viswanathan, P. C., Shaw, R. M. & Rudy, Y. Effects of I_{Kr} and I_{Ks} Heterogeneity on Action Potential Duration and Its Rate Dependence, A Simulation Study. *Circulation* 99: 2466–2474 (1999).

Volders, P. G. A., Sipido, K. R., Carmeliet, E., Spatjens, R. L. H. M. G., Wellens, H. J. J. & Vos, M. A. Repolarizing K^+ Currents I_{to1} and I_{Ks} Are Larger in Right Than Left Canine Ventricular Myocardium. *Circulation* 99: 206–210 (1999).

Volders, P. G. A., Vos, M. A., Szabo, B., Sipido, K. R., De Groot, S. H. M., Gorgels, A. P. M., Wellens, H. J. J. & Lazarra, R. Progress in the understanding of cardiac early afterdepolarizations and torsade de pointes: time to revise current concepts. *Cardiovasc. Res.* 46: 376–392 (2000).

Walcott, G. P., Kay, G. N., Plumb, V. J., Smith, W. M., Rogers, J. M., Epstein, A. E. & Ideker, R. E. Endocardial Wave Front Organization During Ventricular Fibrillation in Humans. *J. Am. Coll. Cardiol.* 39: 109–115 (2002).

Waldo, A. L. Mechanisms of atrial fibrillation. *J. Cardiavasc. Electrophysiol.* 14: S267–S274 (2003).

Wan, X., Chen, S., Sadeghpour, A., Wang, Q. & Kirsch, G. E. Accelerated inactivation in a mutant Na^+ channel associated with idiopathic ventricular fibrillation. *Am. J. Physiol. Heart Circ. Physiol.* 280: H354–H360 (2001).

Wang, D. W., Makita, N., Kirabatake, A., Balser, J. R. & George, A. L. Enhanced Na^+ Channel Intermediate Inactivation in Brugada Syndrome. *Circ. Res.* 87: e37–e43 (2000).

Wang, Z., Fermini, B. & Nattel, S. Rapid and slow components of delayed rectifier current in human atrial myocytes. *Cardiovasc. Res.* 28: 1540–1546 (1994).

Warren, M., Guha, P. K., Berenfeld, O., Zaitsev, A., Anumonwo, J. M. B., Dhamoon, A. S., Bagwe, S., Taffet, S. M. & Jalife, J. Blockade of the Inward Rectifying Potassium Current Terminates Ventricular Fibrillation in the Guinea Pig. *J. Cardiovasc. Electrophysiol.* 14: 621–631 (2003).

Watanabe, M. A., Fenton, F. H., Evans, S. J., Hastings, H. M. & Karma, A. Mechanisms for Discordant Alternans. *J. Cardiovasc. Electrophysiol.* 12: 196–206 (2001).

Wehrens, X. H. T., Abriel, H., Cabo, C., Benhorin, J. & Kass, R. S. Arrhythmogenic Mechanism of an LQT-3 Mutation of the Human Heart Na^+ Channel α-Subunit. *Circulation* 102: 584–590 (2000).

Wehrens, X. H. T., Vos, M. A., Doevendans, P. A. & Wellens, H. J. J. Novel Insights in the Congenital Long QT Syndrome. *Ann. Intern. Med.* 137: 981–992 (2002).

Weidmann, S. The electrical constants of Purkinje fibres. *J. Physiol.* 118: 348–360 (1952).

Weiss, J. N., Chen, P., Qu, Z., Karagueuzian, H. S., Lin, S. & Garfinkel, A. Electrical restitution and cardiac fibrillation. *J. Cardiovasc. Electrophysiol.* 13: 292–295 (2002).

Wellner, M., Berenfeld, O., Jalife, J. & Pertsov, A. M. Minimal principle for rotor filaments. *Proc. Natl. Acad. Sci. U.S.A.* 99: 8015–8018 (2002).

Wellner, M., Berenfeld, O. & Pertsov, A. M. Predicting filament drift in twisted anisotropy. *Phys. Rev. E* 61: 1845–1850 (2000).

Wellner, M., Pertsov, A. M. & Jalife, J. Spiral drift and core properties. *Phys. Rev. E* 59: 5192–5204 (1999).

Werner, C. D., Sachse, F. B. & Dössel, O. Electrical Excitation Propagation in the Human Heart. *International Journal of Bioelectromagnetism* 2 (2000).

Wettwer, E., Amos, G. J., Posival, H. & Ravens, U. Transient Outward Current in Human Ventricular Myocytes of Subepicardial and Subendocardial Origin. *Circ. Res.* 75: 473–482 (1994).

Wiener, N. & Rosenblueth, A. The mathematical formulation of the problem of conduction of impulses in a network of connected excitable elements, specifically in cardiac muscle. *Arch. Inst. Cardiol. Mex.* 16: 205–265 (1946).

Wilders, R., Wagner, M. B., Golod, D. A., Kumar, R., Wang, Y., Goolsby, W. N., Joyner, R. W. & Jongsma, H. J. Effects of anisotropy on the development of cardiac arrhythmias associated with focal activity. *Pflügers Arch., Eur J Physiol* 441: 301–312 (2000).

Winfree, A. T. Scroll-shaped waves of chemical activity in three dimensions. *Science* 181: 937–939 (1973).

Winfree, A. T. *The geometry of biological time.* Springer-Verlag, New York, USA (1980).

Winfree, A. T. Electrical instability in cardiac muscle: phase singularities and rotors. *J. theor. Biol.* 138: 353–405 (1989).

Winfree, A. T. Electrical turbulence in three-dimensional heart muscle. *Science* 266: 1003–1006 (1994).

Winfree, A. T. & Strogatz, S. H. Organizing centers for three-dimensional chemical waves. *Nature* 311: 611–615 (1984).

Winslow, R. L., Rice, J., Jafri, S., Marban, E. & O'Rourke, B. Mechanisms of Altered Excitation-Contraction Coupling in Canine Tachycardia-Induced Heart Failure, II Model studies. *Circ. Res.* 84: 571–586 (1999).

Withers, P. C. *Comparative Animal Physiology,* chapter Circulation. Saunders College Publishing (1992).

Witkowski, F. X., Leon, L. J., Penkoske, P. A., Giles, W. R., Spano, M. L., Ditto, W. L. & Winfree, A. T. Spatiotemporal evolution of ventricular fibrillation. *Nature* 392: 78–82 (1998).

Wu, J. & Zipes, D. P. Transmural reentry during acute global ischemia and reperfusion in canine ventricular muscle. *Am. J. Physiol. Heart Circ. Physiol.* 280: H2717–H2725 (2001).

Wu, J. & Zipes, D. P. Transmural reentry triggered by epicardial stimulation during acute ischemia in canine ventricular tissue. *Am. J. Physiol. Heart Circ. Physiol.* 283: H2004–H2011 (2002).

Wu, R. & Patwardhan, A. Restitution of action potential duration during sequential changes in diastolic interval shows multimodal behavior. *Circ. Res.* 94: 634–641 (2004).

Wu, T., Lin, S., Weiss, J. N., Ting, C. & Chen, P. Two Types of Ventricular Fibrillation in Isolated Rabbit Hearts. *Circulation* 106: 1859–1866 (2002).

Wu, T. J., Ong, J. J. C., Hwang, C., Lee, J. J., Fishbein, M. C., Czer, L., Trento, A., Blanche, C., Kass, R. M., Mandel, W.J., Karagueuzian, H. S. & Chen, P. Characteristics of Wave Fronts During Ventricular Fibrillation in Human Hearts With Dilated Cardiomyopathy: Role of Increased Fibrosis in the Generation of Reentry. *J. Am. Coll. Cardiol.* 32: 187–196 (1998).

Xie, F., Qu, Z., Garfinkel, A. & Weiss, J. N. Effects of simulated ischemia on spiral wave stability. *Am. J. Physiol. Heart Circ. Physiol.* 280: H1667–H1673 (2001a).

Xie, F., Qu, Z., Garfinkel, A. & Weiss, J. N. Electrophysiological heterogeneity and stability of reentry in simulated cardiac tissue. *Am. J. Physiol. Heart. Circ. Physiol.* 280: H535–H545 (2001b).

Xie, F., Qu, Z., Yang, J., Baher, A., Weiss, J. N. & Garfinkel, A. A simulation study of the effects of cardiac anatomy in ventricular fibrillation. *J. Clin. Invest.* 113: 686–693 (2004).

Yan, G., Wu, Y., Liu, T., Wang, J., Marinchak, R. A. & Kowey, P. R. Phase 2 early afterdepolarization as a trigger of polymorphic ventricular tachycardia in acquired long-QT syndrome. *Circulation* 103: 2851–2856 (2001).

Yue, L., Feng, J., Li, G. R. & Nattel, S. Transient outward and delayed rectifier currents, properties and role of isolation methods. *Am. J. Physiol. Heart Circ. Physiol.* 270: H2157–68 (1996).

Zaikin, A. N. & Zhabotinsky, A. M. Concentration wave propagation in two-dimensional liquid-phase self-organizing system. *Nature* 225: 535–537 (1970).

Zaitsev, A.V., Berenfeld, O., Mironov, S.F., Jalife, J. & Pertsov, A.M. Distribution of excitation frequencies on the epicardial and endocardial surfaces of fibrillating ventricular wall of the sheep heart. *Circ. Res.* 86: 408–417 (2000).

Zeng, J., Laurita, K. R., Rosenbaum, D. S. & Rudy, Y. Two components of the delayed rectifier K^+ current in ventricular myocytes of the guinea pig type. Theoretical formulation and their role in repolarization. *Circ. Res.* 77: 140–152 (1995).

Zevitz, M. E. Ventricular Fibrillation [online] <www.emedicine.com/med/topic2363.html> (2004).

Zhou, Z., Gong, Q., Ye, B., Fan, Z., Makielski, J. C., Robertson, G. A. & January, C. T. Properties of HERG Channels Stably Expressed in HEK 293 Cells Studied at Physiological Temperatures. *Biophys. J.* 74: 230–241 (1998).

Zygmunt, A. C., Eddlestone, G. T., Thomas, G. P., Nesterenko, V. V. & Antzelevitch, C. Larger late sodium conductance in M cells contributes to electrical heterogeneity in canine ventricle. *Am. J. Physiol. Heart. Circ. Physiol.* 281: H689–H697 (2001).

Zygmunt, A. C., Goodrow, R. J. & Antzelevitch, C. I_{NaCa} contributes to electrical heterogeneity within the canine ventricle. *Am. J. Physiol. Heart. Circ. Physiol.* 278: H1671–H1678

(2000).

Zykov, V. S. Analytical evaluation of the dependence of the speed of an excitation wave in a two dimensional excitable medium on the curvature of its front. *Biophys.* 25: 906–911 (1980).

Zykov, V. S. *Simulation of wave processes in Excitable Media*. Manchester University Press, Manchester, UK (1987).

Samenvatting

In dit proefschrift wordt onderzoek gedaan naar hartritmestoornissen door middel van numerieke simulatie van wiskundige modellen.

Onder normale omstandigheden bepaalt de sinusknoop, ook wel de pacemaker van het hart genoemd, de frequentie waarmee het hart samentrekt. Eerst trekken de beide atria (boezems) samen, zodat het bloed uit de atria naar de ventrikels (kamers) wordt gepompt. Vervolgens trekken de beide ventrikels samen, zodat het bloed uit de ventrikels naar de longen (rechter ventrikel) en de rest van het lichaam (linker ventrikel) wordt gepompt. Hartritmestoornissen, ook wel aritmieën genaamd, zijn afwijkingen in de timing, volgorde en coördinatie van de contractie van de hart spier. Er zijn heel veel verschillende aritmieën, variërend in ernst van hartkloppingen tot hartritmestoornissen die binnen een paar minuten dodelijk zijn. Hartritmestoornissen behoren daarmee tot een van de meest voorkomende doodsoorzaken. Daarom wordt er veel onderzoek verricht om de precieze oorzaken en mechanismen van aritmieën te achterhalen.

De contractie van individuele hartspiercellen wordt getriggerd door een elektrisch signaal dat 'excitatie' of 'actiepotentiaal' wordt genoemd. Dit elektrische signaal wordt gevormd door ionstromen die door eiwitkanalen in de celmembraan van hartspiercellen lopen. De cellen in de sinusknoop genereren dit elektrische signaal spontaan met een bepaalde frequentie. Doordat de cellen in het hart elektrisch aan elkaar gekoppeld zijn geven de sinusknoop cellen op het moment dat ze een actiepotentiaal genereren een elektrisch stroompje door aan hun buurhartspiercellen. Normale, niet-sinusknoop hartspiercellen kunnen niet spontaan een actiepotentiaal genereren. Echter, deze spiercellen kunnen wel een actiepotentiaal genereren als ze gestimuleerd worden door een elektrische stroompje afkomstig van een buurcel. Samen zorgt dit er voor dat in de sinusknoop golven van elektrische activiteit ontstaan die door de elektrische koppeling tussen de hartspiercellen zich snel over eerst de atria en daarna de ventrikels verspreiden om daar tot spiercontractie te leiden. In de meeste hartritmestoornissen is een afwijking in de propagatie van deze excitatie golf de oorzaak voor de afwijking in de hartspiercontractie.

Naast het experimentele en klinische onderzoek dat wordt verricht aan hartritmestoornissen, wordt er ook veel onderzoek aan aritmieën gedaan met behulp van modellen. Hiervoor zijn twee belangrijke redenen. De eerste reden is dat het gedrag van modellen over het algemeen beter te controleren en begrijpen is dan het gedrag van het complexe werkelijke systeem waarop het gebaseerd is. Ten tweede is er een aantal praktische en ethische beperkingen aan experimenteel onderzoek naar hartritmestoornissen. Een belangrijke beperking is dat in experimenten de excitatie golfpatronen die ten grondslag liggen aan de hartritmestoornis alleen aan het oppervlak van het hart kunnen worden waargenomen. Wat zich binnen in de dikke wand van de ventrikels afspeelt blijft hierdoor onduidelijk. Dergelijke beperkingen gelden niet voor modelonderzoek en modellen zijn daarom uitermate geschikt om te onderzoeken welke driedimensionale excitatie patronen ten grondslag kunnen liggen aan de experimenteel waargenomen oppervlakte golfpatronen.

In dit proefschrift kijken we naar twee specifieke hartritmestoornissen, namelijk ventriculaire tachycardie en ventriculaire fibrillatie. Bij deze aritmieën is er sprake van een afwijkende excitatie en contractie in de ventrikels van het hart. Ventriculaire tachycardie wordt gekenmerkt door een verhoogde frequentie waarmee de ventrikels samentrekken. Omdat de ventrikels hierdoor minder tijd hebben om zich met bloed afkomstig van de atria te vullen, leidt dit tot een verminderde uitstroom van bloed uit de ventrikels en dus tot een afname van de zuurstofvoorziening van het lichaam. Ventriculaire fibrillatie wordt gekenmerkt door een nog hogere frequentie waarmee de ventrikels samentrekken. Bovendien trekken de ventrikels niet langer als één geheel synchroon samen. In plaats daarvan trekken verschillende delen van de ventrikels volledig ongecoördineerd en uit fase samen. Door dit asynchrone samentrekken werken de ventrikels niet langer als een effectieve pomp, en neemt de uitstroom van bloed uit de ventrikels af tot bijna nul. Aangezien dit leidt tot het stilvallen van de zuurstofvoorziening van het lichaam is ventriculaire fibrillatie binnen een paar minuten dodelijk.

Uit studies naar excitatie golf dynamica in simpele modellen van exciteerbare media is het idee naar voren gekomen dat (ventriculaire) tachycardie veroorzaakt wordt door een golf in de vorm van een spiraal. Een spiraalvormige golf kan ontstaan als een normale vlakke golf een niet-geleidend obstakel tegenkomt, hierdoor opbreekt in twee stukken golf met een vrij uiteinde, en deze vrije uiteinden vervolgens omkrullen om twee spiraal golven te vormen. Spiraal golven roteren met een hoge frequentie. Het bijzondere van spiraal golven is bovendien dat ze niet zoals een normaal vlak golffront maar een keer langskomen en het weefsel exciteren, maar ronddraaien en daardoor steeds opnieuw het weefsel exciteren. Als een dergelijke spiraal golf ontstaat in de ventrikels wordt de excitatie- en contractiefrequentie van de ventrikels niet langer bepaald door de sinusknoop, maar door de spiraal golf. De hoge rotatiefrequentie van de spiraal golf leidt zo tot een verhoogde frequentie van de ventriculaire excitatie en contractie. Het optreden van spiraal golven in hartspierweefsel is experimenteel aangetoond (Allessie *et al.*, 1973; Davidenko *et al.*, 1990; Pertsov *et al.*, 1993).

Uit modelstudies blijkt dat niet alle spiraal golven stabiel zijn, maar dat sommige fragmenteren. Dit fragmentatieproces leidt tot een chaotisch golfpatroon bestaande uit vele verschillende golf fragmenten en kleine spiraal golven, die continu gevormd worden door verdere fragmentatie en weer verdwijnen door botsing met elkaar of de rand van het weefsel. Dit golfpatroon leidt tot een excitatie dynamica die sterk overeenkomt met de dynamica tijdens fibrillatie. Op grond hiervan is het idee ontstaan dat (ventriculaire) fibrillatie wordt veroorzaakt door de fragmentatie van een spiraalvormige excitatie golf. Echter, er is tot nu toe geen hard experimenteel bewijs voor deze hypothese. Het probleem is dat, inherent aan de fibrillatie dynamica, het excitatie patroon ongeorganiseerd is en daardoor moeilijk te interpreteren. Bovendien kan in experimenten alleen de excitatie golfdynamica op het oppervlak van het hart worden waargenomen, terwijl de dikke wand van de ventrikels er voor zorgt dat de excitatie dynamica een driedimensionaal (3D) proces is. Dit betekent dat slechts een klein deel van de werkelijk optredende dynamica kan worden waargenomen in experimenten.

In het eerste deel van dit proefschrift wordt gekeken naar de invloed van bepaalde heterogeniteiten op de dynamica van spiraal golven. Het gaat hierbij om heterogeniteiten die optreden in normaal gezond hartweefsel en om heterogeniteiten die voorkomen in ziek hartweefsel dat gevoeliger is voor aritmieën.

In **hoofdstuk 2** kijken we naar de invloed van gradiënten in de grootte van transmembraan ionstromen op de dynamica van spiraal golven. De grootte van deze ionstromen beïnvloedt de duur van de actiepotentiaal en de duur van de rotatie periode van de spiraal golf. Dergelijke gradiënten in ionstromen en actiepotentiaal duur zijn aanwezig in het normale, gezonde hart. Voorbeelden zijn de gradiënt van boven naar onder in de ventrikels, de gradiënt van het linker naar het rechter ventrikel en de gradiënt van de binnenkant naar de buitenkant van de hartwand. Deze spatiale gradiënten zorgen ervoor dat de actiepotentiaal van cellen die het eerst geëxciteerd worden het langst duurt en die van cellen die het laatst geëxciteerd worden het kortst duurt. Dit leidt tot een synchronisatie van het einde van de actiepotentialen over het hart. In bepaalde hartziektes kunnen aanwezige gradiënten versterkt worden of nieuwe gradiënten ontstaan. In de afwezigheid van gradiënten roteert de kern van een spiraal golf rondom een vaste plaats in het medium. Dit betekent dat er geen netto verplaatsing van de spiraal golf optreedt. We laten in deze studie zien dat gradiënten leiden tot een netto verplaatsing van de spiraal golf. Deze verplaatsing treedt altijd op in de richting van de langste spiraal rotatie periode. De verplaatsingssnelheden die we vinden zijn in de orde van 2mm/s voor een spiraal rotatie periode gradiënt van 0.2ms/mm. Dergelijke snelheden leiden tot een significante Doppler verschuiving van de rotatie frequentie van de spiraal golf. Dit zorgt ervoor dat het electrocardiogram (ECG) van een zich verplaatsende spiraal golf minder periodiek is dan het ECG van een zich niet verplaatsende spiraal golf, en daardoor meer lijkt op het ECG van patiënten met polymorfe (=onregelmatige) dan monomorfe (=regelmatige) ventriculaire tachycardie.

In **hoofdstuk 3** bestuderen we de invloed van veel kleine, willekeurig verspreide, niet-geleidende obstakels op de vorming en stabiliteit van spiraal golven. Het grote aantal kleine obstakels staat model voor een diffuse verspreiding van bindweefsel in de hartspier. Bindweefsel doet niet mee aan het excitatie proces en vormt derhalve niet-geleidende obstakels. Uit klinische studies blijkt dat mensen met een hart met een vergrote hoeveelheid bindweefsel een sterk vergrote kans op ventriculaire tachycardie en fibrillatie hebben. De toegenomen hoeveelheid bindweefsel kan zowel gelokaliseerd in grote strengen als in diffuus verspreide kleine stukken optreden. Wij onderzoeken hier het effect van het laatste type bindweefsel verspreiding. We laten zien dat grote aantallen kleine obstakels leiden tot een verhoogde kwetsbaarheid van het medium voor de vorming van spiraal golven (=tachycardie). We vinden echter niet dat de obstakels het weefsel kwetsbaarder maken voor spiraal fragmentatie (=fibrillatie). We vinden juist dat de obstakels spiraal fragmentatie onderdrukken. Dit laatste resultaat lijkt dus in tegenspraak te zijn met de klinische data. Een mogelijke verklaring voor deze tegenstelling is dat alleen grote strengen bindweefsel de kans op fibrillatie vergroten en dat dit niet het geval is voor kleine stukken diffuus verspreid bindweefsel. Een andere mogelijkheid is dat andere veranderingen in weefseleigenschappen die meestal samen met de toegenomen hoeveelheid bindweefsel optreden -veranderingen in exciteerbaarheid, duur van de actiepotentiaal, elektrische koppeling tussen de cellen, etcetera- een belangrijke rol spelen bij het ontstaan van fibrillatie.

Een tweedimensionale spiraal golf roteert om een bepaald punt dat de kern van de spiraal golf vormt. Een driedimensionale spiraal golf kunnen we ons voorstellen als een stapel van tweedimensionale spiraal golven. Een driedimensionale spiraal golf roteert dus om een hele verzameling van punten, die samen een lijn vormen die ‘filament’ wordt genoemd. Uit eerder onderzoek is gebleken dat de vorm van dit filament, en dus ook de vorm van de 3D spiraal golf die er omheen roteert, bepaald wordt door de excitatie voortgeleidingseigenschappen van het medium. In de ventrikels hangt de voortgeleidingssnelheid op een complexe manier af van de richting waarin de golf zich voortplant en de plaats in de ventrikelwand. Dit komt doordat hartspierweefsel is georganiseerd in spierbundels, waarlangs de snelste voortgeleiding plaatsvindt, en het feit dat de oriëntatie van deze spierbundels op een complexe manier door de hartwand heen variëert. Wellner *et al.* (2002) hebben recent laten zien dat de vorm van een filament van een 3D spiraal golf analytisch kan worden voorspeld. Het nadeel van hun voorspellingsmethode is echter dat a priori kennis over de positie van het filament in het medium en de voortgeleidingseigenschappen van het medium beschikbaar moet zijn. Dit zijn gegevens die met name voor echt hartspierweefsel vaak niet bekend zijn. In **hoofdstuk 4** leiden wij af dat het filament van een 3D spiraal golf overeenkomt met het pad van kortste reistijd voor een vlakke golf die door het medium loopt. Dit betekent dat we een filament kunnen voorspellen door de propagatie van een vlakke golf door een medium te simuleren en met een simpel algoritme het kortste golf pad te bepalen. Onze voorspellingsmethode voorspelt naast de filament vorm ook de filament positie. Bovendien vereist onze methode geen voorkennis van de voortgeleidingseigenschappen van het medium of de positie van het filament in het medium. Dit betekent dat onze methode kan worden toegepast op echt hartspierweefsel. Het voordeel van het kunnen voorspellen van filament positie en vorm is dat we op die manier de meest waarschijnlijke posities voor spiraal golven in de hartwand kunnen bepalen.

In het tweede deel van dit proefschrift wordt een gedetailleerd model voor het exciteerbare gedrag van de menselijke ventrikels ontwikkeld. Dit model wordt vervolgens gebruikt om kwalitatieve én kwantitatieve eigenschappen van menselijke ventriculaire tachycardie en fibrillatie -gesimuleerd in dit model- te bestuderen.

Als eerste stap ontwikkelen we in **hoofdstuk 5** een model voor het exciteerbare gedrag van individuele menselijke ventriculaire hartspiercellen. De meeste modellen beschrijven het gedrag van dierlijke hartspiercellen. Echter, het gedrag van dierlijke hartspiercellen en harten verschilt onderling en van dat van de mens in factoren zoals grootte van het hart, bereik van normale hartslagfrequenties, ionstromen die van belang zijn voor het vormen van de actiepotentiaal, duur van de actiepotentiaal, frequenties en golfpatronen tijden hartritmestoornissen, etcetera. Vanwege deze verschillen gebruiken we liever een model voor menselijke ventriculaire cellen om meer inzicht te krijgen in aritmieën in het menselijk hart. Het enige model voor menselijke ventriculaire cellen dat al bestond is geformuleerd toen er nog vrij weinig gegevens voor menselijke hartspiercellen beschikbaar waren. Het nieuwe model dat wij geformuleerd hebben is gebaseerd op recente experimentele data over ionstromen in menselijke hartspiercellen. Om ons celmodel te verifiëren simuleren we ionstromen, actiepotentialen, intracellulaire ionconcentraties en excitatie golfpropagatie snelheden voor verschillende hartslagfrequenties. Vervolgens vergelijken we het gedrag van ons celmodel met een uitgebreide set experimentele observaties aan hartspiercellen. We laten zien dat ons model goed in staat is om het gedrag van individuele hartspiercellen te reproduceren.

In **hoofdstuk 6** combineren we ons nieuwe model voor menselijke ventriculaire cellen met een anatomisch gedetailleerde geometrie van de menselijke ventrikels. We gebruiken dit ventrikel model om de dynamica van ventriculaire tachycardie en fibrillatie in het menselijk hart te onderzoeken. We laten zien dat voor de standaard parameter setting van ons ventriculaire celmodel, die overeenkomt met de condities in gezond menselijk hartspierweefsel, een kunstmatig geïnduceerde spiraal golf een stabiele dynamica heeft. Het ECG, het frequentie spectrum en de dominante frequentie van deze stabiele spiraal golf komen overeen met die van patiënten met ventriculaire tachycardie. We vinden een alternatieve parameter setting voor ons model die leidt tot fragmentatie van de geïnduceerde spiraal golf. Het ECG en de activatie frequentie van het excitatie golfpatroon dat optreedt na spiraal fragmentatie komen overeen met de ECGs en activatie frequenties van patiënten met ventriculaire fibrillatie. Bovendien komen de gesimuleerde golfpatronen die optreden op het oppervlak van ons ventrikel model goed overeen met de oppervlakte golfpatronen waargenomen tijdens ventriculaire fibrillatie in menselijke harten door Nanthakumar *et al.* (2004). Als laatste kwantificeren we het aantal spiraal golven dat aanwezig is in de ventrikels tijdens fibrillatie. We laten zien dat als we alleen kijken naar de golfpatronen die zichtbaar zijn op het oppervlak van de ventrikels, we zelden een spiraal golf zien. Echter, als er wordt gekeken naar de volledige 3D golfpatronen die optreden in de ventrikels, zien we dat er continu een aantal spiraal golven aanwezig is. Een belangrijke uitkomst van ons onderzoek is dat het aantal spiraal golven tijdens fibrillatie rond de 6 ligt, terwijl in veel eerdere modelstudies aantallen tussen de 40 en 110 werden gevonden. Dit impliceert dat de golfdynamica gedurende fibrillatie een stuk georganiseerder en minder chaotisch is dan eerder werd aangenomen.

Samenvattend: In deel I van dit proefschrift hebben we onderzoek gedaan naar de invloed van verschillende typen heterogeniteiten op spiraal golfdynamica. De onderzochte heterogeniteiten waren gebaseerd op condities die optreden in gezonde danwel zieke harten. We hebben laten zien dat deze heterogeniteiten een belangrijke invloed hebben op het ontstaan, de dynamica en de stabiliteit van spiraal golven en hebben dit vertaald naar het gedrag en type van de optredende hartritmestoornis. In deel II van dit proefschrift is een model ontwikkeld dat een gedetailleerde beschrijving van het exciteerbare gedrag van menselijke ventrikel cellen combineert met een gedetailleerde beschrijving van de menselijke ventriculaire anatomie. We hebben laten zien dat we met behulp van dit model kwantitatief onderzoek naar menselijke ventriculaire hartritmestoornissen kunnen verrichten.

Curriculum Vitæ

De auteur van dit proefschrift, Kirsten Hendrika Wilhelmina Johanna ten Tusscher, oftewel Kirsten, werd geboren op 23 februari 1976 in Enschede. Vanaf augustus 1988 tot mei 1994 bezocht zij de Scholengemeenschap Holten, waar zij in juni 1994 het VWO diploma cum laude behaalde. In september 1995 begon zij aan haar studie Biologie aan de Universiteit Utrecht. In september 1996 behaalde zij haar propadeuse Biologie cum laude. In het studiejaar 1997-1998 maakte ze een tijdelijke overstap naar het eerste jaar van Computational Sciences. In 1998 keerde ze terug naar de faculteit Biologie voor een onderzoeksstage bij de vakgroep Theoretische Biologie / Bioinformatica gevolgd door een onderzoeksstage bij de faculteit Informatica van de Universiteit van Amsterdam. In november 2000 behaalde zij haar doctoraal diploma Biologie met als specialisatie Theoretische Biologie / Bioinformatica. Van januari 2001 tot november 2004 was zij werkzaam als onderzoeker in opleiding (OIO) bij de vakgroep Theoretische Biologie / Bioinformatica aan de Universiteit Utrecht, begeleid door Dr. A.V. Panfilov en Prof. P. Hogeweg. De resultaten van dit onderzoek staan beschreven in dit proefschrift.

The author of this thesis, Kirsten Hendrika Wilhelmina Johanna ten Tusscher, or shortly Kirsten, was born on February 23th, 1976 in Enschede, The Netherlands. From August 1988 till May 1994 she attended the Scholengemeenschap Holten in Holten, where she obtained her VWO diploma in June 1994 cum laude. In September 1995 she started her studies at the faculty of Biology of the Utrecht University. In September 1996 she gained her propædeutic diploma cum laude. In the college year 1997-1998 she made a temporary switch to the first year of the faculty of Computational Sciences. She returned to the faculty of Biology in 1998 for a research project in the Theoretical Biology / Bioinformatics group, followed by a research project at the faculty of Informatics at the University of Amsterdam. In November 1999 she obtained her Master's degree in Biology with a specialization in Theoretical Biology / Bioinformatics. From January 2001 till November 2004 she worked as a postgraduate student in the Theoretical Biology / Bioinformatics group, supervised by Dr. A.V. Panfilov and Prof. P. Hogeweg. The results of this research are described in this thesis.

List of Publications

Ten Tusscher, K. H. W. J. & Panfilov, A. V. Reentry in heterogeneous cardiac tissue described by the Luo-Rudy ventricular action potential model. *Am. J. Physiol. Heart Circ. Physiol.* 284: H542–H548 (2003a).

Ten Tusscher, K. H. W. J. & Panfilov, A. V. Influence of nonexcitable cells on spiral breakup in two-dimensional and three-dimensional excitable media. *Phys. Rev. E* 68: 062902–1–062902–4 (2003b).

Ten Tusscher, K. H. W. J., Noble, D., Noble, P. J. & Panfilov, A. V. A model for human ventricular tissue. *Am. J. Physiol. Heart Circ. Physiol.* 286: H1573–H1589 (2004).

TenTusscher, K. H. W. J. & Panfilov, A. V. Eikonal formulation of the minimal principle for scroll wave filaments. *Phys. Rev. Lett.* 93: 108106–1–108106–4 (2004).

Ten Tusscher, K. H. W. J. & Panfilov, A. V. Studies of reentrant arrhythmias in a detailed model of human ventricular tissue. *Heart Rhythm* 1: S85 (2004).

Panfilov, A. V. & Ten Tusscher, K. H. W. J. Predicting shapes of transmural filaments of reentrant arrhythmias in the ventricles of the heart. *Heart Rhythm* 1: S224 (2004).

TenTusscher, K. H. W. J. & Panfilov, A. V. Wave propagation in excitable media with randomly distributed obstacles. *SIAM Multiscale Modeling and Simulation*, in press.

Dankwoord

Op deze plek wil ik graag iedereen bedanken die op directe dan wel indirecte wijze heeft bijgedragen aan het tot stand komen van dit proefschrift. Op de eerste plaats wil ik natuurlijk Sacha Panfilov, mijn co-promotor en directe begeleider bedanken. Ik heb veel van je geleerd over exciteerbare media, spiraal golven, numerieke simulaties en het schrijven van artikelen en kon altijd met de deur in huis komen binnen vallen met problemen en ideeën. Ik ben blij dat we onze goede samenwerking in de toekomst zullen voortzetten. Ook mijn promotor Paulien Hogeweg wil ik op deze plek graag bedanken voor haar enorme enthousiasme, haar creatieve ideeën, haar vermogen tot inspiratie en voor het in het laatste jaar regelmatig een vinger aan de pols houden om te kijken hoe alles ging.

Many thanks also to Denis and Penny Noble, whom I visited a number of times in Oxford, for their hospitality, the nice scientific discussions and fruitfull collaboration. Thanks also to Richard Clayton for inviting me to an interesting and inspiring workshop in Leeds.

Ik wil ook Ronald Wilders, Jeroen van Boxtel, Olivier Bernus en Christian Zemlin bedanken voor nuttige discussies over mijn onderzoek. Dank ook aan de mensen op het SARA, Wim Rijks, Willem Vermin, Bert van Corler, Ron Trompert en Anton Koning, die mij hebben geholpen met het geschikt maken van een aantal van mijn source codes voor de supercomputer en het gebruik van de supercomputer.

Heel erg blij ben ik met de gezellige werkomgeving op de vakgroep en allen die daartoe hebben bijgedragen. Stan, en Ludo, jullie waren OIO toen ik hier ooit als student begon stage te lopen en hebben me met veel geduld computerwegwijs gemaakt. Stan heeft daarnaast als locale latex-goeroe een essentiële rol gespeeld bij het tot stand komen van de technische kanten van dit proefschrift. Jan Kees speelt als systeembeheerder een onmisbare rol in het reilen en zeilen van de vakgroep. Hij heeft bovendien een belangrijke rol gespeeld in het tot stand komen van het onderzoek beschreven in hoofdstuk 6 van dit proefschrift, door te zorgen voor een vlekkeloos functionerend Beowulf cluster waarop ik mijn grote simulaties kon draaien. Verder is Jan Kees een gezellige kamergenoot die gelukkig bestand is tegen mijn enorme papierchaos. Rob, Can, Jose, Hester, Marian, Maite, Eveline, Freek, Pieter, Edwin, Otto, Boris, Milan, Anton, Daniel en Nobuto wil ik bedanken voor alle gezelligheid en onze gesprekken over zaken die ons bezighouden binnen en buiten de wetenschap.

Ik wil mijn loopmaatjes bij atletiekverening Phoenix bedanken voor alle gezelligheid en voor de sportieve ontlading die ik soms nodig had als er een hardnekkig probleem of bug de kop op had gestoken. Mijn oud-huisgenootjes Marieke, Lenneke, Ruben, Esther, Erica en Michel wil ik bedanken voor gezellige kerstdiners en feestjes en het delen van veel lief en leed.

Mijn lieve vrienden Marieke en Dirk, Lennart en Femke, Mirjan, Natascha, en Paula wil ik bedanken voor alle leuke dingen die we samen gedaan hebben, en het aanhoren van al mijn onderzoeksverhalen. Bedankt ook Marieke dat je mijn paranimf wilt zijn.

Dan wil ik natuurlijk mijn ouders bedanken, zij hebben me gemaakt tot wie ik ben en me altijd onvoorwaardelijk gesteund. Bedankt mam, voor alle gezelligheid thuis en over de telefoon. Ik ben er trots op dat ik zoveel op je lijk. Bedankt pap, voor alle geplakte banden, geschilderde kamers en goede adviezen. Ik ben ontzettend blij dat je bij mijn promotie zult zijn en hoop dat je nog bij veel belangrijke gebeurtenissen in mijn leven zult zijn. Ik wil ook Birkitt-Linn bedanken voor het zijn van mijn kleine zusje, voor alle klets-, stap- en winkelplezier, voor alle steun in moeilijke periodes en voor dat je mijn paranimf wilt zijn.

Lieve Harald, tenslotte, bedankt voor al je liefde, geduld, rust en steun, voor het aanhoren van al mijn onderzoeksperikelen, voor het opbellen waar ik toch bleef als ik weer eens achter mijn computer op de Uithof was blijven plakken omdat ik nog héél even het verloop van een simulatie wilde checken, en voor al je leuke ideeën voor uitjes en vakanties waarvan er hopelijk nog vele zullen volgen.